
The Formation and Early Evolution of Protostellar Disks around Low-Mass Stars

Stefanie Walch



München 2008

The Formation and Early Evolution of Protostellar Disks around Low-Mass Stars

Stefanie Walch

Dissertation
an der Fakultät für Physik
der Ludwig–Maximilians–Universität
München

vorgelegt von
Stefanie Walch
geb. am 30. Juli 1979 in Landshut

München, den 09.10.2008

Erstgutachter: Prof. Dr. Andreas Burkert

Zweitgutachter: Prof. Dr. Harald Lesch

Tag der mündlichen Prüfung: 20.11.2008

*Wie alles sich zum Ganzen webt,
Eins in dem andern wirkt und lebt!
Wie Himmelskräfte nieder steigen
Und sich die goldnen Eimer reichen!
Mit segenduftenden Schwingen
Vom Himmel durch die Erde dringen,
Harmonisch all das All durchklingen!*

*Welch Schauspiel! Aber ach! ein Schauspiel nur!
Wo faß ich dich, unendliche Natur?*

Johann Wolfgang Goethe
"Faust"
Der Tragödie erster Teil
447ff

Contents

Zusammenfassung	xv
1 Introduction	1
1.1 Motivation	1
1.2 Scientific Aims	4
2 From Molecular Clouds to Protostars: Observations and Theory	7
2.1 From Molecular Clouds to Prestellar Cores	7
2.1.1 Molecular Clouds: Dark and turbulent	7
2.1.2 Molecular Cloud Cores: Sites of Star Formation	9
2.2 From prestellar cores to protoplanetary disks	17
2.3 Theoretical background	21
2.3.1 Theoretical Ansatz	21
2.3.2 Recent numerical investigations	23
3 Numerical Method: Smoothed Particle Hydrodynamics	27
3.1 Equations of fluid dynamics	28
3.1.1 Continuity equation	28
3.1.2 Euler equation	29
3.2 Equations describing the SPH algorithm	30
3.3 SPH Artificial Viscosity	33
3.4 Integration and Time stepping	34
3.5 MACs and Tree	36
3.6 Boundary Conditions	37
3.7 Cooling Implementation	37
3.8 Resolution	40
4 Protostellar disks in low-mass star formation I	43
4.1 Initial Conditions	44
4.2 Protostellar disk formation: Low angular momentum case	46
4.2.1 Phase I: Isothermal collapse	48
4.2.2 Phase II: Protostellar disk formation	48
4.3 Protostellar disk formation: High angular momentum case	56

4.4	Mass Infall and Accretion	65
4.5	Temperature evolution	68
4.6	Conclusions	70
5	Disk structure as a function of core angular momentum	73
5.1	Core sample	73
5.2	Disk structure, mass and evolution	75
5.3	Disk Fragmentation	79
5.4	Summary: Disk formation as a function of core angular momentum	83
5.5	Conclusions	86
6	Fragmentation properties of observed molecular cloud cores	89
6.1	A critical mean disk density for fragmentation	89
6.2	Application to observations	91
6.3	Conclusions	94
7	Protostellar disks in low-mass star formation II	97
7.1	Turbulent velocities as a source of core angular momentum	98
7.2	Core sample	102
7.3	The global structure of turbulent core collapse	103
7.4	Protostellar disk formation in turbulent core collapse	116
	7.4.1 Quantitative Analysis	121
	7.4.2 Qualitative Analysis	130
7.5	The (re-)distribution of angular momentum	135
7.6	Conclusions	140
8	Summary & Outlook	143
	Acknowledgments / Danksagung	163
	Curriculum Vitae Resume	165

List of Figures

1.1	Initial Mass function of dense cores and stars	3
2.1	NICER extinction map of the Pipe Nebula.	8
2.2	Morphologies of colliding flows	10
2.3	Bonnor-Ebert density contrast vs outer radius	13
2.4	The Eagle Nebula in different hues of IR light	14
2.5	Column density and velocity gradient maps of dense cores	15
2.6	Typical pre-main sequence evolution of a low-mass star	19
2.7	Continuum HST images of edge-on protoplanetary disks.	20
2.8	Theoretical structure of a protoplanetary disk	21
3.1	Sketch of the SPH Kernel	32
3.2	Cooling rate as a function of density	40
3.3	Jeans mass as a function of density	42
4.1	Radial density profile within a slowly rotating, collapsing core.	47
4.2	Protostellar disk formation for low j	49
4.3	Radial density profile after a central object has formed.	50
4.4	Evolution of the radial temperature profile.	51
4.5	Evolution of the radial velocity vs radius.	52
4.6	Azimuthal velocity profile in case of low angular momentum.	54
4.7	Vertical density distribution at three different radii.	55
4.8	Ratio of disk pressure scale height and disk radius.	55
4.9	Protostellar disk formation in case of high angular momentum.	57
4.10	A zoom showing the inner region at $t_0 + 33.7$ kyrs.	58
4.11	Radial density profile in case of high angular momentum.	59
4.12	Radial temperature profile of Run 7.	59
4.13	Circumfragmentary disks.	61
4.14	Azimuthal velocity profiles in case of high rotation.	63
4.15	Radial velocity profile of Run 7.	64
4.16	Vertical density distribution in case of high angular momentum.	64
4.17	Time evolution of the stellar masses in Run 1 and Run 7.	66
4.18	Ratio of accretion and infall rate as a function of time.	66

4.19	Disk masses within different threshold densities.	69
4.20	Evolution of the mean disk temperature.	70
4.21	Temperature of SPH particles as a function of SPH density	71
5.1	Comparison of the evolving disk masses	75
5.2	Stellar mass as a function of time.	76
5.3	Time evolution of the disk concentration.	80
5.4	Toomre Q parameter and ratio of cooling time scale to dynamical time scale.	81
5.5	Disk formation as a function of core angular momentum	84
5.6	Properties of the forming star+disk system as a function of initial core rotation rate	85
6.1	Mean disk density as a function of β	91
6.2	Mean disk density expected for the observed samples	93
7.1	Calculated number distribution of specific angular momenta	99
7.2	Observed distribution of specific angular momenta	99
7.3	Filament structure in Run T1b	104
7.4	Filament structure in Run T1d	105
7.5	Filament structure in Run T1f	105
7.6	Filament structure in Run T6d	106
7.7	Global structure of Run 6d	107
7.8	Positions of forming protostellar objects in all turbulent simulations.	109
7.9	Histogram summarising the radial position of all forming protostars.	110
7.10	Cut through the $z = 0$ plane of two turbulent velocity setups.	111
7.11	Early evolution of $\rho(R)$ for two turbulent runs	112
7.12	Early core evolution of T1b.	113
7.13	Early core evolution of T6d.	114
7.14	Ratio of turbulent kinetic and potential energy for turbulent setups.	115
7.15	Further evolution of T1b up to t_0	117
7.16	Growth of protostellar objects in turbulent simulations.	118
7.17	The most important properties at $t_{\text{turb,fin}}$	119
7.18	Final stages of different turbulent simulations.	120
7.19	Mass infall and accretion rates	124
7.20	Disk concentration of turbulent runs.	125
7.21	Radial density profiles at different times.	126
7.22	Evolution of the azimuthal velocity profiles as a function of cylindrical radius.	128
7.23	Time evolution of the radial temperature profile (T1b, T1d, T1f)	129
7.24	Evolution of T1b after t_0	131
7.25	Time evolution of T6d before t_0	132
7.26	Further evolution of T6d after t_0	133
7.27	Contour plot of the Toomre Q parameter for Run T6d.	134
7.28	Disks formed from turbulent cores vs disks formed from rigidly rotating cores.	136
7.29	Mass vs specific angular momentum.	137

7.30 Cumulative mass distribution for different runs. 139

List of Tables

5.1	The core sample in case of rigid rotation	74
5.2	Final stellar mass and disk parameters for all rigidly rotating runs.	78
7.1	Sample of turbulent and rigidly rotating cores	101

Zusammenfassung

Das Massenspektrum neu entstandener Sterne (IMF) ist von universeller Gültigkeit. So jedenfalls scheint es in verschiedenen Sternentstehungsregionen in der Milchstrasse, die alle derselben Verteilung aufweisen. Hierbei ist die relative Häufigkeit von Sternen mit einer Masse von $1M_{\odot}$ oder weniger, welche als massearm bezeichnet werden, besonders hoch. Die IMF ist von grundlegender Bedeutung für viele Bereiche der Astronomie. Unter Anderem bildet sie die Grundlage für die optische Erforschung ferner Galaxien und die Statistik entstehender chemischer Elemente. Dennoch ist ihre Universalität bezüglich fremder Galaxien oder bei hohen Rotverschiebungen bislang nicht eindeutig wissenschaftlich belegt, da eine vollständige Theorie der Sternentstehung immer noch aussteht. Sternentstehung basiert auf einem äusserst komplexen, nichtlinearen Wechselspiel von Eigengravitation, Hydrodynamik und Druck, sowie von Turbulenz, Strahlung, Magnetfeldern und der Chemie von Staub und Gas. Erschwerend kommt hinzu, dass junge Sterne in die Molekülwolke, aus welcher sie entstehen, eingebettet sind. Daher sind sie nur mittels Molekülspektren im Radio-Wellenlängenbereich zu beobachten.

Eine vielversprechende Möglichkeit um den Sternentstehungsprozess letztendlich zu durchschauen ergibt sich mittels Computersimulationen. Abgesehen von den vielen physikalischen Prozessen liegt die numerische Herausforderung in der grossen Änderung der Längenskala (um mehr als sieben Grössenordnungen), sowie der Dichte (um mehr als 20 Grössenordnungen) während des Kollapses eines dunklen Wolkenkerns. Aus diesem Grund wurden im Rahmen dieser Doktorarbeit nur Eigengravitation, Hydrodynamik, und Turbulenz in Betracht gezogen. Eine geeignete Methode zur Berechnung des Kollapses prestellarer Kerne ist die sogenannte Smoothed Particle Hydrodynamics Methode, ein Teilchen-basiertes Schema, welches die hydrodynamischen Gleichungen in ihrer Lagrangeschen Form löst. Die Simulationen sind vollständig dreidimensional. Da eine direkte Berechnung des Strahlungstransports derzeit immer noch zu zeitintensiv, jedoch die Beschreibung des Gases durch eine einfache Zustandsgleichung relativ unrealistisch ist, wurde im Rahmen dieser Doktorarbeit eine vereinfachte Beschreibung der Gaskühlung mittels tabellierter, optisch dünner Moleküllinien integriert.

Eine vollständige Theorie der Sternentstehung sollte die Entwicklung einzelner Molekülwolkenkerne (MWK) eindeutig vorhersagen können. Dies beinhaltet den Einfluss der Verteilung des Gesamtdrehimpulses des MWKs auf die Multiplizität und die akkretierte Masse der entstehenden Sterne. Das Ziel dieser Doktorarbeit ist daher, die dynamische Entwicklung des kollabierenden Kerns sowie die Entstehung protostellarer Scheiben unter verschiedenen Voraussetzungen zu untersuchen, um gegebenenfalls vorhandene Abhängigkeiten von Scheibenstruktur und physikalischen Anfangsbedingungen in der Gaswolke zu identifizieren.

Im Fall starr rotierender MWKs ist dies möglich. Die durchgeführten Simulationen ergeben, dass sich als Funktion des Anfangsdrehimpulses eindeutig bestimmen lässt, wie groß, konzentriert und warm eine protostellare Scheibe sein wird. Je grösser der Drehimpuls j , desto grösser und kühler auch die Scheibe. Ab einem bestimmten j bilden sich ausgeprägte Spiralarme und die Scheibe fragmentiert. Bei kleinerem j ist die Scheibe sehr konzentriert und heizt sich daher auf. Der zusätzliche thermischen Druck wirkt stabilisierend, weswegen die Fragmentation unterdrückt wird. In Abhängigkeit von Radius, j und Masse des MWKs ist es möglich mittels einer einfachen analytischen Abschätzung eine mittlere Scheibendichte zu berechnen und diese durch eine detaillierte Analyse mehrerer Simulationen grundsätzlicher gleicher Kerne mit unterschiedlichem j zu 'eichen'. Untersucht wurde die mittlere Scheibendichte für die Fragmentation eintritt bzw. unterdrückt wird. Im Vergleich mit Beobachtungen von dunklen MWKs führt die berechnete kritische mittlere Scheibendichte zu einem sehr geringen Anteil an Kernen für welche eine spätere Scheibenfragmentation vorhergesagt wird: nur 13%. Verglichen mit der beobachteten Multiplizitätsrate junger, massearmer Sterne (30% - 50% in Abständen von 14AU-1400AU) ist dieser Wert viel zu klein. Unter der Annahme effizienterer Gaskühlung wäre die kritische mittlere Scheibendichte fast um drei Größenordnungen höher, was die Fragmentation maßgeblich begünstigen würde. Das Fragmentationsverhalten protostellarer Scheiben scheint also von den lokalen thermodynamischen Eigenschaften des Gases bestimmt zu sein.

Mit turbulenten Anfangsbedingungen gestaltet sich die Scheibenentstehung und Entwicklung vollkommen anders. In diesem Fall ergibt sich keine Korrelation von Größe, Konzentration oder Durchschnittstemperatur der Scheibe mit dem Anfangs-Drehimpuls der Gaswolke. Unter dem Einfluss von Turbulenz wird das aufgesetzte hydrostatische Gleichgewicht der Wolke von Anfang an maßgeblich gestört. Im Wechselspiel mit der Eigengravitation des Gases bildet sich in jeder Simulation ein langgezogenes Filament, welches lokal sehr dicht wird. In dichten Filamentgebieten kann die lokale Jeans Masse während des weiteren Kollapses überschritten werden und dort entstehen protostellare Objekte. Vergleichbar mit dem Kollaps dünner, sehr flacher Ellipsoide findet sich der Protostern oftmals in einer Ecke des Filaments. Im Vergleich zur umgebenden Scheibe wachsen die Protosterne im Mittel viel schneller als im starr rotierenden Fall. Die entstehenden protostellaren Scheiben sind viel kleiner, obgleich kühl. Trotzdem sind sie nicht gravitativ instabil. Durch den turbulenten, aber kontinuierlichen Gaseinfall wird die Scheibe in vertikaler Richtung gestört und erscheint daher dicker als im Fall des starr rotierenden Kollapses. Interessanterweise fragmentieren auch in diesem Fall nur 16% aller MWKs. Obwohl Turbulenz den Kollaps maßgeblich beeinflusst ähnelt dieser Wert dem vorhergesagten Wert für echte Kerne im starr rotierenden Fall. Diese Übereinstimmung kann wiederum als Hinweis darauf gewertet werden, dass die lokalen thermodynamischen Eigenschaften des Gases die tatsächliche Fragmentation ermöglichen.

Die im Rahmen dieser Doktorarbeit gewonnene Erkenntnisse geben tiefe Einblicke in die Dynamik der Entstehung und frühen Entwicklung von protostellaren Scheiben. Sie zeigen numerische Schwächen, ebenso wie physikalische Kritikpunkte in modernsten Simulationen des Sternentstehungsprozesses auf. Daher bilden sie die Basis für kompliziertere Rechnungen und sind ein weiterer Schritt in Richtung einer vollständigen Theorie der Sternentstehung.

Chapter 1

Introduction

1.1 Motivation

The universality of star formation is an essential, though still unresolved question in modern astrophysics. All light we observe from distant galaxies and all the conclusions we draw from galactic surface brightness profiles originate from the stars, which are born, live and die within them. The number and mass distribution of stars formed in molecular clouds determine the production of the chemical elements as well as the amount of thermal and kinetic feedback into the interstellar medium, and thus overall influences the formation and evolution of galaxies. Naturally, astrophysicists have been asking, whether or not star formation really is a universal process. While a universal stellar initial mass function (IMF) in combination with a simple star formation recipe is commonly used in simulations of galaxy formation and evolution, we only base this implementation of the IMF on statistics within our own Galaxy. In order to pin down the origin of the stellar IMF and make predictions about its universality - even at high redshifts or in more extreme environments like the galactic center - we need to strongly improve our understanding of star formation.

Observations seem to be ahead of theory in identifying global star formation laws. Apart from similar stellar IMFs in different star forming regions within the Local Group, they also indicate the existence of a strong correlation between the initial mass function of molecular cloud cores and the stellar IMF (Testi & Sargent, 1998; Johnstone et al., 2000; Motte & André, 2001; Motte et al., 1998). Hereby molecular cloud cores are defined to be regions of local over-density within a molecular cloud. They are on average a factor of 100 more dense than the molecular cloud and their optical extinction A_V can be as high as 35 mag (Alves et al., 2001). They are cold ($T \approx 10\text{K}$) and show only subsonic internal motions. Dense cores are generally believed to be the actual sites of star formation within a molecular cloud. Having a number distribution of the same shape, the initial core mass function can be obtained by shifting the stellar IMF towards higher masses by a factor of ≈ 3 . The stellar IMF and core IMF are generally well approximated by a segmented powerlaw or a log-normal type mass distribution with a powerlaw tail (Kroupa, 2001; Chabrier, 2003, see Fig. 1.1). Towards the high-mass end ($M > 0.5 \dots 1 M_\odot$) the powerlaw of Salpeter (Salpeter, 1955, $dN \propto M^{-1.35} d(\log M)$); basically remained unchanged within the

past 50 years (Corbelli et al., 2005). However, defining the shape of the low-mass end (below approximately $0.1M_{\odot}$) suffers from incompleteness, and still remains ambiguous to some extent (Corbelli et al., 2005). Due to the existence of a characteristic mass for stars at about $1M_{\odot}$, special emphasis has been naturally placed on low-mass star formation. Understanding the natural overabundance of low-mass stars means building the foundation for a complete theory of star formation.

Observations of cores in star forming regions (e.g. Meyer et al., 2000) indicate that the IMF is set early on in the star formation process and suggest that the stellar mass distribution is already imprinted in the core IMF. On the other hand, many of the observed cores are gravitationally unbound and might never form any stars (Johnstone et al., 2000). Nevertheless, once a core is collapsing, it is likely fragmenting into a binary or a multiple stellar system (e.g. Goodwin & Kroupa, 2005). Fragmentation would affect the shape of the stellar IMF - at least for cores with masses $> 1M_{\odot}$ (Lada, 2006). As nature is in favour of one solar-mass stars, we ought to understand the physical properties within molecular cloud cores and the physics involved in core collapse, which is responsible for this preference.

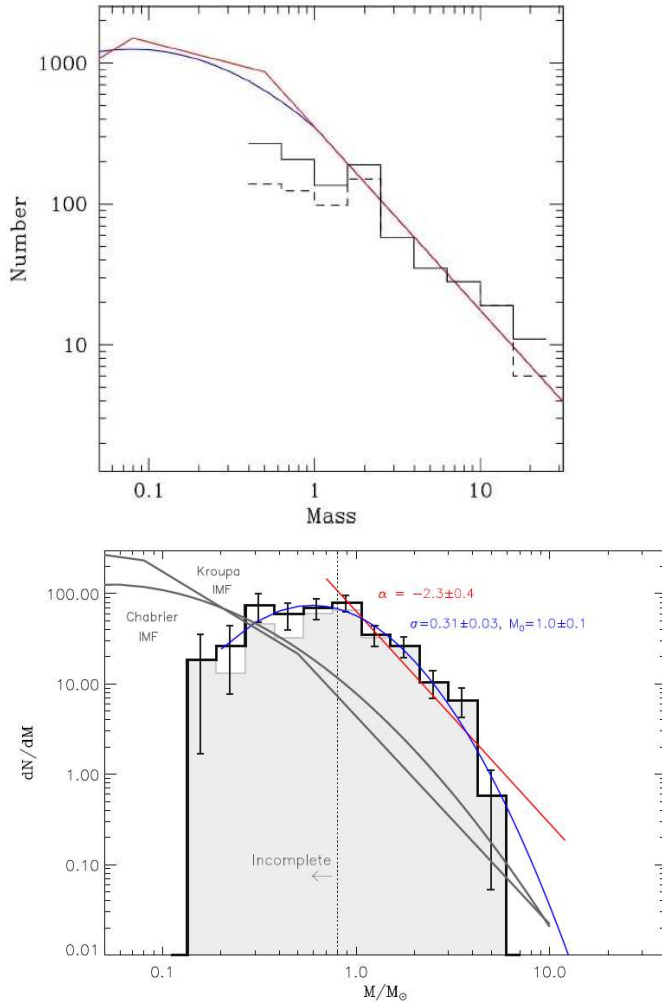


Figure 1.1: *Top panel:* Stellar IMF of NGC 3630 (Stolte et al., 2006) for completeness corrected (solid) and uncorrected (dashed) observed populations. For comparison the best-fitting segmented powerlaw of Kroupa (2001)(red) and the log-normal IMF with a powerlaw tail of Chabrier (2003) (blue) are shown. Figure from Bonnell et al. (2007).

Bottom panel: IMF of dark cores in the Pipe Nebula (Alves et al., 2007). The overplotted stellar IMFs of Kroupa (2001), Chabrier (2003), and of the Trapezium cluster (Muench et al., 2002) were all scaled up by a factor of 3.

However, the star formation and fragmentation process itself remains hidden: Observations fail to resolve the very early and embedded stages of forming protostars in detail. Young stellar objects are highly obscured by their surrounding parental envelope of dense gas and dust, which typically has a very high extinction or might even be completely optically thick at all wavelengths. The flux coming from very young sources is thus small, and might be undetectable. In addition, high spatial resolution is required in order to disclose the usually complex dynamics of the system. The highly filamentary structure of molecular clouds points to them being dynamically complicated and turbulent. Overall, molecular clouds seem to be dominated by supersonic turbulence, whereas purely thermal motions are more relevant on cloud core scales. This indicates that turbulence within a core is of sub- or, at most, transonic nature. Moreover we cannot resolve the turbulent motions within a core because molecular lines are blurred by thermal motions. The total amount of angular momentum extracted for cores is obtained by fitting velocity gradient maps throughout a core's 2D projection. Since rigid rotation provides good fits to the data in many cases the role of turbulence on core scales is unclear. The non-negligible

amount of angular momentum contained in every core is assumed to be mostly conserved during its collapse. Therefore the formation of a circumstellar disk, rather than direct gravitational collapse towards the core's center of mass, is initiated. So-called protoplanetary disks around brown dwarfs, young low-mass (T Tauri) stars and intermediate mass (Herbig Ae/Be) stars are frequent and well observed. In addition to the properties of a young stellar system, the existence of a protoplanetary disk could provide a powerful tracer to link the final outcome of prestellar core collapse to previously existent conditions in the cloud core. In addition, studying the properties of circumstellar disks themselves is interesting as they set the stage for the formation of earth-like as well as gas giant planets. In order to estimate the probability of the existence of extraterrestrial planetary systems, disk evolution needs to be understood. Protostellar disks, the disks which form at roughly the same time as the emerging star, are the precursors of protoplanetary disks. Like very young stars, protostellar disks are not directly observable due to being deeply embedded. Nevertheless, understanding their formation, structure, gravitational stability, and evolution is crucial to bridge the gap between the observable and dark phases of star formation.

Numerical simulations of molecular cloud core formation and core collapse are the only alternative to shed light on the dark phases of the star formation process and to link its initial and final stages. This problem is not at all trivial. We ought to understand the interplay of gravity, fluid dynamics, pressure, radiation transport, chemistry of gas and dust, magnetic fields and turbulence, while at the same time overcoming 17 orders of magnitude in density and 10 orders of magnitude in spatial scale. Numerically the problem of star formation is thus highly demanding with respect to the physical processes that have to be considered, while at the same time being computationally very expensive due to the large dynamical range which needs to be covered. Moreover, it is not sufficient to study individual test cases of core collapse. Thereby achieved results cannot be trivially transferred or extrapolated to structurally different cores. Even if only gravity and hydrodynamics are implemented the initial dynamical state of a core (turbulent or rotating or both) in a computational setup drastically changes the outcome of a simulation with respect to the number and masses of formed stellar objects. We are still missing an unambiguous link between the initial conditions in a molecular cloud core and the properties of the forming stellar system, mostly because we are not yet able to identify the most relevant physics on all the different scales involved. Nevertheless, increasingly realistic simulations are becoming feasible due to tremendous improvement in hardware resources and growing expertise in parallel computing schemes.

1.2 Scientific Aims

This thesis is dedicated to the study of the formation and early evolution of protostellar disks around low-mass stars. For this purpose fully three-dimensional simulations of prestellar core collapse were performed utilising the Smoothed Particle Hydrodynamics (SPH) technique. Protostellar disk properties are investigated in dependence on the initial core angular momentum. The net core angular momentum has been chosen to result from either rigid rotation of the core or turbulent motions with a velocity power spectrum. The purpose of this study is threefold:

- First, the question of how low-mass stars acquire their mass will be addressed. They may either form via direct gravitational collapse or rather grow by subsequent accretion from a circumstellar disk onto an initial seed star. It will be shown that the actual scenario is strongly influenced by the initial velocity field. Rigidly rotating cores typically form central 'nuclear' disks rather than spherically symmetric, pressure supported central objects. Turbulent cores are frequently passing a direct gravitational collapse phase, independent of the total initial core angular momentum. For this reason the distribution of mass versus the amount of specific angular momentum it is carrying - $M(j)$ - evolves in a significantly different manner depending on the initial setup. $M(j)$ is an interesting quantity since most of the angular momentum in our own solar system (99.46%) is carried by the planets (in particular by Jupiter), who only account for a tiny fraction of the mass of the solar system (0.13%). The differences in $M(j)$ in turbulent and rotating setups, as well as the redistribution of angular momentum in both scenarios will be compared and discussed. Attention must be paid to the numerical limitations of SPH in describing physical viscosity - an important ingredient for angular momentum transport.
- Second, the overall structure of protostellar disks will be examined in detail. In a rigidly rotating setup the forming disks show a strong correlation with total core angular momentum in terms of size, gravitational stability, and temperature distribution. Moreover, every core forms a protostellar disk without exception. On the other hand, turbulent cores form overall smaller disks in addition to extended filaments. The size and frequency of disks seems to be uncorrelated with the total core angular momentum. The different disk formation scenarios, and especially the resulting temperature structure, may be imprinted in structural changes within silicate dust grains.
- Third, core and disk fragmentation properties are investigated in both scenarios. It should be noted, that these turn out to be completely different for non-turbulent and turbulent cores. In the case of rigid rotation disks become increasingly gravitationally unstable the higher the initial angular momentum. Disk fragmentation is the only form of fragmentation taking place. Every fragment formed within the extended protostellar disk is surrounded by a small, individual 'circumfragmentary disk'. The formation of wide binaries with separations of 1000AU or more is impossible in this setting. However, turbulent cores show no signs of protostellar disk fragmentation. Instead, the emerging denser filaments can fragment, and this process is also independent of the initial core angular momentum. If a filament happens to fragment, individual stellar objects are produced, which neither share a circumbinary disk nor show signs of individual disks. Very wide binaries can also form. The implications of these results on the formation of planets, brown dwarfs, or low-mass stellar companions are discussed.

The formal concept of this thesis comprises the introductory chapter 1, where fundamental aspects and recent advances in observational and theoretical research on star formation are reviewed. Furthermore the SPH formalism, which forms the basis of the conducted numerical study, is introduced in chapter 3. The results extracted from the performed core collapse simulations will be discussed in chapter 4 - chapter 7.

Chapter 4 - chapter 6 are focused on protostellar disk formation within rigidly rotating cores only. In chapter 4, two examples are discussed in detail. For this purpose a setup with low initial core angular momentum as well as one with high angular momentum has been selected. It has been found that the disk structure is well correlated with the core's initial angular momentum. For low initial angular momenta the resulting protostellar disks are small, very compact and warm. They stay gravitationally stable, whereas fragmentation is taking place within the extended and colder disks formed from high angular momentum cores. The whole sample of performed collapse simulations is compared in chapter 5.

By means of all of these simulations an analytical criterion for disk fragmentation has been derived. With this approach it is possible to predict whether or not a core of a certain size, mass and angular momentum will form fragmenting protostellar disks or not. This finding has been applied to observations. In chapter 6 the method is explained, and the predictions for the multiplicity of young stellar objects as derived from core observations are discussed.

In chapter 7 a comparison of turbulent and rigidly rotating core collapse simulations is presented. The disk structure resulting from a turbulent setup is different in many aspects: The disks are on average smaller and less concentrated. Therefore they are also cooler. However, turbulent infall constantly disturbs the disks and fragmentation is suppressed. In general, none of the formed protostellar disks was fragmenting during runtime. Furthermore there is no clear correlation between core angular momentum and disk size or frequency.

Finally, in chapter 8 the results are summarised. A short outlook completes the thesis.

Chapter 2

From Molecular Clouds to Protostars: Observations and Theory

2.1 From Molecular Clouds to Prestellar Cores

2.1.1 Molecular Clouds: Dark and turbulent

The astrophysical importance of molecular clouds as the sites of all star formation in the Milky Way is well established by now. Therefore understanding the formation, and structure of molecular clouds, as well as the physical conditions within them is of critical importance for understanding the process of star formation.

Molecular clouds are dark. Being almost entirely composed of molecular hydrogen, basically all of the mass contained in a molecular cloud is not directly observable. This has two reasons: First, H_2 is a homonuclear molecule, which lacks a permanent dipole moment and its rotational transitions are very weak. Second, even its low energy rotational transitions are at mid-infrared wavelengths, and thus are too energetic to be collisionally excited at the typically cold temperatures within a molecular cloud ($T \approx 10\text{K}$). The structure and physical conditions of dark clouds must therefore be derived from dust and other tracer molecules, such as CO , NH_3 and HCN . However, the interpretation of molecular lines must be handled with care. Opacity, chemical abundance and excitation conditions may vary strongly within one cloud. Dust is a better tracer of the molecular gas content, since the gas-to-dust ratio (100:1) seems to be a robust constant within interstellar clouds (e.g. Lilley, 1955; Predehl & Schmitt, 1995). Dust extinction (i.e. absorption & scattering of background starlight) measurements are independent of dust temperature and directly proportional to the optical depth as well as the column density of the dust. This powerful method provides the most direct way to measure the dust content of a cloud (Lada et al., 1994; Alves et al., 1998). By combining observations carried out in more than two wavelength bands even more accurate column density measurements can be achieved (Lombardi & Alves, 2001).

Figure 2.1 shows an example extinction map of the Pipe Nebula (Lombardi et al., 2006). The Pipe complex of molecular clouds has a mass of approximately $10^4 M_\odot$, and thus consists of rather small molecular clouds. Giant molecular clouds have masses of $10^5 - 10^{6.5} M_\odot$ and typical

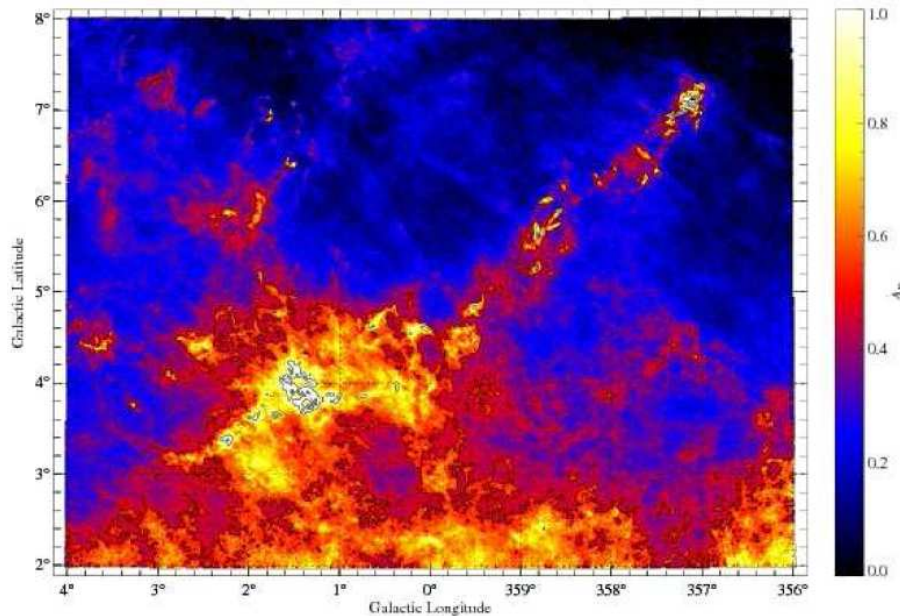


Figure 2.1: NICER extinction map of the Pipe Nebula (from Lombardi et al., 2006), a nearby complex of molecular clouds (distance $\approx 160 \pm 20$ pc). The resolution is 1 arcmin or about 10,000 AU. Star formation within the Pipe is still rare. For this reason it is a good example to study the structure of young molecular clouds.

sizes of 10-60pc. The Pipe map nicely shows, that molecular clouds have a very complicated, filamentary structure. This highly filamentary morphology points to molecular clouds being highly dynamical or turbulent. Turbulence appears to be dynamically important from scales of the whole molecular cloud down to molecular cloud cores (e.g. Larson, 1981; Ballesteros-Paredes et al., 1999; Mac Low & Klessen, 2004). Turbulence within molecular clouds is highly supersonic with respect to the cold gas (Mach number $M \approx 5 - 20$; Zuckerman & Palmer, 1974). Observations show that the internal velocity dispersion of the clouds, which is deduced from the width of molecular emission lines, typically is of the order of a few km/s. On the other hand the isothermal sound speed within the dense and cold parts of a molecular cloud is of the order of a few 0.1 km/s. In fact, models of supersonic turbulence or supersonic and super-Alfénic turbulence are successfully reproducing the observed self-similar, filamentary structure (Padoan & Nordlund, 1999; Padoan et al., 2003, 2004).

The source of molecular cloud turbulence is still a matter of debate. It has been shown, that the turbulent decay time within molecular clouds is shorter than a freefall time - independent of the employed equation of state, purely hydrodynamical or magneto-hydrodynamical (MHD) turbulence (Stone et al., 1998; Mac Low et al., 1998; Padoan & Nordlund, 1999; Pavlovski et al., 2002; Avila-Reese & Vázquez-Semadeni, 2001). Therefore turbulent energy must be constantly injected into a molecular cloud, if it ought to live longer than a freefall time. Observations of nearby molecular clouds show that they are self-similar up to the largest observable scales (Mac Low & Ossenkopf, 2000; Heyer & Brunt, 2004; Padoan et al., 2006). This result suggests

that turbulence is driven on even larger scales than the size of the whole molecular cloud. While stellar feedback certainly is a powerful driver, it acts locally, and only after the first stars have formed within the cloud. Moreover, driving by stellar feedback might be difficult to reconcile with the observed, nearly self-similar, spatial energy distribution. External drivers however suffer from the fact that the cold dense gas acts like a wall to any incoming wave, preventing an efficient energy transfer from the warm diffuse component to the cold dense phase.

With growing evidence for short cloud life times and rapid star formation (Elmegreen, 2000; Hartmann et al., 2001; Hartmann, 2003), a picture in which MCs are envisaged as transient objects in large-scale colliding flows rather than well-defined entities in a quasi-equilibrium state is emerging (Ballesteros-Paredes et al., 1999; Hartmann et al., 2001; Hartmann, 2003; Elmegreen, 1993, 2000). Large-scale gas flows are ubiquitous in our Galaxy. They might be either driven locally by supernova explosions (e.g. Vázquez-Semadent et al., 1995; Joung & Mac Low, 2006) or globally by shear motions in the Galactic disk (Li et al., 2005), gas infall from the halo (Lacey & Fall, 1985), interactions with the central bar (Roberts et al., 1979) or satellite galaxies. On extragalactic scales collisions of galactic disks trigger gas flows, shocks and starbursts (Naab et al., 2006). Colliding gas flows are a powerful mechanism to form cold atomic clouds as precursors of molecular clouds, via a combination of dynamical and thermal instabilities, namely the non-linear thin shell instability (NTSI), the Kelvin-Helmholtz instability (KHI) and the thermal instability (TI). However, due to the rapid onset of star formation in this scenario, the cloud formation process needs to provide the molecular cloud with the observed turbulence and substructure. Global geometry and gravity considerations mandate this substructure to be non-linear (Burkert & Hartmann, 2004). The process of molecular cloud formation is therefore subject to numerical studies by many authors (e.g. Audit & Hennebelle, 2005; Heitsch et al., 2005; Vázquez-Semadeni et al., 2006). Most numerical studies of this process used various grid-based numerical methods. SPH, the alternative method to simulate gas dynamics, has not been shown to be a viable method for simulating the thermally unstable, turbulent interstellar medium. This is of particular interest as SPH might have considerable problems resolving shear flow instabilities (Junk et al., in prep.; Agertz et al., 2007) – a crucial ingredient in the formation of turbulent clouds from colliding flows. Especially the Kelvin-Helmholtz instability (KHI) is important in regions of converging gas flows, because it promotes local density enhancements and leads to dense prestellar core and star formation if the gas viscosity is low. On the other hand dense clumps are likely to be destroyed if viscosity is high (see Fig. 2.2 to receive a first impression of the colliding flow scenario).

2.1.2 Molecular Cloud Cores: Sites of Star Formation

Two of the least understood aspects in star formation are the initial conditions that describe dense molecular cloud cores, which ultimately form stars, and their formation from more diffuse atomic and molecular material within molecular clouds. Molecular cloud cores are regions of significant overdensity within molecular clouds (MCs). Whereas MCs have typical number densities of 10^2cm^{-3} , cloud cores are a factor of 100 - 1000 more dense ($10^5 - 10^6 \text{cm}^{-3}$). As cloud cores develop within MCs, their formation process is naturally coupled to the way MCs are formed. As mentioned in section 2.1.1, the life time and formation mechanism of MCs are still a matter of

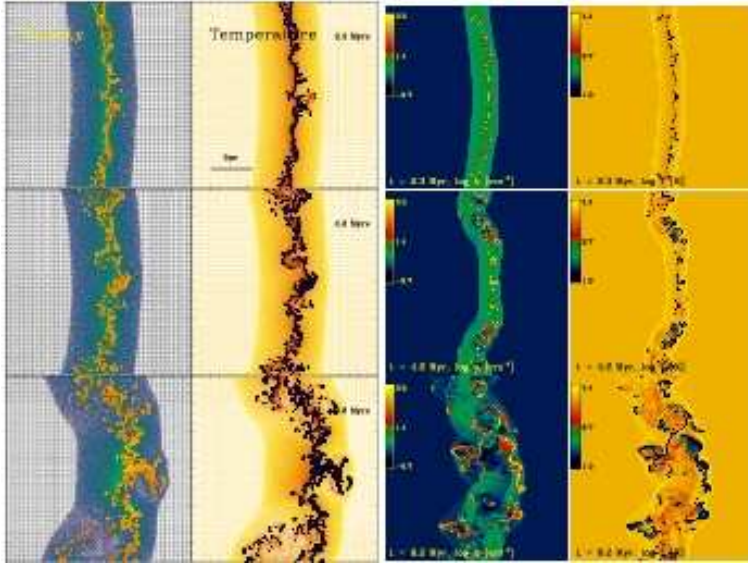


Figure 2.2: Morphologies of colliding gas flows in a comparison between SPH and a grid method (Heitsch, Naab & Walch, submitted). Shown are density and temperature distributions of the center quarter of the simulation domain, at times $t = 2.3, 4.2$ and 9.2 Myrs. *Left:* Density and temperature distribution of SPH particles. *Right:* Density and temperature distribution of the corresponding grid simulation.

debate. However, there is growing theoretical evidence that MCs are transient objects, accumulating and either rapidly collapsing to form stars or dissolving quickly. Quite the contrary is true for molecular cloud cores. The lifetime of starless (dense cores which do not harbour a protostar or young stellar object) and prestellar cores (subset of starless cores which are gravitationally bound and are expected to undergo gravitational collapse) has been estimated to exceed the local freefall time by a factor of 2-5 (Onishi et al., 1998, 2002; Jessop & Ward-Thompson, 2000; Kirk et al., 2005; Kandori et al., 2005). Furthermore, observations generally show that isolated molecular cloud cores are islands of quiescence (Barranco & Goodman, 1998; Belloche et al., 2001; André et al., 2007) within the highly supersonic MC environment. Their observed internal motions are overall dominated by thermal motions. Hence, within prestellar cores, turbulence is of sub- or at most transonic nature if at all present. Prestellar cores appear to have a flat density profile within the central few thousand astronomical units (AU), (Hogerheijde & Sandell, 2000; Motte & André, 2001, e.g.) embedded in a region where $\rho \propto R^{-1.5 \dots -2}$. Often, isolated cores are characterized by sharp outer edges at $r \approx 0.1$ pc, which implies pressure confinement of these objects within a hotter, but low-density medium. This density profile is well fitted by the so-called Bonnor-Ebert profile (Alves et al., 2001; André et al., 2004; Lada et al., 2004, 2007; Teixeira et al., 2005; Kandori et al., 2005; Kirk et al., 2005). The Bonnor-Ebert sphere is a self-gravitating isothermal sphere in hydrostatic equilibrium, which is confined by external pressure (Bonnor, 1956; Ebert, 1955). The multi-phase nature of the interstellar medium (ISM) is essential for the Bonnor-Ebert equilibrium solution. Its attractiveness lies in the natural way, with which the density profiles of real molecular cloud cores are reproduced. For this reason, Bonnor-Ebert spheres are among the preferred initial setups for computational attempts to study star formation. The Bonnor-Ebert solution is formally obtained by solving the dimensionless form of the Lane-Emden equation. An isothermal gas, which obeys the local equation of state of an ideal gas at

every point:

$$P = \rho \frac{k_b T}{\mu m_p}, \quad (2.1)$$

and at the same time satisfies the equation of hydrostatic equilibrium:

$$-\frac{dP}{dR} = \frac{4\pi G \rho}{R^2} \int_0^R \rho y^2 dy \quad (2.2)$$

will have the following density distribution:

$$\frac{1}{R^2} \frac{d}{dR} \left(\frac{R^2 d\rho}{\rho dR} \right) = \frac{-4\pi G \rho \mu m_p}{k_b T}, \quad (2.3)$$

where k_b is the Boltzmann constant, G is the gravitational constant, μ is the mean molecular weight and m_p is the mass of a proton. P denotes the gas pressure, T the gas temperature and ρ the local density. Eq. 2.3 is the so-called Lane-Emden equation (Emden, 1907). Its dimensionless form reads:

$$\frac{1}{\zeta^2} \frac{d}{d\zeta} \left(\zeta^2 \frac{d\Phi}{d\zeta} \right) = e^{-\Phi}, \text{ where} \quad (2.4)$$

$$\zeta \equiv \frac{R}{R_0}; \quad R_0 = \frac{c_s}{\sqrt{4\pi G \rho_0}} \quad (2.5)$$

$$\rho(\zeta) \equiv \rho_0 e^{-\Phi(\zeta)} \quad (2.6)$$

with mixed boundary conditions (von Neumann & Cauchy):

$$\Phi(0) = 0 \quad \text{and} \quad \frac{d\Phi}{d\zeta} = 0. \quad (2.7)$$

Here ρ_0 denotes the central core density and R_0 is the characteristic radius. Note that, up to an integration constant, Φ resembles the gravitational potential of the cloud. The isothermal sound speed $c_s = (k_b T)/(\mu m_p)$. In general, a BES is uniquely described by specifying its central density (e.g. $\rho_0 = 10^{-18} \text{g cm}^{-3}$), its temperature T and its cut-off radius $R_{\text{max}} = \zeta_{\text{max}} \cdot R_0$. The mass of the Bonnor-Ebert sphere can be easily derived. The mass of any sphere with a given density profile is

$$M = N \mu m_p = 4\pi \int_0^R \rho y^2 dy. \quad (2.8)$$

Here, N is the number of molecules contained within the sphere. Combining eq. 2.2 and eq. 2.8, the mass of the BES is

$$M_{\text{BES}} = \frac{R_0 c_s^2}{G} \zeta^2 \frac{d\Phi(\zeta)}{d\zeta}. \quad (2.9)$$

In the same way, pressure and volume of the sphere can be expressed by the dimensionless variables ζ and Φ . With eq. 2.1 and eq. 2.9:

$$P_{\text{BES}} = \frac{c_s^8}{4\pi G^3 M_{\text{BES}}^2} \zeta^4 \left(\frac{d\Phi}{d\zeta} \right)^2 e^{-\Phi}, \quad (2.10)$$

and

$$V_{\text{BES}} = \frac{4\pi}{3}R^3 = \frac{4\pi}{3} \left[\frac{GM_{\text{BES}}}{\zeta \left(\frac{d\Phi}{d\zeta} \right) c_s^2} \right]^3. \quad (2.11)$$

It should be also noted, that $P(V)$ is not a continuous function. However the derivative $(\partial P/\partial V)_{T, M_{\text{BES}}}$ can be found at constant T and mass M_{BES} . Via linear stability analysis (see Bonnor, 1956) it has been found that $(\partial P/\partial V)$ is negative for a sphere who's volume corresponds to $\zeta_{\text{max}} < \zeta_{\text{crit}}$. For increasingly larger ζ_{max} (or radii), $(\partial P/\partial V)$ approaches zero. At $\zeta_{\text{max}} = \zeta_{\text{crit}} = 6.451$, $(\partial P/\partial V) = 0$ and the sphere is marginally stable. In this case a small fluctuation which results in a slight decrease of the sphere's volume V will cause the pressure inside V to decrease as well. This will lead to a further reduction of the volume and so forth. The sphere is collapsing. (Bonnor, 1956) found all spheres with $\zeta_{\text{max}} > \zeta_{\text{crit}}$ to be unstable because small fluctuations cause the sphere to collapse towards the center. On the other hand, those with $\zeta_{\text{max}} < \zeta_{\text{crit}}$ are stable. Thus, ζ_{max} characterises the radial extent of a Bonnor-Ebert sphere, the center-to-edge density contrast, as well as the stability of the equilibrium state against gravitational collapse. In order to place the stability criterion derived for BESs in context, it is interesting to compare it to the stability condition derived by Jeans (Jeans, 1928). Jeans found the maximal radial extent of a stable, spherical gas cloud with a constant density profile to be equal to $\sqrt{\pi/(G\rho)(dP/d\rho)}$. The *critical* masses and sizes of a BES (with $\zeta_{\text{max}} = 6.451$) roughly agree with those predicted by Jeans. This is surprising as Jeans assumed a constant density profile and did not predict the same results for spheres following a non-uniform density distribution.

Moreover, a BES always collapses outside-in. When undergoing gravitational collapse, an initially critically stable Bonnor-Ebert sphere will maintain the typical Bonnor-Ebert profile with ζ_{max} (i.e. the density contrast) systematically increasing (Kandori et al., 2005; Myers, 2005). A more evolved, collapsing prestellar core will appear to be supercritical ($\zeta_{\text{max}} > \zeta_{\text{crit}} = 6.451$). Kandori et al. (2005) investigated the stability of observed Bok globules on the basis of ζ_{max} . They find most starless cores to be well described by nearly critical Bonnor-Ebert spheres, whereas protostellar cores (cores that harbour a young stellar object) are fitted with larger ζ_{max} (see Fig. 2.3). The fact that the structure of both starless and protostellar cores can be fit by Bonnor-Ebert models indicates that the initial conditions for molecular cloud core collapse and star formation must be similar to those described by a critical Bonnor-Ebert configuration. In this framework the Bonnor-Ebert formalism seems to provide robust and well-suited initial conditions for numerical investigations.

All of these findings are in clear contradiction to the suggestion that prestellar cores might be transient, dynamical fluctuations in a turbulent velocity field (e.g. Ballesteros-Paredes et al., 2003). However, not all protostellar cores may be fitted by a Bonnor-Ebert like density profile. In a cluster-forming environment, such as Serpens, Perseus and ρ Ophiuchus, where young stars have already formed and shape their surrounding by winds and radiative feedback, protostellar envelopes are typically an order of magnitude more dense than predicted by models of spontaneous collapse (Motte & André, 2001). In addition, they appear to be truncated at radii of less than 5000AU, which might be a result of merging or interaction with the ambient cloud

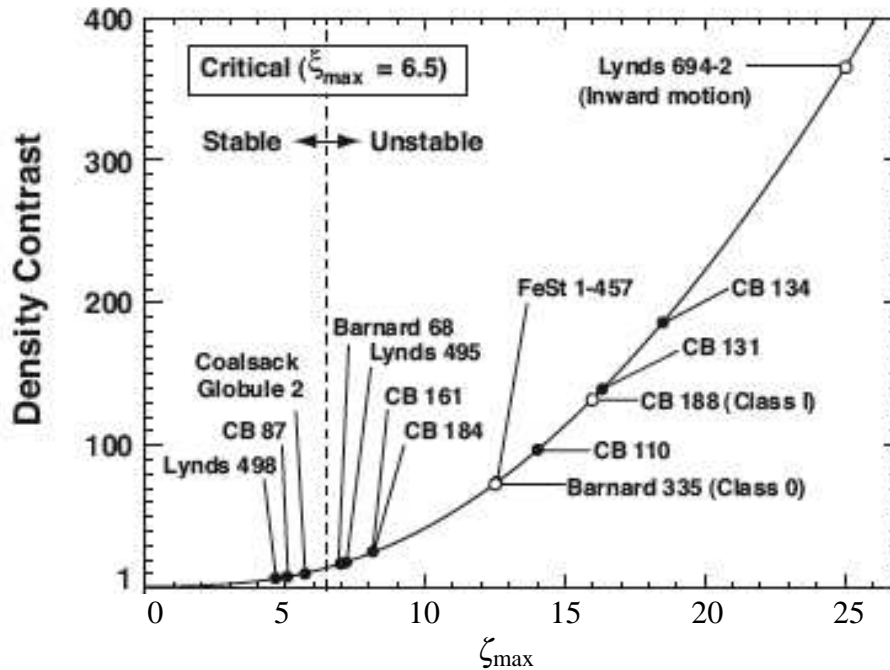


Figure 2.3: Center-to-edge density contrast vs dimensionless outer radius ζ_{\max} for Bonnor-Ebert spheres (Kandori et al., 2005). In addition, 14 observed Bok globules are marked. More than half of the starless globules (filled circles) are located near the critical state $\zeta_{\max} = 6.5 \pm 2$

(Motte et al., 1998; Looney et al., 2003). These observations suggest that the evolution of dark molecular cloud cores is significantly affected by their environment. In unprecedented detail star forming regions like the Eagle Nebula (see Fig. 2.4) have been recently observed with the Spitzer Space Telescope revealing significant heating and triggering by exploded massive stars. Nevertheless, it is still unclear how strongly the formation of an individual star or stellar system is influenced by the surrounding of its parental molecular cloud core. In order to solve this question thoroughly, one has to take one step back and study the collapse of individual prestellar cores.

Even in isolation the evolution of two equally massive cores may not be alike if they contain a different amount of angular momentum. The presence of a net core angular momentum hinders direct gravitational collapse to form a single star. Instead the formation of a circumstellar disk is initiated. Every core, which has a non-negligible amount of angular momentum, will also form a disk and/or a binary or multiple stellar system. Therefore the total core angular momentum as well as the evolution of the specific angular momentum are important parameters, which have to be determined in order to understand star formation.

The amount of angular momentum a prestellar core comprises is difficult to determine. So far, the only way to disentangle the internal kinematics of starless cores is based on observations of molecular line profiles. Internal velocity gradient maps of dense cores can be derived from the variation of tracer molecular line profiles across them. In 1998, Barranco & Goodman were the first to apply this method to starless cores observed in $\text{NH}_3(1,1)$. Thereupon, velocity gradient

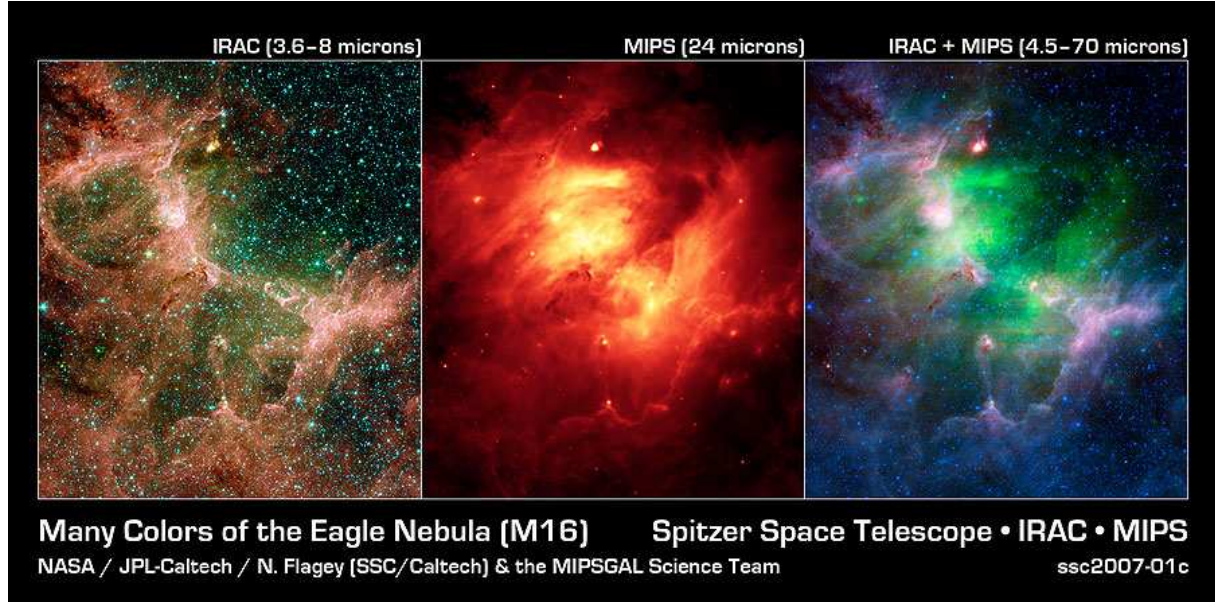


Figure 2.4: The Eagle Nebula as seen in different hues of IR light by the Spitzer Space Telescope. The left image is a composite of IR light at $3.6\mu\text{m}$ (blue), $4.5\mu\text{m}$ (green), $5.8\mu\text{m}$ (orange), and $8\mu\text{m}$ (red). Dust and stars are traced by these wavelengths. The middle image is made up solely of 24-micron light. The shell-shaped distribution of hot dust indicates that a massive star exploded in a supernova. The right image is a composite of light observed with Spitzer: 4.5 to 8.0 microns (blue), 24micron (now in green), and 70micron (red). Dusty star forming clouds surround the heated region around the supernova remnant. Image credit: NASA/JPL-Caltech/N. Flagey (IAS/SSC) & A. Noriega-Crespo (SSC/Caltech).

maps were determined by e.g. Caselli et al. (2002); Lada et al. (2003) and Swift (2006). It turned out that prestellar cores with velocity gradients which are spatially uniform in direction and magnitude, are likely in simple solid-body rotation. The interpretation of velocity gradient maps is difficult as soon as spatial variations in gradient direction and magnitude are found. Spatial variations of velocity gradients are a clear sign of complex, probably turbulent motions (see Fig. 2.5 for example velocity gradient maps as observed by Caselli et al. (2002)).

Nevertheless, if one assumes that the core is in simple solid-body rotation total amount of core angular momentum, respectively its rotational energy, can be approximately determined. Numerical investigations of collapsing prestellar cores have shown that a core's evolution and fragmentation properties are strongly influenced by the ratio of rotational energy to gravitational energy β (see section 2.3.2), observations also tempted to derive β . β may also be called the dimensionless internal rotational parameter. Interestingly, β seems to be roughly independent of core size and varies between 10^{-3} and $\text{few} \times 10^{-1}$ (Barranco & Goodman, 1998; Caselli et al., 2002). The total amount of specific angular momentum j in a molecular cloud core is typically of the order of $J/M = j \approx 10^{21} \text{cm}^2 \text{s}^{-1}$ (Goodman et al., 1993).

Burkert & Bodenheimer (2000) were the first to demonstrate that core internal sub- or trans-sonic turbulence might produce the observed rotational properties of dense molecular cloud

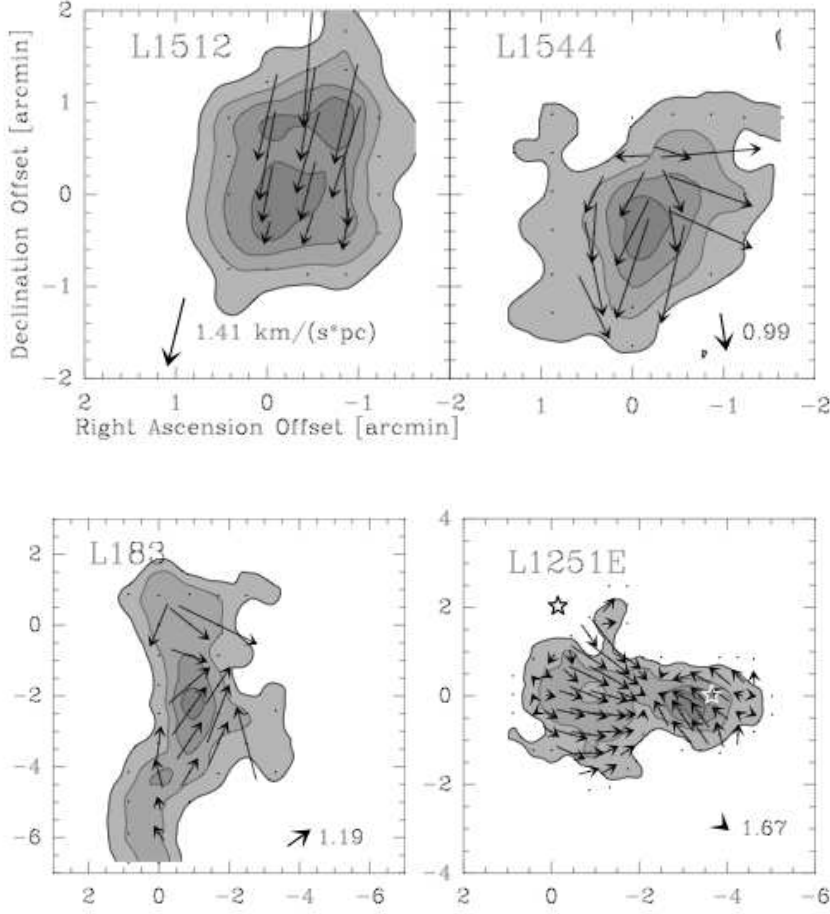


Figure 2.5: Column density maps overlaid by velocity gradient arrows of four low-mass molecular cloud cores observed by Caselli et al. (2002). In L1512 direction and magnitude of the velocity gradient seems to be spatially uniform across the core. L1512 might therefore be in rotating like a solid-body. However all other shown cores have much more complicated inner motions, which might be a result of sub- or transonic internal turbulence.

cores. They superimposed isotropic Gaussian random velocity fields, where the velocity field $\vec{v}(x)$ in every spatial dimension is characterised by its Fourier modes:

$$\vec{v}(x) = \frac{1}{(2\pi)^3} \text{Re} \left(\int \hat{v}(\vec{k}) e^{i\vec{k}x} d^3k \right). \quad (2.12)$$

In this setup, the Fourier components $\hat{v}(\vec{k})$ are completely specified by the power spectrum of $P(k) = k^n$, where $k = |\vec{k}|$ is the wave number and $n = -3..-4$ denotes the power spectral index, on top of centrally condensed density distributions resembling the structure of prestellar cores. $n = -3$ results in more power on smaller scales than e.g. $n = -4$, which corresponds to Burgers power spectrum for incompressible, supersonic turbulence. The correspondence between the turbulent spectrum with random relative phases for the spectral components and Larson's line-width size relation has been suggested by Myers & Gammie (1999). Their work is based on Larson's finding that the observed internal velocity dispersion σ of a molecular cloud region is correlated with its length scale λ (Larson, 1981):

$$\sigma(\lambda) \propto \lambda^q. \quad (2.13)$$

The proportionality of internal velocity dispersion and length scale is a clear sign of turbulence. Typically, kinetic energy is induced into a gas or fluid on large scales. Large scale drivers might for instance be large scale colliding gas flows. Turbulence is a mechanism to redistribute energy through the turbulent cascade, which reallocates the large scale energy input by populating smaller and smaller scales with kinetic energy. According to Kolmogorov's theory of the 'universal equality of scales', energy is neither produced nor consumed within an intermediate range of scales - the inertial subrange - until it is finally dissipated in the dissipation range, which can be based on very small, even molecular scales. In incompressible hydrodynamics the kinetic energy contained in a fluid element E_n is simply proportional to the velocity v_n squared. Thus, the energy dissipation rate ε , which is the energy dissipated in a turbulent element n within a characteristic time τ_n is

$$\varepsilon \propto \frac{E_n}{\tau_n} \propto \frac{v_n^2}{\tau_n} = \frac{v_n^3}{\lambda_n}, \quad (2.14)$$

with $\tau_n = v_n/\lambda_n$. λ_n is the characteristic dissipation length scale and τ_n is typically defined by viscous processes. It follows that

$$v_n \propto \varepsilon^{1/3} \lambda_n^{1/3}. \quad (2.15)$$

In phasespace (and with the wave number $k \propto 1/\lambda$) this relation reads

$$E_n = \int_k E_k dk \approx E_k \cdot k, \quad (2.16)$$

and therefore

$$E_k \propto \frac{v_n^2}{k} \propto \frac{\varepsilon^{2/3} \lambda_n^{2/3}}{k} = \varepsilon^{2/3} k^{-5/3} \quad (2.17)$$

(Kolmogorov, 1941). In three spatial dimensions the equivalent power spectral index is $n = -2 - 5/3 = -11/3$. In terms of Larson's scaling relation the powerlaw index describing the velocity scaling is equivalent to $n = -3.76$ with $q = 0.38$ (Larson, 1981) and $n = -3 - 2q$. This results in an approximate Kolmogorov scaling, which is expected in case of ideal, incompressible hydrodynamics. As real astrophysical gases do not behave in an incompressible manner, Larson's finding was rather unexpected. Later observational work however found $q = 0.5$ on scales larger than 0.1pc (see e.g. Goodman et al., 1998), which corresponds to $n = -4$. The cores' net specific angular momentum is caused by the dominance of long wavelength modes. They find the average value of $J/M = 7 \cdot 10^{20} (R/0.1\text{pc})^{1.5} \text{cm}^2\text{s}^{-1}$ to depend on core radius R . However, the spread in J/M is fairly large. On the other hand, the rotational parameter β seems to be independent of R as observed.

In summary, low levels of turbulence within molecular cloud cores give a suitable physical explanation for the observed angular momentum of molecular cloud cores. Compared to the ansatz of rigid rotation, turbulence appears to be more natural and elegant. However, for some cloud cores like L1512, rigid rotation represents the best fitting model. Therefore, and because rigid rotation results in a well-defined initial setup for numerical experiments, turbulent as well as rigidly rotating core collapse will be studied in this thesis.

2.2 From prestellar cores to protoplanetary disks

Within the past decade a schematic picture of low-mass star formation has emerged. Low-mass, so-called T Tauri stars were first identified by Joy (1949) and the designation of the class derives from its brightest member: T Tauri. Their classification bears on several distinctive features: all T Tauri stars show irregular light variations, are associated with nebulosity, exhibit a bright emission line spectrum of low excitation lines, which resembles the spectral features of the solar chromosphere (e.g. strong emission lines of hydrogen, CaII and iron). T Tauri stars typically have spectral types between F5 and G5 (for comparison the sun is G2) and masses $< 2M_{\odot}$. Ever since their discovery, T Tauri stars were thought to be young stars, which haven't yet arrived at the main sequence. Walker (1956) was the first to definitively prove their pre-main sequence nature based on their position in the color-magnitude diagram (comparable to Hertzsprung-Russell diagram) of star forming regions. His observations already showed, that T Tauri stars are in fact extremely young and still in a state of gravitational contraction when central hydrogen burning has not yet begun.

Starting from prestellar molecular cloud cores, which are gravitationally bound condensations within molecular clouds, the evolutionary stages of cloud core collapse have been divided into four classes. The classification of protostellar cores and young stellar objects is based on the slopes α_{SED} of the spectral energy distributions (SEDs) between 2 and $25\mu\text{m}$ (Lada & Wilking, 1984; Lada, 1987, $\alpha_{\text{SED}} = \text{dlog}(\lambda F_{\lambda}) / (\text{dlog}\lambda)$). Fig. 2.6 depicts the generally assumed formation scenario of a low-mass star as measured indirectly by the evolution of its SED. Class 0 objects harbour the youngest stars or dense central objects, which are completely obscured by the thick surrounding envelope. Therefore their SEDs are dominated by the cold ($T < 30\text{K}$) outer envelope (Andre et al., 2000). On the other hand, Class 0 cores do show signs of a central source powered by the release of gravitational energy within the collapsing cloud. In the innermost regions of the now 'protostellar' envelope, the dust temperature reaches 100K, causing the evaporation of icy dust grain mantles. Molecules like CO, which have been depleted from the gas phase due to freeze-out, are now being injected back into the gas phase. Complex organic molecules, so-called *hot corinos* can be found in the Class 0 stage of star formation. The central object grows by gas accretion from the protostellar envelope to form a young protostar. Once protostar and an eventually formed circumstellar disk are embedded in a diffuse rather than thick envelope of (sub)stellar mass, the source has entered the Class I stage. Class I stars are bolometrically cold ($T_{\text{bol}} < 650\text{K}$; where T_{bol} defines the temperature of a blackbody with the same mean peak frequency as the observed SED; Myers & Fuller (1993)) and have rising mid-infrared spectral slope α_{SED} (e.g. White & Hillenbrand, 2004; Doppmann et al., 2005), which is caused by the disk and the remaining envelope. The protostellar envelope finally vanishes completely by feeding its mass into the circumstellar disk and onto the protostar, or by being blown away due to feedback processes from the young central source, respectively. Protostar and (optically thick) circumstellar accretion disk are now classified as a Class II object. In this stage, which is the most important for observations of circumstellar disks, the protostar has an age of a few $\cdot 10^5 - 10^6\text{yr}$ and is almost fully assembled. Accretion rates are low ($10^{-8} - 10^{-9}M_{\odot}/\text{yr}$) and the formation of rocky earth-like planets might take place within the circumstellar disk. As still more mass is channeled onto the central object by disk accretion, the disks themselves become optically thin

and begin losing gas. The central star is an almost fully developed - but still pre-main sequence - star with an age of a few million years. These objects are known as Class III objects. Class II and III stars are classical or weak-line T Tauri stars, respectively. It is believed that most of the stellar mass is acquired prior to the Class II phase and stars younger than Class II are considered to be true protostars. However, for the embedded stages, it has not been unambiguously shown that the observable diagnostics really traces distinct stellar evolutionary stages, or whether Class I sources are simply less environmentally developed than Class II sources. On the contrary, the mass accretion rates and disk masses observed for Class I and Class II sources in Taurus-Aurigae seem to be alike (White & Hillenbrand, 2004). An understanding for the origin of the stellar properties of Class I systems is needed. So-far the faintness of Class I sources at optical and near-infrared wavelengths ($< 3\mu\text{m}$) has made it difficult to obtain high resolution, high signal-to-noise observations necessary for such a study. However, all stages of circumstellar disk evolution can be well studied by observations at wavelengths longer than $3\mu\text{m}$ - i.e. in the thermal infrared (IR).

The proof that circumstellar disks do exist was finally provided via direct imaging with the Hubble Space Telescope (HST; e.g. Burrows et al., 1996; McCaughrean & O'Dell, 1996; Padgett et al., 1999, see Fig. 2.7). In order to physically interpret the observed SEDs of young stars, understanding the structure and evolution of circumstellar disks is crucial. In addition, circumstellar disks themselves are interesting as they set the stage for planet formation, provide a framework for the redistribution of angular momentum and gas accretion onto the central star, and last but not least are a long-lived tracer for the initial angular momentum contained within the parental molecular cloud core. Disks are associated with at least 50% of classical T Tauri stars in nearby star forming regions (e.g. Kenyon & Hartmann, 1995; Sicilia-Aguilar et al., 2006). The well-studied disks around mostly Class II stars are called 'protoplanetary disks'. Dust plays a major role in protoplanetary disk physics, as the dust completely dominates the SED at a wavelength of $\approx 10\mu\text{m}$ (10 micron feature). The shape of the 10 micron feature can be used to determine the dust composition in the disk and maybe to draw conclusions on the physical conditions within and the evolutionary state of a protoplanetary disk (e.g. Bouwman et al., 2001). However, such an analysis must be considered with care as the spectral features are influenced not only by dust composition, but also by the size of the dust grains, their fractal dimensions and location within the disk (Dullemond & Dominik, 2008). Although dust dominates the spectrum of a young stellar object, it only accounts for a tiny fraction of the total mass. In fact, the interstellar medium mainly consists of gas (about 99%) and only of 1% dust (mainly carbon, amorphous olivine and silicate). Assuming an average dust-to-gas ratio of 1:100, the mass of typical protoplanetary disks (PPDs) appears to be relatively small ($\leq 0.1M_{\odot}$). Direct measurements of the circumstellar gas reservoir will only become feasible with millimeter interferometry, e.g. with ALMA. PPDs have radial extents of $\approx 100 - 400\text{AU}$ (e.g. Vicente & Alves, 2005). Most of the disks show small mass accretion rates of $\dot{M}_{\star} \approx 10^{-7} - 10^{-9}M_{\odot}/\text{yr}$ (Bertout et al., 1988; Hartigan et al., 1995; Gullbring et al., 1998). Their temperature structure is therefore dominated by passive heating from the central star, which causes the disk to flare (Kenyon & Hartmann, 1987, 1995). As a result the coarse vertical structure of a PPD will be two-layered (Chiang & Goldreich, 1997), with a heated flaring upper layer on top of the cold disk midplane. SEDs calculated from these models overall fit the observations fairly well. However, an additional spectral enhancement at

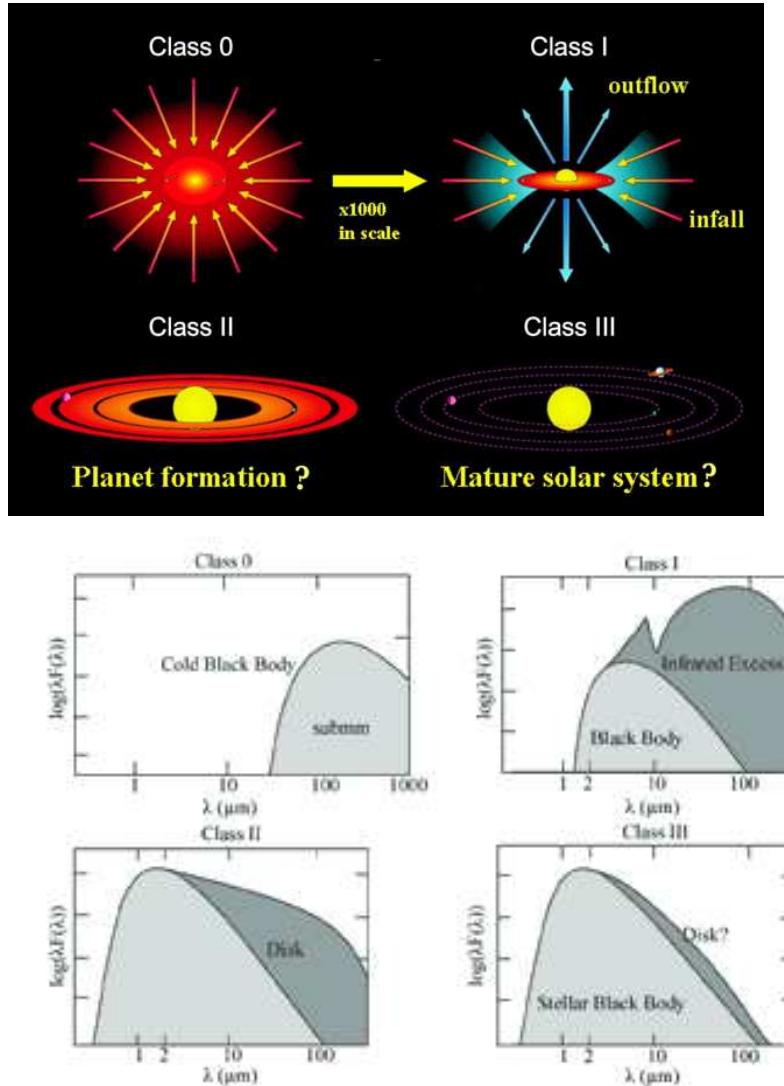


Figure 2.6: *Top:* Evolutionary stages of a forming low-mass star (by McCaughrean). *Bottom:* Typical SED evolution during low mass star formation (by Michael Burton). Initially the core is cold, 20-30K, peaking in the submillimetre (Class 0). Emission from a warm envelope heated by the accretion luminosity causes an infrared excess, which first peaks in the far-IR (Class I). The slope of the SED α_{SED} is positive. Envelope mass is lost and the SED is dominated by emission from a circumstellar disk. The peak shifts to the mid- and near-IR as the spectrum is now dominated by emission from the young (T Tauri) star (Class II). The spectral shape is influenced by the detailed disk properties. Finally, the disk dissipates (Class III).

$2\text{-}3\mu\text{m}$ could only be explained by an additional disk component: The hot inner rim of the disk, which is located at the inner edge of the dusty disk and is directly exposed to stellar irradiation (Dullemond et al., 2001, see Fig. 2.8). These sophisticated models can be used to determine the properties of PPDs by fitting observed SEDs (Dominik et al., 2003).

Even though PPDs are fairly well understood, their formation mechanism (Class 0 stage) and very early evolution (Class I stage) is still unclear. In the following, very young circumstellar disks will be called protostellar disks in order to emphasize the fact that these disks are formed simultaneously with the central protostar. As observed mass accretion rates of Class I and II sources are on average low ($10^{-7} - 10^{-9} M_{\odot}/\text{yr}$) and observations point towards the fact that Class II as well as most Class I stars have already acquired the majority of their final stellar mass (e.g. Motte & André, 2001), the role of protostellar disks (PSDs) in the star formation process

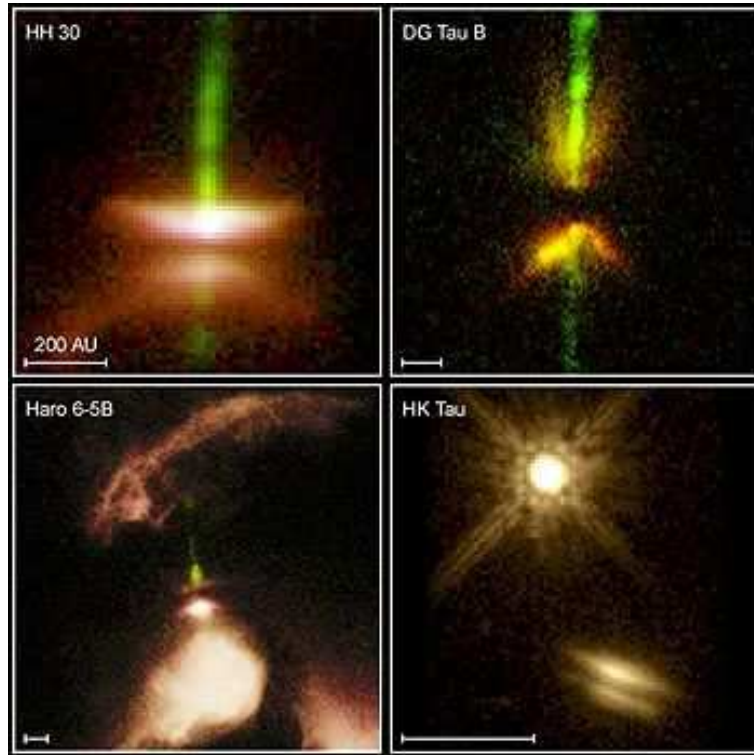


Figure 2.7: Continuum HST images of edge-on protoplanetary disks. Dust absorbs the light from the young central star and causes the disk to appear as a black line enclosed by bright regions, where light is scattered on the disk surface (from McCaughrean & O'Dell, 1996).

becomes even more important. Like all accretion disks, PSDs are important for redistributing the initial core angular momentum, thus allowing for accretion and growth of the forming protostar. The way gas is falling onto the disk from the parental envelope as well as how this gas is accreted through the disk are important parameters in PSD and protostellar evolution. High mass accretion rates are necessary to enable a quick growth of the central protostar within a few 10^5 yr (Class I age). In accordance, the PSD will on average be less massive the higher the mass accretion rate onto the central object, but massive PSDs are more likely becoming gravitationally unstable and might fragment to form stellar companions, brown dwarfs, or gas giant planets. The influence of disk fragmentation on the initial binary population is unclear, mostly because the question of when and within which cores a PSD may arrive in a proper mode to enable its fragmentation remains. Moreover, a high mass accretion rate will result in significant heating of the disk material and its immediate surrounding by the release of gravitational energy within the disk. Chemical reactions, like the crystallization of amorphous silicate, may produce long-term tracers of hot phases in PSD evolution (Dullemond et al., 2006).

The shape, size, mass, density and temperature structure of PSDs, which are the precursors of PPDs can only be studied in expensive numerical calculations and indirectly validated by comparing to observed SEDs of Class O/Class I sources or to the known properties of PPDs. In the next section the theoretical background of molecular cloud core collapse will be summarized. Furthermore recent developments and numerical investigations of individually collapsing cores will be discussed.

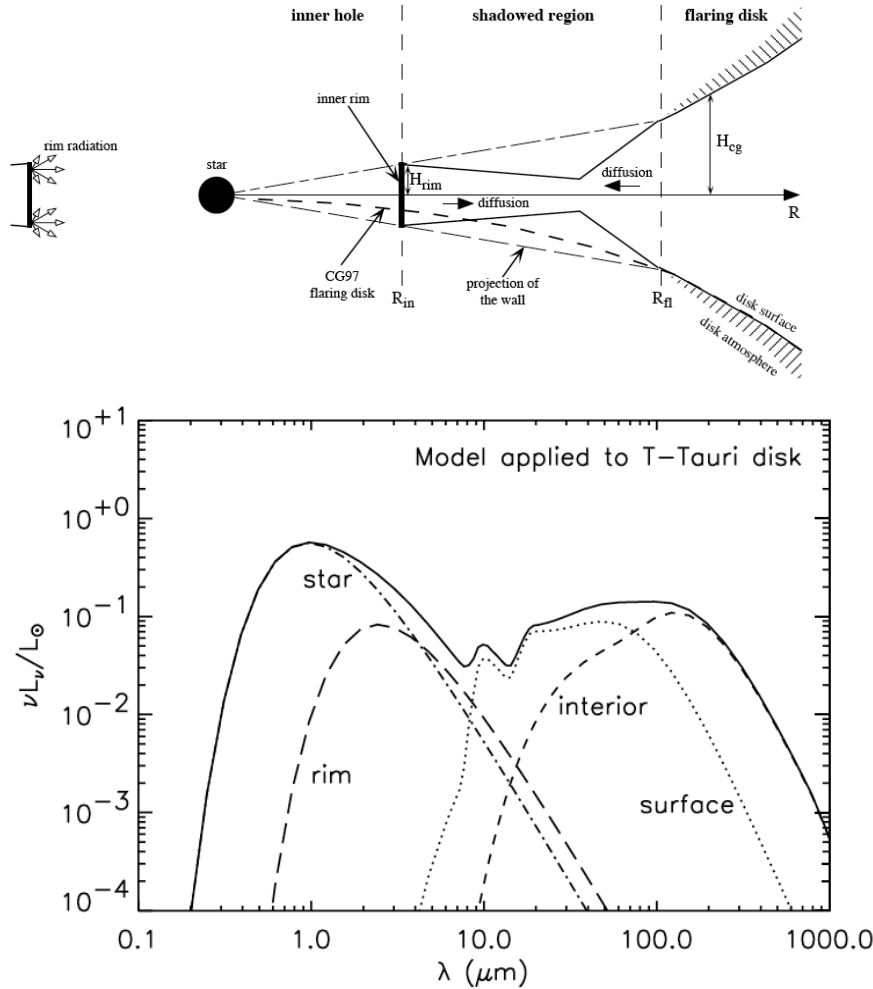


Figure 2.8: Sketch of theoretical PPD structure and resulting SED. The spectrum is decomposed in its four components: Star, inner rim, disk surface layer and disk interior. Figure is taken from Dullemond et al. (2001)

2.3 Theoretical background

2.3.1 Theoretical Ansatz

From a classical point of view the collapse of a molecular cloud core is initiated when its own self-gravity overcomes its thermal pressure. For isothermal initial conditions, this happens when the core has accumulated enough mass to overcome the critical mass - the so-called Jeans mass (Jeans, 1928):

$$M_{\text{Jeans}} = \left(\frac{\pi c_s^2}{G \rho^{1/3}} \right)^{3/2}, \quad (2.18)$$

where c_s is the isothermal sound speed, G is the gravitational constant, and ρ is the mean core density. It should be noted that the Jeans criterion is not self-consistent because it neglects the self-gravity of the whole molecular cloud. Moreover, observed molecular cloud cores typically have centrally condensed, rather than uniform density profiles (see section 2.2). Nevertheless,

the Jeans mass provides a simple estimate of the right order of magnitude if cores or clumps will undergo gravitational collapse.

The first models of molecular cloud core collapse and star formation considered more realistic density profiles, but neglected the effects of slow rotation, not to mention more complicated physics like magnetic fields, turbulence, or radiation transport. These simple models of core collapse, e.g. by Shu (1977), are still attractive because semi-analytical solutions can be obtained. Shu (1977) started from a self-gravitating isothermal sphere in the limit of infinite central concentration - the singular isothermal sphere (SIS), which follows $\rho(r) \propto r^{-2}$ everywhere. Shu (1977) noted that the convergence to an r^{-2} powerlaw represents the tendency of an isothermal self-gravitating gas to approach, as closely as possible, detailed mechanical balance. This tendency will be satisfied as long as different parts of the cloud can communicate acoustically with one another. While the SIS is a sphere of infinite extent, more realistic models of self-gravitating spheres in hydrostatic equilibrium should have a finite radius. For critical Bonnor-Ebert spheres hydrostatic equilibrium is ensured by an additional external pressure. Due to the finite extent of a BES the central density profile is flattened, whereas the outer parts still follow $\rho(r) \propto r^{-2}$. The special feature of a collapsing SISs is the self-similar behaviour of the flow. The collapse proceeds *inside-out* and a constant mass accretion rate onto the central object of $\dot{M}_{\text{infall}} = 0.975c_s^3/G$ was derived. In the case of collapsing Bonnor-Ebert spheres the collapse proceeds *outside-in* and the central mass accretion rate steadily declines after the formation of a seed protostar (Foster & Chevalier, 1993). The infall velocities undergo a smooth transition from homologous inflow to an inflow rate of -3.3 times the sound speed at the origin as the collapse proceeds. This dynamical behaviour is in accordance with the results obtained by Larson (1969); Penston (1969), rather than Shu (1977).

As long as a molecular cloud core rotates slowly compared to the local dynamical timescale, it is possible to treat rotation as a small perturbation to the semi-analytical solution obtained for the non-rotating case (Terebey et al., 1984). Introducing core rotation is however accompanied by another critical problem: The angular momentum problem (Boss, 1980a). Pre-main sequence stars typically have a specific angular momentum (J/M) of about $10^{17} \text{cm}^2 \text{s}^{-1}$, whereas dense molecular cloud cores have $(J/M) = 10^{20..21} \text{cm}^2 \text{s}^{-1}$. The high amount of (J/M) contained in every core leads to a 'centrifugal bounce' and ring formation instead of the formation of a dense central protostar. Ring formation was found in early numerical calculations of prestellar core collapse by e.g. Black & Bodenheimer (1975); Bodenheimer & Tscharnuter (1979); Boss (1980b). Hereupon, Boss (1980a) pointed out that 99.99% of the total core angular momentum must be somehow lost during collapse. On the other hand, Terebey et al. (1984) stated, that it might well be a matter of redistributing (J/M) rather than losing it. Accretion disks play a major role in the redistribution of angular momentum. The transport is enabled by a variety of disk instabilities as well as by shear in a differentially rotating disk. The transport of angular momentum is yet another reason why circum-/ or protostellar disks are supposed to play a major role in star formation.

2.3.2 Recent numerical investigations

Non-turbulent collapse:

Within the past decades many authors have investigated the collapse and fragmentation of molecular cloud cores in numerical studies (for a summary see Goodwin et al., 2006). For example Burkert & Bodenheimer (1993) examined the evolution of spheres with a constant density profile. Like other authors (Miyama et al., 1984) they found the cloud behaviour to depend on two critical parameters, namely the ratio of thermal to gravitational energy α , as well as the ratio of rotational to gravitational energy β (e.g. Miyama et al. (1984) found $\alpha\beta < 0.12$ to be the general criterion for fragmentation). Truelove et al. (1997, 1998), Bate & Burkert (1997), and Boss et al. (2000) demonstrated that earlier simulations utilising either grid-based schemes or the SPH technique, respectively, were frequently affected by numerical fragmentation due to insufficient resolution. Nevertheless, they also confirmed that binary formation is likely happening in case of initial core setups featuring a constant density profile. However, it has also been found that fragmentation and therefore the outcome of collapse simulations is sensitive to the clouds initial density profile (Lynden-Bell, 1964; Boss, 1993; Burkert & Bodenheimer, 1996). Centrally condensed clouds are more stable against fragmentation compared to cores with a uniform mass distribution. For a review see Bodenheimer et al. (2000). In the new millenium, dramatic advances in the development of numerical algorithmic techniques, including adaptive mesh refinement (AMR) and SPH, as well as advances in large-scale parallel machines, have allowed a significant increase in the dynamic range of simulations of low-mass star formation.

The collapse of rigidly (or differentially) rotating Bonnor-Ebert spheres has so far been investigated with grid techniques (Foster & Chevalier, 1993; Matsumoto & Hanawa, 2003; Banerjee et al., 2004). Matsumoto & Hanawa (2003) performed an extensive parameter study of the collapse of a $3M_{\odot}$ rigidly and differentially rotating BES with different rotation rates and bar mode perturbations featuring a barotropic equation of state. They studied the fragmentation properties of the formed star+disk system, and identified $\Omega_c \tau_{ff}$ as the decisive parameter for the formation of either a bar, a ring or a binary system. Bar and ring undergo subsequent fragmentation. In their setup Ω_c denotes the initial central rotation rate and τ_{ff} is the freefall-time, as calculated for the central density of the cloud. Critical values of $\Omega_c \tau_{ff}$ are equivalent to critical combinations of α and β (see above). For $\Omega_c \tau_{ff} > 0.05$ the formed systems were always fragmenting into two or more clumps within a relatively small (up to 100AU in radius) and thin (only a few AU in thickness) protostellar disk. They used a 3D nested grid technique with a resolution of 1AU at the finest level, which is centered around the forming central object. The disk itself is not as well resolved. In order to save computational cost, they employed mirror symmetry with respect to the $z=0$ plane. In addition, the initial grid is not uniform in all three spatial directions, but is four times coarser in vertical (z -)direction as in x and y . However, Nelson (2006) has shown that resolving the vertical structure of a self-gravitating disk is crucial for a proper study of fragmentation.

In 2004, Banerjee et al. followed the collapse of a core ($2.1M_{\odot}$) and cluster ($168M_{\odot}$) BESs, utilizing the 3D AMR code FLASH. All setups feature a 10% $m=2$ perturbation in the initial density profile. They show only one low-mass core collapse with $\Omega_c \tau_{ff} = 0.2$. This system evolves into a bar, which might eventually undergo subsequent fragmentation. Instead of a barotropic equation

of state (EOS), which employs a sudden switch in the adiabatic index to mimic the transition of isothermal to adiabatic gas at high densities ($\rho > 10^{-14...-13} \text{g cm}^{-3}$), they included a more realistic cooling prescription. We also follow this ansatz and employ a parametrisation of radiative cooling by the most abundant molecules as modeled by Neufeld et al. (1995). With this prescription the effective EOS becomes a complex function of temperature and density.

Fragmentation is highly sensitive to the gas thermodynamics (Truelove et al. 1997; 1998). In 2002, Boss was the first to demonstrate that a more precise description of the gas thermodynamics leads to different fragmentation properties of self-gravitating, circumstellar disks. They compared results obtained with a purely isothermal EOS, an adiabatic EOS, and the Eddington approximation of radiative transfer. Disks, which were evolved with a purely adiabatic EOS were stable towards fragmentation, whereas fragments were formed in both other cases, with the Eddington approximation giving intermediate results. They also identified vertical convection to be more efficient in cooling the gas than radiative diffusion. However, parameter studies of fully 3-dimensional simulations with radiation transport have not yet been achieved as they are still too CPU time consuming. Only Krumholz et al. (2006) performed 3D AMR simulations of high-mass core collapse ($100 - 200M_{\odot}$) with radiative transfer. They resolve the collapse on scales of 10AU and found the forming protostellar disks to be rather stable against fragmentation due to radiative feedback from the central star.

Turbulent setups:

Even though many authors already studied the collapse of rigidly (or differentially) rotating Bonnor-Ebert spheres (see above) their turbulent collapse has been barely studied. In general, simulations of turbulent collapse can be subdivided in two different regimes:

Supersonic turbulence (Klein et al., 2001; Klessen, 2001; Bonnell et al., 2003; Bate et al., 2003; Delgado-Donate et al., 2004) and sub-/transonic turbulence (Goodwin et al., 2004a,c, 2006). Collapse simulations featuring supersonic turbulence are applicable to star cluster formation, as molecular clouds seem to be dominated by supersonic motions. In this context, previous work suggests that supersonic turbulence can be very effective in promoting the fragmentation of collapsing clouds. However, for the collapse of individual cloud cores sub-/or transonic motions are important.

In a series of three papers, Goodwin et al. tested the fragmentation properties of moderately turbulent cores in 3D SPH simulations. Goodwin et al. (2004a) computed a sample of 20 cores of $5.4M_{\odot}$, all with different turbulent velocity fields due to a change in the turbulent random number seed. The power spectrum of $P(k) \propto k^{-4}$ was only varied in Goodwin et al. (2004c). They chose a low ratio of turbulent to gravitational energy $\gamma = 0.05$. The cloud cores were modeled as Plummer-like spheres with a central density of $3 \cdot 10^{-18} \text{g cm}^{-3}$ and a flattened inner core region, which is $\approx 5000 \text{AU}$ in radius. Beyond this radius, the density decreases with r^{-4} . Approximately $2M_{\odot}$ of the total $5.4M_{\odot}$ is concentrated within the central 5000AU in radius. Furthermore, they used a polytropic equation of state, mimicing a switch from isothermal to adiabatic gas behaviour at $\rho_{\text{crit}} = 10^{-13} \text{g cm}^{-3}$. Every simulation had only 25000 particles, and convergence (with 50000 and 100000 particles) was only tested for a setup, which formed a single star. Fragmentation into binary or multiple stellar systems was found in 80% of all cases. On average 4.55 stars ($M_{\star} > 0.08M_{\odot}$) and brown dwarfs ($M_{\star} < 0.08M_{\odot}$) were formed from a

single molecular cloud core, and the maximum formed was 10. Low-mass objects ($M_\star < 0.5M_\odot$) were often formed and ejected. Goodwin et al. (2004a) notes that the number and properties of formed objects depends in a chaotic way on the details of the turbulent velocity field. In a subsequent paper, Goodwin et al. (2004c) discussed the effects of different levels of turbulence on the evolution of a molecular cloud core. For this purpose they varied the ratio of turbulent to gravitational energy ($0 \leq \gamma \leq 0.25$). They find that the number of objects formed and their companion frequency both increase with increasing γ . The mass function of these objects is bimodal: They find (1) a flat low-mass segment representing single objects which were ejected from the core before they could accrete much mass, and (2) a Gaussian high-mass segment consisting of objects within the core, which grow by accretion and pair up in multiple systems. Their predicted number of binary systems seems to be too low for $\gamma < 0.025$. Finally, Goodwin et al. (2006) investigated the effects of the turbulent power spectrum by varying the power spectral index n : $P(k) \propto k^{-n}$, with $n=3,4$, or 5 . They find on average one more forming protostellar object for each stepwise increase in n . In addition, the number of ejections is increased, leading to the formation of a larger proportion of single, low-mass objects or a low-mass tail in the mass function. The mean multiplicity decreases. Goodwin et al. (2006) also claim that their results is in contradiction to the results by Delgado-Donate et al. (2004), but this might be due to supersonic turbulent velocities employed by the latter authors.

In contrast to these SPH results, recent AMR calculations of mildly turbulent molecular cloud core collapse with velocities of Mach 1 - Mach 3 (Klein et al., 2004, Klein et al., 2004b) typically form one to (at most) several protostars, with no further evidence of fragmentation of the disks that form around each individual object. Only supersonic turbulent initial conditions may result in binary or low-order multiple stellar systems. These differences are alarming and point out that SPH as well as AMR simulations must demonstrate adequate numerical convergence to be credible.

Numerical Resolution:

It has been known for a long time that sufficient numerical resolution plays a decisive role - not only for simulations of star formation but for all physical, astrophysical or other applications - especially including self-gravity. Bate & Burkert (1997) provided a minimum-resolution criterion for SPH calculations with self-gravity to accurately model fragmentation. The criterion is called the Jeans-condition, as it asks for resolving the local Jeans mass with at least twice the number of SPH neighbours at all times during a simulation. In addition, they found their simulations to give accurate results only if gravitational softening length and hydrodynamic smoothing length are chosen to be equal. Further work on e.g. the optimal gravitational force softening necessary in three-dimensional N-body codes has been done by Dehnen (2001). More recently, Nelson (2006) performed a large investigation of the influence of typical SPH parameters on disk fragmentation and concluded that the better the resolution, the later the fragmentation. In the case of a disk-like geometry he only found his simulations to converge if an even higher resolution than the one proposed by Bate & Burkert (1997) was employed. Furthermore, he defined a new resolution criterion for self-gravitating disks: The Toomre-length criterion, which asks for a high resolution in vertical disk direction. For grid-based schemes Truelove et al. (1997) provided an equivalent criterion to the one introduced by Bate & Burkert (1997): In fixed grid as well as AMR

calculations resolving the local Jeans-length within at least four cells was found to avoid spurious numerical fragmentation. Fragmentation from the same setup has only recently been tested against the numerical method. Commerçon et al. (2008) has published a convergence study and comparison of SPH and AMR technique in the context of molecular cloud core collapse. They studied the collapse of a uniform density sphere weighing $1M_{\odot}$ in slow rigid rotation. They use a standard barotropic equation of state (like e.g. Goodwin et al., 2004a) to mimic the thermal behaviour of the gas. Both techniques seem to agree fairly well, as long as sufficient numerical resolution is used. They also note that the so-called SPH sink particles (Bate et al., 1995), which replace formed protostellar objects at an arbitrary density to reduce computational costs, should be treated with great care.

Chapter 3

Numerical Method: Smoothed Particle Hydrodynamics

The description of gravitational collapse requires a large dynamic range of spatial resolution. An efficient way to achieve this is to use Lagrangian methods for simulating astrophysical, self-gravitating systems. Smoothed particle hydrodynamics (SPH) was first designed to simulate nonaxisymmetric phenomena for astrophysical gases (Lucy, 1977; Gingold & Monaghan, 1977; Benz, 1990; Monaghan, 1992).

The fully three-dimensional simulations of prestellar core collapse and star formation presented in this thesis have been carried out with the OpenMP-parallel SPH and N-body code VINE (Wetzstein et al., 2008; Nelson et al., 2008). Due to its Lagrangian nature SPH has the advantage of following the geometry of the simulation with adaptive spatial resolution. Thus, the main advantage of SPH is its strict Galilean-invariant property. In particular, dissipative properties do not depend on geometry or direction, which can be a severe problem for grid-based methods without physical dissipation control. SPH is a particle based method. A gas, fluid or other dynamically evolving form of matter is represented by a set of particles N_p , to which physical quantities such as mass, position, velocity and internal energy are assigned or computed. Resolution elements are concentrated in high-density regions in SPH methods, naturally concentrating the computational work in the most interesting areas of the flow. This can be an advantage as well as a disadvantage of the method. For instance, studies of turbulence decay may be problematic with SPH as they require a rather uniform resolution on all scales and good shock capturing (for supersonic turbulence). Therefore it is still necessary to prove the applicability of SPH to shock or instability dominated problems, which is currently work in progress (Junk et al., in prep; Agertz et al., 2007). However, SPH is ideally suited to solve gravity dominated problems, which require the resolution of many orders of magnitude in spatial scale and density, respectively. For this purpose, running SPH on single processors is by far not enough to compensate the high computational costs of modern high-resolution simulations. The VINE code has therefore been developed for the use on multi-processor shared memory architectures using OpenMP (Deagum & Menon, 1999). OpenMP is a suite of compiler directives to effectively share work among a number of processors.

In the following I will briefly discuss the basics of the SPH formalism. SPH is based on the Euler

equations, which describe the dynamical evolution of a fluid. Their derivation will be reviewed in the first section. In addition, within the framework of my research, I implemented a numerical prescription to treat cooling radiation by molecular lines. This method will be described in the last section of this chapter.

3.1 Equations of fluid dynamics

The mathematical description of the state and motion of a fluid depends on two thermodynamical quantities (e.g. the density $\rho(x, y, z, t)$ and the pressure $P(x, y, z, t)$) and on the velocity distribution $\vec{v} = \vec{v}(x, y, z, t)$ within it. P and ρ are linked with all other thermodynamical parameters via an equation of state. Thus the complete system of equations describing a hydrodynamical flow, consists of five equations to account for the five unknowns (2 thermodynamical quantities and 3 velocity components). The aim of this section is to introduce the basic hydrodynamical equations necessary to describe a self-gravitating, viscous fluid. These are the continuity equation (conservation of mass) and the Euler equation (three components), which describes the conservation of momentum. To close the set of equations, conservation of energy is required. In the SPH code VINE, this part is governed by evolving the internal energy u , which is linked to the pressure P and the density ρ through an equation of state (EOS). For further reading see Landau & Lifschitz (1966).

3.1.1 Continuity equation

The mass of a fluid with the density ρ in a certain volume V is estimated as $\int \rho dV$. Thus the amount of fluid, which flows through a surface element of size $|d\vec{f}|$ of the volume per unit time is $\rho \vec{v} \cdot d\vec{f}$. The total mass streaming out of the volume V per unit time is hence given by

$$\oint \rho \vec{v} d\vec{f}. \quad (3.1)$$

On the other hand the decrease in fluid mass inside the volume can be written as

$$-\frac{\partial}{\partial t} \int \rho dV. \quad (3.2)$$

Conservation of mass implies that the decrease in mass per unit time must be equal to the amount of outstreaming mass. This yields

$$\frac{\partial}{\partial t} \int \rho dV = - \oint \rho \vec{v} d\vec{f} \quad (3.3)$$

$$= - \int \vec{\nabla} \cdot (\rho \vec{v}) dV \quad (3.4)$$

$$\Leftrightarrow \int \left[\frac{\partial \rho}{\partial t} + \vec{\nabla} \cdot (\rho \vec{v}) \right] dV = 0. \quad (3.5)$$

Eq.3.4 is obtained by applying Gauss's law.

Since eq.3.5 must be valid for every volume V , the continuity equation may finally be written as

$$\frac{\partial \rho}{\partial t} + \vec{\nabla} \cdot (\rho \vec{v}) = 0. \quad (3.6)$$

3.1.2 Euler equation

Analogous to the section 3.1.1 the change of total momentum $\rho \vec{v}$ of a fluid element dV is

$$\frac{\partial}{\partial t} \int \rho \vec{v} dV. \quad (3.7)$$

On the other hand the total momentum change of dV is due to the total force exerted on it (this is the pressure P) and the total momentum flux through it. Thus, the change of momentum is according to

$$- \oint P d\vec{f} - \oint \rho \vec{v} \vec{v} \cdot d\vec{f}. \quad (3.8)$$

Conservation of momentum implies that eq.3.7 must be equal to eq.3.8:

$$\frac{\partial}{\partial t} \int \rho \vec{v} dV + \oint P d\vec{f} + \oint \rho \vec{v} \vec{v} \cdot d\vec{f} = 0 \quad (3.9)$$

$$\Leftrightarrow \frac{\partial}{\partial t} \int \rho \vec{v} dV + \int \vec{\nabla} P dV + \int \vec{\nabla} \cdot (\rho \vec{v} \vec{v}) dV = 0 \quad (3.10)$$

$$\Rightarrow \frac{\partial}{\partial t} (\rho \vec{v}) + \vec{\nabla} P + \vec{\nabla} \cdot (\rho \vec{v} \vec{v}) = 0, \quad (3.11)$$

where Gauss law was applied again. With

$$\frac{\partial}{\partial t} (\rho \vec{v}) = \rho \frac{\partial \vec{v}}{\partial t} + \vec{v} \frac{\partial \rho}{\partial t} \quad \text{and} \quad (3.12)$$

$$\vec{\nabla} \cdot (\rho \vec{v} \vec{v}) = \vec{v} \vec{\nabla} \cdot (\rho \vec{v}) + \rho \vec{v} \cdot \vec{\nabla} \vec{v} \quad (3.13)$$

it follows that eq.3.11 can be written as

$$\rho \frac{\partial \vec{v}}{\partial t} + \underbrace{\vec{v} \frac{\partial \rho}{\partial t} + \vec{v} \vec{\nabla} \cdot (\rho \vec{v})}_{= 0} + (\rho \vec{v} \cdot \vec{\nabla}) \vec{v} + \vec{\nabla} P = 0 \quad (3.14)$$

$$\Rightarrow \rho \frac{\partial \vec{v}}{\partial t} + (\rho \vec{v} \cdot \vec{\nabla}) \vec{v} + \vec{\nabla} P = 0. \quad (3.15)$$

Eq.3.15 is the Euler equation for a compressible but non-viscous fluid. If the fluid is in a gravitational potential the volume element dV experiences the additional force $\rho \vec{g}$, where \vec{g} is the acceleration due to gravity. In this case the Euler equation yields

$$\rho \frac{\partial \vec{v}}{\partial t} + (\rho \vec{v} \cdot \vec{\nabla}) \vec{v} = -\vec{\nabla} P - \rho \vec{g}. \quad (3.16)$$

Note that all these equations were derived without considering internal friction, respectively viscosity. As a consequence this description cannot treat an active accretion disk, because the flow is not viscous as required in order to transport angular momentum (i.e. the radial velocity v_R is zero in this case). Thus, an ideal fluid as presented here is clearly not sufficient to describe the motion in a circumstellar disk correctly.

In a viscous fluid an additional irreversible momentum transfer due to internal friction (e.g. molecular or turbulent viscosity) occurs within the flowing material. This must be considered in eq.3.16 by adding an additional term: the so-called viscous stress tensor σ (σ is a symmetrical tensor of second order), which is defined as¹

$$\sigma_{ik} = \rho \nu \left(\frac{\partial v_i}{\partial x_k} + \frac{\partial v_k}{\partial x_i} - \frac{2}{3} \delta_{ik} \frac{\partial v_l}{\partial x_l} \right) + \zeta \delta_{ik} \frac{\partial v_l}{\partial x_l}, \quad (3.17)$$

where $\nu [\frac{cm^2}{s}]$ is the kinematic viscosity and ζ the bulk viscosity due to the fluid's compressibility. In an accretion disk ζ plays a minor role, since the inward flow of disk material occurs on a much longer time scale than the azimuthal motion and may therefore be neglected (for a more detailed derivation of Eq.3.17 see Landau & Lifschitz (1966)).

Thus, the Euler equation 3.16 becomes²:

$$\rho \frac{\partial \vec{v}}{\partial t} + (\rho \vec{v} \cdot \vec{\nabla}) \vec{v} = -\vec{\nabla} P - \rho \vec{g} + \rho \nu \left[\Delta \vec{v} + \frac{1}{3} \vec{\nabla} (\vec{\nabla} \cdot \vec{v}) \right] \quad (3.18)$$

Eq.3.18 is also known as *Navier-Stokes equation* and represents the equation of motion for a viscous, compressible fluid. The numerical solution of the Navier-Stokes equations is more difficult than the integration of the Euler equations, as the viscous term depends on the second derivative of the velocity. In the SPH formalism, an artificial viscosity is used instead of the real physical viscosity in Eq. 3.18. Therefore the Euler equations (Eq. 3.16) provide the basis for SPH.

3.2 Equations describing the SPH algorithm

A system of SPH particles is dynamically evolved by computing gravitational and hydrodynamical forces of the particles on each other. Time integration of the particles' equations of motion and additional equations for e.g. internal energy, is the problem to be solved. Hereby time integration should be quick, but accurate enough to achieve reliable results. In case particles only interact gravitationally ('N-body simulations') the motion of each particle i is described by

$$\frac{d\vec{x}_i}{dt} = \vec{v}_i \quad (3.19)$$

¹ δ_{ik} is the Kronecker symbol

² where $\Delta \equiv \vec{\nabla} \cdot \vec{\nabla}$

and the equation describing the conservation of momentum is

$$\frac{d\vec{v}_i}{dt} = -\frac{\nabla\vec{\Phi}}{m_i}, \quad (3.20)$$

where all of the $6N_p$ equations (in three dimensions) are coupled through the gravitational potential $\vec{\Phi}$. If one is interested in additional interactions of the particles (SPH), these have to be included in equation 3.20. Gas dynamics asks for the description of forces due to pressure gradients. Therefore the ideal form of the SPH momentum equation is

$$\frac{d\vec{v}_i}{dt} = -\frac{\nabla\vec{\Phi}}{m_i} - \frac{\nabla P}{\rho}, \quad (3.21)$$

where p and ρ denote the pressure and density of the fluid, respectively.

In addition to an expansion of the momentum equation, the picture of point masses sufficient to describe an N-body system has to be revised. SPH can be regarded as an interpolation technique. Point masses rather become fluid elements with a certain size and density. Therefore an interpolation kernel has been introduced. The widely used W4 SPH smoothing kernel (Monaghan & Lattanzio, 1985) in its 3-dimensional form is defined as

$$W(r_{ij}, h_{ij}) = \frac{1/\pi}{h_{ij}^3} \begin{cases} 1 - \frac{3}{2}v^2 + \frac{3}{4}v^3 & \text{if } 0 \leq v \leq 1, \\ \frac{1}{4}(2-v)^3 & \text{if } 1 \leq v \leq 2, \\ 0 & \text{otherwise,} \end{cases} \quad (3.22)$$

with the dimensionless separation $v = r_{ij}/h_{ij}$. The kernel $W(r_{ij}, h_{ij})$ connecting particle i and j is a function of their distance $r_{ij} = |\vec{r}_i - \vec{r}_j|$ and their characteristic smoothing length scale $h_{ij} = (h_i + h_j)/2$, where h_i and h_j are the individual smoothing lengths assigned to particle i and j , respectively. An important characteristic required to ensure conservation of momentum is the symmetry of the SPH kernel under the exchange of particle indices. Most differences between SPH implementations also come from the way force symmetry between pairs of particles is handled. With these definitions, particles whose separations are $v < 2$ contribute to the summations of each others forces or density as *neighbours*. For instance the SPH density is defined as

$$\rho_i \equiv \rho(\vec{r}_i) = \sum_{j=1}^N m_j W(r_{ij}, h_{ij}), \quad (3.23)$$

where m_j is the mass of each of the N neighbour particles of particle i , which contribute to the density of particle i . Fig. 3.1 depicts the extent and shape of the SPH smoothing kernel.

Not only the kernel function itself, but also the equation of momentum conservation needs to be written in a symmetric form:

$$\frac{d\vec{v}_i}{dt} = -\sum_{j=1}^N m_j \left(\frac{p_i}{\rho_i^2} + \frac{p_j}{\rho_j^2} + \Pi_{ij} \right) \vec{\nabla}_i W(r_{ij}, h_{ij}) - \frac{\nabla\vec{\Phi}}{m_i}, \quad (3.24)$$

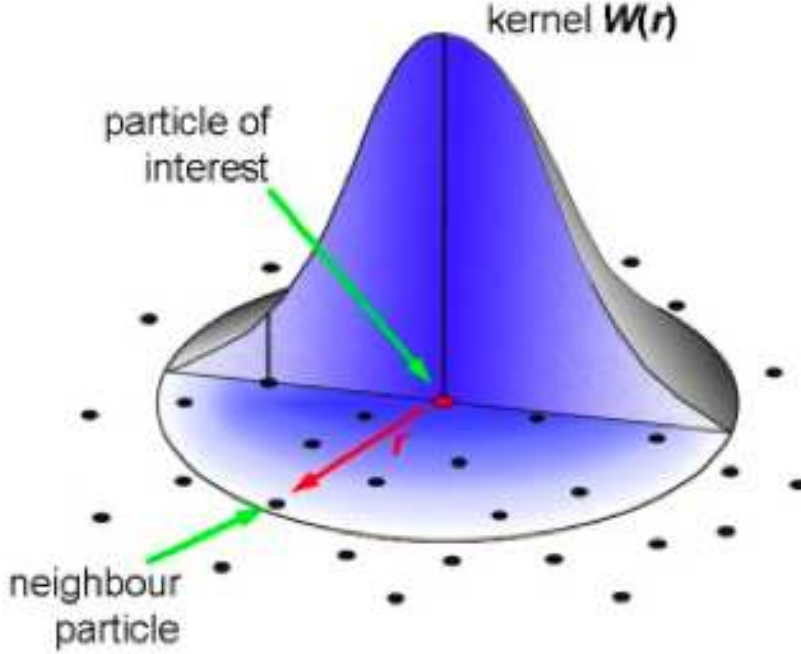


Figure 3.1: Sketch of the SPH Kernel

where $\vec{\nabla}_i$ means take the gradient with respect to the coordinate of particle i (for a detailed derivation see Benz, 1990). The additional artificial viscosity pressure Π_{ij} included to model dissipative effects (like shocks or viscosity), has no counterpart in Eq. 3.21. Alternatively a dissipative term modeled on the viscous terms in the Navier-Stokes equations might be included.

The choice of a particle's smoothing length is a critical issue in SPH simulations and goes hand in hand with the computational costs on the one hand and the accuracy of the interpolation scheme on the other, as the accuracy of SPH depends on the number of neighbouring particles taken into account in sums like Eq. 3.23, making high numbers of neighbours or large smoothing lengths desirable. On the other hand, the count and computation of a large number of neighbour quantities increases the computational effort and decreases the spatial resolution of the simulation, since only scales larger than h are resolved. These two competing effects lead to the requirement that the number of neighbours should stay roughly constant at a level where correct interpolation is assured without wasting computational resources or losing resolution. Therefore particle smoothing lengths need to be variable in space and time. The time-dependent individual particle smoothing length $h_i(t)$ is evolved according to (Benz, 1990):

$$\frac{dh_i}{dt} = -\frac{1}{3} \frac{h_i}{\rho_i} \frac{d\rho_i}{dt} = \frac{1}{3} h_i \vec{\nabla} \cdot \vec{v}_i. \quad (3.25)$$

If the evolution of eq.3.25 leads to a neighbour count outside a given range, an exponential correction term pushes $h_i(t)$ such that more or less neighbours are found on the next step. In the standard implementation of the employed SPH code VINE (Wetzstein et al., 2008; Nelson et al., 2008) the number of neighbours will be kept within the range of [30, 70], with a mean number

of 50 neighbours and an allowed deviation of $\Delta N = 20$. According to Attwood et al. (2007) a smaller value of ΔN might be more appropriate to avoid numerical dissipation.

In addition to these equations, the change in the thermodynamic state of the fluid requires an equation of state and an energy equation. For an ideal gas without external heating or cooling terms, only compressional heating and cooling are important and the internal energy u is evolved according to

$$\frac{du}{dt} = -\frac{p}{\rho} \vec{\nabla} \cdot \vec{v}, \quad (3.26)$$

where v is the local fluid velocity. The SPH formulation of eq. 3.26 implemented in e.g Benz (1990) and Wetzstein et al. (2008) is

$$\frac{du_i}{dt} = -\frac{p_i}{\rho_i^2} \sum_{j=1}^N m_j \vec{v}_{ij} \cdot \vec{\nabla}_i W(r_{ij}, h_{ij}) + \frac{1}{2} \sum_{j=1}^N m_j \Pi_{ij} \vec{v}_{ij} \cdot \vec{\nabla}_i W(r_{ij}, h_{ij}), \quad (3.27)$$

with the first term corresponding to the reversible 'PdV' work, and the second term describing the irreversible thermodynamic dissipation from shocks and viscosity through the artificial viscous pressure Π_{ij} .

The energy equation has to be modified, when external heating or cooling processes are included. This has been done in the framework of this PhD thesis (see section 3.7). To close the set of equations, an equation of state, which relates internal energy, density and pressure, needs to be defined. Simple EOS include the one describing isothermal, isentropic or adiabatic gas behaviour and ideal gases.

3.3 SPH Artificial Viscosity

Following the *standard prescription*, the viscous pressure includes both a bulk viscosity (α) to eliminate subsonic velocity oscillations and a von Neumann-Richtmyer viscosity (β) to convert kinetic energy to thermal energy and prevent the interpenetration of particles in shocks (Monaghan & Gingold, 1983):

$$\Pi_{ij} = \begin{cases} (-\alpha_{ij} c_{ij} \mu_{ij} + \beta_{ij} \mu_{ij}^2) / \rho_{ij} & \vec{v}_{ij} \cdot \vec{r}_{ij} \leq 0, \\ 0 & \vec{v}_{ij} \cdot \vec{r}_{ij} > 0. \end{cases} \quad (3.28)$$

μ_{ij} is the velocity divergence:

$$\mu_{ij} = \frac{h_{ij} \vec{v}_{ij} \cdot \vec{r}_{ij}}{\vec{r}_{ij}^2 + \eta^2 h_{ij}^2} f_{ij} \quad (3.29)$$

with $\eta \approx 10^{-1} - 10^{-2}$ to prevent singularities. In its original form (Lattanzio et al., 1986), f_{ij} is set to unity in Eq. 3.29. In general $f_{ij} = 1/2(f_i + f_j)$. Balsara & Norman (1990) and Balsara (1995) found that this form gives rise to large entropy generation in pure shear flows, which he suppressed by de defining an additional factor f to reduce the contribution selectively in shear flows. In the so-called *Balsara* implementation f_i is defined as

$$f_i = \frac{|\langle \vec{\nabla} \cdot \vec{v}_i \rangle|}{|\langle \vec{\nabla} \cdot \vec{v}_i \rangle| + |\langle \vec{\nabla} \times \vec{v}_i \rangle| + \eta'} \quad (3.30)$$

with η' preventing divergence once more. The factors α and β in Eq. 3.28 are parameters controlling the strength of the artificial viscosity. The best choice for their values depends on the problem which has to be solved (see e.g. Steinmetz & Mueller, 1993; Lombardi et al., 1999), but values near $\alpha = 1$ and $\beta = 2$ are most commonly used. In order to reduce and minimize unwanted viscous dissipation throughout a simulation, Morris & Monaghan (1997) invented a *time-varying* viscosity prescription, where each particle is assigned time dependent viscous parameters. The individual viscosity parameter α_i of particle i is then evolved in time according to a source and decay equation:

$$\frac{d\alpha_i}{dt} = -\frac{\alpha_i - \alpha_*}{\tau_i} + S_i. \quad (3.31)$$

The first term forces the value of α_i to decay asymptotically to a value of α_* on a time scale τ , given by

$$\tau_i = \frac{\delta_\alpha h_i}{c_s \sqrt{(\gamma - 1)/2\gamma}}. \quad (3.32)$$

The decay timescale is converted to a more convenient decay length scale through δ_α . Morris & Monaghan (1997) further derived the decay time from the post-shock Mach number for strong shocks, combined with the sound speed c_s and smoothing length. Due to the source term S_i in eq. 3.31, artificial viscosity will be increased in strong compressions or shocks (see Rosswog et al., 2000).

3.4 Integration and Time stepping

In the simulations performed throughout this thesis particles were advanced in time by using the Leapfrog integration scheme (Hockney & Eastwood, 1981). The Leapfrog is an offset integrator, which means that position and velocity calculations are offset from each other in time by half a current time step. Alternate updates of position and velocity advance from one half step behind to one half step ahead of the other update in the sequence, effectively ‘leapfrogging’ over each other in the integration scheme, which takes its name by analogy from the children’s game. In a non-offset form positions and velocities are written as

$$v^{n+1} = v^n + a^{n+1/2} \Delta t^n \quad (3.33)$$

$$x^{n+1} = x^n + \frac{1}{2} (v^n + v^{n+1}) \Delta t^n \quad (3.34)$$

where indices n denote quantities at time t^n and Δt^n is the time interval from n to $n + 1$. The offset form is recovered when positions and accelerations are actually defined on half timesteps. The position update is effectively split into two halves. With a fixed increment Δt , each position update as defined in eq. 3.34 uses the velocity corresponding to two separate velocity updates, half from timestep n , $v^n/2$, and half from timestep $n + 1$, $v^{n+1}/2$, so that, effectively, updates of position are only half completed at any ‘full’ time step n . The velocity update requires accelerations to be calculated on half steps, $n + 1/2$. For simulations involving selfgravity

and hydrodynamics, the accelerations depend on particle positions, so that a separate, temporary update of the positions to their correctly offset temporal location is required:

$$x^{n+1/2} = x^n + \frac{1}{2}v^n \Delta t^n. \quad (3.35)$$

Other hydrodynamical quantities such as internal energy or smoothing lengths are defined on full timesteps. Their derivatives must be calculated on half timesteps at the same time as the accelerations. Complications arise because for most of these variables the derivative is a function of the variable itself or of other variables defined on full timesteps. Linear interpolation from n to $n + 1/2$ is employed in such cases, such that the integration scheme itself remains formally second order accurate.

The integration scheme is only accurate and stable as long as integration timesteps are small enough. At the same time, timesteps should not be much smaller than required in order to save computational costs. For this purpose, individual particle timesteps (Porter, 1985; Ewell, 1988; Hernquist & Katz, 1989) can be implemented. Individual particle time steps are especially useful in simulations which cover a wide range in density (more than 20 orders of magnitude in a star formation simulation) as different physical time scales are naturally introduced in such a simulation. During the simulation the next time step for a particle i is the minimum time step derived from k criteria:

$$\Delta t_i^{n+1} = \min_k \left(\Delta t_{i,k}^{n+1} \right). \quad (3.36)$$

Time step criteria are for example based on changes in a particle's

$$\text{acceleration:} \quad \Delta t_{\text{accel}}^{n+1} = \tau_{\text{accel}} \sqrt{\frac{h}{|\vec{a}|}}, \quad (3.37)$$

$$\text{velocity:} \quad \Delta t_{\text{vel}}^{n+1} = \tau_{\text{accel}} \frac{h}{|\vec{v}|}, \quad (3.38)$$

$$\text{both:} \quad \Delta t_{\text{velacc}}^{n+1} = \tau_{\text{accel}} \frac{|\vec{v}|}{|\vec{a}|} \quad (3.39)$$

where \vec{a} is the acceleration of the particle i at the previous time step, and $\tau_{\text{accel}} \approx 0.5$ is a tuning parameter. In many cases it is sufficient to include only the acceleration based criterion. However, for SPH, two additional criteria are required.

- The Courant-Friedrichs-Lewy (CFL) condition in its SPH form (Monaghan, 1989)

$$\Delta t_{\text{CFL}}^{n+1} = \tau_{\text{CFL}} \frac{h_i}{c_i + 1.2 (\alpha_i c_i + \beta_i h_i \max_j (\mu_{ij}))} \quad (3.40)$$

including the artificial viscosity parameters α_i and β_i and the sound speed c_i of particle i . $\tau_{\text{CFL}} \approx 0.3$ gives good results (Monaghan, 1989). The CFL condition ensures that information or flux is not propagated further than a smoothing length scale.

- and the smoothing length scale criterion

$$\Delta t_h^{n+1} = \tau_h \frac{h_i}{\bar{h}_i} \quad (3.41)$$

with $\tau_h \approx 0.1 - 0.15$ in order to ensure that particles encountering a strong shock require several time steps to pass through the shock interface.

3.5 MACs and Tree

One of the most costly calculations in almost any simulation including gravity is the computation of the gravitational forces of the particles on each other. In 'collisionless' systems a direct calculation of the gravitational forces each particle exerts on every other particle is unnecessary. Approximate forces are accurate enough, but significantly faster to compute. The gravitational force is then approximate in the sense that contributions of distant particles are merged into one single interaction. The difficulty of the scheme is the decision, which particles to define as distant particles. For this purpose it is necessary to organise the particles in a *tree* data structure, and then use tree nodes as proxies for groups of particles. The tree structure implemented in the VINE code is called the *nearest neighbour binary tree* (Press, 1986; Benz, 1990). The advantage of this tree is that particles are naturally grouped in the tree as they are grouped in space. When constructing the tree, the nearest neighbours of all particles or nodes for which no nearest neighbour has yet been found and to associate such pairs into higher order nodes. Fully traversing the tree will then produce a list of nodes, which are acceptable for interaction with a given particle, and a list of single particles (the neighbours) for which an exact force calculation is required. With this method, the computational effort for calculating the gravitational force is reduced to $O(N_p \log N_p)$, instead of $O(N_p^2)$ for complete direct summation. Nevertheless, a tree is only efficient if one chooses a fast method to traverse it, and if an efficient method to decide what to do with specific nodes is used. As the contribution of nodes, which contain particles with relatively large distance to the particle of interest, is approximated by a multipole expansion, the acceptability of a node is based on the convergence radius of the multipole expansion as well as on limits on the errors due to series truncation. Different implementations of these so-called 'Multipole Acceptance Criteria' (MACs) are known. The MAC used in the performed calculations within this thesis is the 'Gadget MAC' (Springel et al., 2001):

$$r_{ij}^6 > \frac{M_j h_j^4}{\theta |\vec{a}_{\text{old}}|} \quad (3.42)$$

where the gravitational constant is set to $G = 1$. a_{old} is the value of the acceleration for a particle at the last time step and θ is a dimensionless, relative error in the acceleration to be allowed to any single node. h_j is the physical size of the tested node and r_{ij} is the separation between the current node and the particle, whose forces are to be computed. In addition, the 'geometric' MAC with an accuracy parameter $\theta = 1$ has to be satisfied in order to prevent an overlap of particle and node in space, which would violate the convergence of the multipole expansion:

$$r_{ij}^2 > (h_j + h_i)^2. \quad (3.43)$$

For additional details on the MACs and calculation of the gravitational acceleration see Wetzstein et al. (2008); Nelson et al. (2008). To determine the tree accuracy for the gravitational force calculation in the following simulations, we use the tree opening angle criterion of Springel et al. (2001) with $\theta = 5 \cdot 10^{-3}$.

3.6 Boundary Conditions

Usually, only a small portion of the universe is modeled in one individual simulation. This requires conditions at the boundaries of the computational domain to be specified in order to model the influence of gas and matter outside it. For a cubic volume at least two types of boundary conditions are necessary to complete the set of equations: One for gravity and one for the dynamical or hydrodynamical evolution. For the purpose of individual prestellar core collapse it is best to assume that the sphere truly is in isolation - at least with respect to the gravitational potential. This assumption is reasonable, since the average density within a prestellar core is a factor 100 or more higher than within the surrounding molecular cloud. Thus, the freefall time of a prestellar core is also much shorter (10^5 yr instead of $10^6 - 10^7$ yr) than the freefall time of the whole molecular cloud. Therefore, isolated gravity boundary conditions were employed in the following simulations.

For the SPH part, periodic boundaries are useful, as they assure the code's stability by preventing particles from accidentally leaving the box. As required for Bonnor-Ebert spheres, the cold and dense prestellar cores in the performed calculations are embedded in a warm (2000 Kelvin) and diffuse ambient medium. In order to avoid boundary effects the diameter of the sphere spans only half of the computational domain. Thus, warm 'boundary' particles surrounding the collapsing core are not of particular dynamical interest, but are required in order to abide the external pressure confining the Bonnor-Ebert sphere. These 'boundary' particles are allowed to move freely through the surfaces of the computational domain and also to feel each other in terms of neighbour contributions from across box boundaries. Periodic boundary conditions in SPH thus require the modification of the SPH neighbour search, such that a particle close to the box boundary will not see the volume beyond the boundary as a void without any neighbour particles. Instead the particle needs to find those particles as neighbours, which are close to the boundary at the opposite side of the box.

As this procedure is invoked for any neighbor search, not only quantities like density or velocity divergence are computed correctly, but also the pressure gradients and contributions to the derivative of the internal energy because a particle feels the pressure exerted by such periodic neighbors as originating from the volume outside of the simulation box.

3.7 Equation of State and Molecular Line Cooling

To close the set of equations describing the fluid flow, an additional equation is required: The Equation of State (EOS). An EOS is used to relate the internal energy of a particle to its density

and pressure. The most simple formulation is obtained for an ideal gas:

$$P = u\rho(\gamma - 1), \quad (3.44)$$

where P is the gas pressure, u is the internal energy, γ the adiabatic index defining the stiffness of the EOS, and ρ is the density within the gas element of interest. More precisely, γ is the ratio of specific heats C_p/C_v , where C_p is the specific heat at constant pressure and C_v is the specific heat at constant volume. The internal energy u is directly proportional to the local sound speed c_s :

$$u = \frac{c_s^2}{\gamma(\gamma - 1)} \quad (3.45)$$

The local sound speed depends on the gas temperature T :

$$c_s = \sqrt{\frac{\gamma k_B T}{\mu m_p}}, \quad (3.46)$$

where k_B is the Boltzmann constant, m_p is the mass of a proton and μ is the mean molecular weight of an average gas molecule.

The adiabatic index can be related to the degrees of freedom f of a molecule by

$$\gamma = \frac{f + 2}{f}. \quad (3.47)$$

For a monoatomic gas with three degrees of freedom follows $\gamma = 5/3 = 1.67$, whereas for a diatomic gas with five degrees of freedom we obtain $\gamma = 7/5 = 1.4$. For a diatomic gas only translational and rotational degrees of freedom are considered, because vibrations are only excited at very high temperatures. The most abundant molecule found in molecular cloud cores is molecular hydrogen ($\mu = 2$). Therefore the adiabatic index $\gamma = 1.4$ will be used in the following simulations. This EOS corresponds to a purely adiabatic behaviour for diatomic gas (e.g. Bate (1998)).

However, Inutsuka & Masunaga (2001) found that the collapse usually proceeds in an isothermal fashion at low densities ($\rho < \rho_{\text{crit},0} = 10^{-13} \text{g cm}^{-3}$). In this regime the cooling time scale is short compared to the free-fall or dynamical time scale. Therefore the gas cools instantaneously and keeps a constant temperature. The corresponding EOS for an isothermal gas can be approximated by setting $\gamma = 1$ and $u = c_s^2$. At higher densities ($10^{-8} \text{g cm}^{-3} > \rho > \rho_{\text{crit},0}$) the molecular gas within a dense core is typically assumed to be optically thick at all wavelengths. In this regime it behaves adiabatically. It is however not clear whether the transition from the isothermal to the adiabatic regime during prestellar core collapse is continuous or abrupt. Various other authors (Goodwin et al., 2004b; Bate, 1998; Matsumoto & Hanawa, 2003), introduce a rather abrupt transition. For instance Bate (1998) used a barotropic EOS to follow the collapse of a prestellar core up to stellar densities. Therefore he had to consider several different density regimes

$$\gamma = \begin{cases} 1.0 & \rho \leq 1.0 \cdot 10^{-13} \text{g cm}^{-3}, \\ 1.4 & 1.0 \cdot 10^{-13} \text{g cm}^{-3} < \rho \leq 5.7 \cdot 10^{-8} \text{g cm}^{-3}, \\ 1.15 & 5.7 \cdot 10^{-8} \text{g cm}^{-3} < \rho \leq 1.0 \cdot 10^{-3} \text{g cm}^{-3}, \\ 1.67 & \rho > 1.0 \cdot 10^{-3} \text{g cm}^{-3}, \end{cases} \quad (3.48)$$

throughout which the gas pressure was required to change continuously ($P = K\rho$ with $K = c_s^2$ only for $\rho \leq 10^{-13} \text{g cm}^{-3}$). In his model, the gas behaves isothermally below densities of $10^{-13} \text{g cm}^{-3}$. Above this density the cooling time scale is comparable to the dynamical time scale of the system and the adiabatic index is varied according to the current state of the gas: We find $\gamma = 1.4$ for molecular hydrogen gas, which is optically thick at all wavelengths and cannot cool anymore. $\gamma = 1.15$ above $\rho \approx 10^{-8} \text{g cm}^{-3}$ and a temperature of 2000K, where gravitational energy is not purely transformed into heat but used to dissociate H_2 molecules. In this phase, the collapse will be accelerated as compared to the adiabatic stage. Therefore some authors call this stage the 'second collapse'. Once H_2 is completely dissociated a second adiabatic stage begins. Now $\gamma = 1.67$ is assumed as expected for monoatomic gas. However, in simulations of core fragmentation and protostellar disk formation, the collapse of an individual object cannot be resolved up to stellar densities. The computational cost of such a simulation is still too high. Instead of using an artificial setup to describe the transition of the gas' thermal behaviour, we use an adiabatic index of $\gamma = 1.4$ throughout the whole simulation - independent of the local gas density. In addition, we account for radiative cooling due to optically thin molecular lines, excited by collisions, in a subsequent step of the internal energy calculation done for every SPH particle. The cooling rate coefficient, which was provided by Neufeld et al. (1995), is a function of three parameters: volume density ($10^3 \leq n(\text{H}_2) \leq 10^{10} \text{cm}^{-3}$), temperature ($10 \leq T \leq 2500 \text{K}$) and the optical depth parameter $\tilde{N}(M)$. The optical depth parameter is defined as $\tilde{N}(M) = \frac{gn(M)}{dv_z/dz}$ (see Neufeld et al., 1995, Eq.1), where dv_z/dz is the local velocity gradient and g is a dimensionless geometric factor. The considered coolants are the most abundant molecules in MCCs (CO , H_2O , H_2 , HCl , O_2 , C and O). Equilibrium state molecular abundances have been assumed. More elaborate effects like CO freeze-out have been neglected in these calculations. Since typical molecular cloud cores have a density profile close to $\rho(R) \propto R^{-2}$ over a large range of radii, we employ the provided optical depth parameter for a singular isothermal sphere:

$$\tilde{N}_{\text{SIS}} = 5.1 \cdot 10^{19} \left(\frac{n(\text{H}_2)}{\text{cm}^{-3}} \right)^{1/2} \frac{1 \text{ km}}{\text{cm}^2 \text{ s}}$$

(see Neufeld & Green, 1994). This prescription captures at least part of the thermodynamics of the system. Compared to the usually adopted EOS (see Eq. 3.48), it definitely provides a more realistic physical estimate of the temperature structure around the dense parts of the evolving system. In Fig.3.2, we show the adopted cooling rates as a function of density. At lower temperatures cooling becomes overall less efficient and the position of the maximum cooling rate is shifted to lower densities. Molecular line cooling is applicable as long as the gas density does not exceed the critical value $\rho_{\text{crit},0} = 10^{-13} \text{g cm}^{-3}$, above which the gas becomes optically thick at all wavelengths. For $\rho < \rho_{\text{crit},0}$, the gas is partly optically thin, mostly at sub-mm to mm wavelengths. The characteristics of the cooling function already gain importance when the density rises above $\rho_{\text{crit},1} \approx 3 \cdot 10^{-16} \text{g cm}^{-3}$. This can be shown by comparing cooling and free-fall time scales, which become comparable at roughly this density.

Concerning the SPH implementation of molecular line cooling, the tabulated cooling rates are interpolated linearly in temperature and density phase space to match a particle's current SPH density and internal energy (Particle i has ρ_i and u_i). We then calculate the change of a parti-

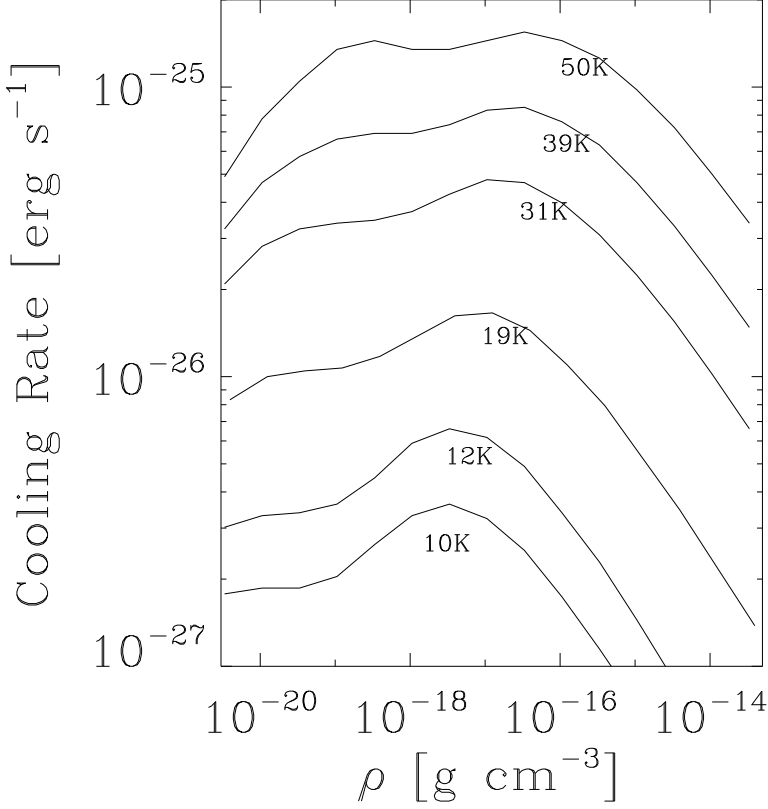


Figure 3.2: Cooling rate as a function of density for different temperatures following Neufeld et al. (1995). Cooling in molecular cloud cores is only efficient up to $\rho_{\text{crit},0} = 10^{-13} \text{g cm}^{-3}$. Beyond this density the gas is assumed to become optically thick at all wavelengths and molecular line cooling is shut off.

cle's internal energy $\frac{du_{i,\text{cool}}}{dt}$ due to this cooling rate. This additional change in internal energy is considered after the internal energy of a particle has been calculated via the standard equation of state (see Eq. 3.44). In a subsequent step u_i is then reduced by $\frac{du_{i,\text{cool}}}{dt} \cdot \Delta t_i^n$. Here Δt_i^n is the individual particle time step of particle i , used to advance the current calculation time t_i^n to t_i^{n+1} . For more details on how the internal energy energy is updated in VINE see section 3.4.

3.8 Resolution

Each of the simulations which are presented in the following sections will contain 430000 'core' SPH particles. Since the cores are confined in a hot, but low-density ambient medium, we add a little over 24000 hot 'boundary' SPH particles, which are not allowed to cool. These particles are distributed such that the pressure at the core boundary is maintained (see section 2.1.2). In our simulations, the Bonnor-Ebert spheres are setup slightly supercritical in order to ensure collapse: $\zeta_{\text{max}} = 6.9$. Furthermore, in all simulations the maximum density at the core center is $\rho_0 = 10^{-18} \text{g cm}^{-3}$. The spheres are initially isothermal at a temperature of 20K within the core region. With these three paramters, the Bonnor-Ebert sphere is unequivocally defined. Integrating over the resulting three-dimensional density distribution results in a total mass of the sphere of $5.5M_{\odot}$. We artificially enhance the mass of the sphere by 10% to compensate for additional rotation or

turbulent velocities adopted in our simulations. Therefore the total mass of the sphere M_{total} adds up to $6M_{\odot}$.

SPH has mass-limited resolution. It automatically gives higher spatial resolution in high density regions. Bate & Burkert (1997) pointed out that the minimum resolvable mass should always be less than the Jeans mass (Eq. 2.18) in order to reliably resolve collapse and fragmentation. They also found that the minimum resolvable mass is represented by $2N_{\text{neigh}}$ SPH particles. In three dimensions, the typical number of neighbours used in SPH simulations is 50. Thus, assuming that all particles have equal mass,

$$M_{\text{resolved}} \approx M_{\text{total}} \left(\frac{2N_{\text{neigh}}}{N_{\text{total}}} \right) \quad (3.49)$$

where N_{total} is the total number of particles. Following Bate & Burkert (1997), the resolvable mass in a simulation with 430000 'core' SPH particles is $M_{\text{resolved}} = 1.405 \cdot 10^{-3} M_{\odot}$, and every SPH particle has a mass of $m_{\text{part}} = 1.405 \cdot 10^{-5} M_{\odot}$.

SPH is ideally suited to follow the collapse of a prestellar core because the problem involves a minimum Jeans mass - but no minimum Jeans length - due to the changing gas thermodynamics. In the isothermal regime, M_{Jeans} drops continuously with increasing density. However, this behaviour is reversed in the adiabatic regime (Tohline, 1982) because for an arbitrary adiabatic index $M_{\text{Jeans}} \propto \rho^{1.5\gamma-2}$. For $\gamma_2 = 1.4$ one obtains $M_{\text{Jeans}} \propto \rho^{0.1}$ and therefore an increasing Jeans mass with increasing density. In Fig. 3.3 I plot the Jeans mass as a function of local density for an EOS as given in Eq. 3.48 and for a sound speed according to a temperature of 9K. I use 9K instead of 20K to calculate the minimum Jeans mass as the gas in our simulations is allowed to cool down to this temperature. We follow the collapse up to a density of about 10^{-9}g cm^{-3} . Within this regime, we find a minimum Jeans mass of is $1.51 \cdot 10^{-3} M_{\odot}$. With the setup give above, this mass is always resolved. In fact the actual mass resolution of the simulations is better than given by this limit because the higher the density of an SPH particle the less likely it will cool down to 9K. Therefore, with the employed EOS, these parameters guarantee sufficient resolution up to a density of 10^{-5}g cm^{-3} .

As we are not interested in resolving the second collapse of the dense central object, but rather the surrounding protostellar disk region, we do not follow the collapse up to densities of 10^{-5}g cm^{-3} or more. In order to limit the collapse process to limit the computational cost of a simulation we introduce a minimum smoothing length h_{min} . CPU time consumption needs to be constrained in order to be able to follow the formation and early evolution of the protostellar disk. With the chosen parameters each simulation already took more than three weeks running parallel on eight processors. The faster a dense central object is formed in the simulations, the longer it takes to calculate to a comparable collapse stage. We do not use sink particles to describe the collapsed center, as these seem to promote artefacts and artificial fragmentation. h_{min} represents the most critical resolution constraint applied to our simulations. In the standard simulations we choose $h_{\text{min}} = 2\text{AU}$ in order to resolve typical disk scales, but neglect details of the central object formation. All the details on scales below 2AU are smoothed out. In order to limit numerical errors due to the integration, we chose a small value for the CFL tolerance criterion in all presented simulations (CFL parameter = 0.1!).

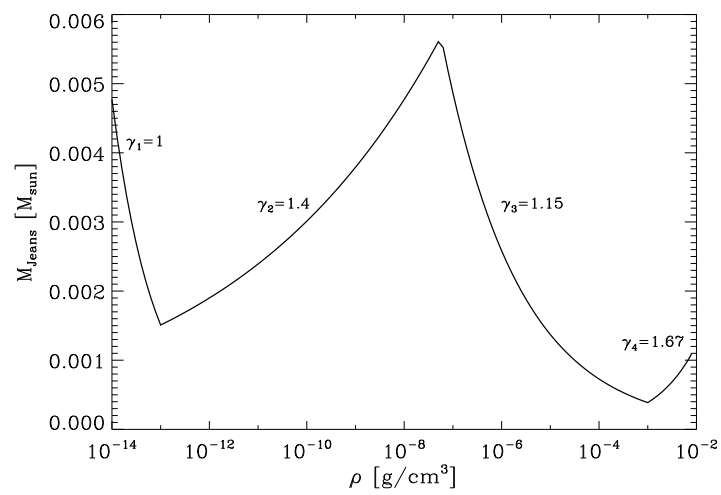


Figure 3.3: Jeans mass as a function of density calculated according to the barotropic EOS given in Eq. 3.48.

Chapter 4

Protostellar disks in low-mass star formation - I. Collapse of rigidly rotating prestellar cores

Stars form from the gravitational collapse of dense molecular cloud cores (MCCs). However, radial gravitational collapse is hindered by the non-negligible amount of angular momentum contained in every core (Goodman et al., 1993; Barranco & Goodman, 1998; Burkert & Bodenheimer, 2000). According to the standard picture of low-mass star formation, angular momentum is conserved during the collapse phase. This may lead to either the formation of a more or less massive protostellar disk, and/or to fragmentation into binary or multiple stellar systems. Even before a clear correlation between the initial mass function of molecular cloud cores and the stellar initial mass function was discovered (Motte et al., 1998; Testi & Sargent, 1998; Young et al., 2006), the fragmentation properties of collapsing cores and protostellar disks had been of great interest to the astrophysical community. Also the observed frequency of protoplanetary disks as well as binary and multiple stellar systems asks for models, with which the initial conditions in prestellar cores can be unambiguously linked to the final outcome of core collapse and star formation.

Therefore the collapse of low-mass prestellar cores, as well as the formation and the early evolution of protostellar disks is investigated using three-dimensional SPH simulations with the 3D OpenMP-parallel SPH code VINE (Wetzstein et al., 2008; Nelson et al., 2008), which has been described in the previous chapter. We study the effect of gas thermodynamics and rotation on the fate of the formed protostellar disks. For this purpose we analyse a sample of cores, all with the same mass, but with varying specific angular momenta. In this chapter we only study protostellar disk formation from cores in initial rigid rotation. The according sample of mildly turbulent cores will be discussed in one of the following chapters (chapter 7). Many authors already studied the collapse of rigidly rotating cores (Miyama et al., 1984; Burkert & Bodenheimer, 1993), but most of them considered spheres with a constant density profile, a powerlaw density distribution or a Plummer-like profile instead of the collapse of Bonnor-Ebert spheres. Here, the initial prestellar cores are modeled as slightly supercritical Bonnor-Ebert spheres (see section 2.1.2), as this density profile provides the best fit to many observed molecular cloud cores. We decided on investigating the collapse of BESs in rigid rotation in order to test the influence of

our cooling prescription on disk formation and fragmentation. Moreover, our simulations have a higher resolution than all previous studies of protostellar disk formation. Due to the SPH technique we are also able to resolve the whole three-dimensional disk structure with unprecedented resolution, unlike e.g. nested grid codes with a predefined geometry (Matsumoto & Hanawa, 2003). The resolution requirements found by Truelove et al. (1997, 1998) and Bate & Burkert (1997) are fulfilled throughout the whole simulation. This is important, as e.g. Boss et al. (2000) demonstrated that earlier simulations utilising either grid-based schemes or the SPH technique, respectively, were frequently affected by numerical fragmentation due to insufficient resolution. (see section 2.3.2).

Various speed of rigid rotation represent different total angular momenta of the cores. It will be shown that in case of rigid rotation the properties of a forming protostellar disk are predefined by the initial angular momentum contained within the parental core. Disks forming from slowly rotating cores are moderately sized (100-200AU), highly concentrated and warm. They are stable against local gravitational instabilities, e.g. fragmentation. Heating by accretion and infall plays a major role in stabilising the disk. On the other hand, more rapidly rotating cores form more extended disks (500-1000AU), which are less concentrated and cooler. They show extended spiral arm structures and are undergoing fragmentation during all early evolutionary stages. The transition from small and concentrated to large and fragmenting disks is a roughly continuous function of core angular momentum. α , the ratio of thermal to gravitational energy is not arbitrary in our simulations with molecular line cooling. Therefore we find the disk properties to be solely a function of β , the ratio of rotational to gravitational energy of the core.

This chapter will be focused on analysing the structure and characteristics of the forming protostellar disks for two simulations in detail: In section 4.2 and 4.3, we will closely follow the evolution of two protostellar disk systems until a significant amount of mass has collapsed. First, the case of relatively low initial core angular momentum will be discussed. Afterwards the case of high angular momentum will be shown. We discuss the influence of the cooling prescription and rotation on the protostellar disk structure. Beforehand, the cloud core model is shortly summarised in section 4.1.

4.1 Initial Conditions

- **Density Profile:**

By modeling column density profiles, molecular cloud cores usually turn out to have radial density profiles consistent with $\rho(r) \propto r^{-p}$ with $p \approx 1.5 - 2$ for $4,000\text{AU} \leq r \leq 20,000\text{AU} \approx 0.1\text{pc}$. However, they appear to have a flattened distribution in the central core region (e.g. Hogerheijde & Sandell, 2000; Motte & André, 2001). Often, isolated cores are characterized by sharp outer edges at $r \approx 0.1\text{pc}$, which implies pressure confinement of these objects within a hotter, but low-density medium. BESs (Bonnor, 1956; Ebert, 1955) generally provide the best fits to the structure of isolated prestellar cores (see e.g. Ward-Thompson et al., 1999; Alves et al., 2001; Hennebelle et al., 2003). The following parameters clearly define the BES:

- The outer radius of the sphere:
 $\zeta_{\max} = 6.9 \cong 0.083\text{pc}$,
- The central density:
 $\rho_0 = 10^{-18}\text{g cm}^{-3}$,
- And the initially isothermal gas temperature:
 $T = 20\text{K}$.
- It follows that $M_{\text{core}} \cong 6M_{\odot}$,
- And the external pressure $P_{\text{ext}}/k_B = 5 \times 10^5$ is comparable to the typical ISM pressure.

It should also be noted, that spheres with $\zeta_{\max} = \zeta_{\text{crit}} = 6.451$ are marginally stable. The ones with $\zeta_{\max} > \zeta_{\text{crit}}$ are unstable against gravitational collapse, whereas those with $\zeta_{\max} < \zeta_{\text{crit}}$ are stable. We choose a slightly supercritical sphere and add a 10% density enhancement in order to ensure collapse despite additional rotation. It follows that the total mass enclosed within R_{core} is $6M_{\odot}$ in our standard setup. Utilizing these parameters, we estimate the central free-fall time as well as the sound crossing time of the system to be

$$\begin{aligned}\tau_{\text{ff}} &= \sqrt{\frac{3\pi}{32G\rho_0}} \approx 6.67 \cdot 10^4 \text{yr} \\ \tau_{\text{sc}} &= R_{\text{cut}}/c_s \approx 2.8 \cdot 10^5 \text{yr},\end{aligned}\tag{4.1}$$

where c_s is the initial isothermal sound speed.

- **Velocities:**

In this study we solely consider spheres in initially rigid rotation. Therefore only the azimuthal velocity is nonzero, and is calculated according to

$$v_{\Phi}(r) = \Omega_0 \cdot r,\tag{4.2}$$

where r is the radial component in cylindrical coordinates and Ω_0 is the initial rotational frequency. In our sample we effectively only vary Ω_0 , which takes different constant values. Prestellar cores are known to have fairly narrow, hence thermal, line widths (Barranco & Goodman, 1998; Belloche et al., 2001; André et al., 2007). Unlike the conditions on molecular cloud scales, the absence of a more pronounced line-broadening on core scales indicates that rotation is at most as important in supporting the core against its own self-gravity than its internal thermal pressure. Gas velocities inside the molecular cloud cores are hence at very low Mach numbers (up to transonic or Mach 1). The choice of Ω_0 is therefore limited by two criteria. On the one hand, the total amount of specific angular momentum j in a low-mass MCC is typically of the order of $\log_{10}(j[\text{cm}^2\text{s}^{-1}]) \approx 21$ (Goodman et al., 1993) for a core of comparable size and mass as the ones in our sample. On the other hand, the typical speed of sound implies an upper limit for the rotational gas velocities within the core. With an isothermal sound speed of 0.29 km/s and a core size of 0.083pc, Ω_0 cannot exceed about $1.2 \cdot 10^{-13}\text{s}^{-1}$ for circular velocities to remain within the subsonic regime. This corresponds to a ratio of rotational to gravitational energy of

10%. Nevertheless, in order to further explore the parameter space, we do include some simulations, which achieve initial supersonic rotation in the outer parts (see Table 5.1: For $\Omega_0 = 2 \cdot 10^{-13} \text{s}^{-1}$ rotation is supersonic beyond a cylindrical radius of about 9,600AU or 0.047pc, respectively).

- **Temperature & EOS:**

As the BE solution is a solution for an *isothermal* sphere in hydrostatic equilibrium, we start with a constant core temperature of $T = 20\text{K}$. Throughout the collapse an ideal gas EOS with an adiabatic index $\gamma = 1.4$ (for molecular hydrogen) is used to capture the heating of the gas through the release of gravitational energy and shocks. In addition the gas is able to cool through optically thin radiation by the most abundant molecules. Implementing the cooling prescription into the VINE code was part of this project and is described in section 3.7.

- **Resolution:**

- 430,000 'core' SPH particles
- $\approx 24,000$ hot 'boundary' SPH particles
- $m_{\text{part}} = 1.405 \cdot 10^{-5} M_{\odot}$

Following Bate & Burkert (1997), the resolvable mass is $2N_{\text{neigh}} \cdot m_{\text{part}} = 1.405 \cdot 10^{-3} M_{\odot}$. On the other hand, assuming a temperature of 9K, the minimum Jeans mass limiting the SPH resolution within the partially isothermal regime ($\rho < \rho_{\text{crit},0}$) is $1.51 \cdot 10^{-3} M_{\odot}$, which is always resolved. With the employed EOS, these parameters guarantee sufficient resolution up to a density of 10^{-5}g cm^{-3} .

4.2 Protostellar disk formation: Low angular momentum case

In this section we show the typical evolution of a collapsing cloud, which is rigidly rotating. We distinguish between two main collapse phases: The initial isothermal collapse phase will be called Phase I. In Phase I the collapse roughly proceeds on a free-fall time scale because radiative cooling is efficient and the gas behaves isothermally. The maximum density ρ_{max} within the core stays below $\rho_{\star} = 10^{-11} \text{g cm}^{-3}$ in this phase. We define the central object mass or the 'stellar mass' as all the mass at densities greater than ρ_{\star} . It should be noted, that we do not follow the collapse up to stellar densities and that the 'central object' in our simulations will typically occupy a region of few AU in radius. Therefore the central object does not have the structure or size of a star, which is of the order of $\frac{1}{10} - \frac{1}{100} \text{AU}$. Phase I ends as soon as a dense central object is formed. In Phase II, $\rho_{\text{max}} > \rho_{\star}$. A dense central object and a growing and evolving disk are now present. We will hence call Phase II the protostellar disk formation phase, since most of the disk mass is acquired in this stage. We define t_0 to be the time at which the maximum density begins to exceed ρ_{\star} , or at which the collapse enters Phase II, respectively. The systematic differences in t_0 listed in table 5.1 are caused by the different initial core rotation rates - fast spinning cores collapse somewhat slower. In addition, we define t_{final} to be the time at which 28% (ca. $1.7M_{\odot}$)

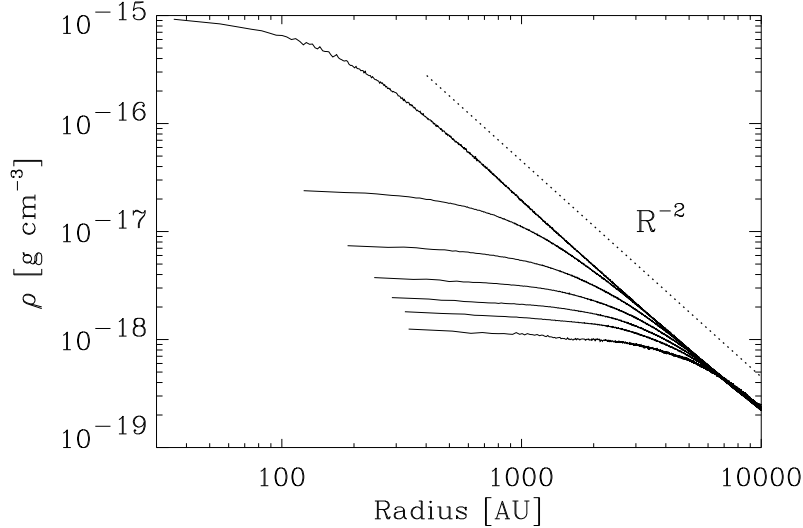


Figure 4.1: Radial density profile at different times in the purely isothermal regime. As soon as the collapse has commenced, the initial hydrostatic equilibrium profile (bottom line) is altered to resemble a flat core region enclosed in an R^{-2} -envelope. The dotted line illustrates a perfect slope of -2 . From bottom to top the output times are 0yr and $4.1 \cdot 10^4$ yr to $9.1 \cdot 10^4$ yr in steps of 10,000yr.

of the total core mass has collapsed to densities above $10^{-16} \text{g cm}^{-3}$. Even though we evolved many simulations for longer - especially the ones with high initial angular momentum - we find a characteristic disk structure to be established at t_{final} . Finally, we will compare all our simulations at t_{final} , the time at which 28% of the total core mass have collapsed to densities $\rho > 10^{-16} \text{g cm}^{-3}$. This collapse fraction is motivated by the observed, average star formation efficiency of dense molecular cloud cores (e.g. Motte et al., 1998).

We choose density thresholds to define the protostellar disk. The lowest threshold is $10^{-16} \text{g cm}^{-3}$. In this component we still observe significant flattening, and therefore it clearly belongs to the disk, rather than the core envelope component of the collapsing system. The highest density threshold we define is $10^{-13} \text{g cm}^{-3}$. This disk component is completely adiabatic as molecular line cooling is inefficient at these densities. Two corresponding radii will be defined for comparison: R_{13} is the radius at which the cylindrically averaged disk density is equal to $10^{-13} \text{g cm}^{-3}$ and R_{16} the radius at which $\rho(R) = 10^{-16} \text{g cm}^{-3}$, respectively. Thus, R_{13} is the radius of the very dense inner disk component, whereas R_{16} is the outer disk radius. In addition we will discuss R_{half} , the radius which encloses 50% of the total disk mass ($M(\rho_* > \rho > 10^{-16} \text{g cm}^{-3})$). In the following, we will discuss the differences in disk structure and evolution in case of low and high angular momentum.

4.2.1 Phase I: Isothermal collapse

The collapse of a super-critical BES is initiated at the outer boundary of the sphere. The BE hydrostatic equilibrium profile is soon changing towards a flattened core region surrounded by an $1/R^2$ -envelope, which is continuously growing in size. The collapse wave, which forms the edge of the flattened central region, accelerates towards the center and precedes the free-falling envelope material. In that stage the cooling time scale is very short compared to the local free-fall time ($\tau_{\text{cool}}/\tau_{\text{ff}} \ll 1$), so the gas behaves approximately isothermal. Once the density rises above $\rho_{\text{crit},1} = 3 \cdot 10^{-16} \text{ g cm}^{-3}$ cooling starts to become less efficient and the purely isothermal stage ends. Fig.4.1 shows the evolution of the sphere's radial density profile within the first $9.1 \cdot 10^4$ years for Run 1. The radial density profile has been calculated by averaging the density of SPH particles found at a spherical radius R from the core center at $(0,0,0)$. Every point of the curve is an average over 100 SPH particles, which are adjacent to each other when sorted by spherical radius. As the collapse problem is spherically symmetric in Phase I, Fig. 4.1 shows the real density profile in any radial direction from the core center. In the most advanced stage the flat central region has a radius of about 300AU, enclosing a mass of $0.06M_{\odot}$. Note that during the isothermal collapse stage, the amount of global rigid core rotation does not significantly alter the collapse on scales of a few 1000AU because centrifugal forces are small ($\tau_{\text{rot}} \gg \tau_{\text{ff}}$). Even for the highest rotational frequency in our sample ($2 \cdot 10^{-13} \text{ s}^{-1}$) the orbital timescale $\tau_{\text{rot}} \approx 1.6 \cdot 10^5 \text{ yr}$ is a factor of 2 longer than the freefall timescale τ_{ff} (see Eq. 4.1). For this reason the isothermal collapse phase will proceed in approximately the same manner for all of our test cases.

4.2.2 Phase II: Protostellar disk formation

After $t_0 = 9.1 \cdot 10^4 \text{ yr}$ the system has formed a dense and thus adiabatic central object with $\rho > 10^{-11} \text{ g cm}^{-3}$. In the following, we refer to this dense central clump as central object, star or young stellar object. In addition the formation of a protostellar disk - rather than a spherically symmetric growth of the central object - is initiated, since the specific angular momentum of the infalling material is roughly conserved (see Fig. 4.2). At this point the local freefall time becomes very short. Star and disk formation happens within a few 10^3 to 10^4 years, causing the simulations to become very demanding and CPU time consuming.

In Fig.4.3 we show the evolution of the mass-weighted, radial density profile in Phase II. Again, we calculate the density profile by averaging the SPH particle densities for 100 adjacent particles in spherical radius. As the collapse proceeds more and more particles assemble close to the x-y plane forming a disk-like inner envelope around the center, whereas regions above and below the disk plane are depleted of SPH particles (see also Fig. 4.2). Therefore the shown density profile is a mass-weighted density profile, revealing the disk component at smaller radii where almost all found particles reside within the disk, and still showing the the outer parental envelope which follows $\rho \propto R^{-2}$. 20,000 years after the central star has begun to form, the dense circumstellar component with $\rho_{\star} > \rho > 10^{-14} \text{ g cm}^{-3}$ extends out to about 200AU and is slowly but continuously growing in size. We will refer to this dense circumstellar component as the protostellar disk (PSD). It is a matter of choice whether to define the outer disk radius to be the

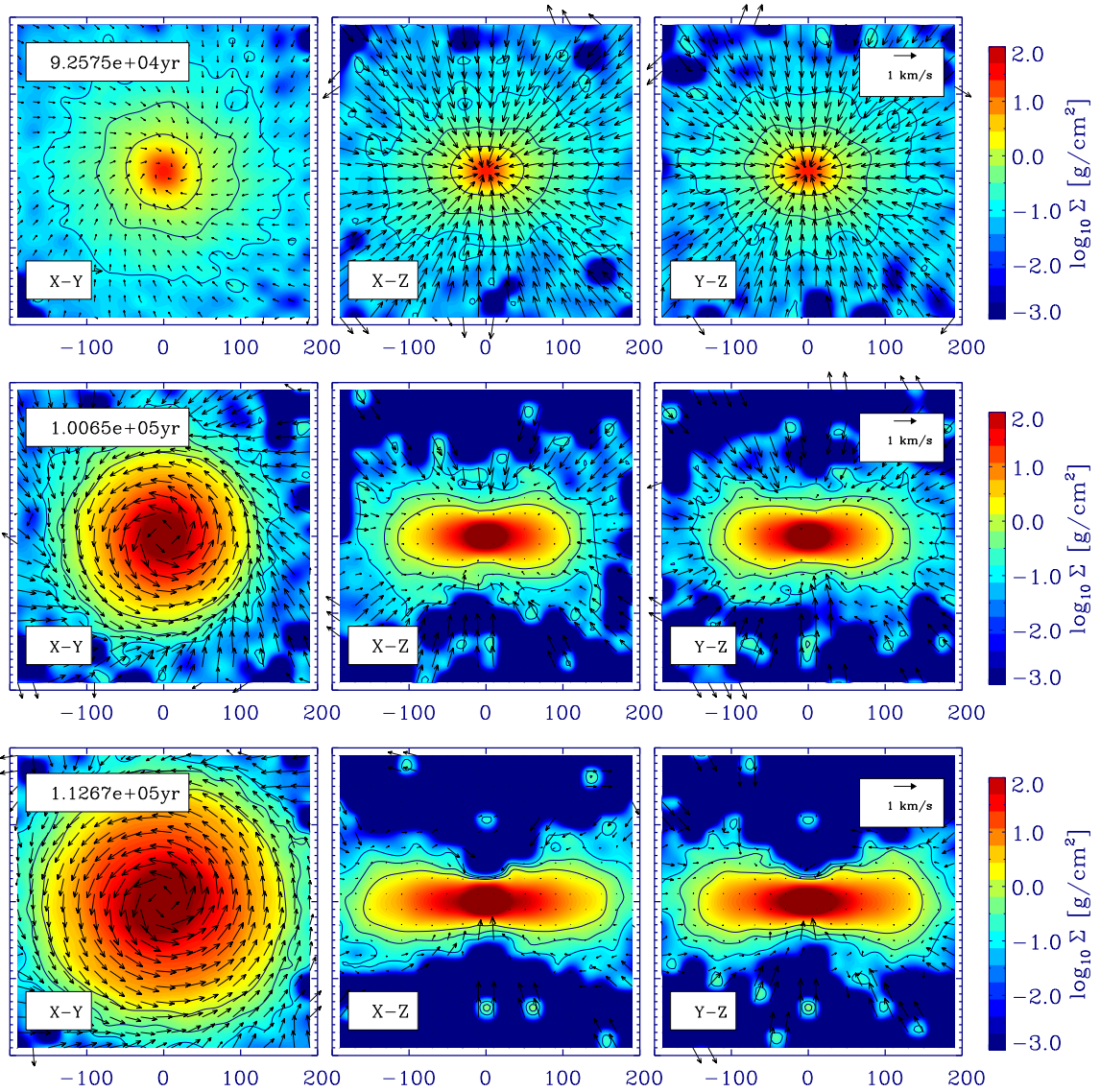


Figure 4.2: Disk formation during the collapse of a rigidly rotating BES. We show an evolutionary sequence of surface density and the velocities within the inner 400AU of the parental molecular cloud core. From inside out, the overlaid isocontours correspond to 1, 0.3 and 0.1g cm⁻². The output times are $t_0 - 1.9$ kyr (upper plot), $t_0 + 6.2$ kyr (middle) and $t_0 + 18.2$ kyr (lower plot).

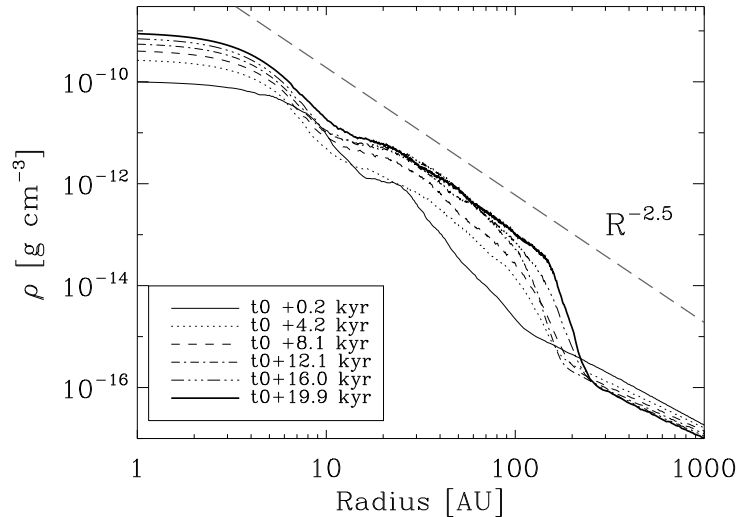


Figure 4.3: Radial density profile at different times in the non-isothermal stage. The given output times are relative to the time of first core or central object formation t_0 . Therefore, at t_0 , a central density enhancement has formed, which slowly evolves and further grows in density as time goes on. In addition, a second dense, but more extended component is forming: The circumstellar disk.

radius at which $\rho > 10^{-14} \text{g cm}^{-3}$ or $\rho > 10^{-16} \text{g cm}^{-3}$, since - in this case - we find the outer edge to be rather sharp anyway. At radii smaller than 10 or 20AU the density profile is steep ($\rho \propto R^{-3}$). When looking at the geometry of the central object in more detail, we find that it has the shape of a *nuclear disk* rather than a spheroid or sphere. Within the disk region (20AU - 150AU) the density profile is well described by a powerlaw with slope of -2.5. For a constant ratio of disk pressure scale height H to disk radius R this results in an intermediately steep surface density profile: $\Sigma = \rho H \propto R^{-1.5}$. Compared to observations of protoplanetary disks (observed disks surrounding a pre-main sequence star in much later evolutionary stages) $\Sigma \propto R^{-1.5}$ lies within the typical range of surface density powerlaws, determined from fitting observed SEDs of protoplanetary disks (Dullemond et al., 2001). However, as the spectral energy distribution (SED) of a protoplanetary disk is only weakly dependent on the actual surface density powerlaw, this powerlaw index is somewhat uncertain. A change in the powerlaw index mainly effects the balance between near-IR and far-IR radiation and the slope of the SED at far-IR/submillimeter wavelengths

A more interesting parameter is the value of H/R itself. From fitting the vertical density distributions found within the self-gravitating disks in our simulations, we deduce that $H/R \approx \text{constant}$ for all simulations. The fitting of the vertical density profile is discussed later in this section (see Fig.4.8). This behaviour is quite surprising as it is not expected for a self-gravitating disk. On the other hand, a flaring disk structure is typically obtained for protoplanetary disks. In protoplanetary disk models, the flaring results from irradiation and heating of the disk surface layer by the central star, which is not included in our simulations. In our simula-

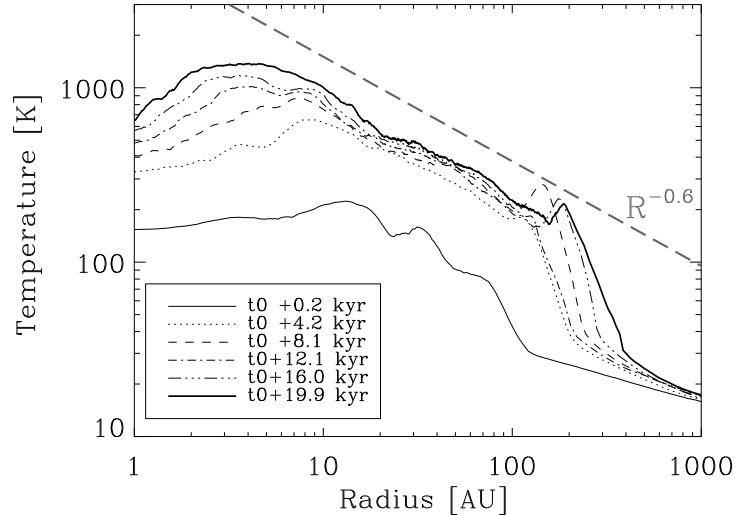


Figure 4.4: Radial temperature profile at different times in the disk formation stage. We show the same time steps as in Fig.4.3. The dense, central parts of the core heat up rapidly. Soon, a powerlaw temperature profile is established within the disk region. In addition, there is shock heating at the outer boundary of the adiabatic core.

tions, the disks are dynamically heated by accretion and shocks. Models of passive (not actively accreting), irradiated and flaring protoplanetary disks result in $0.1 \dots 0.3$, with a mean value of $H/R \approx 0.18$ (Dullemond et al., 2001). Therefore both models give very similar results even though they are significantly different. This result suggests that external heating of the disk is not necessary to explain a 'flaring' disk structure in early evolutionary phases.

With the employed cooling function (see section 3.7) cooling becomes less and less efficient above a density of $10^{-16} \text{g cm}^{-3}$, that is within the disk region. Therefore part of the released potential energy which is transferred into heat cannot be radiated away immediately, slowing down the collapse due to an increase in thermal pressure. The central object as well as parts of the disk where $\rho > \rho_{\text{crit},0} = 10^{-13} \text{g cm}^{-3}$ evolve adiabatically and heat up. Within the central object further contraction can only proceed on a Kelvin-Helmholtz time scale and gravitational energy is completely transformed into internal energy. The adiabatic component of the disk is preferentially confined to the disk midplane within a radius of about 100AU. This dense and optically thick part of the disk is significantly heated by the release of potential energy via gas infall onto the disk and accretion within the disk. But also the outer disk regions are partly heated in this highly dynamical evolutionary stage, since envelope material, which is raining down with highly supersonic speed, is decelerated and shocked (see Fig.4.4). After $t = t_0 + 8 \text{kyr}$, shock heating results in a local temperature spike located at the outer disk radius. A powerlaw temperature profile ($T \propto R^{-3/4}$) is established within the disk region, which holds throughout the whole protostellar disk phase. It should be noted, that the temperature profile of passive, irradiated (protoplanetary) disks follows $T \propto R^{-1/2}$ which is flatter (Dullemond et al., 2001). On the other hand a typical protoplanetary disk, which is predominantly heated by viscous accretion can have a midplane

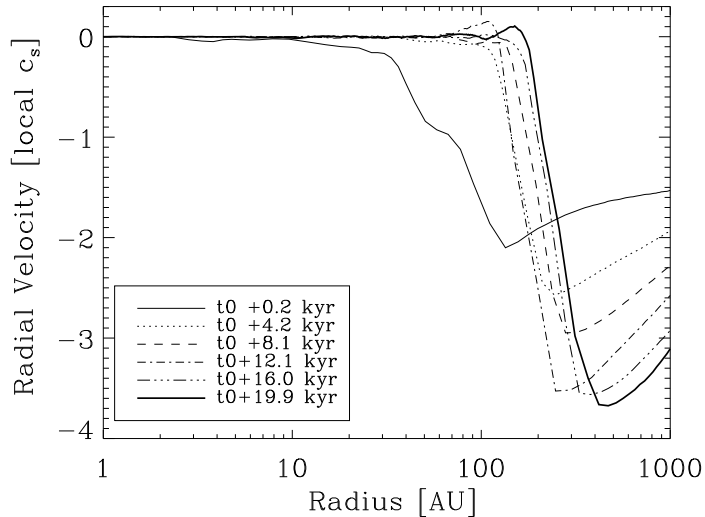


Figure 4.5: Radial velocity vs. radius at different times. After the time of first central object formation, the shape of the radial velocity profile changes dramatically. Close to the outer edge of the formed flattened region, matter is falling in with highly supersonic speed, while v_R is negligible within the central region. This fast deceleration leads to an accretion shock, which is heating the outer edge of the center (see also Fig.4.4).

temperature profile with a slope as steep as -1 . We do not consider irradiation by the forming central star. However, the temperature evolution shows, that this source of heat does not contribute significantly to the thermal energy budget of a very young protostellar disk. Heating by the release of gravitational energy due to collapse and viscous evolution and by shocks due to infalling gas at supersonic velocities is all-dominant. However, the vertical temperature gradient is reversed in the simulations as compared to passively heated protoplanetary disks, where the disk surface is hotter than the midplane. A hot disk surface layer is necessary to explain the 10 micron silicate feature in the SED of a protoplanetary disk to be observed in emission rather than absorption. This suggests, that a disk in transition from the protostellar to the protoplanetary stage will pass through a phase where internal heating of the disk ceases with decreasing gas infall from the envelope and disk accretion and external heating increases according to the luminosity of the central star. So far we do not cover this transition in our simulations, as it would also require to include radiation transport.

In agreement with the accretion shock seen in the temperature profile, the radial velocity profile (see Fig.4.5) exhibits maximum infall velocities of Mach 3-4 after $t = t_0 + 8.3$ kyr. In general, the radial velocity distribution shows a clear accretion shock profile at the outer disk boundary, which develops quickly after the formation of the central object. A characteristic profile is established: From large to small radii, the absolute value of the radial velocity v_R is at first increasing, illustrating the acceleration of gas towards the center of mass. Gas acceleration is abruptly stopped in an accretion shock once the material hits the outer disk region. Within the disk region $v_R \approx 0$.

Interestingly, the azimuthal velocity profile changes completely once a protostellar disk is forming. In Fig. 4.6 we plot the rotational velocity component as a function of cylindrical radius. Initially $v_\Phi \propto R$, but as more and more matter is falling in the v_Φ -profile is reversed and approaches $v_\Phi \propto R^{-1}$ between 150 and 2000AU. In the outer core regions ($R > 2000$ AU) the rotational velocity profile changes less dramatically, and the original profile seems to be roughly maintained. Within the protostellar disk region ($R \leq 150$ AU at $t_0 + 19.3$ kyr) the rotational velocity profile is more shallow. Between 5 AU and 150 AU v_Φ is roughly proportional to $R^{-1/4}$, hence decreasing slowly from a maximum value of 6 km/s at 5 AU down to about 2 km/s at 150 AU. A flat rotation curve corresponds to differential rotation within the disk, and thus angular momentum transport due to shear viscosity can be expected. At even smaller radii ($R < 5$ AU), v_Φ is falling off rapidly ($v_\Phi \propto R$), which again corresponds to the rotation profile of a solid body. As the original rotation profile is maintained within the inner 5 AU, angular momentum has not been redistributed efficiently within and close to the central object, which has the form of a 'nuclear disk', rather than being spherically symmetric and round. Nevertheless, from the lower panel of Fig. 4.6, which shows the ratio of azimuthal velocity and local sound speed (or velocity dispersion in this case), we deduce that the center is still pressure supported. v_Φ/c_s decreases rapidly with radius, like it does within the outer regions ($R > 5000$ AU) or at earlier times (before t_0). The disk itself is clearly rotationally supported. Within the outer disk regions ($R > 50$ AU), where the temperature is decreasing slowly, rotational support slightly gains importance. In the upper panel, the grey line enveloping the set of rotation curves, shows the expected curve for a spherically symmetric, rotating system in centrifugal equilibrium with a mass distribution $M(R)$ equal to the present mass distribution of central object and disk at $t = t_0 + 19.3$ kyr:

$$v_{\Phi,ex} = \sqrt{\frac{GM(R)}{R}}.$$

Within the disk region, the difference between the characteristics of $v_{\Phi,ex}$ and the actual disk rotation curve is insignificant, showing that the (vertically thick) disk seems to be close to centrifugal equilibrium. However, at small radii, where the central object is dominating $M(R)$, both profiles differ strongly, again showing that the central object is supported by pressure rather than rotation. For comparison, we also show the Keplerian velocity profile expected for the central potential of a point mass with mass M_\star at $t_0 + 19.3$ kyr. Despite giving azimuthal velocities of the right order of magnitude within the disk region, the Keplerian profile does not fit the present one. This shows, that the disk is self-gravitating and altering the profile due to the non-negligible disk mass. At small radii, the difference becomes more and more pronounced, showing that the central object cannot be well approximated by a point mass like distribution.

In Fig. 4.7 we discuss the vertical disk structure at $t_{\text{final}} = 114.8$ kyr at three different radii: R_{13} , R_{16} and R_{half} . In addition, we show the ratio of disk pressure scale height to disk radius as a function of disk radius at the same time step in Fig. 4.8. In z direction the gravitational force is balanced by the non-negligible pressure force resulting from the stiffening of the equation of state at high densities. Therefore vertical hydrostatic equilibrium is established. $\rho(z)$ rises steeply towards the disk midplane and exceeds $\rho_{\text{crit},0} = 10^{-13} \text{ g cm}^{-3}$ within the inner 20 AU above the disk midplane for R_{half} and within the inner 10 AU for R_{13} . The gas within this region obeys a

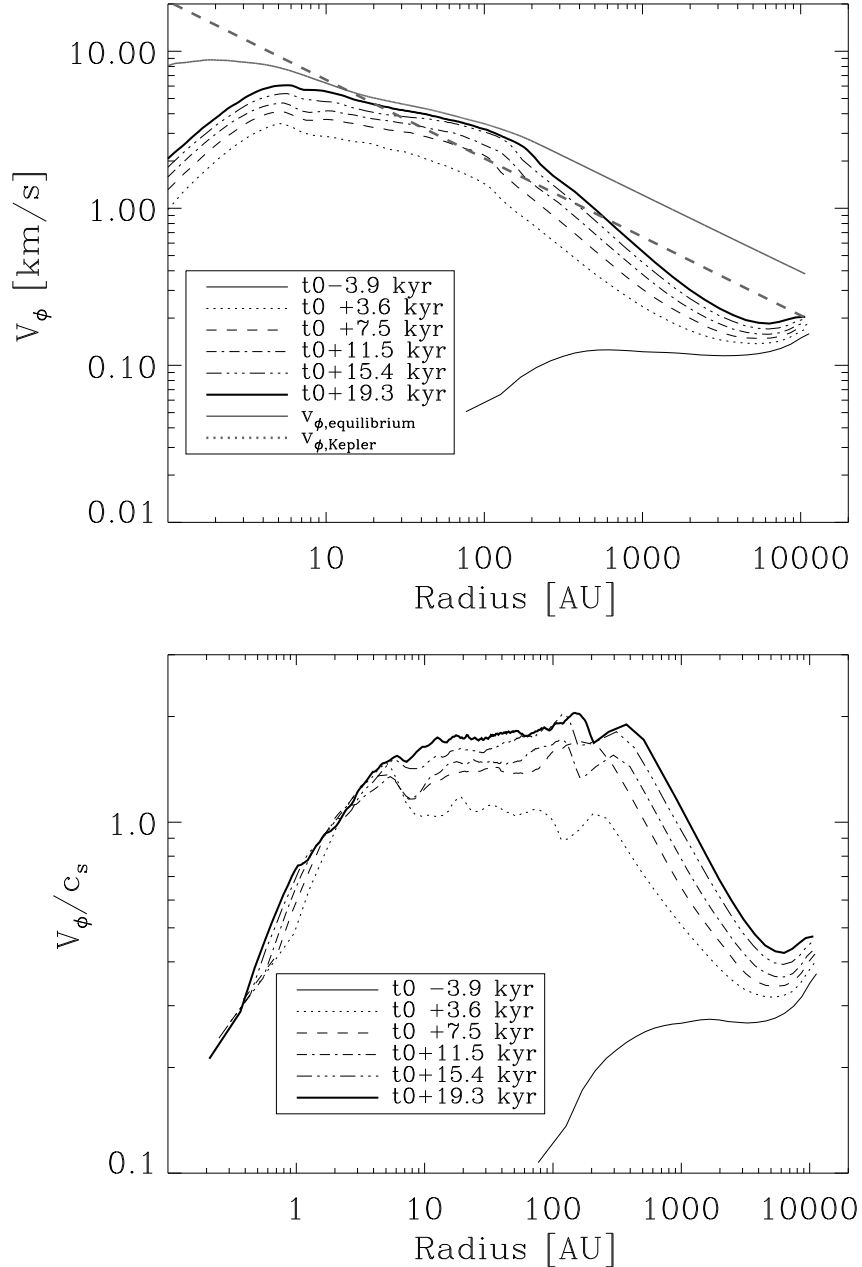


Figure 4.6: *Upper panel:* The azimuthal velocity profile changes completely during core collapse - especially when a protostellar disk is forming. Within the disk v_ϕ is only mildly dependent on cylindrical radius, a signature of differential rotation. For comparison we show the rotation curve for $v_\phi = \sqrt{GM(R)/R}$ (grey line) of a spherically symmetric, rotating object in centrifugal equilibrium, and the expected Keplerian rotation curve $v_\phi = \sqrt{GM_\star/R}$ (grey dashed line) with $M(R)$ and M_\star taken at $t_0 + 19.3$ kyr. *Lower panel:* Ratio of rotational velocity and local sound speed or velocity dispersion. The disk is clearly supported by rotation.

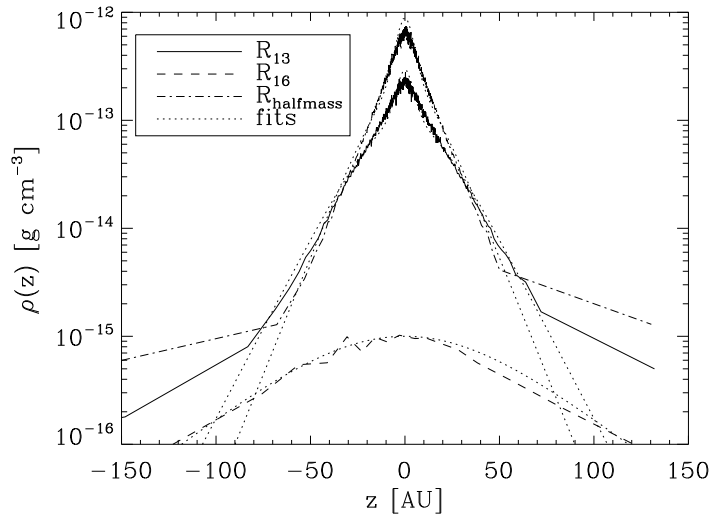


Figure 4.7: Vertical density distributions at R_{13} , R_{16} and R_{half} at $t_{\text{final}} = 115.4$ kyr. We fit the density profile with a sum of two sech^2 -distributions, as usually applied for **isothermal** self-gravitating disks in hydrostatic equilibrium.

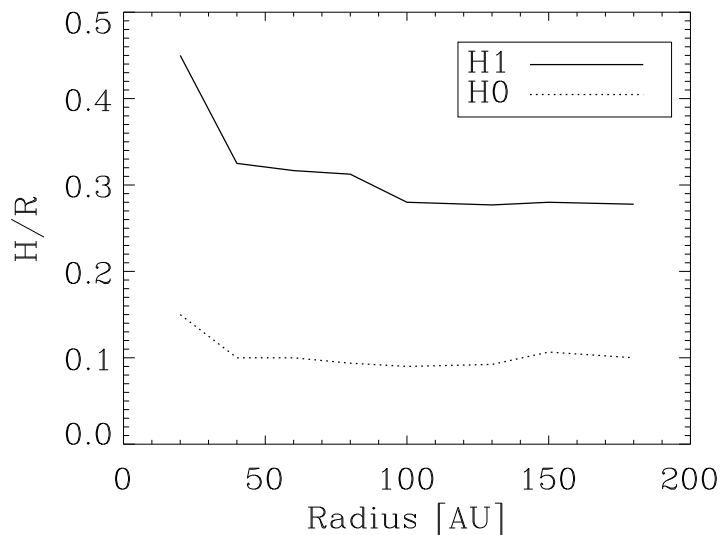


Figure 4.8: Ratio of disk pressure scale height to disk radius at $t_{\text{final}} = 115.4$ kyr. The pressure scale height H_1 as well as the scale height of the disk midplane H_0 were both obtained from fitting the vertical density profile with a sum of two sech^2 -distributions at every radius. H/R is roughly constant throughout the disk. At small radii $\rho(z)$ is very steep and it is therefore difficult to obtain an unambiguous fit.

purely adiabatic equation of state and is heating up. The high temperature within the adiabatic region causes a strong pressure force, which hinders the dense gas to be further compressed. At intermediate height ($10\text{AU}-20\text{AU} < z < 50\text{AU}-70\text{AU}$), the density remains below $\rho_{\text{crit},0}$. Even though the density is still high, the gas is therefore able to cool on a timescale comparable to the dynamical timescale (see also Fig. 5.4). Heating due to infall and accretion causes the temperature to be above 100 Kelvin within about 60AU above the midplane at R_{half} . At these two radii the vertical disk structure is twofold, with ρ following a steeper slope within the innermost region and a somewhat flatter one at $z > 10\text{AU}-20\text{AU}$ above the disk midplane. It can be well fitted by a sum of two sech^2 -functions (fits are the dotted lines in Fig. 4.7):

$$\rho(z) = \rho_0 \text{sech}^2(z/H_0) + \rho_1 \text{sech}^2(z/H_1), \quad (4.3)$$

An isothermal, self-gravitating disk in hydrostatic equilibrium is supposed to settle into a distribution, which is well described by a sech^2 -function (Spitzer, 1942). In our case, a roughly constant temperature of 700K only exists within the disk midplane (inner 5AU). This hot and dense component accounts for the first of the two sech^2 -terms. The outer parts of the disk are well described by a second sech^2 -function. Although the temperature is decreasing between 5AU and 50AU-70AU above the midplane, but only by a factor of about 10. Thus, the temperature variation is still small compared to the vertical density variation, which spans several orders of magnitude. However, at the largest of all three radii, R_{16} , the maximum density is below $10^{-13} \text{g cm}^{-3}$. Therefore we obtain the best fit at R_{16} with only one sech^2 -function. We obtain the following parameters for the three different radii:

- $R_{\text{half}} = 64\text{AU}$:
 $\rho_0 = 8 \cdot 10^{-13} \text{g cm}^{-3}$, $H_0 = 6\text{AU}$
 $\rho_1 = 2 \cdot 10^{-13} \text{g cm}^{-3}$, $H_1 = 19\text{AU}$.
- $R_{13} = 96\text{AU}$:
 $\rho_0 = 10^{-13} \text{g cm}^{-3}$, $H_0 = 9\text{AU}$
 $\rho_1 = 7 \cdot 10^{-14} \text{g cm}^{-3}$, $H_1 = 28\text{AU}$.
- $R_{16} = 250\text{AU}$:
 $\rho_0 = 0$, $H_0 = -$
 $\rho_1 = 10^{-15} \text{g cm}^{-3}$, $H_1 = 65\text{AU}$.

We will refer to the second scale height H_1 as the disk's pressure scale height. and list H_1 in Table 5.2 for all simulations.

4.3 Protostellar disk formation: High angular momentum case

For a core rotational frequency of $\Omega = 2 \cdot 10^{-13} \text{s}^{-1}$ we find that a flattened, dense, disk-like structure forms before the central density exceeds $\rho_* = 10^{-11} \text{g cm}^{-3}$. Therefore we define a pure 'protostellar disk dominated phase', which lasts for about 15kyr and is terminated - by definition - as soon as ρ_* is exceeded at t_0 . Note that ρ_* was exceeded before a protostellar disk

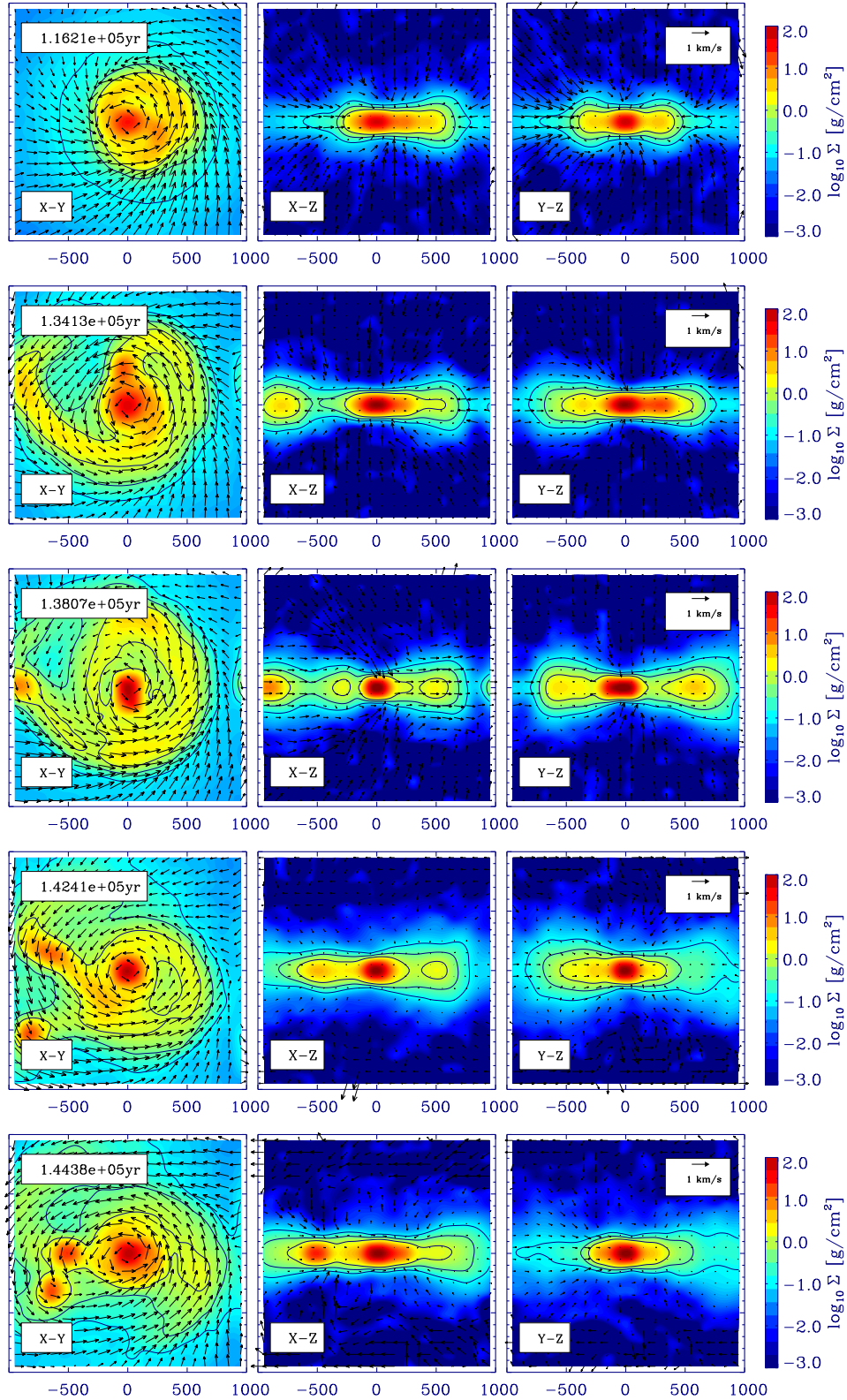


Figure 4.9: Surface density and velocities showing the evolution of Run 7 within the inner core region ($-1000, +1000$)AU after t_0 . Output times are $t_0 + 11.8\text{kyr}$, $t_0 + 29.7\text{kyr}$, $t_0 + 33.7\text{kyr}$, $t_0 + 38.0\text{kyr}$, and $t_0 + 40.\text{kyr}$. From inside out, the overlaid isocontours correspond to $1, 0.3$ and 0.1 g cm^{-2} .

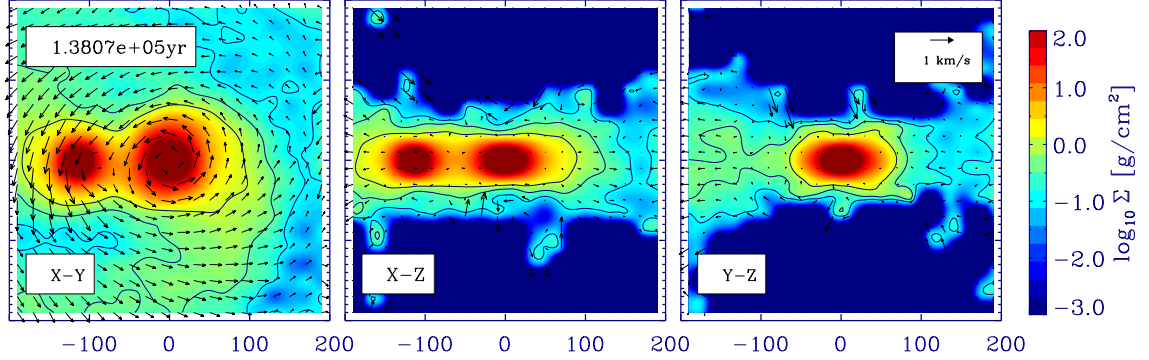


Figure 4.10: Zoom showing the inner ± 200 AU of the surface density profile at $t_0 + 33.7$ kyr. At this stage second dense fragment has formed which will eventually merge with the central object after 142 kyr ($t_0 + 37.6$ kyr).

was formed in case of low core angular momentum (Run 1). We show the radial density profile at different timesteps in Fig. 4.11, this time starting within the protostellar disk dominated phase at $t_0 - 12$ kyr. At this time ($t \approx t_0 - 12$ kyr), the protostellar disk extends out to 200 AU and keeps growing rapidly. At t_0 the disk radius is already very large (600-700 AU). Within this protostellar disk dominated phase, the disk becomes massive enough to develop weak spiral arms (see Fig. 4.10), which grow and cause the redistribution of angular momentum via gravitational torques. The young disk undergoes viscous evolution. Gas is accreted towards the center and slowly the dense central object is growing in mass (see Fig. 4.17). In this scenario most of the stellar mass is accreted through the protostellar disk.

After t_0 , we find the density profile between 100 AU and 600 AU to be well represented by a single powerlaw with slope -2. This is significantly flatter than in the case of slow rotation, where $\rho(R) \propto R^{-2.5}$ within the inner 200 AU. The flattening in powerlaw is even more pronounced when focusing on the scales of 10 AU-100 AU. Here a powerlaw as shallow as $R^{-1.5}$ provides the best fit. On the other hand at radii smaller than 10 AU the density profile is significantly steeper. When looking at the geometry of the central object in more detail, we again find that it has the shape of a *nuclear disk*. For rigidly rotating molecular cloud cores, all simulations result in central *nuclear disks*, but these become more and more extended the higher the amount of angular momentum contained in a core. Even though SPH is thought to be rather too dissipative, angular momentum cannot be transported efficiently enough to allow for the formation of a spheroidal, hydrostatic, central object, which is not rotationally but only pressure supported. This problem has been previously recognized by other authors.

In summary, a more extended disk forms in this rapidly spinning molecular cloud core. A significant part of mass at radii greater than 100-200 AU. The gas is not distributed evenly over azimuthal direction. Extended spiral arms corresponding to $m=2$ and/or $m=3$ perturbations to the disk's gravitational potential are forming naturally. The spiral arm structure leads to a stratification in the density distribution. High densities ($\rho > 10^{-14} \text{ g cm}^{-3}$) are only reached within the spiral arm. Lower density regions envelope the spiral arm, and for $10^{-15} > \rho > 10^{-16} \text{ g cm}^{-3}$

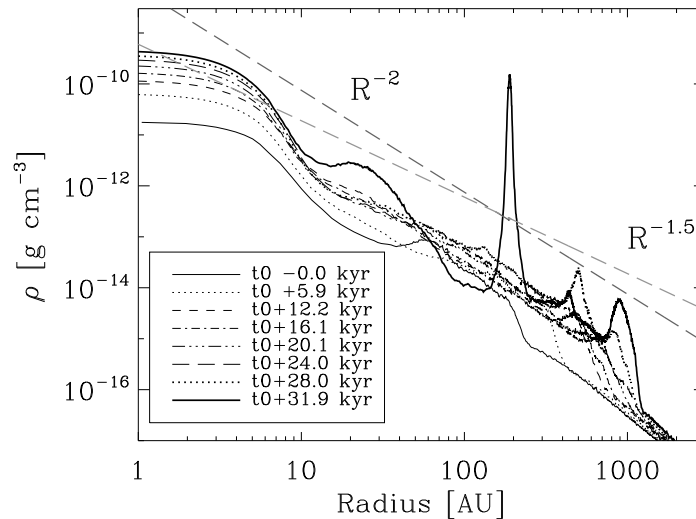


Figure 4.11: Radial density profile of Run 7. Due to the high amount of angular momentum, protostellar disk formation precedes the formation of the first core. Later the outer disk radius is moved outward. The disk becomes more extended (almost as big as 1000AU) and fragments. At the outer edge, the density distribution merges smoothly with the surrounding protostellar core distribution. There is no sharp outer edge as seen in Fig. 4.3.

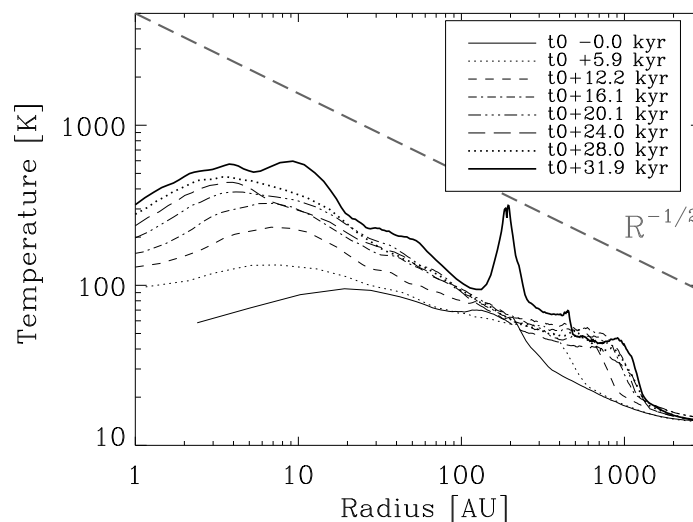


Figure 4.12: Temperature profile of Run 7. Most of the disk material stays cold (below ice evaporation temperature of $\approx 80\text{K}$) throughout the evolution and the profile follows an $R^{-1/2}$ powerlaw. In the last snapshot the profile is dominated by fragmentation, which causes the density to rise and peak in a local maximum at 200AU.

form a cohesive disk. The disk is built up inside out. As enough mass is accumulated at larger radii where the temperature is moderately cold, the self-gravitating disk becomes Toomre unstable (see section 5.4). The disk is fragmenting. Gravitational instability grows efficiently enough to form a dense fragment at 200AU within only a few kyrs. At even larger radii (1000AU) disk substructure is continuously changing. We see density enhancements forming and being sheared apart. Not all of the forming disk substructure evolves into a gravitationally bound fragment. The stiffer the EOS, the higher the minimum mass required to promote further gravitational contraction of a local density enhancement. Therefore a certain region, which could in principle evolve into a bound fragment has to accrete a sufficient amount of mass as it condenses. In the outer disk regions the mass supply is not sufficiently high to fulfill this criterion before $t_0 + 20\text{kyr}$ in this simulation. However, after $t_0 + 20\text{kyr}$ two bound fragments form within the outer disk at radii of approximately 500 and 700AU (see Fig. 4.10). These grow in mass, but at the same time also spiral inwards towards the central object. It is not clear, if they will survive, in which case the system would evolve into a multiple stellar system, or whether they will merge with the central object like the first fragment, which originally formed at 200AU. It has been shown that the formation and survival of fragments are both very sensitive to the gas thermodynamics as well as to numerical intricacies like SPH artificial viscosity (see Commerçon et al., 2008). A more detailed study of the system's further evolution is required, which will be presented in a future paper (Walch et al., in prep).

It should be noted that a *circumfragmentary disk* forms around each of the fragments. In Fig. 4.13, we show the individual disks around the three fragments formed in this simulation. In order to make the circumfragmentary disk visible, we transformed the SPH particles into the system of inertia of the shown clump. With a radial extent of 30 - 60AU we find the circumfragmentary disks to be quite large.

We conclude that cores with a high initial angular momentum, form massive, large disks, which develop spiral arms. Gravitational torques are essential for the formation of a central star, as the central object acquires almost all of its mass through disk accretion. Therefore the formation of low-mass stars from slowly spinning cores is very different than the formation within rapidly spinning ones. In the first case, low-mass stars mostly form via direct gravitational collapse, whereas in the latter case, they form through accretion.

Even though the density profile is much more shallow in case of rapid core rotation, the temperature profile has a similar slope as seen in case of slow rotation ($T(R) \propto R^{-0.5}$) (see fig.4.12). However, the average disk temperature is below 100K and therefore roughly a factor of 4 smaller as in Run 1. The disk becomes hot only in the very center ($R < 10\text{AU}$) and in the fragments, but stays cool otherwise. This is an important result with respect to the disk chemistry. A disk as hot as in Run 1 will show significant amount of dust crystallisation and ice evaporation, whereas the large disk in Run 7 will not exhibit any of these features, since the temperature stays below 800K throughout the simulation (Walch et al., 2008, in prep. Dullemond et al., 2006, for a 1D approach).

By comparing Fig.4.15 and Fig. 4.5 we deduct that the shape of the radial velocity profile is independent of the cloud rotation frequency at early evolutionary stages. Nevertheless, the scaling is slightly different. In Run 7 the rotationally supported inner part ($v_R \approx 0$) is more extended as in Run 1, in agreement with the larger disk in Run 7. Moreover, for the extended, cold disk

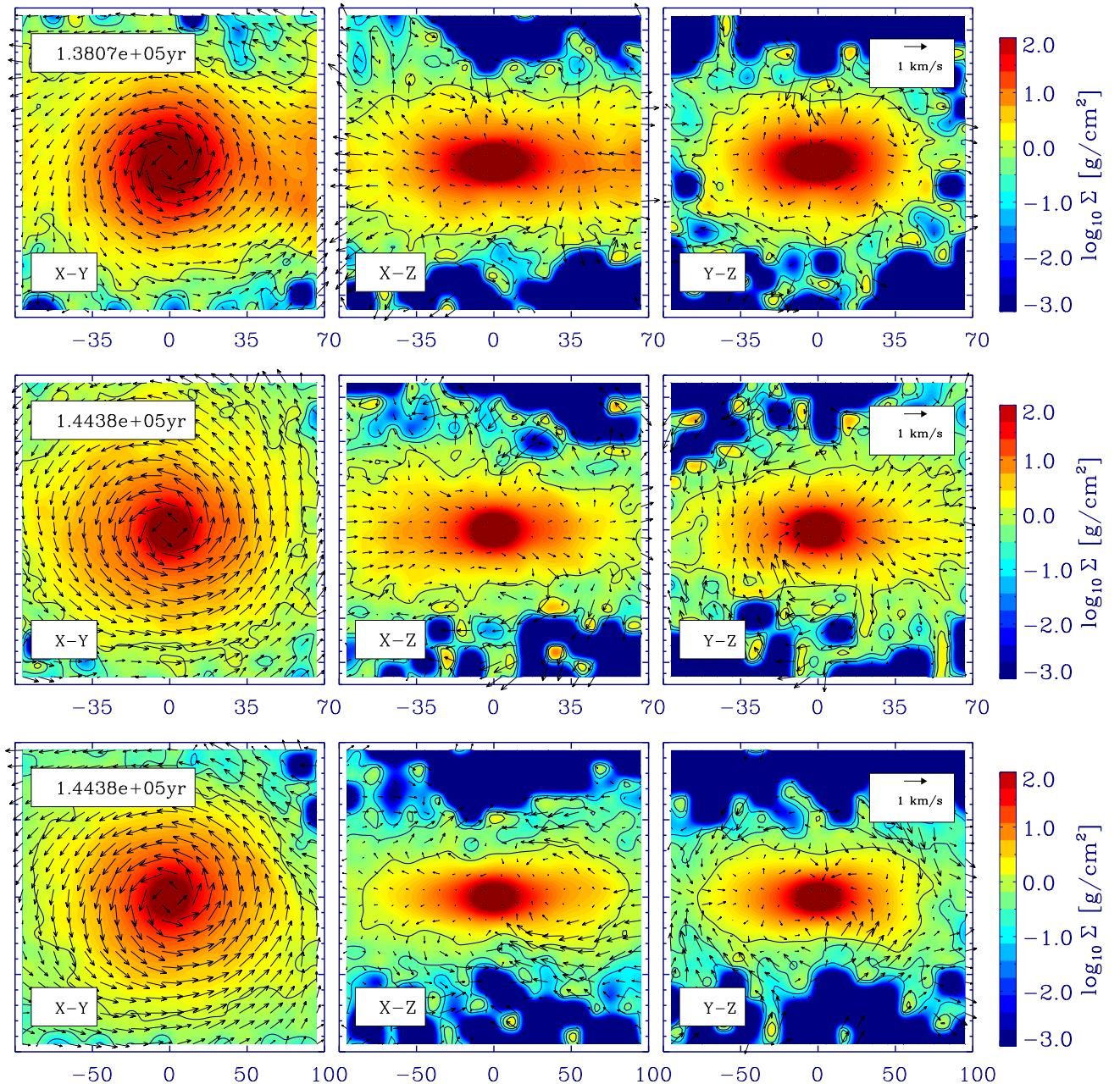


Figure 4.13: Circumfragmentary disks from Run 7. Again we depict colour-coded surface density and velocities arrows. Each panel shows the individual disk around one of the three fragments that formed in Run 7 (see Fig. 4.10): Uppermost plot: 1st fragment formed at 200AU, which later on merges with the central object. Middle and Third: Lower fragment (middle) and upper fragment (third plot) of the two seen in the last panel of Fig. 4.10. Note that the upper and middle panel show a range of $[-70\text{AU}; 70\text{AU}]$, whereas the last plot extends over $[-100\text{AU}; 100\text{AU}]$.

v_R is not perfectly zero within the disk region. This can be attributed to the spiral structure of the disk, which is constantly changing. The transition between centrifugally supported region and infalling region is less pronounced, and the inflow velocity reaches an absolute maximum value of Mach 2 at $t = t_0 + 20\text{kyr}$. The profile is finally altered when fragmentation sets in. Clear signatures of a circumfragmentary disk surrounding the first fragment, which is located at a radii of about 200AU, are also found in Fig.4.15 as well as in Fig. 4.14. It causes the transition of sub- to super-equilibrium disk rotation around 200AU. Due to the fragment's self-gravity, gas which is close to the fragment is deflected and dragged towards it. Therefore, with respect to the fragment, the circumfragmentary disk is rotating in the same counter-clockwise direction as the big protostellar disk. Within the circumfragmentary disk, gas at intermediate radii (between fragment and central object) is counter-rotating with respect to the big disk and thus appears to be rotating more slowly, whereas rotation appears to be faster at radii larger than the fragment's position. Efficient angular momentum transport is caused by this effect. At intermediate radii angular momentum is lost efficiently, whereas at large radii angular momentum is gained and gas is moving outwards. Circumfragmentary disks seem to play an important role in the redistribution of angular momentum within large protostellar disks.

Also in case of high angular momentum, the resulting vertical density profile of the disk is similar to the low angular momentum case. In Fig. 4.16 we show the vertical density profiles at three different radii at $t_{\text{final}} = 130.4\text{kyr} = t_0 + 26\text{kyr}$. However, in Run 7, the half mass radius of $R_{\text{half}} = 317\text{AU}$ is much larger than $R_{13} = 79\text{AU}$, which is about 20AU smaller than in Run 1. Therefore $\rho(z, R_{13})$ is the only profile, which exceeds the critical density of $\rho_0 = 10^{-13}\text{g cm}^{-3}$. Nevertheless, for both profiles (at R_{13} and at R_{half}) we obtain the best fitting vertical profile by superposing two sech^2 functions. Again, for $R_{16} = 952\text{AU}$, only one sech^2 function is required to fit $\rho(z)$. We obtain the following parameters for all three radii:

- $R_{13} = 79\text{AU}$:
 $\rho_0 = 10^{-13}\text{g cm}^{-3}$, $H_0 = 7\text{AU}$
 $\rho_1 = 8 \cdot 10^{-14}\text{g cm}^{-3}$, $H_1 = 20\text{AU}$.
- $R_{\text{half}} = 317\text{AU}$:
 $\rho_0 = 4 \cdot 10^{-15}\text{g cm}^{-3}$, $H_0 = 44\text{AU}$
 $\rho_1 = 6 \cdot 10^{-16}\text{g cm}^{-3}$, $H_1 = 120\text{AU}$.
- $R_{16} = 952\text{AU}$:
 $\rho_0 = 0$, $H_0 = -$
 $\rho_1 = 3 \cdot 10^{-16}\text{g cm}^{-3}$, $H_1 = 190\text{AU}$.

At smaller radii the pressure scale height H_1 is smaller in this case than in Run 1. The inner disk of Run 7 is thinner and cooler than in Run 1. This also explains the different fragmentation properties.

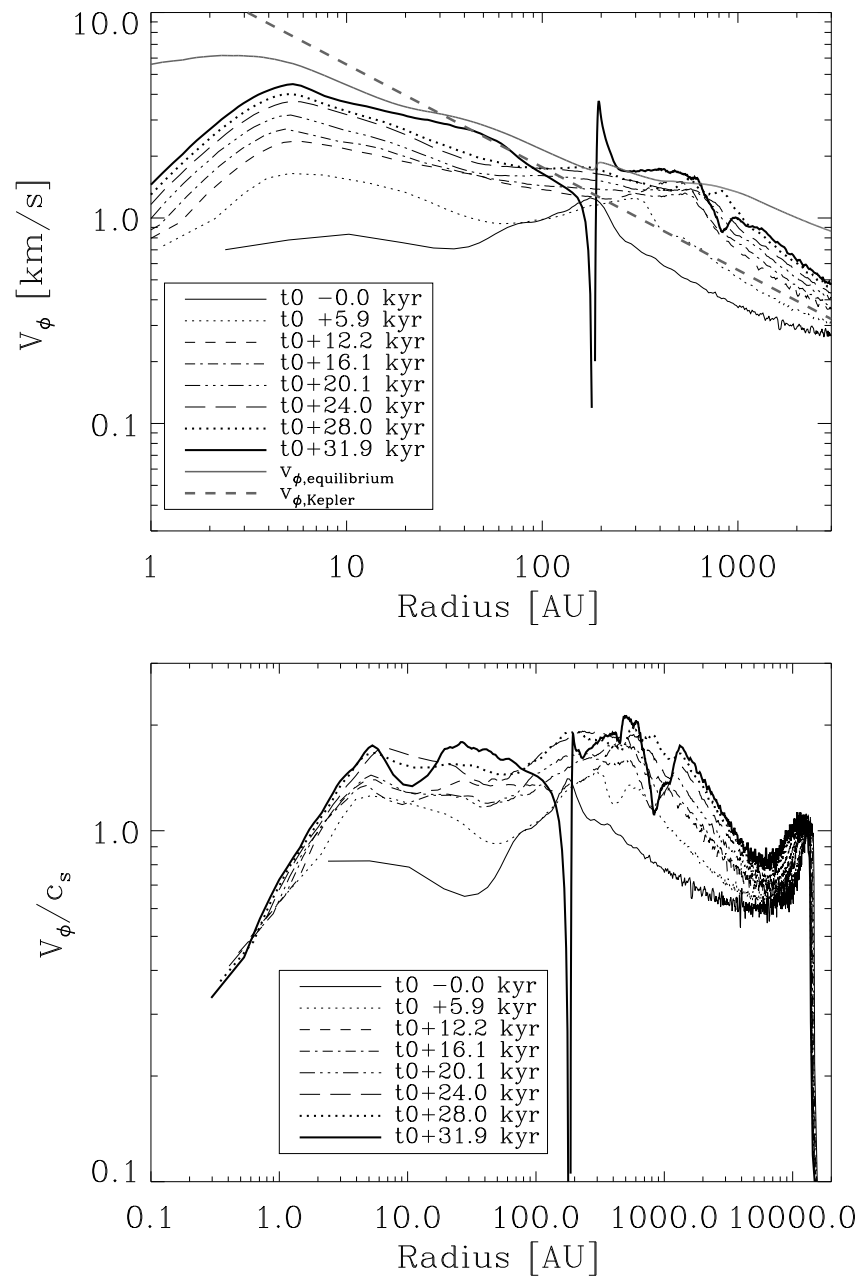


Figure 4.14: Disk rotation curve of Run 7. The disk is slowly evolving towards centrifugal equilibrium (grey line). The shallow profile within the disk region is perturbed due to fragmentation at $t = t_0 + 20$ kyr. Close to the fragment (200AU) some gas undergoes a fast transition from highly sub- to superkeplerian rotation driving gas inward/outward, respectively (see Fig.4.15).

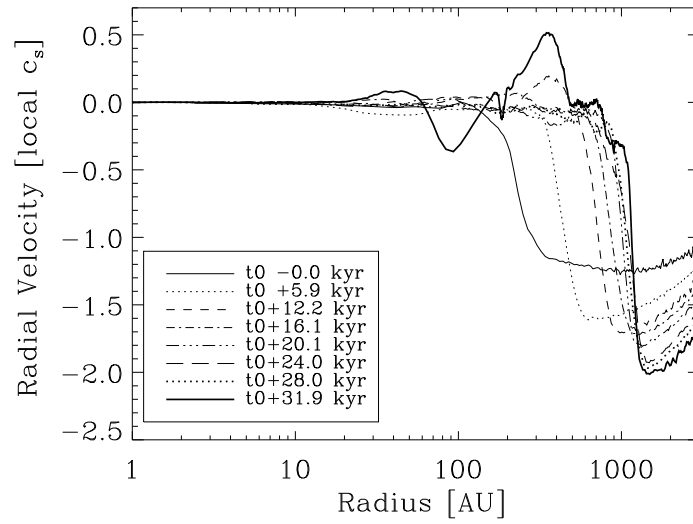


Figure 4.15: Radial velocity profile of Run 7. Inflow velocities are on average lower than in the case of slow rotation. At $t + 20$ kyr we see enhanced inflow and partial outflow as expected from Fig.4.14

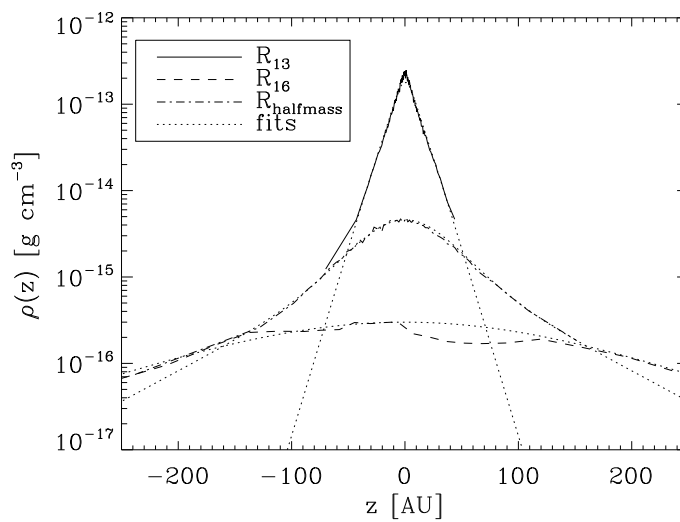


Figure 4.16: Vertical density distributions at R_{13} , R_{16} and R_{half} of 7 at $t_{\text{final}}=130.4$ kyr.

4.4 Mass Infall and Accretion: Detailed comparison of low and high angular momentum (Run 1 vs Run 7)

The seal on the fate of a single molecular cloud core is set by rotation, gas thermodynamics and of course gravity. Since all the cores in our sample have the same initial mass, gravity should intrinsically act alike in all simulations. In this section we discuss the influence of rotation and gas thermal behaviour on the disk structure and state of fragmentation as well as on the mass of the forming star. Here all particles with a density higher than $10^{-11} \text{g cm}^{-3}$ will be considered to contribute to the forming central star. As mentioned previously, we do not use sink particles but resolve the system down to a minimum smoothing length (see section 3.8). We distinguish between *the* central object, which we define to be located at the most massive collection of dense particles and possibly existing fragments, if these have a radial distance of at least 20AU from the central star. We do not define the disk geometrically, but found it more physical to study certain density components within the collapsing cloud core. In order to disentangle the detailed, stratified disk structure, we look at different components:

- Star or fragment:
 $\rho > 10^{-11} \text{g cm}^{-3}$
- The densest, adiabatic disk component:
 $10^{-11} \text{g cm}^{-3} > \rho > 10^{-13} \text{g cm}^{-3}$
- Other disk components, which successively contain more mass, if low density gas is enveloping the densest component:
 $10^{-11} \text{g cm}^{-3} > \rho > 10^{-14} \text{g cm}^{-3}$ to
 $10^{-11} \text{g cm}^{-3} > \rho > 10^{-16} \text{g cm}^{-3}$

We also discuss the way the central object and protostellar disk accumulate their mass. Therefore, we differentiate between 1) gas infall, as infalling matter from the surrounding molecular cloud core, which has not been part of a certain density component within disk or star before, and 2) gas accretion as matter, which has been moved through the disk, but has already been part of the disk or a certain density component at the previous time step. For instance the mass accretion rate onto the central object is defined as the amount of mass, the object has accumulated within a certain time, divided by the time.

We stop the simulations at the point, where the central object has a mass of roughly $0.5M_{\odot}$. Also accounting for the disk, the total mass of the formed system varies between 1.2 and $2.2M_{\odot}$. In Fig.4.17 and Fig. 4.18 we illustrate that the formation of a dense central object differs in Run 1 and 7: **Run 1:**

Run 1 quickly collapses to form a dense center with a mass of $0.1M_{\odot}$ at $t_0 = 94\text{kyr}$ (see Fig. 4.17). From this point on, the mass of the central object is growing at a roughly constant rate of $\dot{M}_{\text{accr}} \approx 2.1 \cdot 10^{-5} M_{\odot}/\text{yr}$. It should be noted, that after t_0 all the mass is gathered through pure disk accretion! Direct gas infall onto the center is negligible. In Fig.4.18, we show the ratio of mass accretion rate onto the center vs. the infall rate of gas onto the disk. As previously

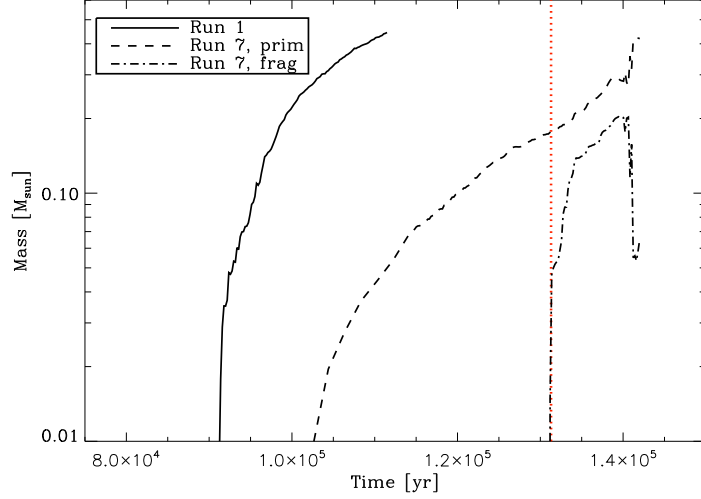


Figure 4.17: Time evolution of the stellar masses in Run 1 and Run 7. In 1 a seed star of $0.1M_{\odot}$ is formed via direct gravitational collapse (solid line), whereas all the stellar mass is accreted through a protostellar disk in Run 7 (dashed line). 7 also forms fragments after 131kyr (dash-dotted line), which eventually merge with the central object in the last view timesteps.

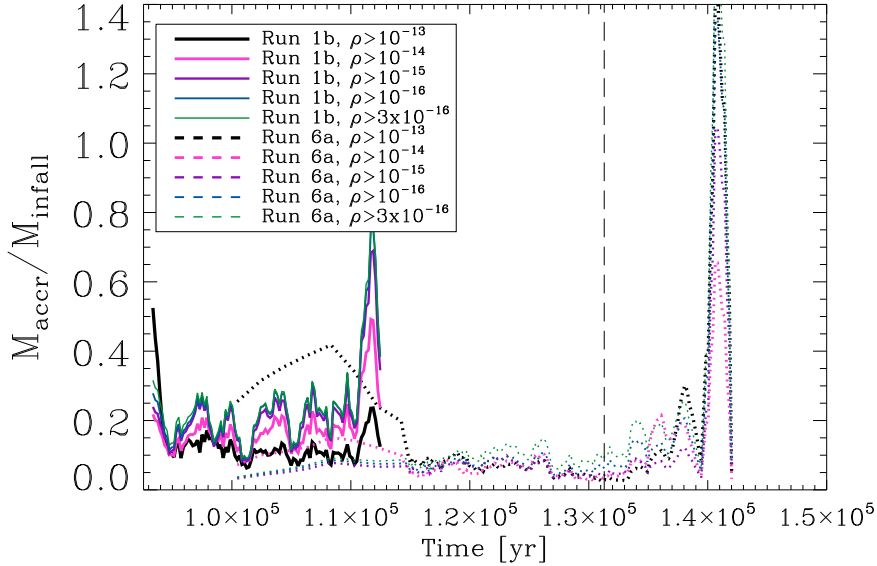


Figure 4.18: Ratio of accretion to infall rate as a function of time. Different line colours denote different disk definitions, utilizing various threshold densities. For example in case of $\rho > 10^{-14} \text{g cm}^{-3}$, all the mass within $10^{-11} > \rho > 10^{-14} \text{g cm}^{-3}$ is considered to belong to the disk component. The mass accretion rate onto the central object remains the same for all different threshold densities within one simulation. Only the gas infall rate is changing for different threshold densities.

motivated, we use various threshold densities to define the disk. For a threshold of $10^{-13} \text{g cm}^{-3}$, all the gas mass at densities in between $10^{-11} \text{g cm}^{-3}$ and $10^{-13} \text{g cm}^{-3}$ is considered as disk mass, for $10^{-14} \text{g cm}^{-3}$ the mass between $10^{-11} \text{g cm}^{-3}$ and $10^{-14} \text{g cm}^{-3}$ is integrated, and so forth. During most of the simulation, mass accretion and infall rate keep a roughly constant ratio, the accretion rate reaching a mean value of 0.1 times the infall rate for the highest threshold density of $\rho > 10^{-13} \text{g cm}^{-3}$. Hence in these early evolutionary stages the protostellar disk is constantly growing in mass. For lower density thresholds the infall rate is also lower and therefore $\dot{M}_{\text{accr}}/\dot{M}_{\text{infall}}$ is somewhat increased. This behaviour can be explained by additional adiabatic contraction within the disk region, promoting the formation of high density gas within the disk. Due to gas equilibration, the contraction process appears to be periodic at an amplitude of 0.1 and a period of 30kyr. The disk is literally pulsating in vertical direction. The redistribution of angular momentum and thus the accretion of gas is a result of gravitational torques, which are caused by the formation of weak spiral arms. After $t_0 + 18\text{kyr}(=112\text{kyr})$ the disk surface density is high enough to generate stronger spiral arms (see section 5.3 and Fig. 5.4) and the mass accretion rate is temporarily increased to about $5 \cdot 10^{-5} M_{\odot}/\text{yr}$. Therefore $\dot{M}_{\text{accr}}/\dot{M}_{\text{infall}}$ is raised to 0.8. This effect seems to be stronger for low density thresholds where \dot{M}_{infall} remains roughly constant. $\dot{M}_{\text{accr}}/\dot{M}_{\text{infall}}$ is only slightly increased for the high density components. Due to the formation of spiral arms, which leads to additional contraction, the infall rate onto the high density component appears to be increased

Run 7:

On the other hand, in Run 7, the dense central object develops slowly. At $t_0 = 116\text{kyr}$ a mass of $0.007M_{\odot}$ has accumulated. From Fig.4.11 we drew the conclusion, that one can speak of a protostellar disk dominated phase before t_0 in case of high angular momentum. The disk dominated phase starts 104kyr after the collapse has commenced and lasts for about 12kyr until t_0 . A direct gravitational collapse phase is missing in this case. All of the stellar mass is continuously accumulated through disk accretion.

Before t_0 the average mass accretion rate onto the center is three times smaller ($6 \cdot 10^{-6} M_{\odot}/\text{yr}$), and the infall rate is with $5 \cdot 10^{-5} M_{\odot}/\text{yr}$ similar to the rates in Run 1 right after t_0 (Run 1).

Regarding Fig.4.18, $\dot{M}_{\text{accr}}/\dot{M}_{\text{infall}}$ seems to be large at a threshold of $10^{-13} \text{g cm}^{-3}$ before 110 kyr, because the mass infall rate for this component is small - only very little mass is accumulating at $\rho > 10^{-13} \text{g cm}^{-3}$ (see Fig.4.4). After 114 kyr spiral arms grow within the protostellar disk, and generate local high density regions within them. As a result \dot{M}_{infall} on the high density component increases and $\dot{M}_{\text{accr}}/\dot{M}_{\text{infall}}$ drops. After 114kyr, the mass accretion rate is $1.15 \cdot 10^{-5} M_{\odot}/\text{yr}$ and the average gas infall rate is $10^{-4} M_{\odot}/\text{yr}$, thus leading to a roughly constant ratio of 0.1. Despite the strong spiral arms in this case the disk is again growing continuously in mass.

At $t = 131\text{kyr}$ the disk is so massive that it becomes gravitationally unstable and fragments (see Fig.4.17). In all plots from 4.17 to 4.20 the transition to fragmentation at roughly 131 kyr is marked with a dashed vertical line. Disk fragmentation scoops up gas, which has already been sitting at high densities more quickly than it can be replaced, since fragmentation happens on a short time scale. However, the dense disk component reforms after it has been depleted. At $1.42 \cdot 10^5 \text{yrs}$ the closest formed fragment merges with the central star and the stellar mass is rapidly increased by $0.1M_{\odot}$ (see Fig. 4.17). This leads to a very high apparent mass accretion

rate and causes $\dot{M}_{\text{accr}}/\dot{M}_{\text{infall}} \approx 1.4$.

Both simulations do not intrinsically enter a 'self-regulated' stage, where the ratio of mass infall and accretion is balanced. However, in case of low angular momentum, the formation of weak spiral arms is sufficient to sequentially increase $\dot{M}_{\text{accr}}/\dot{M}_{\text{infall}}$ to 0.8, at least for the low density disk component. But this is not an equilibrium feature. In case of high angular momentum, spiral arms do not transport enough mass towards the center to significantly influence $\dot{M}_{\text{accr}}/\dot{M}_{\text{infall}}$. In this case the gravitational instability grows and locally causes fragmentation. We will further discuss the disks' fragmentation properties as a function of angular momentum in section 5.3.

Altogether, speaking about only one specific disk mass is quite a vague concept in a 3-dimensional calculation. The disk scale height is not well constrained as it would be required for an unequivocal definition. The variation in disk mass on the basis of several disk threshold densities (as in Fig.4.18) is illustrated in Fig.4.4. In case of low angular momentum (Run 1) the disk mass in the densest component is finally $0.4M_{\odot}$ smaller than the disk mass for $\rho > 10^{-14} \text{g cm}^{-3}$ or lower threshold density. This is a difference of 50%. The situation is more extreme for Run 7. Here, the fraction of disk mass at high densities stays low throughout the simulation and doesn't exceed $0.3M_{\odot}$, whereas $1.7M_{\odot}$ reside within $\rho > 10^{-16} \text{g cm}^{-3}$ when fragmentation is just about to set in (dashed vertical line). This is a difference of almost 600%! We conclude, that we can draw a clear distinction between Run 1 and Run 7, and we quantify the difference in disk structure depending on initial core angular momentum by analysing the *disk concentration*. The disk concentration will be precisely defined in the following chapter (5).

In addition Fig.4.4 shows how the disk mass is altered by the formation of spiral arms and fragmentation. Spiral arms self-regulate gas accretion onto the center. In Run 7 the rapid initial disk growth is reduced by gas accretion through spiral arms between $t_0(7a)$ and 131kyr. When fragmentation sets in, the disk mass decreases because mass is used to build up the fragment. Later on it again grows due to further gas infall from the parent core.

4.5 Temperature evolution

Figure 4.20 and 4.21 complete the picture of the two different types of disk. It shows the mean disk temperature as a function of time, again considering different density thresholds. The phase transition from hot concentrated disks in case of low core angular momentum towards cold disks of low concentration in case of high core angular momentum is clearly visible. In Run 1 we find an average disk temperature of 400K throughout most of the simulation. In Run 7 the gas temperature stays below 150K for all components, or even below 90K for a threshold of $\rho > 10^{-15} \text{g cm}^{-3}$, respectively. The first step-like growth in the disk temperature of Run 7, happens at $t = 114 \text{kyr} \approx t_0$, and can be explained by the formation of spiral arms together with a dense disk component (see Fig.4.4: At the same time $M_{\text{disk}}(\rho > 10^{-13} \text{g cm}^{-3})$ increases). After 131kyr, fragmentation causes a temporarily significant temperature increase in Run 7. However this raise might well be an artifact of our disk definition, since it disappears after the most mas-

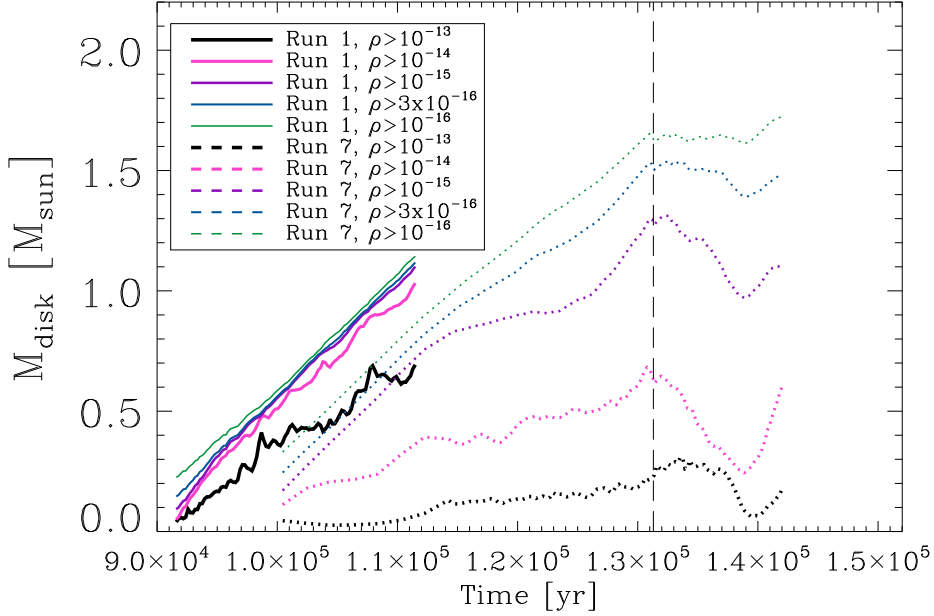


Figure 4.19: Disk masses as calculated within different threshold densities as a function of time.

sive fragment (formed at $R=200\text{AU}$) merges with the central star at $1.42 \cdot 10^5\text{yr}$. Fig. 4.21 shows the distribution of SPH particles in temperature and density phase space. In both cases, the maximum temperature reached is similar and between 2000K and 3000K . Nevertheless, the resulting distributions are completely different for these two cases. In case of low angular momentum (Run 1, top panel), most particles are found at high disk densities. Therefore the average temperature of the disk is dominated by the dense and adiabatic component, which is warm ($\approx 300\text{K}$). The maximum temperature is reached everywhere throughout the dense component. At lower density (between $10^{-15} - 10^{-14}\text{g cm}^{-3}$) the distribution shows a clear transition from the warm, dense component to a cold component of low density. The temperature in the cold component is relatively well defined and the scatter is small. In summary, the dense, warm component can be attributed to the protostellar disk, whereas the cold component is made up by the gas of the parental core, collapsing and enveloping the disk. The bottom panel shows the high angular momentum case, Run 7, at t_{final} . As we have shown before, the disk is much less concentrated in this case and harbours a lot of mass within the the low density component with $\rho > 10^{-16}\text{g cm}^{-3}$. Therefore there is no clear transition separating the disk from the core envelope. On the contrary, disk and envelope merge smoothly. Maximum temperatures are only reached close to the adiabatic component, where shocked material is heated efficiently. It should be noted, that ice and dust chemistry is very sensitive to temperature changes within the disk and core envelope. Therefore we can expect disk chemistry variations depending on the initial angular momentum of cold molecular cloud cores (Dullemond et al., 2006).

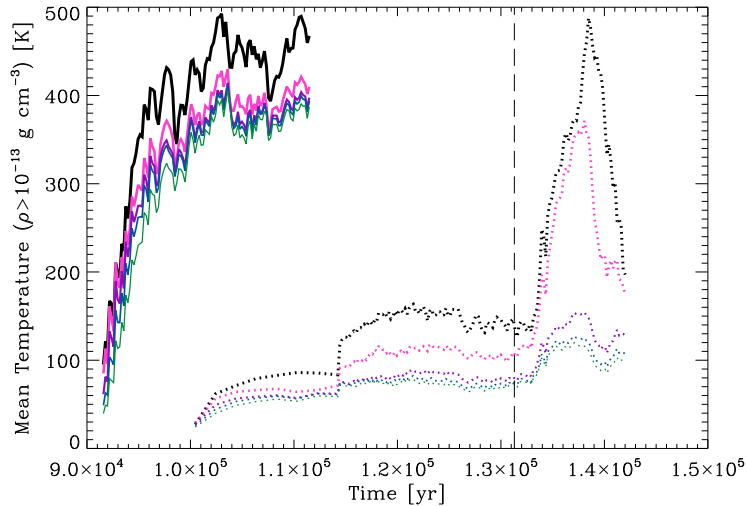


Figure 4.20: Mean disk temperature evolution. The dominance of the dense and hot component in Run 1 is clearly visible. Run 7 stays overall cool throughout the simulation.

4.6 Conclusions

In this chapter we compared the evolution of collapsing cores in slow or fast rigid rotation in detail. We found that slowly rotating cores ($\Omega < 10^{-13} \text{s}^{-1}$) result in normally sized ($R \approx 100 - 200 \text{AU}$), but relatively warm disks. Most of the disk mass is accumulated at densities higher than $\rho_{\text{crit},0} = 10^{-13} \text{g cm}^{-3}$ in this case. Since gas, which is denser than $\rho_{\text{crit},0}$ behaves adiabatically and cannot cool efficiently the disk heats up. In Run 1 the midplane temperature exceeds 800K within the inner 15-20AU in radius. Due to the high temperature as well as fast azimuthal velocities within the disk, fragmentation is suppressed. However, angular momentum is transported through weak spiral arms, allowing for a mass accretion rate of approximately $\dot{M}_* = \text{few} \cdot 10^{-5} M_\odot/\text{yr}$. We find the disk to be in vertical hydrostatic equilibrium. The vertical density profile can be fitted by a sum of two *sech*²-functions through which the disk pressure scale height is defined. Due to the way the cores are collapsing the forming protostellar disks have a 'flaring' structure: The ratio of pressure scale height to radius is roughly constant and equal to 1/4. This behaviour is typically expected for protoplanetary disks which are heated by stellar irradiation. The irradiation causes the disk surface layer to expand and flare. In these early stages of circumstellar disk evolution the flaring structure is a secondary effect. The inner disk region (close to the rotation axis of the system) is depleted of gas as material close to the rotation axis has low angular momentum and is collapsing first.

Disks formed from rapidly rotating cores ($\Omega > 10^{-13} \text{s}^{-1}$) are large ($R \approx 500 - 1000 \text{AU}$) and cold. The average disk temperature is below 100K within the disk region. Although their total

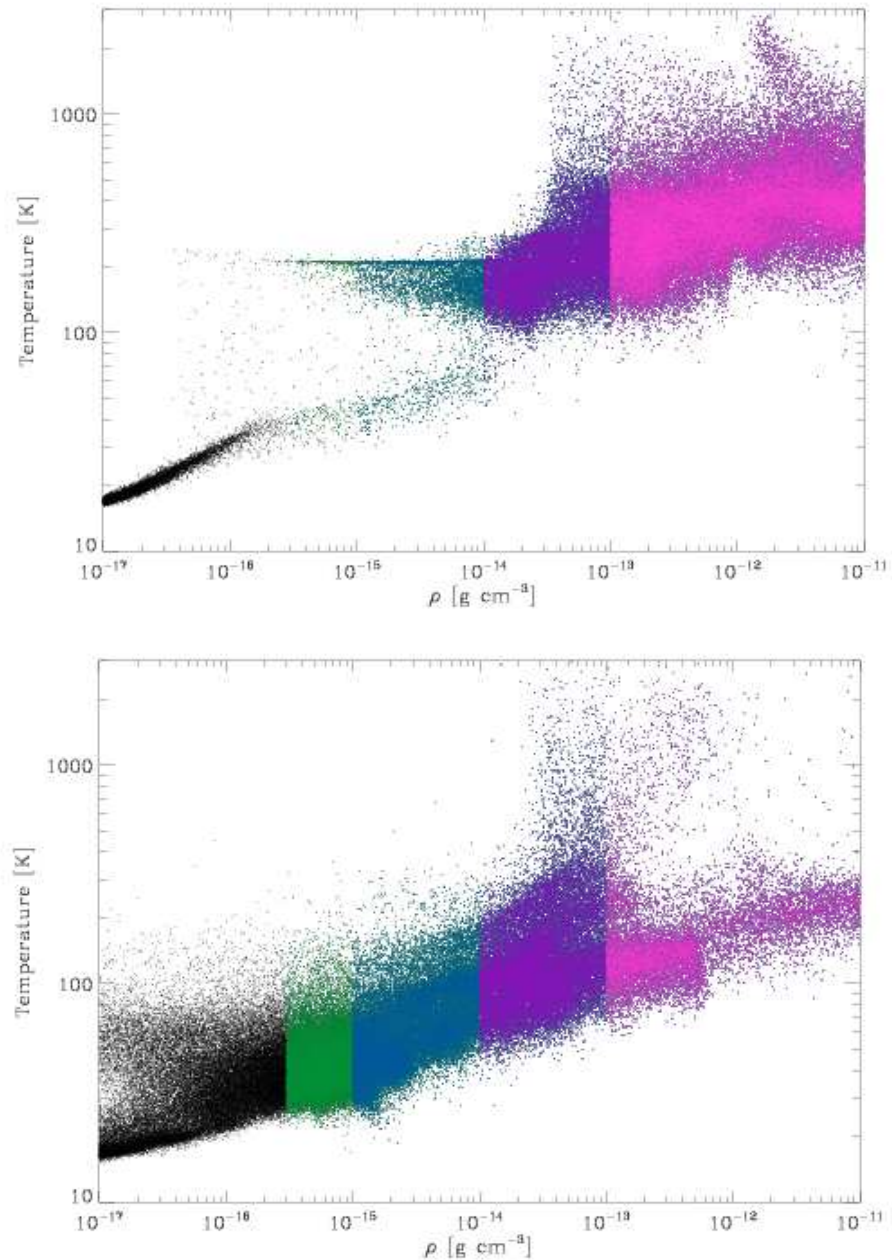


Figure 4.21: Temperature of SPH particles as a function of SPH density. We show the distribution for Run 1 at t_{final} in the *top panel* and the distribution for Run 7 at t_{final} in the *bottom panel*. Colour-coded are the different disk components: All SPH particles marked with the pink colour belong to the adiabatic disk component ($\rho > 10^{-13} \text{g cm}^{-3}$), in purple we show $10^{-13} \text{g cm}^{-3} > \rho > 10^{-14} \text{g cm}^{-3}$ and so on.

mass is comparable to the total disk mass accumulated in Run 1, their structure is completely different. Their radial density profile is flatter than in case of low angular momentum (flatter than R^{-2}). The disks show strong spiral arms. Within the spiral arms a small fraction of the core gas locally exceeds $\rho_{\text{crit},0}$. Fragmentation occurs within the spiral arms if the local Jeans mass is exceeded. The spiral arms are surrounded by a massive disk-like envelope of low density gas. As most of the disk is made up of low density gas ($10^{-16} > \rho > 10^{-14} \text{g cm}^{-3}$) it can still cool, thus allowing for disk fragmentation. They grow by mass accretion through circumfragmentary disks, which are important for the redistribution of angular momentum. After t_0 , the average mass accretion rate in this case is about $\dot{M}_* = 10^{-5} M_\odot/\text{yr}$. Therefore the growth of the central object is somewhat slower in this case. Before t_0 , \dot{M} is lower by a factor of two. It should be noted that we find a pure protostellar disk phase in Run 7 before a central object is formed at t_0 . It should also be noted that the disk pressure scale height is different for different components in Run 7. This is however the case because the outer disk radii are so large in this case. At large radii the vertical density profile is very flat and the derived scale height is large.

In both simulations the radial velocity is close to zero within the disk region and exhibits fast infall velocities at radii larger than the disk radius. The ratio of azimuthal velocity profile changes completely during collapse. Whereas $v_\phi \propto R$ initially, v_ϕ rather decreases with increasing radius after a disk has been formed. Therefore the disk is differentially rotating and shear flows are expected to play an important role in redistributing the angular momentum of the gas. At the same time, the disk is massive and its self-gravity cannot be neglected. A Keplerian velocity profile calculated according to the mass of the central object does not match the calculated results. The ratio of rotational velocity to local velocity dispersion (approximately equal to sound speed) is close to one within the disk region in both simulations, which is a clear sign of rotational support. The central object is not spherical, even though pressure becomes more and more important towards smaller radii. Instead, the central object has the shape of a nuclear disk - a sign that not enough angular momentum has been transported outward so far. The loss of angular momentum of the central object is of great importance. The spin-up of the central object by collapse and accretion of material without a sufficient loss of angular momentum may halt gravitational collapse when accelerating the central object to break-up speed (about 120 km/s for T Tauri stars) It is a strong observational constraint that protostars have an average total specific angular momentum of $10^{-17} \text{cm}^2 \text{s}^{-1}$ and T Tauri stars rotate with a velocity of ≈ 20 km/s, respectively. Moreover, within our solar system most of the angular momentum is contained in a very small amount of mass. Jupiter carries most of the angular momentum of the whole system. This transport is not found in our simulations.

Chapter 5

Disk structure as a function of core angular momentum

In this section, we discuss the resulting disk structure for all the runs in our sample. After giving an overview over all included simulations in section 5.1, the most important parameters like disk radius, disk scale height and stellar mass will be compared. We also give a qualitative overview over the disk structure as a function of angular momentum by showing the surface density profiles of all simulations at t_{final} . In addition, a new parameter, the *disk concentration*, will be introduced. We will show that the disk concentration is a powerful parameter in describing the disk structure in case of rigid rotation. Furthermore we will discuss the stability of the disk towards fragmentation as a function of initial core angular momentum in section 5.3. For this purpose we calculate the local Toomre Q parameter for the disks and compare the cooling time scale to the local dynamical time scale. We find that disks formed from high angular cores frequently become unstable to local gravitational instability and fragment. On the other hand, higher temperatures and rotational velocities prohibit disk fragmentation in case of low angular momentum core collapse. In the next chapter (chapter 6), we will place this finding in the context of recent observations.

5.1 Core sample

All cores have a total mass of $M_0 = 6M_{\odot}$. Their radial density profile follows a BES with a central density of $\rho_0 = 10^{-18} \text{g cm}^{-3}$. The initial temperature is 20K and we use a mean molecular weight of 2 (predominantly H_2 gas). The cutoff radius is 0.083pc, which corresponds to a dimensionless radius of $\zeta_{\text{cut}} = 6.9$ (see 2.1.2).

Following previous studies (Matsumoto & Hanawa, 2003), we parameterise our setups according to the energy budget of each simulation. We define the ratio of thermal to gravitational energy α to be the same for all cores:

$$\alpha = \frac{5 c_s^2 R_0}{2 GM_0} = 0.265. \quad (5.1)$$

Run	Ω_0 [s^{-1}]	J/M [$cm^2 s^{-1}$]	β_{const}	β_{BES}	t_0 [kyr]	t_{final}
0	$1.0 \cdot 10^{-14}$	$1.7 \cdot 10^{20}$	0.0007	$1.5 \cdot 10^{-4}$	92.6	-
1	$6.0 \cdot 10^{-14}$	$1.03 \cdot 10^{21}$	0.025	$4.5 \cdot 10^{-3}$	94.5	114.8
2	$8.0 \cdot 10^{-14}$	$1.37 \cdot 10^{21}$	0.045	$8.0 \cdot 10^{-3}$	94.5	115.4
3	$1.0 \cdot 10^{-13}$	$1.71 \cdot 10^{21}$	0.071	$1.3 \cdot 10^{-2}$	96.5	118.4
4	$1.2 \cdot 10^{-13}$	$2.06 \cdot 10^{21}$	0.105	$2.1 \cdot 10^{-2}$	96.5	119.2
5	$1.5 \cdot 10^{-13}$	$2.57 \cdot 10^{21}$	0.159	$2.8 \cdot 10^{-2}$	98.5	123.3
6	$1.6 \cdot 10^{-13}$	$2.74 \cdot 10^{21}$	0.181	$3.2 \cdot 10^{-2}$	102.4	126.7
7	$1.8 \cdot 10^{-13}$	$3.00 \cdot 10^{21}$	0.229	$5.0 \cdot 10^{-2}$	104.4	130.4

Table 5.1: We list the various initial rotational frequencies Ω_0 and resulting specific angular momenta J/M. β_{const} gives the ratio of rotational to gravitational energy according to equation 5.2, β_{BES} the one calculated from equation 5.3 respectively. A wide range of observed β 's is covered by the simulations, where $2 \cdot 10^{-3} < \beta < 1.4$ following Goodman (1993) or even smaller (Caselli et al., 2002). All runs feature 430000 'core' SPH particles, are evolved with the artificial viscosity implementation of Balsara (Balsara, 1995), and have a spatial resolution limit of 2AU.

Here c_s denotes the isothermal sound speed, G is the gravitational constant. Instead, we vary Ω_0 and, as a result, the ratio of rotational to gravitational energy β is varied throughout our sample. We introduce two definitions for β : The standard definition, which only includes the total mass of the sphere, but which does not incorporate information on the mass distribution (respectively the central condensation of the core), is given by

$$\beta_{\text{const}} = \frac{\Omega_0^2 R_0^3}{3GM}. \quad (5.2)$$

For a Bonnor-Ebert-like mass distribution, a more exact formulation of the importance of rotational velocities is given by:

$$\beta_{\text{BES}} = \frac{16}{15\pi^2} \frac{\zeta_{\text{cut}}^2 (\tau_{\text{ff}} \Omega_0)^2}{\Phi_c + q_c - \Phi}. \quad (5.3)$$

Φ is the total gravitational potential and Φ_c is the potential at the critical radius of the sphere (at $\zeta_{\text{crit}} = 6.451$). The integrated dimensionless mass factor $q = c^2 \Phi'$ was introduced by McLaughlin & Pudritz (1996), and is proportional to the gravitational acceleration Φ' at a certain radius.

In Table 5.1 we list both, β_{const} and β_{BES} , in order to illustrate the influence of central condensation on the energy budget. Taking into account the central condensation of the sphere, the ratio of rotational to gravitational energy is on average smaller by a factor of 5 than calculated from the standard definition - a rather non-negligible factor. In the following we will still adopt β_{const} as our standard β , simply because observational estimates of β are based on this prescription.

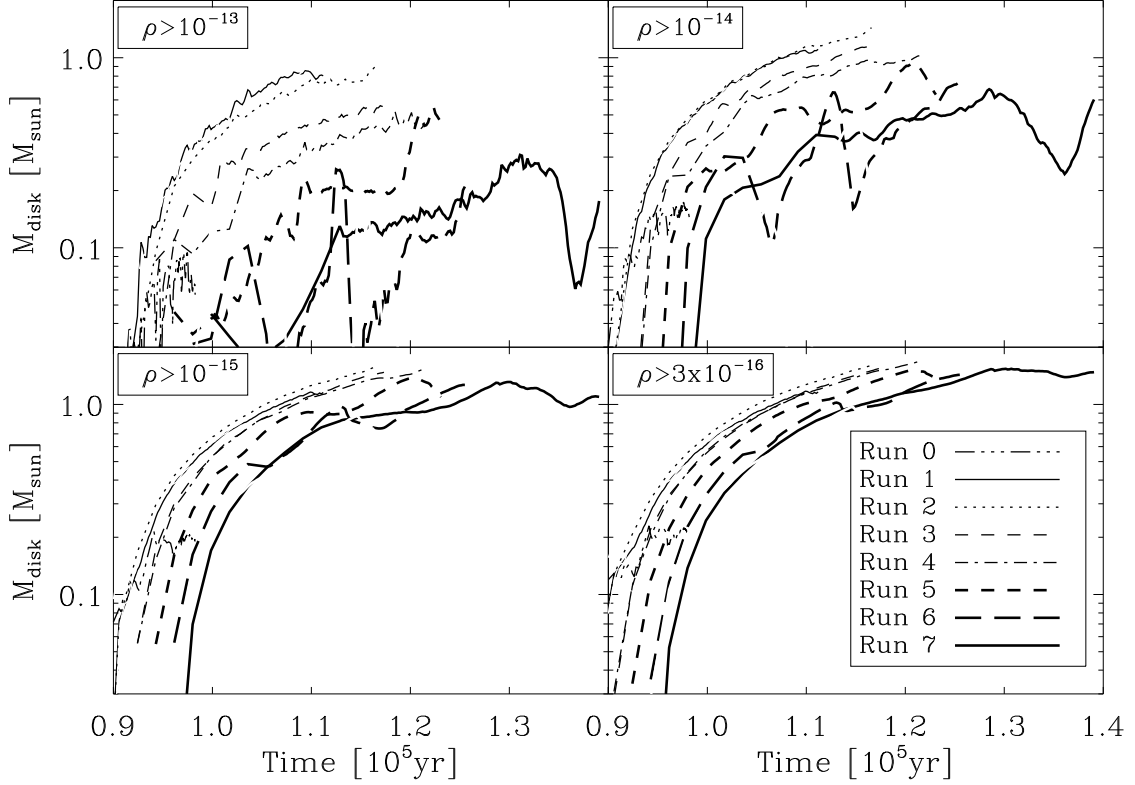


Figure 5.1: Comparison of the evolving disk masses as calculated for a) $\rho > 10^{-13} \text{ g cm}^{-3}$, b) $\rho > 10^{-14} \text{ g cm}^{-3}$, c) $\rho > 10^{-15} \text{ g cm}^{-3}$ and d) $\rho > 3 \cdot 10^{-16} \text{ g cm}^{-3}$.

5.2 Disk structure, mass and evolution

First we compare the evolution of the disk masses for four different density thresholds in Fig. 5.1. On average the time, at which a dense disk component is formed, is systematically increasing with core angular momentum. Even though all cores have the same freefall timescale, we see a difference of a few 1000 years between the runs. This effect becomes more and more pronounced, the denser the disk component of interest (from d) to a)). In all runs the disk mass is smoothly growing with time at lower threshold densities ((c) and d)). Only for Run 0 - 4 the growth is similar at high densities. In these cases the disk mass is dominated by the dense component (see Fig.5.1). In addition, these disks are warm and stable against gravitational instability and fragmentation. However, for Run 5 - 7 mass variations are quite significant within the densest disk components. In a) and b) strong local minima occur, which are caused by fragmentation. Fragments grow from the densest component, and thus causes the strong variations therein as it is depleted and reformed.

On the other hand most of the disk mass in Run 5 - 7 is located within a low density 'disk envelope'. Therefore the variations seen in a) and b) play only a minor role with respect the total disk mass (see c) and d)), which is finally above $1M_{\odot}$ in all simulations. In summary, disks from high

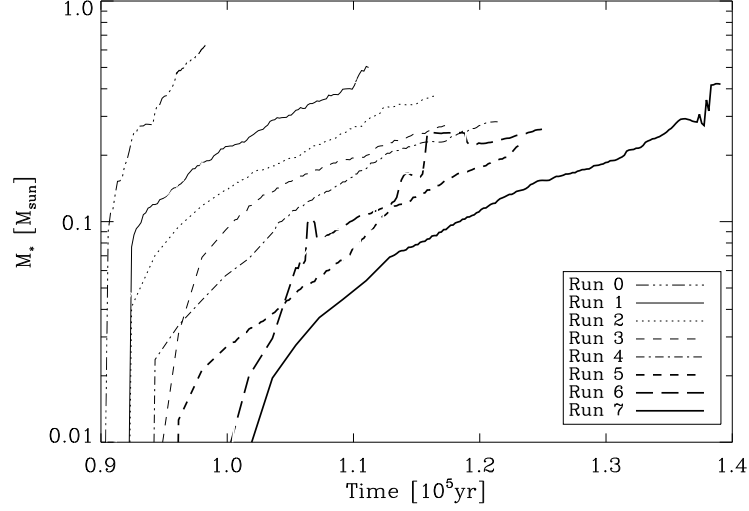


Figure 5.2: Stellar mass as a function of time for all simulations of the sample

angular momentum cores are cooler and feature a massive 'disk envelope' surrounding a light but dense disk component, which undergoes fragmentation.

For all simulations, we list the mass of the central object, as well as the disk mass M_{disk} and the disk radius R_{disk} for two threshold densities in Table 5.2. We use $\rho > 10^{-13} \text{g cm}^{-3}$ and $\rho > 10^{-16} \text{g cm}^{-3}$, respectively. These are the highest and the lowest of the previously used density thresholds. All given quantities are of course changing with time. We decided to compare the results at time t_{final} , the time at which 28% of the total core mass (or $\approx 1.8M_{\odot}$) has collapsed to densities greater than $10^{-16} \text{g cm}^{-3}$. t_{final} is listed in Table 5.1. We determine the disk radius from the radially averaged density profiles at t_{final} . We also compare the mean disk surface density $\bar{\Sigma}$ as calculated from:

$$\bar{\Sigma} = \frac{M_{\text{disk}}}{\pi R_{\text{disk}}^2} \quad (5.4)$$

in Table 5.2. We directly obtain the disk height H_{disk} from fitting the vertical density profile at the corresponding radii (see Fig.4.7 and Fig. 4.16). For comparison, we illustrate all calculated parameters in Fig. 5.6.

First, even though the same amount of mass has collapsed to densities greater than $10^{-16} \text{g cm}^{-3}$ at t_{final} , the mass of the central object is systematically decreasing with increasing core angular momentum. We find $M_{\star} = 0.53M_{\odot}$ for Run 1 with $\Omega = 6 \cdot 10^{-14} \text{s}^{-1}$ and $M_{\star} = 0.16M_{\odot}$ for Run 7 with $\Omega = 2 \cdot 10^{-13} \text{s}^{-1}$. The same trend is present for the gas mass located at $10^{-11} > \rho > 10^{-13} \text{g cm}^{-3}$. Here we find $M_{13} = 0.75M_{\odot}$ for Run 1, but only $M_{13} = 0.19M_{\odot}$ for Run 7 - almost a difference of a factor of 4. Accordingly, M_{16} is larger in Run 7, as M_{16} and M_{\star} add up to give 28% of the total core mass: $M_{16} = 1.54M_{\odot}$ for Run 7, but $M_{\star} = 1.17M_{\odot}$ for Run 1. In summary, in simulations with high core angular momentum most of the mass of the emerging disks is allocated at low densities. The dense disk component settles in a small circular accretion

disk around the center, around a forming fragment or in the center of strong, established spiral arms. Most of the disk is however low density material enveloping the dense component. On the other hand, disks formed from slowly spinning cores are highly concentrated, which means that most of the disk mass is located at high densities. There is no extended disk envelope present. In fact about 90% of the total **disk mass** resides at $\rho > 10^{-14} \text{g cm}^{-3}$ in Run 1.

The disk radii R_{half} and R_{16} are again systematically increasing with core angular momentum. Just R_{13} is slightly decreasing for larger angular momenta. However, as mentioned previously, the detailed structure including spiral arms is very different in all simulations. As a result, the disk surface density is decreasing with increasing core angular momentum. This trend is clearly visible in $\bar{\Sigma}_{16}$: $\bar{\Sigma}_{16}$ is an order of magnitude smaller in Run 7 (53 g/cm^2) as compared to Run 1 (5 g/cm^2). The high surface density in case of low angular momentum is responsible for the significant heating of the disk in this case (see Fig.4.20).

The fitted disk pressure scale height H_{13} is also roughly constant, whereas H_{16} is again increasing with increasing core angular momentum. High angular momentum disks only seem to be more extended, because they are in general less concentrated and feature a massive *disk envelope*. Fig. 5.6 shows the ratio of $H_{\text{disk}}/R_{\text{disk}}$. For all non-fragmenting disks (Run 0-4) we find the same $H/R \approx 0.25$ in all density components. For all fragmenting runs (Run 5-7) the components behave differently. For instance Run 6 appears to be very thick ($H/R \approx 0.5$) at $\rho > 10^{-13} \text{g cm}^{-3}$ and within the half mass component, but very flat ($H/R \approx 0.1$) in the total disk component.

Run	$M_{\star}[M_{\odot}]$	$\rho > 10^{-13} \text{g cm}^{-3}$			$\rho > 10^{-16} \text{g cm}^{-3}$			Half Mass		frag
		$M_{13}[M_{\odot}]$	$R_{13}[\text{AU}]$	$H_{1,13}[\text{AU}]$	$M_{16}[M_{\odot}]$	$R_{16}[\text{AU}]$	$H_{1,16}[\text{AU}]$	$R_{\text{h}}[\text{AU}]$	$H_{1,\text{h}}[\text{AU}]$	
0	0.66	0.095	27	-	0.24	233	-	34	-	-
1	0.528	0.750	96	28	1.17	250	65	64	19	-
2	0.311	0.746	110	25	1.39	344	85	89	20	-
3	0.250	0.518	92	24	1.45	433	110	125	27.5	-
4	0.229	0.427	102	23	1.46	567	135	155	30	yes
5	0.174	0.277	69	21	1.52	739	155	246	50	yes
6	0.244	0.114	50	24	1.46	1091	155	271	120	yes
7	0.161	0.185	79	20	1.542	952	190	317	120	yes

Table 5.2: Final stellar mass and disk parameters for all runs in our sample. We compare all runs at t_{final} , where 28% of the total core mass has collapsed to densities $\rho > 10^{-16} \text{g cm}^{-3}$. Run 0 is the only exception to this rule. In this case the angular momentum is so low that the collapse is unhindered and no disk is formed. Due to numerical limitations the evolution could only be followed until 15% of the total core mass has collapsed. The small amount of j results in a flattening of the central object which contains most of the collapsed mass within $R < 15 \text{AU}$. The definition of a disk scale height makes no sense in this case and is skipped. The disk mass components M_{13} and M_{16} , radii R_{13} and R_{16} , and disk scale heights $H_{1,13}$ and $H_{1,16}$ at t_{final} are listed for two threshold densities: For the highest threshold of $10^{-13} \text{g cm}^{-3}$ and the lowest threshold of $10^{-16} \text{g cm}^{-3}$. In addition we give the half mass radius R_{h} and the scale height $H_{1,\text{h}}$ at R_{h} , where $M_{\text{half}} = 0.5M_{16}$. The disk scale heights were obtained by fitting the vertical density profiles according to Eq. 4.3. More precisely we give H_1 , the scaling parameter of the second sech^2 -function. H_0 is always between 5 and 9AU and is therefore less interesting. The fragmentation state of the disks is given in the last column. We don't constrain the system's final multiplicity, because it may be changed completely by secular evolution.

We define the *disk concentration* c according to

$$c \equiv \frac{M_{\text{disk}}(\rho > 10^{-13} \text{ g cm}^3)}{M_{\text{disk}}(\rho > 10^{-16} \text{ g cm}^3)} \quad (5.5)$$

is illustrated in Fig.5.3. The concentration gives the percentage of disk mass, which resides at high densities ($\rho > 10^{-13} \text{ g cm}^3$) and builds up the warm, almost adiabatic disk component. It should be noted that the disk concentration stays approximately constant with time after an initial disk formation phase, which is rather short compared to all runtimes. Therefore the average concentration is a robust measure of disk structure. On average the concentration is decreasing with increasing core angular momentum. More precisely in Run 0 - 4, 40% to 80% of the disk mass is in the warm component. In all other runs, the average concentration is of order 0.1, with relatively strong variations due to fragmentation. For instance in Run 7 fragmentation sets in at 131kyr. From this time on the concentration is decreasing until the fragment merges with the central object at 140kyr.

Compared to Run 7, fragmentation starts earlier in Run 5 and especially in Run 6. In Run 5 and 6 the disk is a little more concentrated than in 7, but at the same time cooler than in the first three runs. In Run 7 the onset of gravitational instability first leads to the formation of extended spiral arms. Once enough mass has been acquired and transported through the spiral arms, fragmentation sets in. For intermediate angular momenta, where the surface density is still moderately high, but low enough to allow for short cooling timescales, fragmentation sets in immediately. There is no phase of spiral arm formation without fragmentation. We thus find a critical amount of specific angular momentum above which disks are fragmenting and below which they remain stable. This critical core angular momentum is between $2.1 \cdot 10^{21} \text{ cm}^2 \text{ s}^{-1}$ and $2.6 \cdot 10^{21} \text{ cm}^2 \text{ s}^{-1}$, corresponding to a rotational frequency between $1.2 \cdot 10^{-13} \text{ s}^{-1}$ and $1.5 \cdot 10^{-13} \text{ s}^{-1}$, respectively.

5.3 Disk Fragmentation

Disk fragmentation is important for the formation of binary and multiple stellar systems, brown dwarf companions (Whitworth & Goodwin, 2005) or even for the formation of gas giant planets (Kuiper, 1951; Boss, 1998; Mayer et al., 2004). Therefore we focus on the fragmentation properties of our sample in this subsection. In general we find that the warm & compact disks, which are formed from cores with low total angular momenta, are stable against fragmentation, whereas extended disks formed within high angular momentum cores fragment easily. In order to quantitatively explore the gravitational stability of the forming protostellar disks we utilize the Toomre criterion (Toomre, 1964):

$$Q = \frac{c_s \kappa}{\pi G \Sigma} < 1. \quad (5.6)$$

Here c_s is the local sound speed within the disk, κ is the epicyclic frequency, G the gravitational constant and Σ denotes the surface density. Differentially rotating accretion disks are expected to be gravitationally unstable towards non-axisymmetric perturbations for $3 > Q > 1$. In this case the formation of large spiral arms is promoted. For $Q \leq 1$ (Liverts et al., 2000, , and references

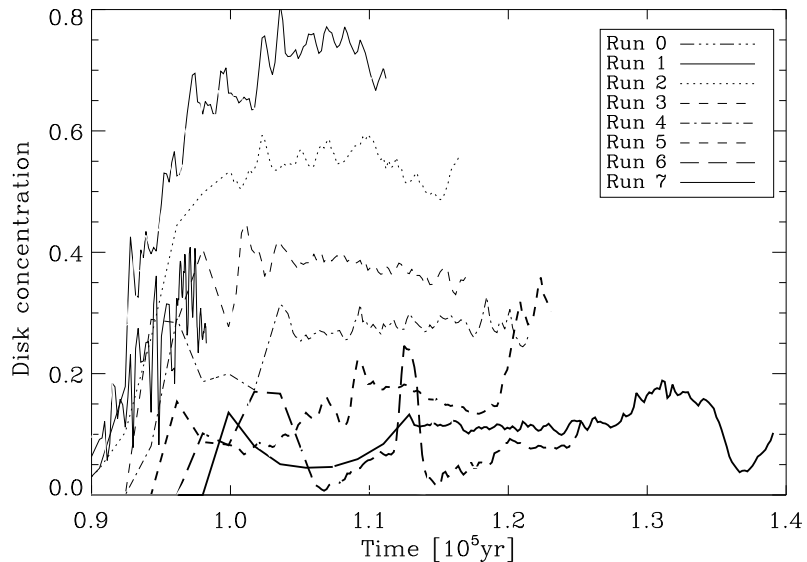


Figure 5.3: Time evolution of the disk concentration c for the whole sample

therein) the disk will be unstable towards axisymmetric perturbations and disk fragmentation may occur locally. Therefore a gravitationally unstable disk can either fragment into one or more gravitationally bound objects, or it can evolve into a quasi-stable state in which gravitational instabilities lead to the outward transport of angular momentum. In Figure 5.4 we show the Toomre Q parameter for the face-on projection of the two protostellar disks formed in Run 1 and 7, respectively. In Run 1, which is stable against fragmentation, the Q -isocontours reveal a spiral arm structure within the inner disk region, which is not clearly visible in the surface density distribution. More detailed analysis shows, that the density perturbation is of the order of 10%. Q stays above 1 everywhere in the disk. However, Q is below 3 within a significant fraction of the inner disk. This demonstrates that angular momentum transport due to gravitational torques in spiral arms is an important effect within the disk in Run 1, although 1 is stable to local disk fragmentation. In Run 7, Q is also < 3 throughout the pronounced spiral arm structure. However, Run 7 is unstable towards fragmentation and shows two regions where Q drops below 1 (green). Within this part of the disk two gravitationally bound fragments are forming.

The detailed evolution of a gravitationally unstable region depends on the rate at which it may cool or at which it heats up. It has been suggested (Goldreich & Lynden-Bell, 1965) that a feedback loop may exist through which Q is maintained at a value of ≈ 1 . Gammie (2001) has shown using a local isolated disk model that a quasi-stable state can only be maintained if the cooling time τ_{cool} is longer than the local dynamical timescale $\tau_{\text{dyn}} = \Omega^{-1}$ by at least a factor of 3. For shorter cooling times, the disk fragments. This finding is consistent with Pickett et al. (1998, 2000), who noted that 'almost isothermal' conditions are necessary for fragmentation. It has been suggested, however, that self-gravitating discs strictly require a global treatment (Balbus & Papaloizou, 1999), and while global effects are highly unlikely to stabilize a locally

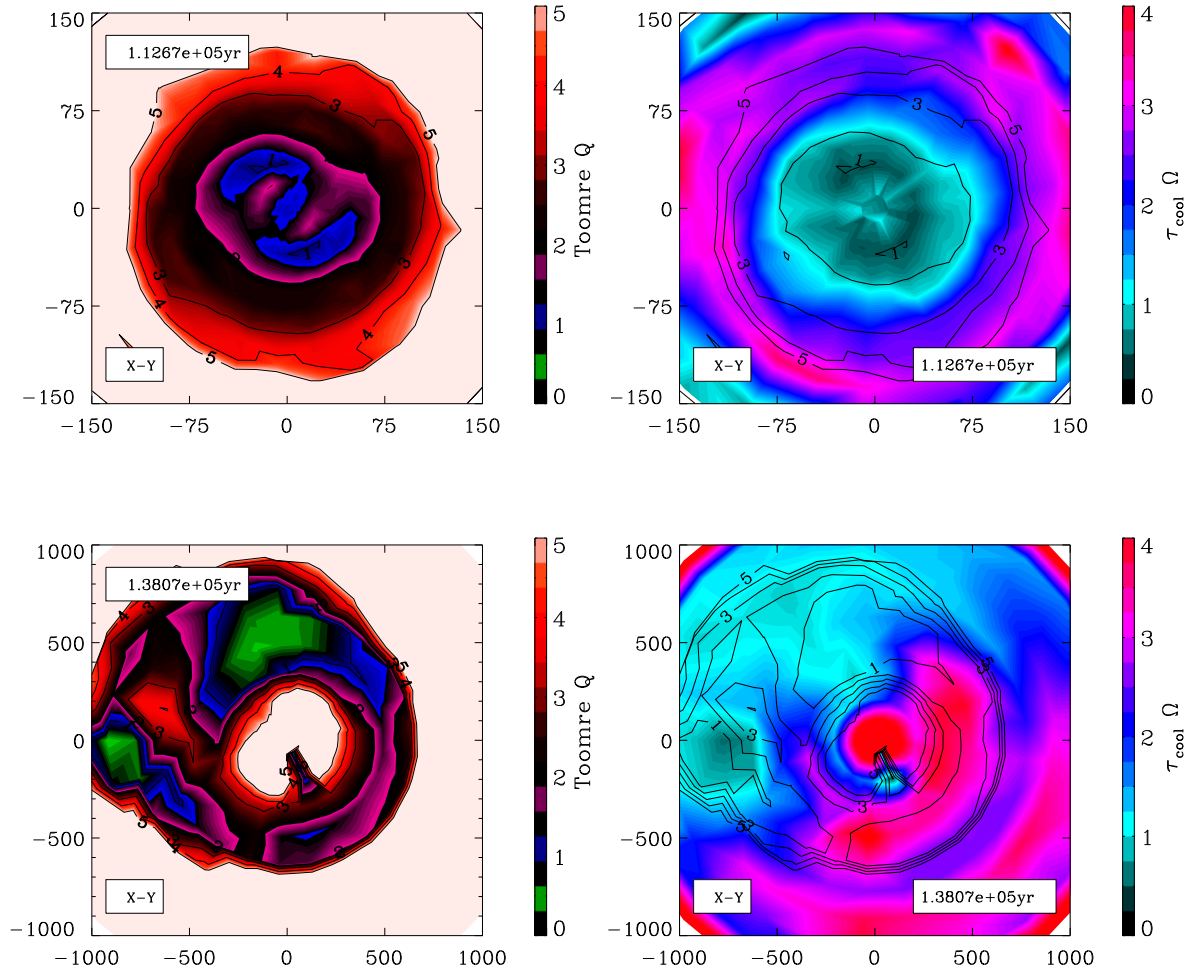


Figure 5.4: Toomre Q parameter and ratio of cooling time scale over dynamical time scale $\tau_{\text{cool}}\Omega$ as calculated for the face-on projections of Run 1 (upper plot) at $t_0 + 18.3 \text{ kyr}$ and Run 7 (lower plot) at $t_0 + 21.5 \text{ kyr}$. The warm and concentrated disk in Run 1 shows a non-axisymmetric structure. The Toomre Q is greater than 1 everywhere, but drops below 3 within the disk. In Run 7 the large spiral arm, which is also clearly visible in the surface density distribution (see Fig.4.10), is dense enough to be gravitationally unstable and undergoes fragmentation in the region where $Q < 1$.

unstable disk, they could well allow fragmentation within disks that would locally be stable. In 2003, Rice et al. (2003) roughly confirmed the result of Gammie (2001) in 3D SPH simulations of isolated disks. However, they found that more massive disks could still be fragmenting for even longer cooling times ($\approx 5\Omega$). In their setup the disk undergoes a viscous evolution, allowing for heat production by gravitational instabilities as well as turbulence. Heating by shocks and PdV work of infalling gas was not considered.

In the formation phase of a protostellar disk, the parental molecular cloud core, which envelops the disk, is still massive. Mass is falling onto the disk at a total rate of $\approx 10^{-5}M_{\odot}/\text{yr}$. According to the virial theorem, 50% of a gas element's energy is transformed into heat while moving inwards. In this stage of disk formation one has to consider efficient additional heating through the release of gravitational energy as well as by shocks, which occur once the rapidly infalling gas is decelerated at the disk surface and outer edge. Here we find that fragmentation is suppressed in a young protostellar disk, which would likely be fragmenting in isolation. In Fig. 5.4 (right plots) we show the stability criterion $\tau_{\text{cool}}\Omega$ (Gammie, 2001) and overplot the corresponding Toomre Q isocontours of the disks. We calculated the theoretical cooling time according to

$$\tau_{\text{cool}} = \frac{E_{\text{therm}}}{\Lambda}, \quad (5.7)$$

where $E_{\text{therm}} = \frac{3}{2}k_bT$ is the current thermal energy. In order to calculate the cooling rate Λ for every SPH particle according to its current density and temperature, we again utilize the implemented cooling prescription (following the table of Neufeld et al. (1995)). If left in isolation the disk would therefore cool at a rate Λ .

Interestingly, even though the disk in Run 1 is not fragmenting, we find $\tau_{\text{cool}}\Omega < 3$ within all of the inner disk region in this case. We may therefore conclude that the disk is predominantly heated by the infalling parental envelope and accretion. This means that concentrated protostellar disks are initially stabilized against fragmentation via heating by infall and accretion. Stable protostellar disks may therefore be more massive in collapsing envelopes than disks studied in isolation. On the other hand the structure of the cooling stability criterion correlates well with the Toomre Q-isocontours found in Run 7. In this case $\tau_{\text{cool}}\Omega$ is also below 3 within a large disk region, but drops below 1 only within the fragmenting part. In this case heating by infalling material is less efficient than for Run 1 because the disk is large and gas infall is hence distributed over a much larger surface area. The disk behaves more like an 'isolated disk', which leads to a better applicability of the cooling criterion.

Whether or not concentrated disks will undergo fragmentation within some later evolutionary stage requires further investigation. One might argue that the infall phase (10^5 years) is rather short compared to the typical disk lifetime (few $\times 10^6$ years) and that subsequent disk fragmentation is eventually happening after the parental envelope has mostly vanished. A comparison of prestellar core and stellar initial mass function points towards the fact that the star formation efficiency of a core is about 30% (e.g. Alves et al., 2007). This means that 2/3 of the initial core mass are not involved in the star formation process. So far it is not clear, which physical process is responsible for shutting down gas infall onto the disk and when exactly this is happening. Most

likely gas infall is stopped by efficient feedback (irradiation, winds, jets and outflows) from the central star. On the other hand, once the parental envelope has been destroyed, protostar and disk become observable. The disks, which are then called protoplanetary disks, typically have rather small masses (about $0.1M_{\odot}$ within a 100AU disk). This means that most of the original protostellar disk mass is probably accreted before a disk enters the protoplanetary phase. Binary star formation within a protoplanetary disks is thus unlikely, however, the formation of brown dwarf companions or gas giant planets is still possible.

5.4 Summary: Disk formation as a function of core angular momentum

In this section we summarise the most important results. In Figure 5.5 we show the surface density profiles of all runs at t_{final} on the same scale of $[-1000\text{AU}, 1000\text{AU}]$. From top to bottom the initial core rotation rate is increasing. Cores in slow initial rotation ($\Omega \leq 10^{-13}\text{s}^{-1}$; Run 0-4) do not form fragmenting protostellar disks, whereas disk fragmentation is happening frequently for higher angular momenta (Run 5-7). More quantitatively, we compare the most important characteristic disk quantities as a function of core angular momentum in Fig. 5.6. The data within Fig. 5.6 corresponds to the values given in Table 5.2. Concerning the disk structure, slow rotation results in relatively small ($\approx 100\text{AU}$), highly concentrated disks, which have accumulate most of their mass at densities $> 10^{-14}\text{g cm}^{-3}$. Since gas at these high densities cannot cool efficiently anymore, low angular momentum disks are significantly hotter than their high angular momentum counterparts. Disks formed from high angular momentum cores are large (up to 1000AU in radius) and form extended spiral arms, which harbor dense gas within them. Most of the disk mass is located at lower densities ($10^{-15} - 10^{-16}\text{g cm}^{-3}$), enveloping the the spiral arm structure. Thus, as the disk mass in the low density component increases with increasing core angular momentum, the mass accumulated in the high density component as well as the mass of the formed central object are decreasing. The radial extent of the high density component is roughly constant, whereas the outer disk radius (R_{16}) and the half mass radius (R_{half}) are systematically increasing. Surprisingly the ratio of pressure scale height to disk radius is roughly constant and around 0.25 for all non-fragmenting simulations and all different density components. The disk pressure scale height was obtained from fitting the vertical density profiles at the corresponding radii. In simulations with ongoing fragmentation H/R is less well-defined and varies between 0.1 and 0.5 in the most extreme case (Run 6). In summary, the disks appear to have a flaring geometrical shape, like typical protoplanetary disks. However, in this case, the flaring is not caused by stellar irradiation, but rather by the way matter is falling onto the disk.

The infall rate of gas onto the disk from the parental molecular cloud core is roughly constant in time and rather independent of initial core angular momentum: $\dot{M}_{\text{infall}} \approx 7 \cdot 10^{-5} - 10^{-4}M_{\odot}/\text{yr}$ for $\rho > 10^{-16}\text{g cm}^3$. Infall is dominated by the global gravitational potential. The mass accretion rate onto the central object is between $1 - 5 \cdot 10^{-5}M_{\odot}/\text{yr}$. In case of low angular momentum, the mass accretion rate is on average twice as high as in case of high angular momentum, even though spiral mode perturbations have a strenght of only 10% in this case. In general, gravita-

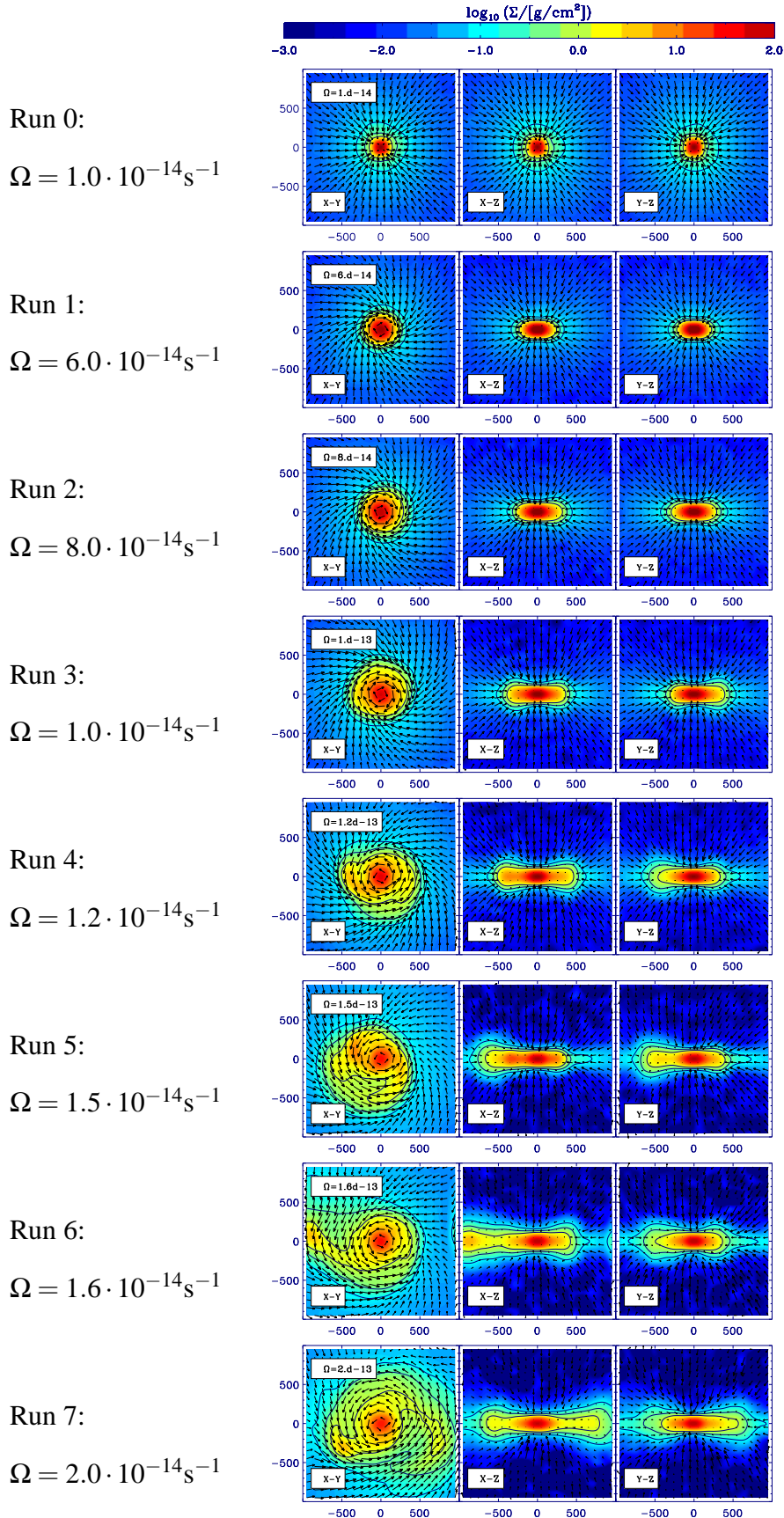


Figure 5.5: Disk formation as a function of core angular momentum

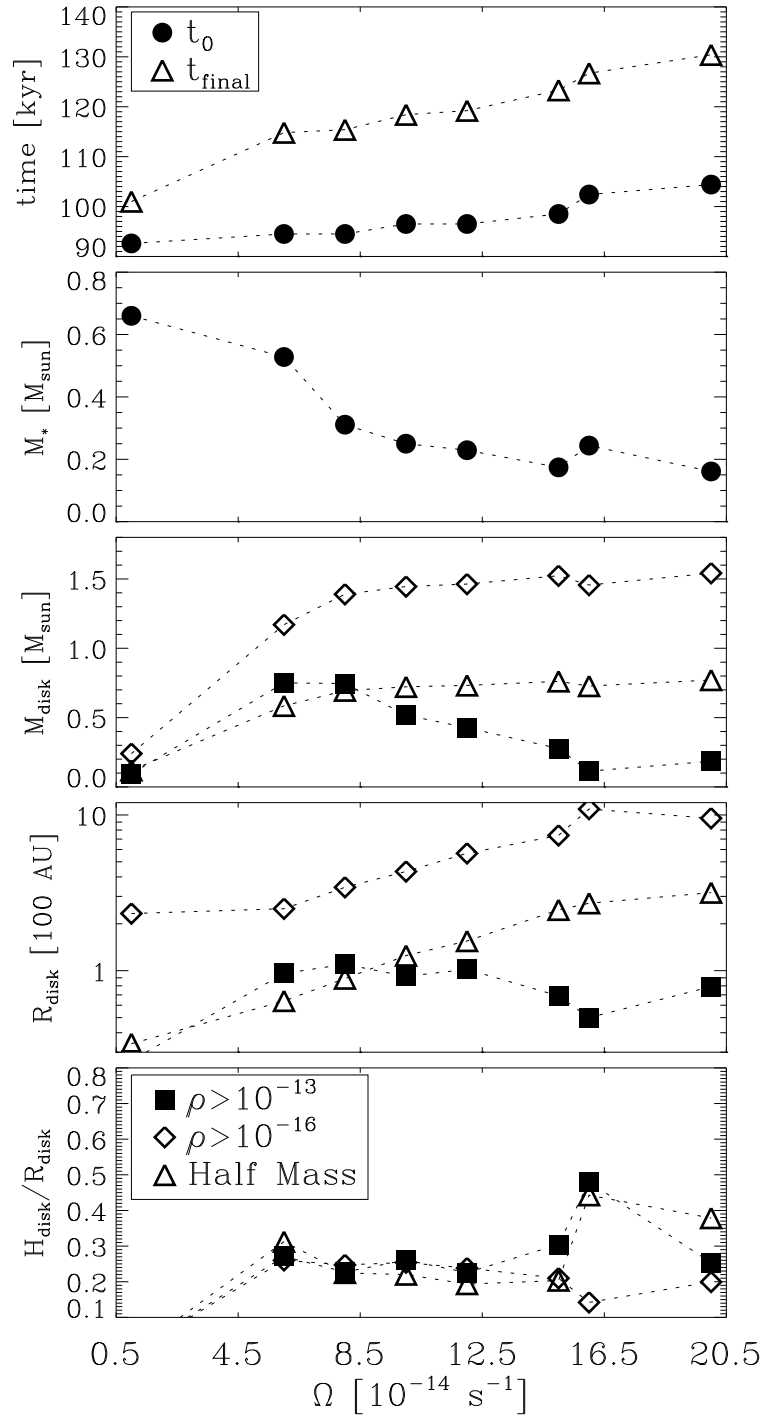


Figure 5.6: Properties of the forming star+disk system as a function of initial core rotation rate. All results are listed in Table 5.2.

tional torques seem to transport angular momentum more efficiently in the low angular momentum runs, where the disk surface density is higher.

5.5 Conclusions

In this section we investigated the change of the most important disk properties with increasing core angular momentum. We find the disk half mass radius as well as the outer radius of the low density component to systematically increase with increasing β . The outer radius of the adiabatic component (R_{13} , where $\rho(R) > 10^{-13} \text{ g cm}^{-3}$) stays roughly constant or is slightly decreasing, respectively. This behaviour results from the change in disk structure with β . When studying the disk mass evolution within different density components as a function of time, one finds that the dense, adiabatic component contains less mass in case of high angular momentum at all times. However, the low density component is much more massive in this case, resulting in a total disk mass (mass in gas at $\rho > 10^{-16} \text{ g cm}^{-3}$) which is comparable in all simulations. We conclude that the total disk mass accumulated at high densities is defined by the depth of the gravitational potential of the core or the total initial core mass, respectively. We quantify this finding by the definition of the *disk concentration*, which relates the mass in high and low density component. Thus, disks formed from low angular momentum cores have a high concentration (up to 80%), whereas the extended disks formed from high angular momentum cores have a low concentration (as low as 10%). Still, only large disks with low concentration undergo fragmentation. The fragments feed from the high density component, which is formed within the extended spiral structure. Therefore we see strong variations within the adiabatic component as a function of time. Similar to the adiabatic component, the central objects form earlier in case of low angular momentum and t_0 increases with β . After t_0 the central objects also grow much faster in case of low angular momentum, since a larger reservoir of low angular momentum gas is present, which is rapidly accreted during collapse.

In summary it is the disk concentration, from which we can deduce whether or not a protostellar disk will undergo subsequent fragmentation. The local fragmentation properties can be well understood by applying the Toomre criterium. Fragmentation occurs if the Toomre parameter Q is below 1, whereas the formation of spiral arms is promoted if $1 < Q < 3$. We can therefore conclude that spiral arm formation is enabled in all simulated protostellar disks allowing for the redistribution of angular momentum via gravitational torques. In the early evolutionary stages of protostellar disks mass accretion and viscous evolution is dominated by these effects. In addition, we find that the local disk stability against gravitational fragmentation is more accurately described by the Toomre criterium than by a comparison of local cooling and dynamical timescales. The cooling time scale criterium (fragmentation taking place if $\tau_{\text{cool}}/\Omega < 3$) is probably only accurate for non-accreting disks in isolation. We find that the stable disk formed in Run 1 would actually be gravitationally unstable in isolation as it would cool further. Additional heating by accretion and infall stabilises the disk in early evolutionary stages. Nevertheless, these disks might be able to undergo fragmentation during a later stage when gas infall is reduced. The fragmentation into binary or multiple stellar systems can still be expected to happen during early

embedded stages of protostellar evolution (Class 0), as observed protoplanetary disks typically have very small masses ($\approx 0.1M_{\odot}$). Late disk fragmentation thus might be in favour of brown dwarf and gas giant planet formation.

Chapter 6

Mean disk density and fragmentation properties of observed molecular cloud cores

From the SPH simulations of core collapse we find a clear correlation of disk structure and total core angular momentum, as long as rigid rotation is assumed (see previous chapters). The difference in disk structure results in a transition from disks which are stable against local gravitational instabilities and fragmentation to disks, which are fragmenting frequently. Thus, we use our simulations to determine the critical amount of angular momentum that defines the transition of fragmenting to stable disks. We find that this transition can be linked to a critical mean density of the disk (see section 6.1). With this result, we are able to predict whether or not a certain core will form a fragmenting protostellar disk and is therefore able to form a binary or multiple stellar system, if core mass, size and ratio of rotational to gravitational energy β are known. We apply our finding to observed core samples and compare the expected frequency of multiple stellar systems to observations. We find that disk fragmentation might not be the dominant mode of multiple star formation within collapsing dense cores. We show that -with this ansatz- a high mass core will more likely form a disk which can fragment into a multiple stellar system than a low-mass core which contains the same total angular momentum. As observations indicate a higher stellar multiplicity fraction the higher the mass of the constituents of the system, this trend is expected from an observational perspective. However, it has never been shown in simulations. This trend will be discussed in section 6.2

6.1 A critical mean disk density for fragmentation - Application of 3D SPH results

In Fig.4.7 we showed, that the thick disk is in approximate vertical hydrostatic equilibrium. The local gas pressure is given by the adopted equation of state, whereas the disk properties (mass & radius) are set by the initial core conditions and the collapse time scale.

We found that cores in slow rotation form small, compact disks, which accumulate most of their

mass at high densities. Therefore we expect these disks to have a higher mean disk density $\bar{\rho}$ than the extended disks formed from rapidly rotating cores. $\bar{\rho}$ could thus be considered as a critical indicator for the concentration and gravitational stability of a protostellar disk. Intuitively we can define $\bar{\rho}$ as

$$\bar{\rho} = \frac{\bar{\Sigma}}{H_{\text{disk}}} = \frac{M_{\text{disk}}}{\pi R_{\text{disk}}^2 H_{\text{disk}}}. \quad (6.1)$$

We found the disk pressure scale height and the disk outer radius to have a roughly constant ratio of

$$H_{\text{disk}} = \eta \cdot R_{\text{disk}}, \quad \text{with } \eta \approx 0.25. \quad (6.2)$$

With this relation, $\bar{\rho}$ is

$$\bar{\rho} = \frac{4M_{\text{disk}}}{\pi R_{\text{disk}}^3}. \quad (6.3)$$

If we assume that the angular momentum of each gas element is conserved during collapse we can connect the disk radius to the properties within the parental cloud core. In case of rigid core rotation, the dimensions of the disk are given by the centrifugal radius R_c :

$$R_c = \beta \cdot R_{\text{core}} = \frac{\Omega^2 R_{\text{core}}^4}{GM_{\text{core}}}, \quad (6.4)$$

where the centrifugal radius is defined as the equilibrium disk radius, at which gravitational and centrifugal forces are balanced in a central potential. M_{core} is the total core mass, and R_{core} the initial radius of the molecular cloud core. Moreover, we find in our simulations that the actual outer disk radius, which we define to be equal to the radial extent R_{16} of the low density component $\rho > 10^{-16} \text{g cm}^{-3}$, is always about a third of R_c :

$$R_{16} = \frac{1}{3} R_c. \quad (6.5)$$

Combining Eq. 6.3, Eq. 6.4 and Eq. 6.5 leads to

$$\bar{\rho} = \frac{12M_{\text{disk}}}{\pi\beta^3 R_{\text{core}}^3}. \quad (6.6)$$

For the same critical core mass and core radius, we expect the mass infall rate onto the disk to be roughly constant (e.g. solution by Shu (1977) and result from our numerical simulations). Accordingly, M_{disk} is only a function of time, and rather independent of β or initial core rotation (compare to Fig.4.4). We calculated $\bar{\rho}$ at t_{final} for all our simulations (see Fig. 6.1). For the disk mass we used M_{16} from Table 5.2. In our sample of equally large and massive cores, β is a direct measure of rotational energy or angular momentum. According to Eq.6.6, the mean disk density is rapidly decreasing with core angular momentum. We probed, at which $\bar{\rho}$ we find the transition from non-fragmenting to fragmenting disks, and find that disks with a mean density of $\bar{\rho} \geq \rho_{\text{crit},1} = 3 \cdot 10^{-16} \text{g cm}^{-3}$ are gravitationally stable and do not undergo fragmentation at any time during their evolution (Run 0-4). On the other hand, we see efficient disk fragmentation in

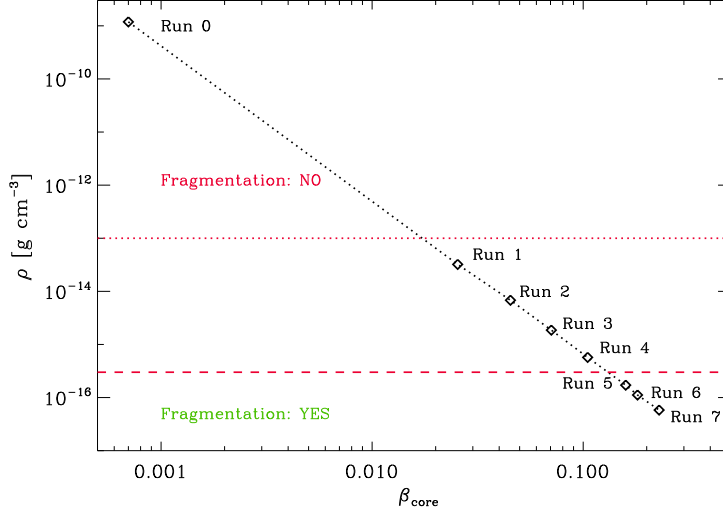


Figure 6.1: $\bar{\rho}$ as a function of core rotation as calculated from our runs. We derived that $\bar{\rho} \propto \beta^{-3}$. The red dashed line at $\rho_{\text{crit},1} = 3 \cdot 10^{-16} \text{g cm}^{-3}$ indicates the critical density, below which fragmentation is found in our calculations. Assuming a different cooling prescription, in which the gas behaves isothermally up to $\rho_{\text{crit},0} = 10^{-13} \text{g cm}^{-3}$, fragmentation might be possible up to this limit (red dotted line). We will use both critical densities for comparison with observations.

Runs 5-7, which all have $\bar{\rho} < \rho_{\text{crit},1}$. Disks with a mean density of $\bar{\rho} \geq \rho_{\text{crit},1}$ are always gravitationally stable, compact disks, whereas disks with a lower mean density are always extended, less compact and will undergo disk fragmentation. At first sight our findings may seem counter-intuitive. It would rather be more intuitive to assume that more compact disks with high $\bar{\rho}$ are fragmenting more effectively than less compact ones, simply because the Toomre Q parameter is inversely proportional to the disk surface density $\bar{\Sigma}$. These considerations however neglect the thermal behaviour of the gas, which is heated due to infall and accretion.

In our prescription of the gas thermodynamics, there are two critical densities: $\rho_{\text{crit},1} = 3 \cdot 10^{-16} \text{g cm}^{-3}$, and $\rho_{\text{crit},0} = 10^{-13} \text{g cm}^{-3}$. As we have mentioned (see section 3.7) cooling by molecular lines slowly becomes inefficient at densities higher than $\rho_{\text{crit},1}$. In other numerical simulations which include a barotropic EOS (e.g. Bate, 1998; Goodwin et al., 2004b) the gas is assumed to undergo a sudden transition between isothermal and adiabatic behaviour at $\rho_{\text{crit},0}$. For Run 1 - 4 (or Ω_{core} between $6 \cdot 10^{-14} \text{s}^{-1}$ and $1.2 \cdot 10^{-13} \text{s}^{-1}$) the disks' fragmentation properties might therefore be different in simulations with a barotropic EOS. Therefore we will discuss both, $\rho_{\text{crit},0}$ and $\rho_{\text{crit},1}$ in the framework of recent core observations.

6.2 Application to observations

Our findings can be applied to observed prestellar cores. We use two samples observed by Barranco & Goodman (1998), Goodman et al. (1993) and Caselli et al. (2002). Both studies list

core radii and estimate the ratio of rotational to gravitational energy β from fitting velocity gradient maps. We calculate the expected mean disk density from these values according to Eq.6.6. However, the core mass changes throughout the observed sample. We therefore assume the disk mass to be dependent on the core mass. For every core the disk mass is varied between 1% and 30% of the core mass. A maximum disk mass of $0.3M_{\text{core}}$ is motivated by the typical star formation efficiency of prestellar cores of $\approx 33\%$ (e.g. Motte et al., 1998).

In Fig. 6.2 the theoretically expected dependence of $\bar{\rho}$ on core radius is depicted by the solid lines (for a disk mass of $0.1M_{\text{core}}$) and the dot-dashed lines ($M_{\text{disk}} = 0.3M_{\text{core}}$) for three different values of β . For these theoretical curves, we assume $M_{\text{core}} \propto R$ in the upper panel or $M_{\text{core}} \propto R^2$ in the lower panel of Fig. 6.2, respectively. We use our initial conditions ($6M_{\odot}$ and 0.083pc) to normalise the powerlaws. Observations indicate a powerlaw index of around 2. An index of 3 would correspond to a sphere of constant density. The dotted vertical lines indicate core masses of $3M_{\odot}$, the mass at which the core mass function reaches its maximum (Motte et al., 1998), and of $1M_{\odot}$. In order to indicate the sensitivity of the problem with respect to the critical density regime ($3 \cdot 10^{-16}\text{g cm}^{-3} < \rho < 10^{-13}\text{g cm}^{-3}$) we overplot these two critical densities (red dotted lines).

Fig.6.2 shows that for the sample of Goodman et al. (1993) and Barranco & Goodman (1998) between 19% (for $M_{\text{disk}} = 0.3M_{\text{core}}$) and 31% (for $M_{\text{disk}} = 0.05M_{\text{core}}$) of all cores are predicted to undergo subsequent fragmentation, whereas 0% of all cores are expected to fragment in Caselli et al. (2002). On average 13% of all cores should thus form protostellar disks, which will fragment within the first 10^5 yrs of their evolution. For an isothermal collapse of the gas up to $\rho_{\text{crit},0}$ we infer that 75% - 81% of all cores in Goodman et al. (1993) and 30%-45% of all cores in Caselli et al. (2002) would form gravitationally unstable disks. This results in an average of 58%.

According to a high resolution near-infrared imaging survey of Duchêne et al. (2007), of low-mass embedded Class I sources located in Taurus-Aurigae, Ophiuchus, Serpens and L1641 in Orion, the observed multiplicity rates within the separation range of 45-1400AU are $32 \pm 6\%$ and $47 \pm 8\%$ within 14-1400AU, respectively. These rates are much larger than our predicted results including cooling by thin molecular lines, and smaller than in case of isothermal cooling down to 10^{-13}g cm^{-3} . This means that 1) either gas cooling in molecular cloud cores is much more efficient than assumed in our prescription or 2) that disk fragmentation is not the dominant mode of fragmentation to form binary or multiple stellar systems. For example low levels of turbulence within prestellar cores may efficiently alter their fragmentation properties (Goodwin et al., 2004b). However, in this case we speak of core fragmentation rather than disk fragmentation. The effects of initially sub- or transonic turbulence will be discussed in the next chapter. In addition, the physics of gas cooling within the density regime of 10^{-16} and 10^{-13}g cm^{-3} is extremely important for disk fragmentation. In order to ascertain the critical disk density for fragmentation our findings deserve further numerical investigation with more realistic dust cooling and radiation transport.

Nevertheless - even from our simple approach - we conclude that large and massive cores fragment more easily than small, less massive cores, provided that the concept of a 5%-30% star formation efficiency is applicable. In this case one can assume that $M_{\text{disk}} \propto M_{\text{core}}$. Observations find $M_{\text{core}} \propto R^{-p}$, with $1 \leq p \leq 2.3$ (Larson, 1981; Myers, 1983; Hubber & Whitworth, 2005). In

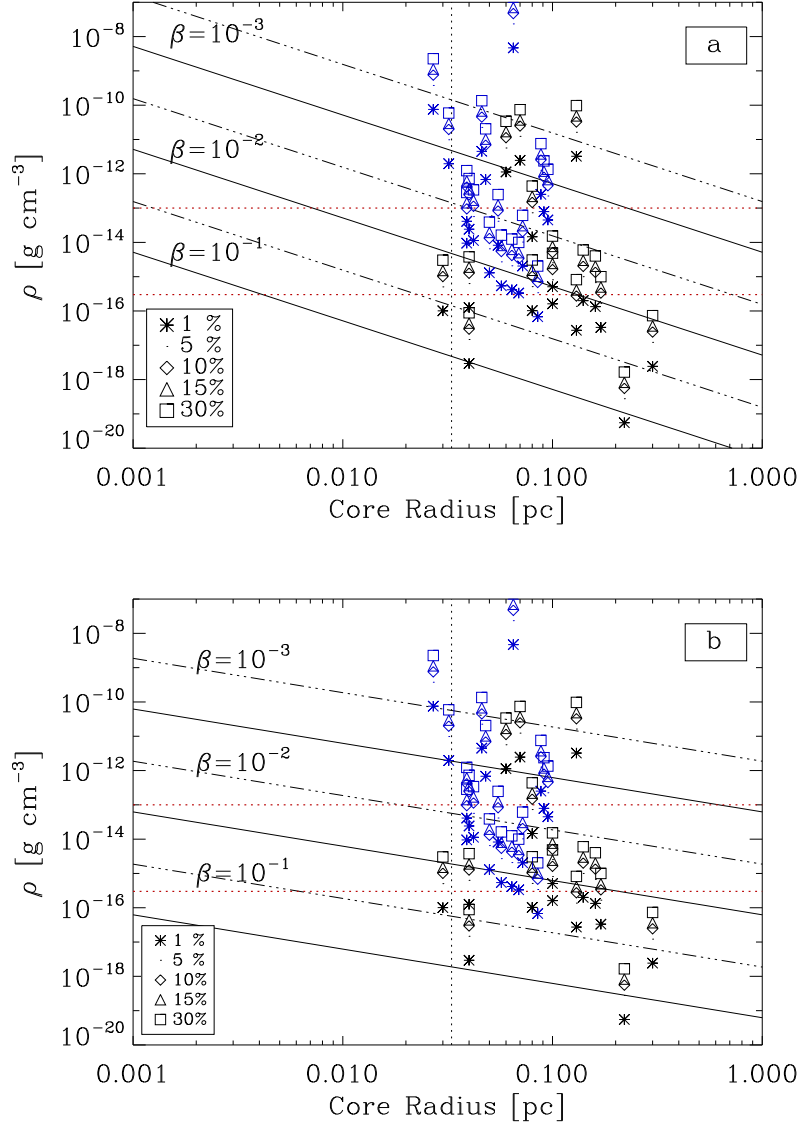


Figure 6.2: Mean disk densities calculated for the observed core samples of Barranco & Goodman (1998) and Goodman et al. (1993) (black symbols) as well as Caselli et al. (2002) (blue symbols). We also show $\bar{\rho}$ for three constant values of β ($\beta = 10^{-3}$, 10^{-2} , 10^{-1}). For every β the disk mass is assumed to be between $0.01M_{\text{core}}$ (solid lines) and $0.3M_{\text{core}}$ (dash-dotted lines). For the derivation of the theoretical a powerlaw dependency of core masses and core radius has been assumed: M_{core} proportional to a) R and b) R^2 , respectively. We used our setup to calibrate the mass-radius relation. The dotted vertical line indicates a core mass of $3M_{\odot}$. It should be noted that the initial core mass function is observed to peak at $3M_{\odot}$. For the observed cores we used core masses published in Caselli et al. (2002). The red dotted lines show the fragmentation limits $\rho_{\text{crit},0}$ and $\rho_{\text{crit},1}$, where $\rho_{\text{crit},1}$ was determined from our simulations.

Fig. 6.2 two example powerlaw indices are discussed. In a) $M_{\text{core}} \propto R_{\text{core}}$ was assumed, whereas $M_{\text{core}} \propto R_{\text{core}}^2$ in b). From Eq. 6.6 it follows that $\bar{\rho} \propto \frac{1}{\beta^3 R_{\text{core}}^2}$ in a) and $\bar{\rho} \propto \frac{1}{\beta^3 R_{\text{core}}}$ in b).

In general, the higher $p < 3$, the smaller the dependence of $\bar{\rho}$ on core radius. For cores of constant density ($p = 3$), we infer the fragmentation properties of the formed disk to be completely independent of core size. For $1 < p < 3$ smaller, and thus less massive cores form more concentrated disks, as compared to larger and more massive cores with equal β . The more concentrated a disk, the less likely it will form fragments during its early evolution. As β is observed to be roughly independent of core size (Goodman et al., 1993, 1998), this ansatz is able to explain the observational trend that stellar multiplicity seems to be higher for more massive stars (e.g. Lada, 2006).

6.3 Conclusions

In this chapter we presented a simple analytical prescription predicting the fragmentation properties of collapsing prestellar cores in dependence on three initial core properties: Core mass, radius and ratio of rotational to gravitational energy β . From these three parameters the mean density of the forming protostellar disk, $\bar{\rho}$, can be deduced. The simulations show that disk fragmentation is enabled if this mean disk density is below a critical density ρ_{crit} , whereas it is prohibited if $\bar{\rho} > \rho_{\text{crit}}$. We ascribe this behaviour to the cooling properties of the gas. In our prescription, gas cooling mimics complete isothermal behaviour for densities below $\rho_{\text{crit},1} = 3 \cdot 10^{-16} \text{g cm}^{-3}$. Above $\rho_{\text{crit},1}$ cooling slowly becomes inefficient and the gas finally behaves in a completely adiabatic manner at $\rho_{\text{crit},0} \approx 10^{-13} \text{g cm}^{-3}$. Many other authors employ a barotropic equation of state, which employs a rapid transition from isothermal to adiabatic gas at a critical density, which is typically equal to $\rho_{\text{crit},0}$. From our numerical calculations, we find the critical density for disk fragmentation ρ_{crit} to be roughly equal to $\rho_{\text{crit},1}$. A mean disk density of $\rho_{\text{crit},1}$ corresponds to a critical core rotation of $\approx \Omega = 10^{-13} \text{s}^{-1}$ or $\beta \approx 0.1$ for the simulated prestellar cores of $6M_{\odot}$ at a radius of 0.083 pc. When this finding is applied to observational samples of prestellar cores, one finds that -with this simple prescription only - an important observational trend can be reproduced. Observations show that the stellar binary or multiple frequency increases with the mass of the system's constituents. One additional assumption had to be included to arrive at this conclusion. In order to calculate $\bar{\rho}$ the mass of the disk has to be known. We therefore assumed the disk mass to be a fraction of the core mass, i.e. $0.01M_{\text{core}} < M_{\text{disk}} < 0.3M_{\text{core}}$. As the typical star formation efficiency for prestellar cores is of the order of 1/3, the upper limit of the disk mass is well approximated by $0.3M_{\text{core}}$. Observations show that β is roughly independent of initial core radius. For constant β , $\bar{\rho} \propto M_{\text{disk}} R_{\text{core}}^{-3}$. The observed mass-radius relation for prestellar cores suggests a powerlaw dependence of $M_{\text{core}} \propto R_{\text{core}}^p$, with a powerlaw index p of $1 \leq p \leq 3$. In many studies $p \approx 2$ has been found. In this case $\bar{\rho}$ is inversely proportional to the core radius. Therefore a low-mass core, which is typically small, is less likely forming a protostellar disk which is able to fragment, than a larger, high-mass core with the same β . Low-mass cores are hence more stable towards disk fragmentation than high-mass cores. If the principle of a global star formation efficiency (typically 30%) is applicable, the mass of the stars which form within a certain core is on average correlated to the total initial core mass. This means that lower-mass cores also form

lower-mass stars and vice versa. Therefore low-mass stars formed from low-mass cores tend to be singles rather than multiples. In case of $p = 3$ the core would have a constant density profile. In this case $\bar{\rho} = \text{const}$ for the same β , and the fragmentation properties of every core are preset by the amount of angular momentum it contains.

We apply our findings to observational samples of prestellar cores for which mass, size and core β are known. For the critical density $\rho_{\text{crit},1}$, which was extracted from our numerical simulations, the fraction of predicted multiple stellar systems is too low. On average only 13% of all cores are predicted to undergo subsequent disk fragmentation. However, since the critical density is probably related to the specific description of gas cooling, a second critical density ($\rho_{\text{crit},0}$) has been investigated. The application of $\rho_{\text{crit},0}$ can e.g. be motivated by further dust cooling in regions where all molecular lines are optically thick. In this case 58% of all cores in the sample are expected to undergo disk fragmentation - all high-mass cores (apart from 1) but also many cores of intermediate mass (few M_{\odot}). This fraction agrees well with observations. Dust cooling has not been included in these simulations, since it would require the inclusion of radiation transport, dust chemistry and dust grain evolution. Currently numerical limitations prohibit consideration of dust physics in core collapse simulations. However, also in our sample of simulations $\rho_{\text{crit}} = \rho_{\text{crit},0}$ would imply the fragmentation of all but one formed protostellar disks. (Run 0 would form a single star).

Our conclusions from this study are threefold:

- 1) If $\rho_{\text{crit},1}$ is assumed to be the more realistic critical density, disk fragmentation cannot be the dominant mode of binary or multiple formation. In the next chapter we will show that low levels of turbulence in a prestellar core may lead to core fragmentation instead of the formation of larger protostellar disks and subsequent disk fragmentation.
- 2) Fragmentation within later evolutionary stages (the 'late phases of hot disks') cannot be excluded. In protostellar disks which are further evolved heating by accretion and infall subsides, since the gas infall from the parental envelope decreases, and the disks become less massive as most of their mass has been accreted. Observed protoplanetary disks typically have small masses ($\approx 0.1M_{\odot}$). However, the late fragmentation of low mass disks will be more important for brown dwarf and gas giant planet formation, rather than for the formation of multiple stellar systems, simply because most of the gas reservoir is gone. The formation of multiple stellar systems thus has to take place during early evolutionary stages of young protostars (Class 0 phase).
- 3) We found that gas cooling within the density regime of 10^{-16}g cm^{-3} to 10^{-13}g cm^{-3} is of immense importance to the fragmentation properties of protostellar disks. Therefore the comparison of different numerical treatments of the gas thermodynamics within core collapse simulations plays a key role in improving our understanding of star formation and fragmentation. This problem has to be addressed in further studies.

Chapter 7

Protostellar disks in low-mass star formation - II. Collapse of turbulent molecular cloud cores

The isolated collapse of turbulent prestellar cores and the subsequent formation of embedded protostellar disks is investigated in this chapter. This project is based on the idea that sub- or transonic turbulence may cause a net specific angular momentum within prestellar cores. Various authors have already suggested the connection between turbulence and apparent core rotation (Goldsmith & Arquilla, 1985; Goodman et al., 1993; Dubinski et al., 1995). With a large sample of turbulent setups Burkert & Bodenheimer (2000) showed that random Gaussian velocity fields with power spectra $P(k) \propto k^{-3}$ to k^{-4} are a viable source of net angular momentum for dense molecular cloud cores. In addition, turbulent power spectra of this form can reproduce both, the observed line width-size relationship and the observed projected rotational properties of molecular cloud cores. Hence, such initial conditions provide a powerful tool to generate turbulent prestellar cores with rotational properties that agree with observations. In very dense cores the line widths of observed molecular emission tend to undergo a 'transition to coherence' (Barranco & Goodman, 1998), implying that turbulence has been dissipated to sub- or transonic levels on core scales. For this reason we focus on the impact of low levels of turbulence on the protostellar disk formation process. More details on the turbulent nature of molecular clouds and cores can be found in chapter 2.1.2.

We show, that the structure of the whole core becomes significantly different in a moderately turbulent environment as soon as it collapses. As a result, protostellar disk formation and evolution is also heavily affected. The formed disks are on average smaller and stable against fragmentation. Core fragmentation is in favour over protostellar disk fragmentation in this case. Core fragmentation only happens in three out of 11 simulations, that is in 27% of all cases. This result is not in agreement with calculations by Goodwin et al. (2004b), who tested the fragmentation properties of moderately turbulent cores with a Plummer-like initial density profile and a polytropic EOS with the SPH code DRAGON. They found fragmentation into binary or multiple stellar systems in 80% of all cases. However, they use sink particles and evolve the simulations for a much longer time scale.

In section 7.1, the turbulent initial conditions are briefly described. The effect of turbulence on the global core structure will be discussed in section 7.3. Results on protostellar disk formation from turbulent prestellar cores will be shown and discussed in section 7.4. We will also compare turbulent and non-turbulent case in this and the following section. Conclusions are drawn in section 7.6.

7.1 Turbulent velocities as a source of core angular momentum

On scales of ≈ 0.1 pc velocity gradient maps observed protostellar cores show both, irregular as well as regular, motions (Caselli et al., 2002), and prestellar cores are known to have fairly narrow, hence thermal, line widths (Barranco & Goodman, 1998; Belloche et al., 2001; André et al., 2007). The former indicates, that the internal motions of many cores are not likely to be caused by ordered rotation, but rather by turbulent motions. However, the magnitude of any internal velocities is constrained to be at most transonic.

Unlike the conditions on molecular cloud scales, the absence of a more pronounced line-broadening on core scales indicates that turbulent pressure is at most as important in supporting the core against its own self-gravity as its internal thermal pressure. Therefore MCCs feature sub- or transonic levels of internal turbulence. According to Jijina et al. (1999) the observed ratio of turbulent to gravitational energy $\gamma = E_{\text{turb}}/E_{\text{grav}}$ within dense cloud cores is between 0 and 0.3, but always smaller than 0.5. Burkert & Bodenheimer (2000) showed that these low levels of turbulence still cause total specific core angular momenta, which are in good agreement with the observed rotational properties of prestellar cores. The total amount of specific angular momentum j in a low-mass MCC is typically of the order of $j_{\text{tot}} \approx 10^{21} \text{ cm}^2 \text{ s}^{-1}$ (Goodman et al., 1993). Following Burkert & Bodenheimer (2000) this amount of specific angular momentum is easily generated via a superimposed, turbulent powerlaw spectrum of $P(k) = k^n$, where k is the wave number and $n = [-3, -4]$ denotes the power spectral index. $n = -3$ results in more power on smaller scales than e.g. $n = -4$, which corresponds to Burger's power spectrum for supersonic turbulence. The correspondance between the turbulent spectrum with random relative phases for the spectral components and Larson's line-width size relation has been suggested by Myers & Gammie (1999). Their work is based on Larson's finding that the observed internal velocity dispersion σ of a molecular cloud region is correlated with its length scale λ (Larson, 1981):

$$\sigma(\lambda) \propto \lambda^q. \quad (7.1)$$

Larson suggested $q = 0.38$. This results in an approximate Kolmogorov scaling, which is expected in case of ideal, incompressible hydrodynamics. Later observational work however found $q = 0.5$ on scales larger than 0.1 pc (see e.g. Goodman et al., 1998). Finally, the power spectral index n is unequivocally related to q as $n = -3 - 2q$. It follows that $q = 0.38$ results in $n = -3.76$ (close to Kolmogorov's power spectral index of $(n = -\frac{11}{3})$), whereas $n = -4$ for $q = 0.5$.

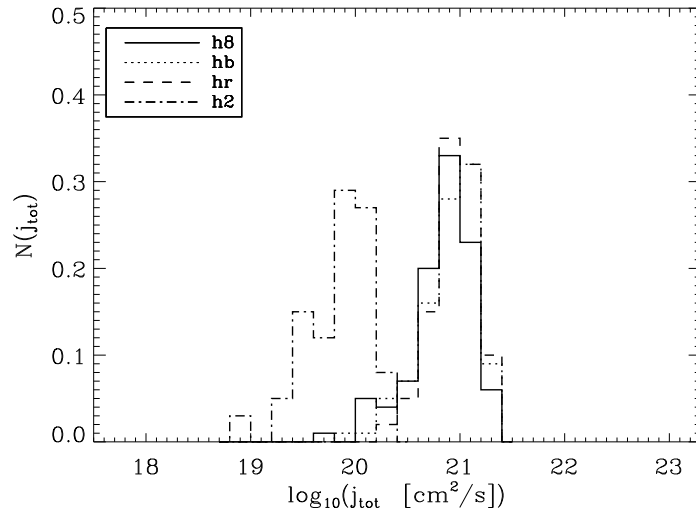


Figure 7.1: Calculated j_{tot} distributions of turbulent BESs. Each sample contains 100 equal cores, on which we apply random Gaussian velocity fields with the power spectrum $P(k) \propto k^{-4}$ and a mean absolute velocity of Mach1. Different random seed generators (sample hb,hr) or a population of the 8 largest modes (h8), instead of the 4 largest ones (hb,hr) does not influence the distribution significantly. However, j_{tot} is on average reduced by a factor 10, when the spatial scale of the largest mode corresponds to the radius (h2) rather than the diameter of the core.

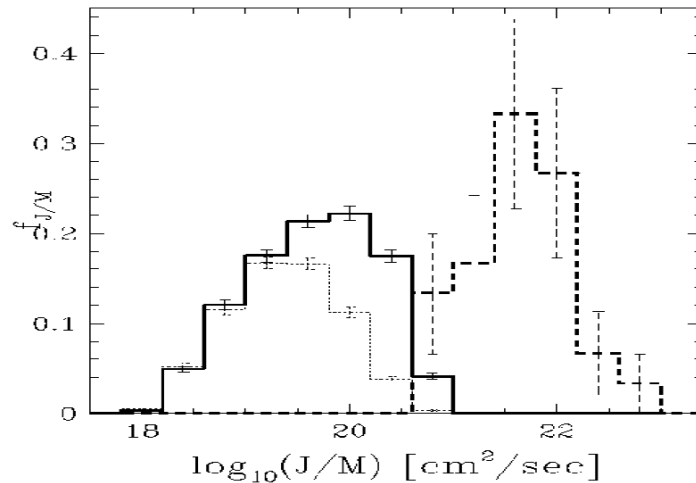


Figure 7.2: The observed specific angular momentum distribution of molecular cloud cores by Goodman et al. (1993) is shown as the dashed histogram. The initial binary-star population, depicting the result of prestellar core collapse and fragmentation, is plotted as the solid histogram. It evolves into the dot-dashed histogram after passing through a typical star cluster (Kroupa, 1995). Figure taken from Goodwin et al. (2006).

We only populate the largest modes of the system, allowing for the turbulent cascade to establish naturally over time. In Figure 7.1, we show four different distributions of initial core angular momenta, each resulting from a powerlaw spectral index $n = -4$ and a mean absolute value of Mach 1. For every shown distribution, we apply 100 different realisations of the turbulent velocity field to our standard core setup. The turbulent setups generated to produce the four distributions differ slightly in populated modes and/or random seed generator. In samples 'hb', 'hr' and 'h8' the largest mode corresponds to the diameter of the sphere. Distributions 'hb' and 'hr' only differ in the turbulent seeds employed for every individual setup. In both samples the initially populated modes are the four longest ones ($k = 1..4$), whereas modes $k = 1..8$ are populated in sample 'h8'. All of these distributions result in approximately the same mean specific angular momentum ($j_{\text{tot}} \approx 10^{21} \text{cm}^2 \text{s}^{-1}$). However, the mean value of sample 'h2' is about an order of magnitude lower, even though 'h2' resembles 'hr' or 'hb' in strength, power spectral index and turbulent seeds. The only difference is the population of wave numbers $k = 2..4$, starting from the second longest mode or the radius of the sphere. For comparison the distribution of specific angular momenta of molecular cloud cores observed by Goodman et al. (1993) is shown in Fig. 7.2. The initial binary-star population for late-type stars ($M_{\text{primary}} \leq 1M_{\odot}$) and the evolution of the binary-star population when passing through a typical star cluster are also included in Fig. 7.2. This figure was taken from Goodwin et al. (2006), who suggested that the distribution of J/M of molecular cloud cores forms a natural extension to the initial stellar binary population, possibly suggesting an evolutionary sequence. In 2001, Kroupa & Burkert inferred that the initial binary period distribution, which is correlated with the j_{tot} -distribution of the initial binary star population, is a result of core fragmentation. They performed N-body computations studying the influence of stellar-dynamical interactions in embedded star clusters.

It should be noted that the cores included in the sample of Goodman et al. (1993) are low-mass dense cores, but have different sizes and masses. Therefore the observed distribution of specific core angular momenta is broader than the distribution obtained by superimposing turbulent velocity fields on a single core realization. Moreover, the cores observed by Goodman et al. (1993) are typically somewhat larger than the core in our example, which could explain that the average j_{tot} is a factor of 10 smaller in our calculated samples. The maximal angular momentum in our sample could however only be increased by shifting to supersonic turbulence (Mach number $M > 1$).

On scales of 0.1pc, low-mass molecular cloud cores are observed to have net specific angular momenta of approximately $10^{21} \text{cm}^2 \text{s}^{-1}$. Thus, the idea that prestellar cores ought to be subject to turbulence on core diameter scales is suggestive. Provided that turbulence is indeed the only source of net angular momentum present, the typical core scale seems to be set by the turbulent dissipation scale or the scale corresponding to the transition from super- to subsonic turbulence, respectively. These results have to be tested in the framework of molecular cloud and core formation, which is left to future work.

Run	Sample	Ω_0 [s^{-1}]	J/M [cm^2s^{-1}]	β or γ	t_0 [kyr]	AV
0	-	$1.0 \cdot 10^{-14}$	$1.7 \cdot 10^{20}$	$7 \cdot 10^{-4}$	92.6	Balsara
T0a	h233	-	$1.0 \cdot 10^{20}$	0.39	160.7	Const
T0b	h881	-	$1.3 \cdot 10^{20}$	0.36	98.7	Const
T0c	hr5	-	$2.2 \cdot 10^{20}$	0.33	130.8	Const
T0d	hb6	-	$6.34 \cdot 10^{20}$	0.28	96.7	Const
1a	-	$6.0 \cdot 10^{-14}$	$1.03 \cdot 10^{21}$	0.025	91.0	Const
1b	-	$6.0 \cdot 10^{-14}$	$1.03 \cdot 10^{21}$	0.025	92.6	Balsara
1c	-	$6.0 \cdot 10^{-14}$	$1.03 \cdot 10^{21}$	0.025	90.6	Bals+Time
T1a	hb27	-	$1.0 \cdot 10^{21}$	0.41	145.8	Const
T1b	hb27	-	$1.0 \cdot 10^{21}$	0.41	151.7	Balsara
T1c	hb58	-	$1.0 \cdot 10^{21}$	0.284	109.5	Const
T1d	hb58	-	$1.0 \cdot 10^{21}$	0.284	110.3	Balsara
T1e	hr3	-	$1.0 \cdot 10^{21}$	0.393	137.7	Const
T1f	hr3	-	$1.0 \cdot 10^{21}$	0.393	135.9	Balsara
2	-	$8.0 \cdot 10^{-14}$	$1.37 \cdot 10^{21}$	0.045	92.6	Balsara
T2a	h81	-	$1.3 \cdot 10^{21}$	0.466	132.6	Const
T2b	h81	-	$1.3 \cdot 10^{21}$	0.466	137.9	Balsara
3	-	$1.0 \cdot 10^{-13}$	$1.71 \cdot 10^{21}$	0.071	94.5	Balsara
T3a	hb66	-	$1.7 \cdot 10^{21}$	0.327	126.1	Balsara
4	-	$1.5 \cdot 10^{-13}$	$2.57 \cdot 10^{21}$	0.159	96.5	Balsara
T4a	hr66	-	$2.59 \cdot 10^{21}$	0.63	152.3	Const
T4b	hr66	-	$2.59 \cdot 10^{21}$	0.63	159.5	Balsara
6	-	$1.6 \cdot 10^{-13}$	$2.74 \cdot 10^{21}$	0.181	100.5	Balsara
T6a	hb17	-	$2.72 \cdot 10^{21}$	0.483	99.07	Const
T6d	hb17	-	$2.72 \cdot 10^{21}$	0.483	112.3	Balsara
T6f	hb17	-	$2.72 \cdot 10^{21}$	0.483	99.07	Const+BigHmin
7	-	$1.8 \cdot 10^{-13}$	$3.00 \cdot 10^{21}$	0.229	116.6	Balsara

Table 7.1: We list the various initial rotational frequencies Ω_0 and resulting specific angular momenta $J/M = j_{\text{tot}}$. For the turbulent cores, we give the sample number of each core. For all rigidly rotating cores, β gives the ratio of rotational to gravitational energy according to Eq. 5.2, whereas for the turbulent cores we list γ , the ratio of turbulent to gravitational energy contained within the core. Furthermore, we calculated the time of central object formation t_0 . The last column contains information on the employed implementation of SPH artificial viscosity as discussed in section 3.3. With these setups, we roughly span the observed ranges of $10^{-4} < \beta < 1.4$ (Goodman et al., 1993; Caselli et al., 2002) or $\gamma < 0.5$ (Jijina et al., 1999), respectively. Run 5 is missing, as we did not calculate any turbulent setup with a corresponding angular momentum.

7.2 Core sample

Apart from a different velocity setup, the same density profile, temperature, cooling prescription and numerical resolution as in the previous chapters is employed. Several turbulent setups are picked from the four distributions shown in Fig. 7.1. Every selected turbulent core setup has a total angular momentum, which is comparable to a core in pure rigid rotation, which has already been discussed in detail in the former chapters. In case of rigid rotation, we found the most important disk properties to be a function of core angular momentum. All calculations are listed in Table 7.2. The structure is as follows: The same core number in the naming convention implies equal j_{tot} . In addition, runs where j_{tot} is based on a turbulent velocity field are marked with a 'T' in front of the core number. Runs with equal j_{tot} but different implementations of SPH artificial viscosity or more than one turbulent realization are distinguished by an additional letter 'a'-'f'. The sample from which we took the turbulent velocity field is listed in the second column of Table 7.2. The differences between the four named samples has been introduced in section 7.1. In case of rigid rotation, we list the rotational frequency Ω in column 3. j_{tot} for all cores is given in the fourth column. Furthermore, in case of rigid rotation, the standard definition of $\beta = \beta_{\text{const}}$, the ratio of rotational to gravitational energy, has been calculated according to

$$\beta_{\text{const}} = \frac{\Omega^2 R_{\text{core}}^3}{3GM_{\text{core}}}, \quad (7.2)$$

where R_{core} and M_{core} are outer radius and total core mass, respectively. G is the gravitational constant. In case of turbulence, we give γ , the ratio of turbulent kinetic energy to total gravitational energy within the prestellar core instead of β . We calculated γ from

$$\gamma \equiv \frac{E_{\text{turb}}}{E_{\text{grav}}} = \frac{\sum_{i=1}^{N_{\text{part}}} \frac{1}{2} m_i \vec{v}_{i,\text{turb}}^2}{\sum_{i=1}^{N_{\text{part}}} m_i \Phi_i}, \quad (7.3)$$

where Φ_i is the initial gravitational potential of particle i , $\vec{v}_{i,\text{turb}}$ is its turbulent velocity and m_i its mass. N_{part} is the number of particles within the sphere's outer radius.

Finally, we list the time of central object formation t_0 , which is defined to be the time of the first snapshot at which the gas density exceeds $\rho_{\star} = 10^{-11} \text{g cm}^{-3}$. The last column shows the specific SPH artificial viscosity (AV) implementation. We find the general trend, that it takes slightly longer for the core to reach t_0 when using the Balsara implementation as compared to the standard constant AV. However, we do not find any correlation of γ with t_0 or j_{tot} with t_0 in the turbulent cases, whereas t_0 is clearly correlated with Ω , β and j_{tot} in case of rigid rotation. In general, central object formation happens later in the turbulent cases. This results from the early braking of the radial symmetry of the core collapse in these cases.

Run 1b and Run 7 have been accurately studied in chapter 4. Unfortunately none of the turbulent cores has a total specific angular momentum as high as in Run 7. On the other hand, the evolution of the rigidly rotating core of Run 6 is very similar to Run 7. Therefore we will use Run 6 to study the core collapse in case of high angular momentum.

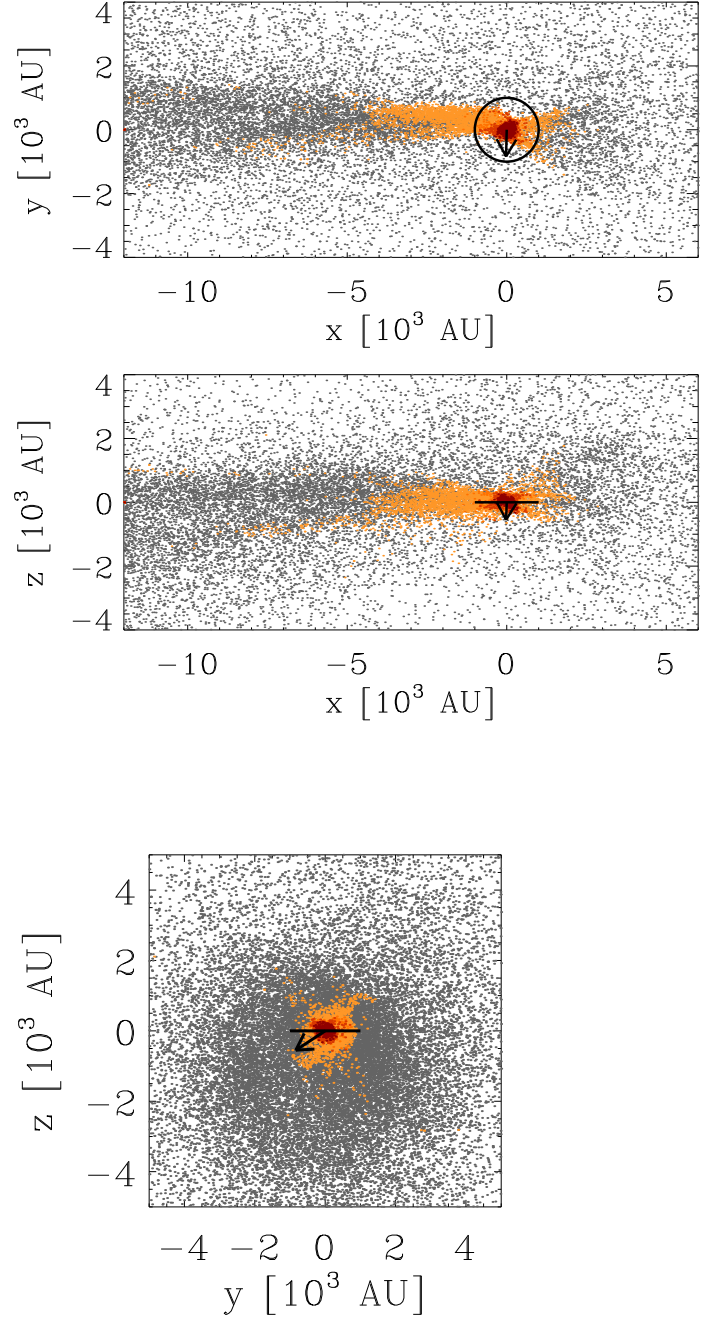
7.3 The global structure of turbulent core collapse: Warm filaments

In the following the evolution of three cores (Runs T1b, T1d, T1f) with equally low initial angular momentum $j_{\text{tot}} = 10^{21} \text{cm}^2 \text{s}^{-1}$, which is comparable to the rigidly rotating case with $\Omega = 6 \cdot 10^{-14} \text{s}^{-1}$ (Run 1), and one core with high initial angular momentum (Run T6d with $j_{\text{tot}} = 2.72 \cdot 10^{21} \text{cm}^2 \text{s}^{-1}$), which is comparable to $\Omega = 1.6 \cdot 10^{-13} \text{s}^{-1}$ (Run 6a) will be shown. We picked three different realizations of the same angular momentum in order to demonstrate the dependence on the turbulent velocity field - despite equal j_{tot} .

We start by comparing the global core structure of turbulent and rigidly rotating cores after they have collapsed to form one or more dense central objects. The collapse of a super-critical BES is initiated at the outer boundary of the sphere. In case of rigid core rotation, the BE hydrostatic equilibrium profile is soon changing towards a flattened core region surrounded by an $1/R^2$ -envelope, which is continuously growing in size. The collapse wave, which forms the edge of the flattened central region, accelerates towards the center and precedes the free-falling envelope material. In that stage the cooling time scale is very short compared to the local free-fall time ($\tau_{\text{cool}}/\tau_{\text{ff}} \ll 1$) and the gas behaves rather isothermal. On global scales the collapse initially proceeds in a spherically symmetric manner. Later on, centrifugal forces lead to a further collapse in cylindrical symmetry (see Fig. 7.7 for comparison). In a turbulent scenario, the collapse symmetry is broken early on during the simulation. Extended dense filaments are forming before the formation of a central object is possible. As a result, we do not find any correlation of the time of central object formation t_0 with the relative amount of turbulent energy γ or the total specific core angular momentum j_{tot} in the turbulent cases. In the following, the mass and dimensions of the forming filaments will be discussed.

As the dense central object is typically forming offset from the core center and the emerging protostellar disks are oriented in an initially unpredictable direction, the data has been shifted and transformed. First, the forming central object is shifted to the origin of the new coordinate system. Second, all particle coordinates have been transformed to the system of inertia of the dense central region at every time step. For this purpose we found the dense central region to be well represented by the M_{16} component which contains all SPH particles with $\rho > 10^{-16} \text{g cm}^{-3}$. For T1b-T1f as well as T6d, the resulting distributions of SPH particles in the face-on and the two edge-on projections are shown in Fig. 7.3 - 7.6. The particles are colour-coded according to their current temperature. Black: cold gas with $T < 20\text{K}$, Orange: $T > 20\text{K}$, Red: $T > 50\text{K}$. In all simulations most of the core gas belongs to a cold, low density component surrounding one filamentary structure which is forming within the core. We find the embedded filament to be somewhat warmer than the average core gas ($T > 20\text{K}$). In the following, gas with $T > 20\text{K}$ will be defined as *the filament*. The filament always has an elongated, prolate shape. It is well known, that the substructure within star-forming molecular clouds often appears to be filamentary (e.g. Narayanan et al., 2008). Dense prestellar cores are observed to be embedded within filaments, and themselves can have dynamically complicated shapes (Caselli et al., 2002). However, the resolution of recent observations is not good enough to resolve the internal structure of prestellar cores.

Figure 7.3: Face-on (top panel) and two edge-on projections of SPH particles for Run T1b (hb27+Balsara) after 168 kyrs. Different colours denote different temperature regimes: Grey: $T < 20\text{K}$; Orange: $T > 20\text{K}$; Red: $T > 50\text{K}$. The forming protostar has been shifted to the origin and the whole system has been transformed to the system of inertia of the M_{16} density component, which includes all SPH particles with $\rho > 10^{-16}\text{g cm}^{-3}$. In this coordinate system the disk is oriented along the long axis of the filament structure. The $[x, y]$ -plane shows the face-on projection of the small forming disk. The circle indicates 'face-on', whereas the two *edge-on* projections are indicated by the solid black line plotted in the $[x, z]$ and $[y, z]$ projections. Neither the length of the solid line nor the radius of the circle are correlated with the actual size of the disk, simply because the rotationally supported disk is too small to be visible here ($R_{\text{disk}} \approx 60\text{AU}$). The black vector depicts the direction of the total angular momentum of the M_{16} density component, and is normalised to $j_{\text{tot}, M_{16}} = 1.03\text{AU}^2/\text{s}$. As the total angular momentum vector does not point in the direction of any of the principal axis of inertia, the M_{16} component is precessing.



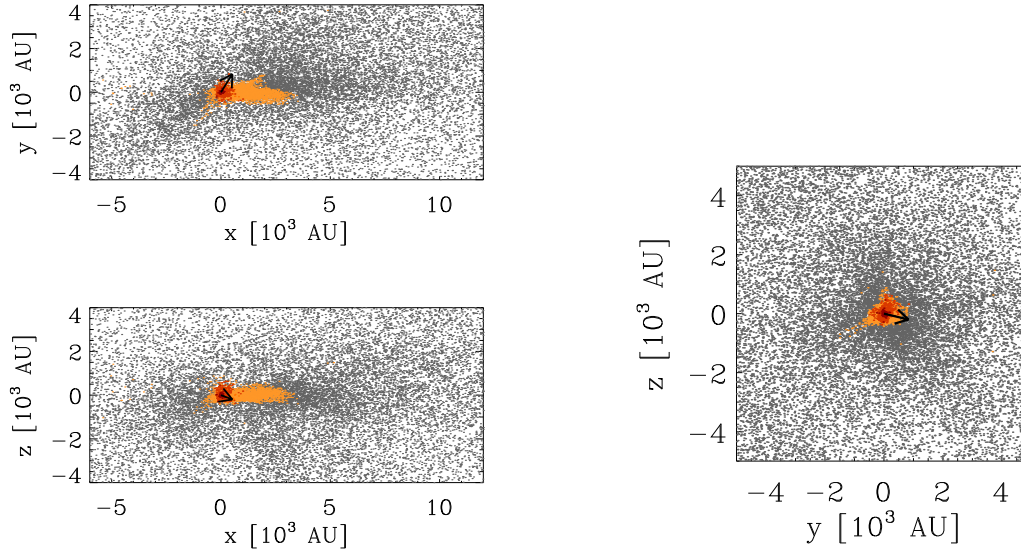


Figure 7.4: Face-on and two edge-on projections of SPH particles for Run T1d (hb58+Balsara) at the last snapshot of the simulation (120 kyrs). Colour-coding and projections are similar to Fig. 7.3. In this case, no disk but a rather spherically symmetric central object is forming. Therefore the black solid line indicating the disk plane is not shown. The angular momentum vector has been normalised to $j_{\text{tot},M_{16}} = 0.012\text{AU}^2/\text{s}$, which is much smaller than in Run T1b.

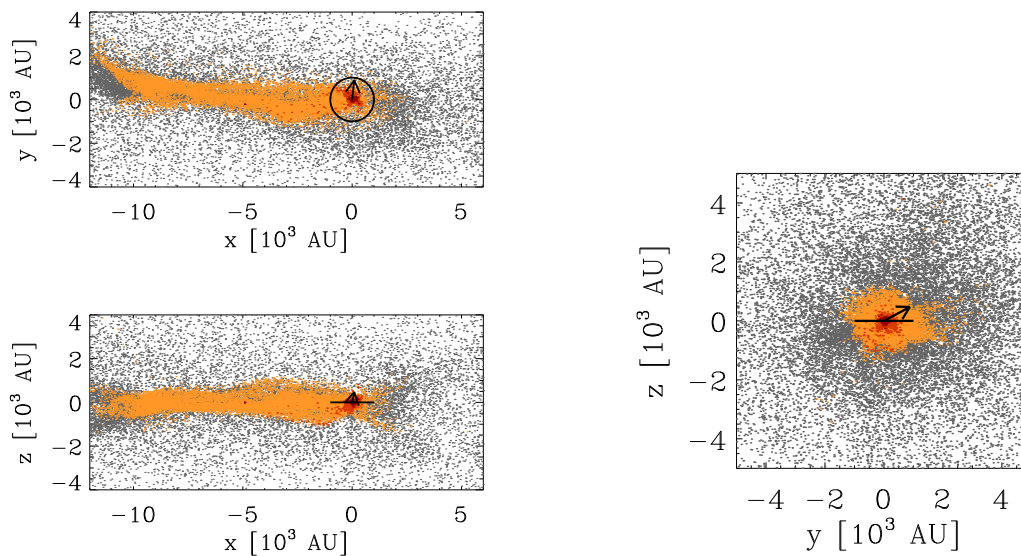


Figure 7.5: After 152 kyrs a small disk, which is again oriented along the filament has formed in Run T1f (hr3+Balsara). The total angular momentum here is $j_{\text{tot},M_{16}} = 0.21\text{AU}^2/\text{s}$.

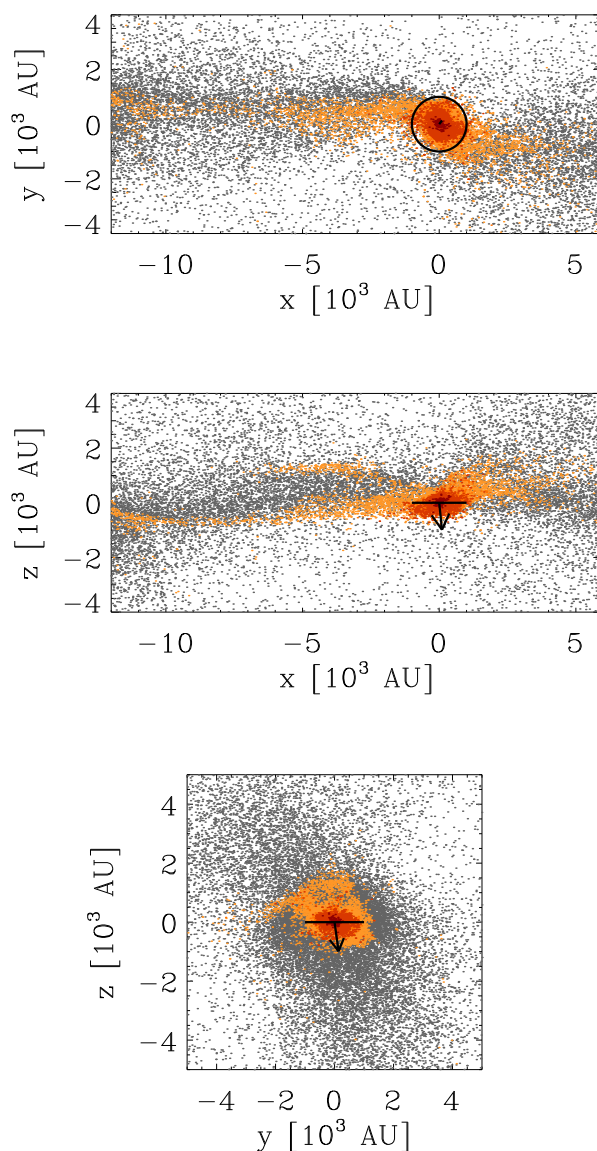


Figure 7.6: The largest of all disks is formed in Run T6d (hb17+Balsara). Shown is the last simulation snapshot at 138 kyr. The setup of T6d contains the highest initial core angular momentum of all setups in our four samples. This time the disk is very well defined by the M_{16} component and the angular momentum vector is almost perfectly aligned with the z -principal axis of inertia. Again, the disk is aligned along the filament. The angular momentum vector has been normalised to $j_{\text{tot},M_{16}} = 0.19\text{AU}^2/\text{s}$.

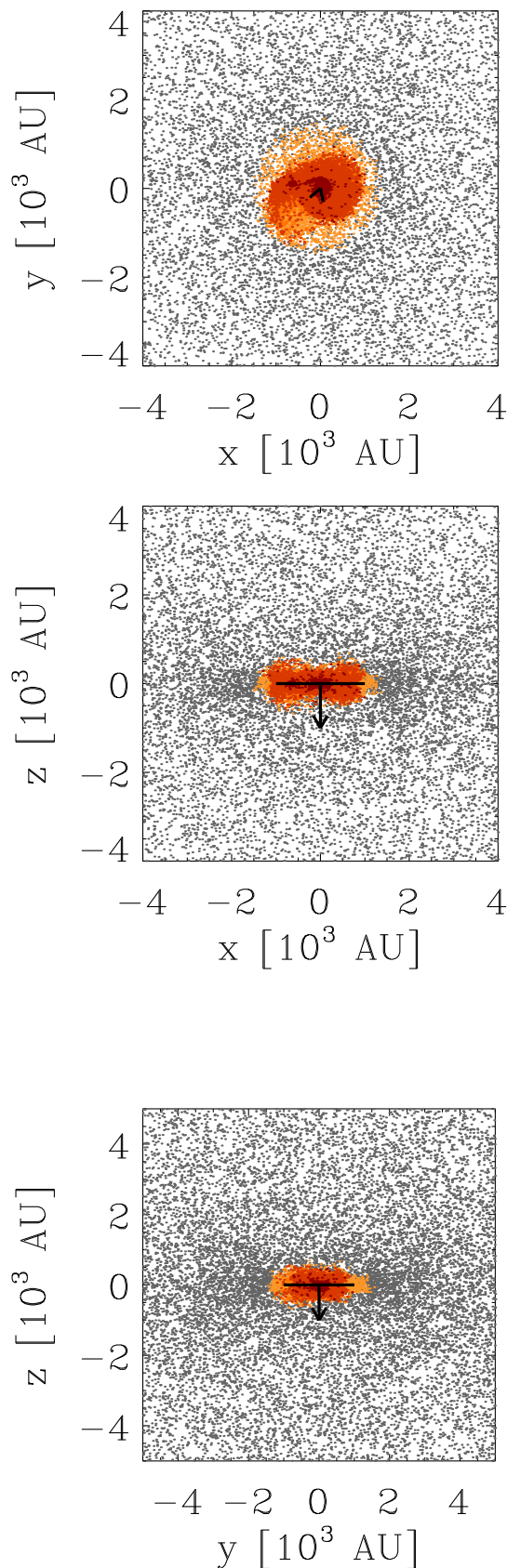


Figure 7.7: The global structure of rigidly rotating collapse Run 6d is shown for comparison. In this case no filament is forming. The collapse results in a well-defined disk, which is warmer than the rest of the core. The output shows the disk after 130kyrs, where a warmer spiral arm has already formed within the disk. Close to the central object the gas temperature locally exceeds 100K (dark red). The disk is not pressing and the angular momentum vector has been normalised to $j_{\text{tot},M_{16}} = 0.40\text{AU}^2/\text{s}$ in this case.

We also include the angular momentum vector of the M_{16} component for all projections, as well as the disk plane for both edge-on projections. Solely in T6d the angular momentum vector is aligned with one principal axis of inertia. For all other runs we do not find perfect alignment, which is a clear sign of precession of the M_{16} component. T6d is also the only run in which an extended protostellar disk is formed. The precession seen in T1b-T1f result from this component not being in centrifugal equilibrium. However, the deviation of the angular momentum vector from the principal axis of inertia is small.

In all simulations, the forming protostellar disks are roughly aligned with the long axis of the filament. This result can be tested against observations of young stellar objects. Under the assumption that a disk's orientation does not change dramatically once it has formed (i.e. if angular momentum is conserved), one can expect the protostellar objects formed in our simulations to launch jets and outflows which are oriented perpendicular to the filament. It is generally presumed that protostellar outflows, which are probably driven by torsional MHD waves propagating along magnetic field lines anchored in the circumstellar disk, are directed close to its rotation axis, along its angular momentum vector, and orthogonal to any attendant accretion disk, respectively (Pudritz & Norman, 1986). Anathpindika & Whitworth (2008) studied the orientation of observed outflows from young protostars relative to the filament within which they were born. These observed filaments are larger than the filamentary structure which is forming in the turbulent simulations. Regarding the way filamentary structure forms in a turbulent environment, it is however plausible that the filaments, which form within the cores are oriented along rather than perpendicular to the larger filaments surrounding the prestellar cores. Anathpindika & Whitworth (2008) found that about 72% of outflows were within 45° of being orthogonal to the filament in cases where the directions of the filaments and outflows were well defined. Even though circumstellar disks are not directly observable within the dense filaments, they concluded that most of the disks must be aligned along the filaments. In this framework, our results are in agreement with observations of embedded young stellar objects. Unfortunately, the launch of jets and outflows is not directly included in these simulations because the employed numerical method does not feature the prescription of magnetic fields. In addition, the required resolution of sub-AU scales is not included. As this problem is numerically very ambitious, it has not yet been addressed in any simulation of prestellar core collapse.

It has already been mentioned, that all protostellar objects in our simulations form offset from the original center of the Bonnor-Ebert sphere. The radial positions of all central objects are illustrated in Fig. 7.8 (red symbols, using spherical radius). The underlying blue-shaded contour plot shows the initial density profile of the prestellar core with a maximum, central density of $\rho_0 = 10^{-18} \text{g cm}^{-3}$. The outer radius of the sphere, which is cut off at the dimensionless radius $\zeta_{\text{max}} = 6.9$, is $R_{\text{BES}} = 17.2 \cdot 10^3 \text{AU}$. When studying the radial offset of the forming young stellar objects from the original center of mass of the parental prestellar core, we find a remarkable trend: As the parental core is set up to follow a Bonnor-Ebert density distribution, the core features a flat density profile within the inner few thousand AU and an outer envelope, where ρ falls off proportional to R^{-2} . In our case this transition is found at a radial distance of 5000AU-7000AU from the original core center. 45% of the central objects formed in our sample are located close to this transition region, which is shaded in grey in Fig. 7.9, where all radial

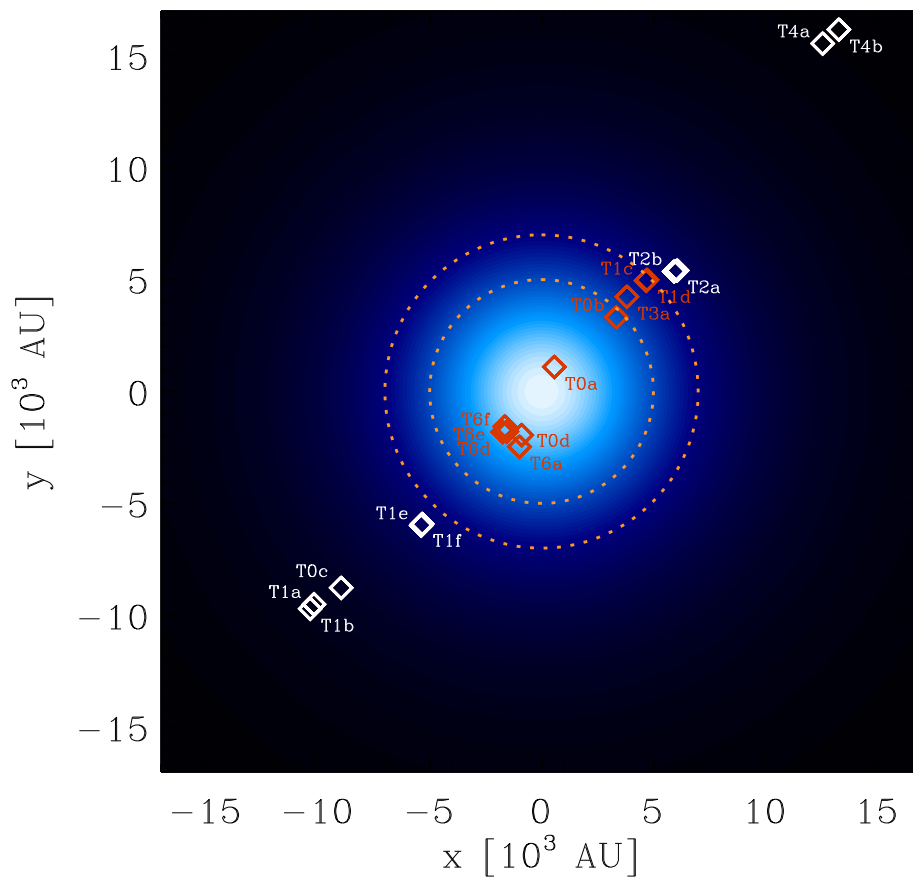


Figure 7.8: The blue-shaded contour plot shows the initial density profile of the simulated prestellar cores: A BES with $\rho_0 = 10^{-18} \text{g cm}^{-3}$, $T = 20\text{K}$ and $\zeta_{\text{max}} = 6.9$ or $R_{\text{BES}} = 17.2 \cdot 10^3 \text{AU}$, respectively. The density profile of this BES is flat out to a radius of 5000 - 7000AU, and falls of proportional to R^{-2} at larger radii. Red points show the radial position of each forming protostellar object.

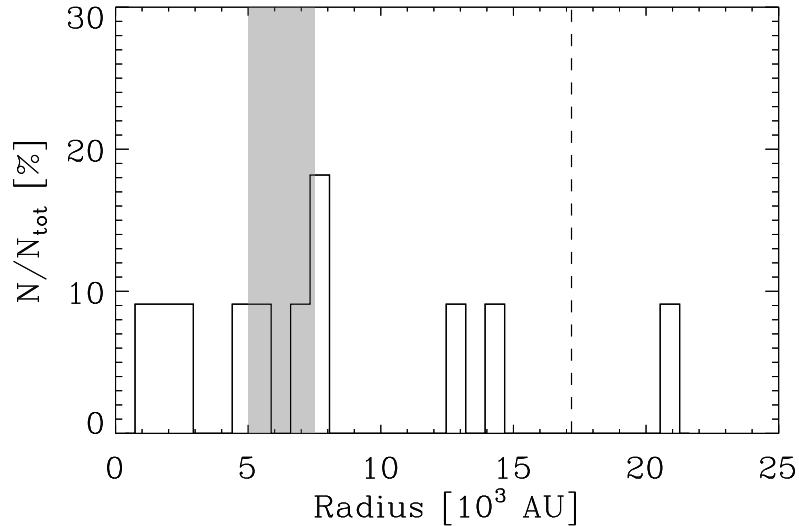


Figure 7.9: Histogram of the radial positions of all forming protostars. The radius at which the BE density profile undergoes the transition from flat central region to $\rho(R) \propto R^{-2}$ is shaded in grey. The outer radius of the sphere is marked by the dashed vertical line.

positions are summarised in a histogram. Furthermore, 27% of all central objects form at radii smaller than 6000 AU. 18% of these are setups which result in very low total core angular momenta. Equally many (27%) collapse at larger radii. One object even forms beyond R_{BES} , which is marked by the dashed vertical line. The origin of these radial offsets will be explained in the following.

In order to understand the generated offset, several aspects of turbulent collapse have to be considered. First, unlike the collapse of a singular isothermal sphere, or a core with a Plummer-like powerlaw density distribution, the collapse of a Bonnor-Ebert sphere is initiated at its outer boundary, rather than at the core center. The collapse is *outside-in*. This means that even without the disturbing influence of an additional velocity field, the dense central region would roughly stay in hydrostatic equilibrium, while the outer parts of the core are already collapsing towards the center. As the collapse wave is driven towards the core center, the effective pressure at the shrinking boundary of the unperturbed region within the collapse wave is increased. In order to retain hydrostatic equilibrium the pressure increase is compensated by an increase in the central density of the BES. In case of rigid core rotation (and before t_0) the radial collapse proceeds more or less unhindered because the rotational velocity is directly proportional to the cylindrical radius r . Thus, at small r or along the rotation axis, respectively, the kinetic energy added by rotation E_{kin} is small ($E_{\text{kin}} \propto \Omega r^2$). However, in case of turbulent core collapse the velocity field and consequently the kinetic energy does not simply depend on radius. Fig. 7.10 shows two cuts through the turbulent velocity fields of T1b and T1d in the plane defined by $z = 0$. The absolute value of the three-dimensional velocity field has been normalised to the isothermal sound speed of the setup $c_s = 0.29\text{km/s}$ (according to $T = 20\text{K}$). One clearly finds regions containing high

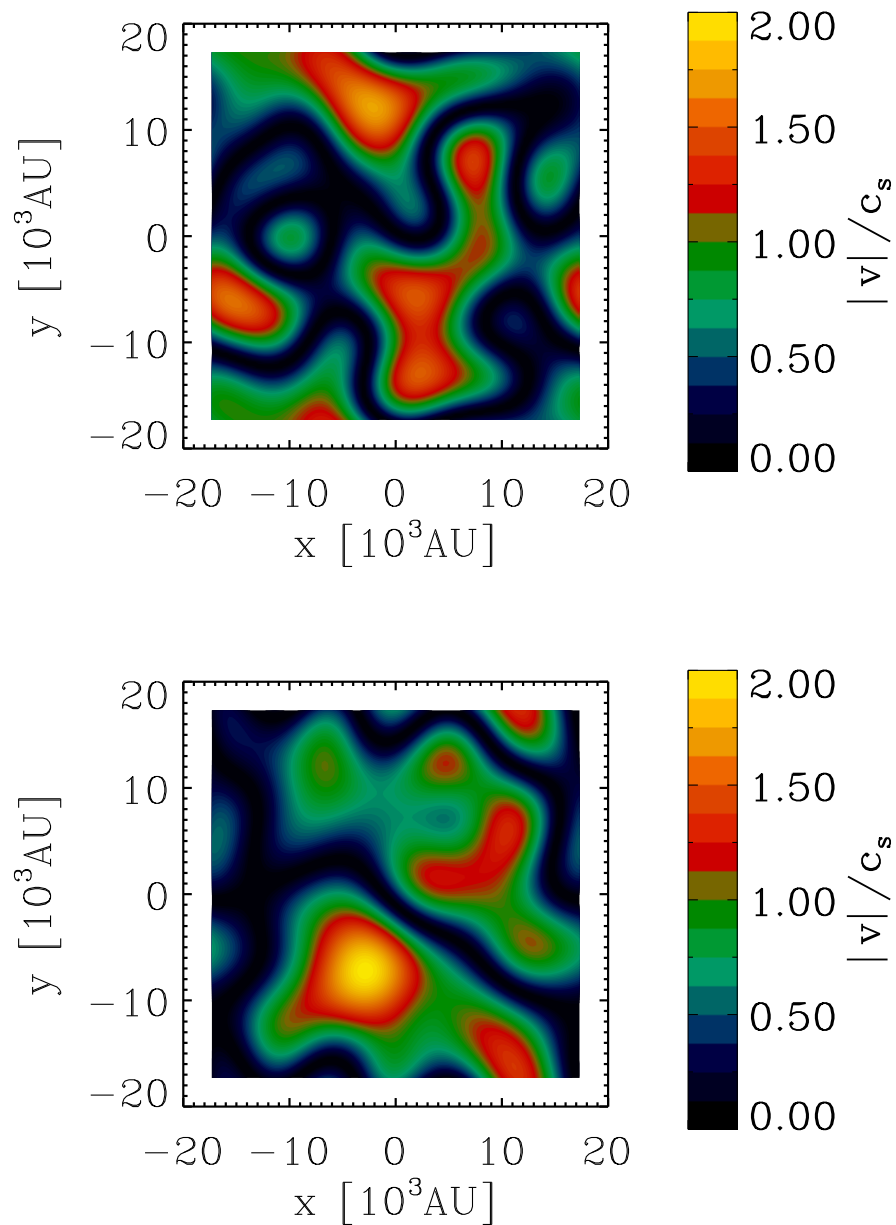


Figure 7.10: Cut through the 128^3 turbulent velocity cube at $z = 0$. *Top*: Setup for T1b. *Bottom*: Setup for T6d. Colour-coded is the absolute value of the three-dimensional velocity vector relative to the local soundspeed c_s of the system. c_s is initially constant and equal to 0.29 km/s within the core region. Within the hot ambient medium, which is not involved in the collapse, all velocities are set to zero.

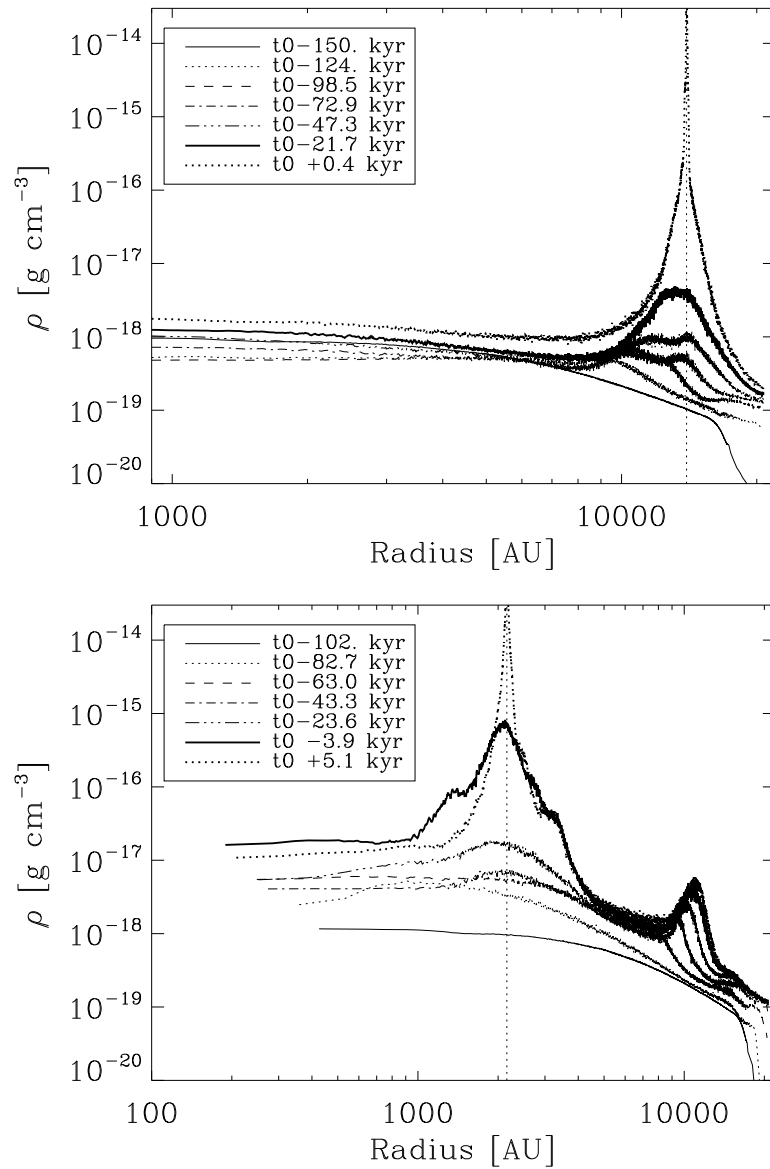


Figure 7.11: Density distribution of SPH particles plotted against spherical radius. The first time step reflects the initial setup. In this plot, the collapse has been followed until a dense protostellar object has formed at t_0 .

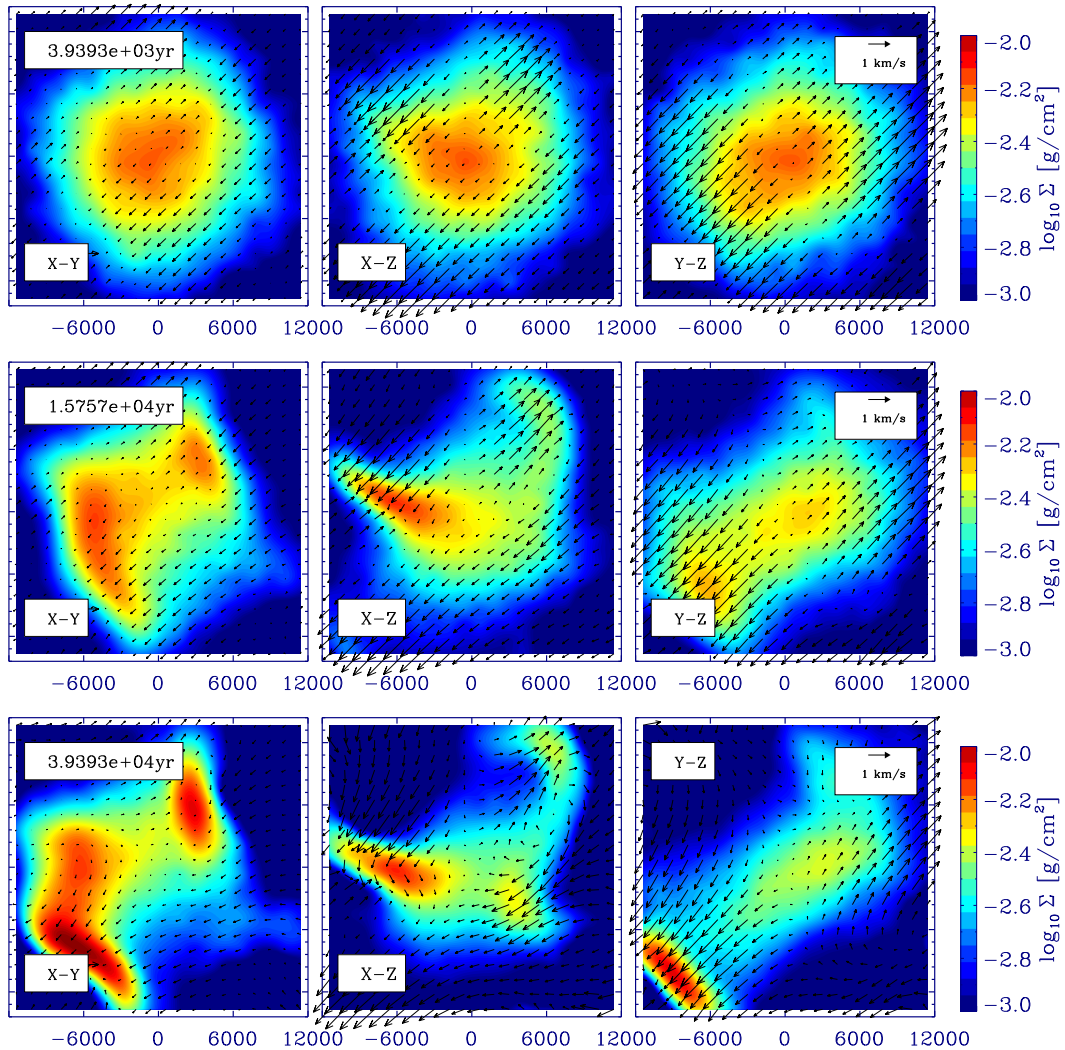


Figure 7.12: Shown is the evolution of surface density and velocities of T1b in the first few thousand years after the start of the simulation at $t = 0$ kyr. From top to bottom at every output time the three cuts show $[x, y]$ - (left), $[x, z]$ - (middle), and $[y, z]$ -plane (right) within a quadratic region of $[-12000 \text{ AU}, +12000 \text{ AU}]$. Every slice has a thickness of 1000 AU , resulting in a surface density. It should be noted that the actual boxsize is almost three times larger than the plotted region.

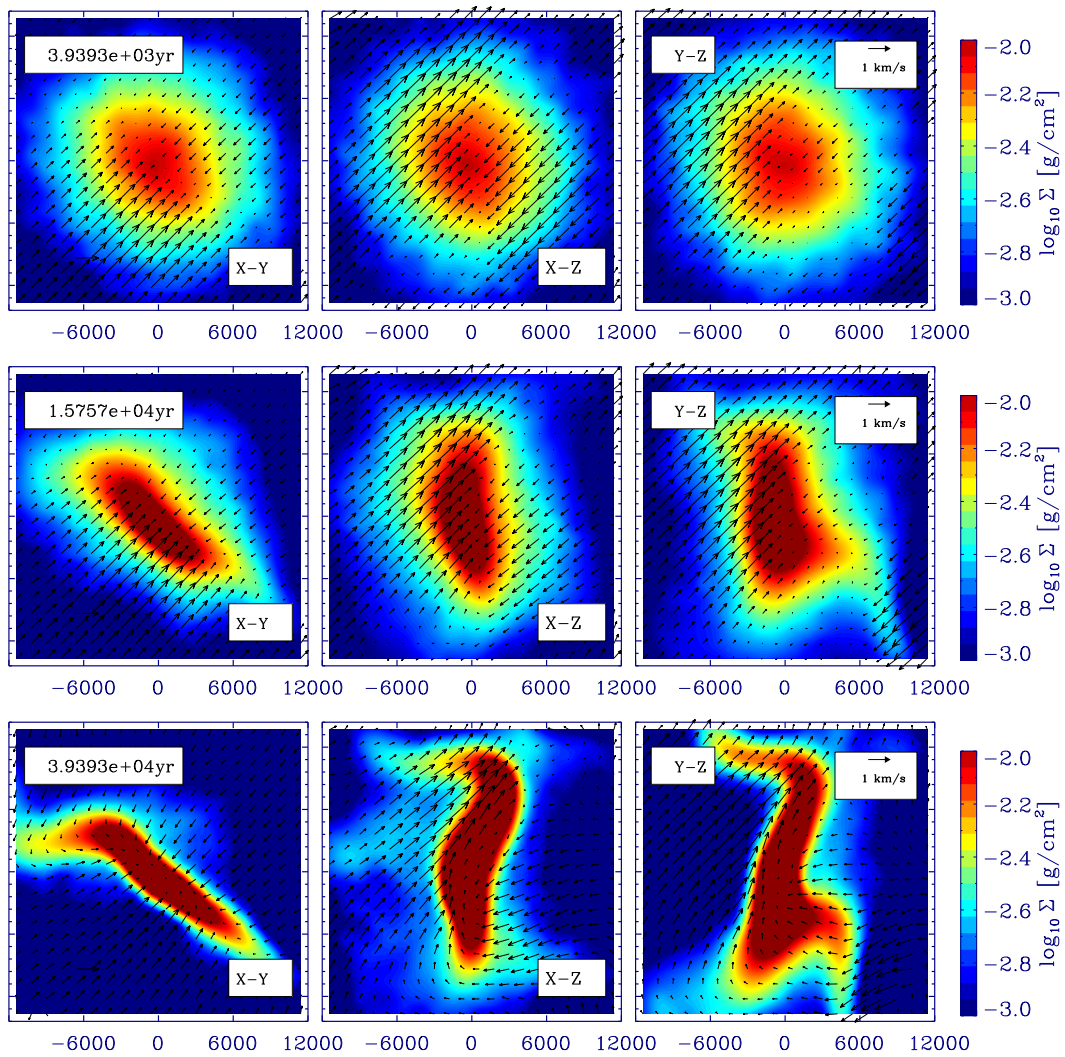


Figure 7.13: Early core evolution of Run T6d. The size of the plotted volume, the slice thickness and colour-coding as well as the output times are equal to Fig. 7.12. In T6d, the core seems to be compressed rather than torn apart in the $[x, y]$ -plane. Therefore a dense, elongated filament forms quickly.

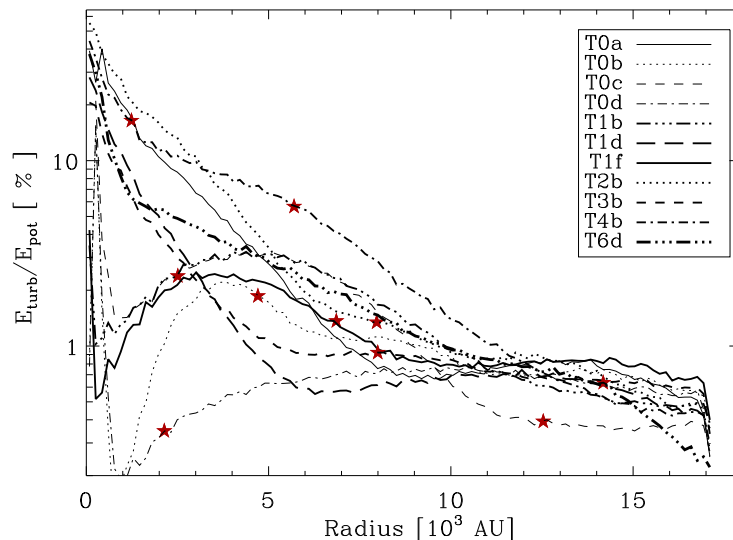


Figure 7.14: Ratio of turbulent kinetic to potential energy as a function of spherical radius for the initial conditions of 11 different collapse simulations. The positions of forming central objects are indicated by the red stars. Formed binaries are not resolved. More than half of the setups show a strong increase of $E_{\text{turb}}/E_{\text{pot}}$ with decreasing radius.

and low amounts of turbulent kinetic energy. Within islands of high kinetic energy, the local absolute velocities even exceed the local sound speed by up to a factor of two. As the velocity field has been setup to be anisotropic in all three spatial directions, regions with $|v| > \sqrt{3}c_s = 1.73c_s$ contain slightly supersonic velocities. The energy budget of all turbulent initial conditions is further explored in Fig. 7.14, which shows the ratio of turbulent kinetic energy to potential energy of the BES as a function of radius at $t = 0$. The relatively large amount of kinetic energy, which has been superimposed onto the inner core regions causes the center to expand in an irregular manner. Fig. 7.12 shows cuts through density and velocity field of Run T1b within the first few thousand years of evolution. The distributions have not been transformed to any system of inertia, but rather show the structure in the original coordinate system of the setup. The expansion is fast at radii where $E_{\text{turb}}/E_{\text{pot}}$ is high, which is the case around a radius of 5000AU in run T1b. Fig.7.12 also illustrates how a filamentary structure is typically forming in turbulent collapse simulations. The symmetry of the system is already broken by the turbulent initial conditions, which enforce the elongation of the prestellar core. Within the first few thousand years, the expansion results in a slight decrease of the central core density as seen in Fig. 7.11. The upper panel of Fig. 7.11 shows the density profile of Run T1b, whereas the profile of T6d is depicted in the lower panel for comparison. In T1b the collapsing outer core shells are halted and pushed together due to the turbulent energy stabilising the inner core region. In T6d the collapse is also altered, but the overall expansion of the central region is not as strong. In the $[x, y]$ -plane the core even appears to be compressed rather than torn apart (see Fig. 7.13). Therefore the prestellar core is directly forced into the filamentary shape. In this case, a protostellar object can form much

closer to the center of the original cloud. However, the outer parts of the cloud are also affected by turbulence and the formation of a second protostellar object is initiated at a radius of about 10^4 AU. The reason for the slight offset between the position of the central object which is noticeable when comparing Fig. 7.14 and Fig. 7.11 is the motion of the 'protostar' with respect to the core. However this relative velocity is very small (of the order of 0.1 km/s) - a velocity which is comparable to the relative motions of young stellar objects derived from SCUBA observations by Jørgensen et al. (e.g. 2007).

Fig. 7.15 shows the further evolution of the whole core. This time, the density and velocity field within a cube of volume $(12000\text{AU})^3$ is shown in three projections ($[x,y]$, $[x,z]$ and $[y,z]$). Whereas outflowing velocities completely dominate the dynamics of the core in the beginning of the simulation, the overall collapse takes over after about a free-fall time. The core, which has been violently shaped by turbulence is reformed to one collapsing dense filament. The last snapshot in Fig. 7.15 shows the core structure right after a dense prestellar object has formed within the high density region in the lower left corner of all projections. At this stage of the collapse gas is falling onto the filament from all sides. Whereas the velocities within the filament are relatively low. A protostellar object may therefore grow by direct gas infall onto it or by accretion of gas through the filament.

In summary, the interaction of gravity and turbulence causes the core to adopt a global filamentary shape. Then the collapse to a dense protostellar object is triggered **somewhere** along the filament, just at a place where the local Jeans mass is exceeded. In case of T1b the protostellar object is formed at the edge of the filament. However, the formation of a protostar is not always initiated at the edge of the filamentary structure as would be expected in case of the collapse of finite, self-gravitating, gaseous sheets with an elliptical outer boundary (Burkert & Hartmann, 2004). For instance in Run T6d, where we find the largest protostellar disk, the protostellar object forms well within the filament (see also Fig. 7.6).

7.4 Protostellar disk formation in turbulent core collapse

It has already been mentioned that all of the turbulent collapse simulations evolve differently and, in most cases, independently of the initial core angular momentum. Concerning the numerical calculations, the evolution time scale of the collapse is determined by the maximum density and the amount of mass accumulating at high densities ($\rho > \rho_*$). SPH particles sitting at high densities significantly slows down the calculation. In the following it will be shown that many of the turbulent cores quickly form central objects. Due to numerical limitations, it has hence not been possible to follow the collapse to a stage where about 28% of the total core mass has collapsed to densities higher than 10^{-16}g cm^{-3} in all simulations. Therefore the criterion, which has been used to constrain t_{final} in case of rigid rotation cannot be applied in the turbulent case.

In case of rigid rotation we found the mass of the central object (M_*) at t_{final} to be around $0.23M_\odot$ for all simulations except Run 0 and Run 1. In Run 1, where j_{tot} is low, $M_*(t_{\text{final}})$ is about twice as high ($M_* \approx 0.54M_\odot$). In Run 0 M_* is even higher. In all turbulent simulations, a mass of $M_* = 0.23M_\odot$ is reached (see Fig. 7.4). Even in Run T6d, where the central object grows slowly,

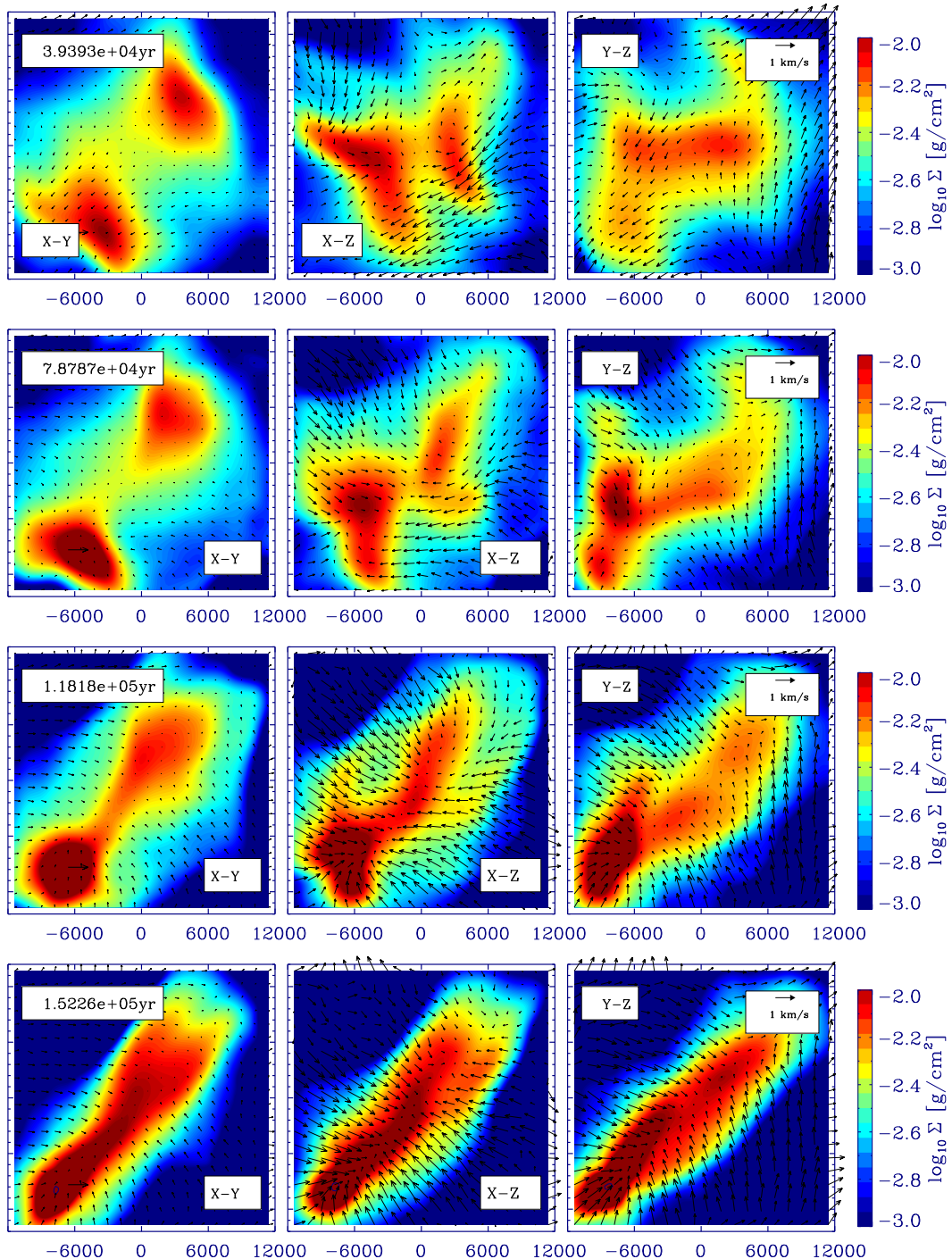


Figure 7.15: Further evolution of Run T1b. Here, we show three projections of a cube of volume $(12000\text{AU})^3$ around the original center of the core at every output timestep. Accordingly, the velocity arrows depict the mean projected velocities within the whole volume. The first three snapshots still show the core before a protostellar object has been formed. The last snapshot (lowest panel) shows the system at $t_0 + 0.6\text{kyrs}$, right after a protostellar object has just formed at $(-7911.\text{AU}, -8425.\text{AU}, -8216.\text{AU})$ from the center. In this case the protostellar object forms in the focal point of the collapsing filament.

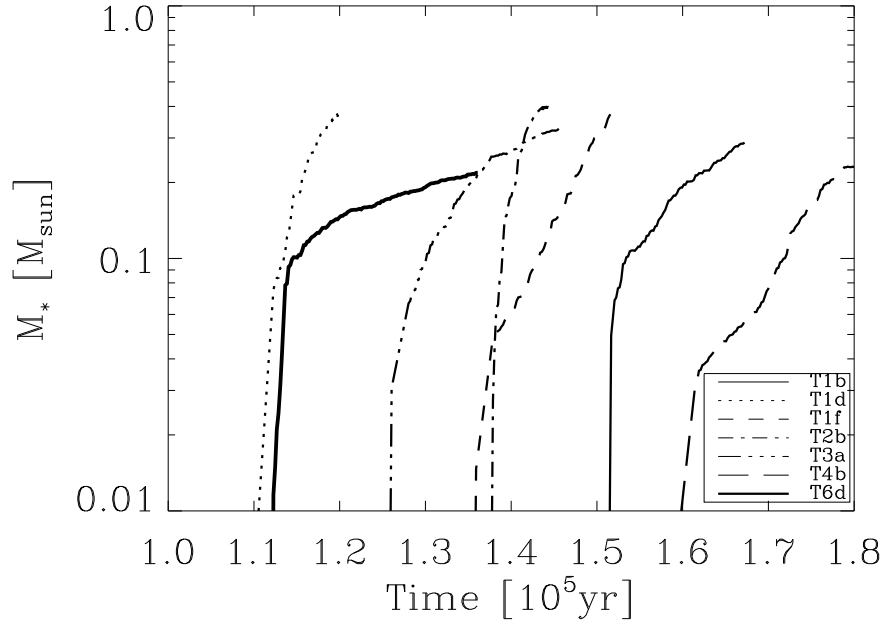


Figure 7.16: Mass of the forming central object as a function of time for all turbulent runs.

$M_* = 0.23M_\odot$ after 138.1 kys. This M_* is the maximal protostellar mass, which all turbulent simulations have in common. Thus, we define $t_{\text{fin,turb}}$ to be the time at which $M_* = 0.23M_\odot$ for the first time in a simulation. Though the masses of the forming protostellar objects are comparable in turbulent and rigidly rotating collapse simulations, the disks forming in the turbulent case are much smaller. Thus the disk component with $\rho > 10^{-16} \text{g cm}^{-3}$ is missing in most cases and M_{16} contains less mass than in the rigidly rotating case. For this reason, the 28% criterion applied to compare all rigidly rotating calculations cannot be used in the turbulent case, even though the simulations were evolved for a comparable time - with respect to physical and CPU time.

All turbulent simulations evolve individually, and a simple universal behaviour concerning protostellar disk formation cannot be identified. Therefore two approaches will be used to disentangle the dynamical evolution of turbulent core collapse. On the one hand, $t_{\text{fin,turb}}$ will be used to quantitatively compare the evolutionary stage of the collapsing gas as well as the protostellar disk formation stage. Though $t_{\text{fin,turb}}$ might be short after t_0 in rapidly collapsing setups, and later information is not taken into account in this case, $t_{\text{fin,turb}}$ represents a robust parameter for all simulations. On the other hand, many simulations ran for a much longer time than $t_{\text{fin,turb}}$. In order to include this information, some runs will be discussed qualitatively by analysing the evolution between t_0 and the time at which the simulation has been stopped (t_{stop}). We find that some systems evolve significantly between $t_{\text{fin,turb}}$ and t_{stop} , whereas others don't. Nevertheless, in all cases where a disk is formed from a turbulent setup, it is already visible at $t_{\text{fin,turb}}$ (see Fig. 7.18). In this respect the comparison of the simulations at $t_{\text{fin,turb}}$ can be justified.

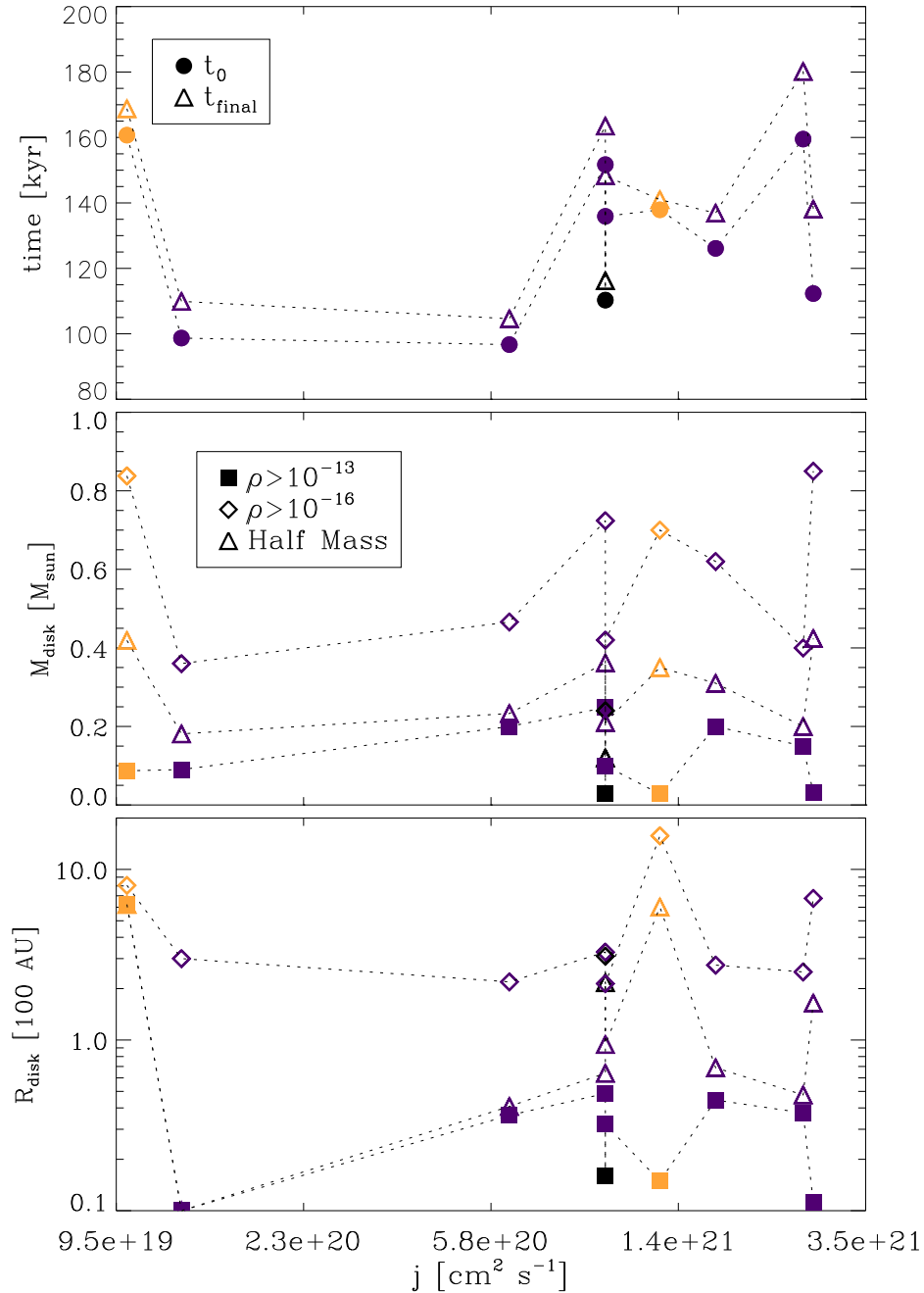


Figure 7.17: The most important properties like collapse time, collapsed mass and radial extent at $t_{\text{fin,turb}}$ are summarised for all turbulent simulations. Three different components have been studied: M_{13} , which contains all mass in SPH particles at densities $\rho_* > \rho > 10^{-13} \text{ g cm}^{-3}$, M_{16} with $\rho_* > \rho > 10^{-16} \text{ g cm}^{-3}$ and $M_{\text{half}} = 0.5M_{16}$. Concerning M_{half} , the corresponding radius R_{half} is especially interesting. Different colours of the plot symbols indicate the final outcome of each simulation. Yellow symbols stand for cores which form two prestellar objects, purple symbols indicate the formation of a protostellar disk and runs with black symbols neither fragment nor form a protostellar disk. The only run which is simply collapsing to a single protostellar object is T1d.

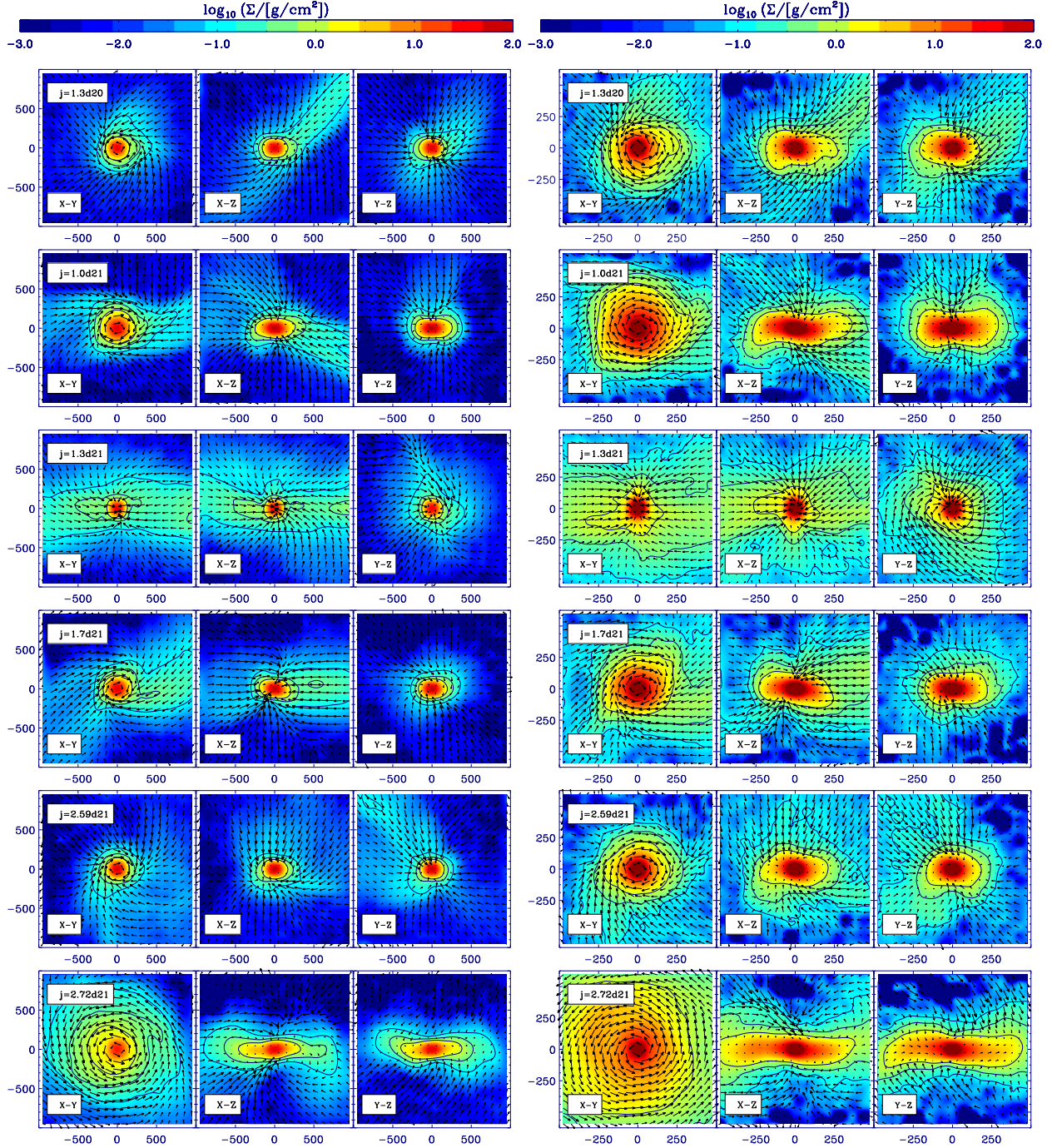


Figure 7.18: Evolutionary stage of turbulent cores at $t_{\text{fin,turb}}$. All panels on the right hand side show a region of $[-500\text{AU}; +500\text{AU}]$ around the forming protostellar object, whereas on the left hand side somewhat bigger regions ($[-1000\text{AU}; +1000\text{AU}]$) of the same simulations are plotted. The plot demonstrates that - if a disk is forming at all - it is already visible at $t_{\text{fin,turb}}$, even though at this stage only small parts of it are rotationally supported.

7.4.1 Quantitative Analysis

In Fig. 7.17 the most important properties like collapse time t_0 and $t_{\text{fin,turb}}$, collapsed mass and radial extent at $t_{\text{fin,turb}}$ are summarised for all turbulent simulations. Three different components have been studied: M_{13} , which contains all mass in SPH particles at densities $\rho_* \equiv 10^{-11} \text{g cm}^{-3} > \rho > 10^{-13} \text{g cm}^{-3}$, M_{16} with $\rho_* > \rho > 10^{-16} \text{g cm}^{-3}$ and $M_{\text{half}} = 0.5M_{16}$. Concerning M_{half} , the corresponding radius R_{half} is especially interesting. Different colours of the plot symbols indicate the final outcome of each simulation. Yellow symbols stand for cores which form two prestellar objects, purple symbols indicate the formation of a protostellar disk and runs with black symbols neither fragment nor form a protostellar disk. Disk formation is found in 82% of all cases, fragmentation in only 12% of all cases. A disk frequency of about 80% fits very well to observed values (e.g. in Chamelaen II, see Alcalá et al., 2008). The only run which is simply collapsing to a single protostellar object is T1d.

First of all, there is no correlation between the collapse time and the total amount of angular momentum contained in the prestellar cores. The central object has acquired a mass of $M_* = 0.23M_{\odot}$ after $t_0 + 5\text{kyrs}$ to $t_0 + 20\text{kyrs}$. The shortest time differences are found in the two cases where the core is fragmenting early on during the simulation, or directly collapsing to form one single protostellar object without a circumstellar disk. In all other cases, the formation of a protostellar disk is initiated and the central object grows somewhat slower. The largest time difference is found in Run T6d at $j_{\text{tot}} = 2.7 \cdot 10^{21} \text{cm}^2 \text{s}^{-1}$. This run, which contains the largest initial angular momentum also forms a large disk, which contains a significant amount of mass in the lowest density component. The fraction of gas accumulated in the M_{13} component is quite low in this case. For some disks half mass and M_{13} are approximately equal. In these cases the half mass radius R_{half} is also comparable to R_{13} and around 40AU - 60AU. The radius of the lowest density component R_{16} is always much larger than R_{13} and R_{half} . R_{16} is larger than 200AU and between 200AU-300AU in most cases. In case of fragmentation R_{16} cannot be attributed to one of the objects but rather surrounds both protostellar objects and therefore appears to be very large. For Run T0a with $j_{\text{tot}} = 10^{20} \text{cm}^2 \text{s}^{-1}$, the second fragment even affects all density components and R_{13} as well as R_{half} seem to be equally large. In summary, turbulence influences the prestellar core collapse in a nonlinear manner. Close to the core center the turbulent velocities are much higher than the rotational velocity in a rigidly rotating setup. Therefore the hydrostatic equilibrium close to the core center is impetuously disturbed before gravity takes over and the central regions collapse. As a result, Fig. 7.17 shows that the clear correlation of collapse time, disk mass and radius with the initial core angular momentum which has been found in case of rigid rotation is not at all present in turbulent collapse simulations. We will however discuss the mass evolution of the different components as well as mass infall rates and disk concentration as a function of time in the next section. This will be done in order to demonstrate that the results depicted in Fig. 7.17 are not biased by the choice of $t_{\text{fin,turb}}$.

Evolution of the collapsed mass

Fig. 7.19 illustrates the mass evolution in three different density components (M_{13} in black, M_{16} in pink and M_{filament} in blue) as well as the mass infall rates onto M_{13} and M_{16} . M_{filament} repre-

sents the mass of the warm filament forming within the core and contains all the mass in gas with $T > 20\text{K}$. An increasing amount of gas is accumulated from M_{filament} to M_{13} , or from the bottom to the top panel on the left hand side of Fig. 7.19, respectively. At the end of each simulation, at t_{stop} , each filament typically contains between $1M_{\odot}$ and $1.8M_{\odot}$. Only a fraction of the filament (between 20% and 50%) has a density of $\rho > 10^{-16}\text{g cm}^{-3}$, and just a small amount of mass assembles within the adiabatic density component: M_{13} only contains between 0.04 and $0.4M_{\odot}$. In general M_{13} is low if M_{16} is also low and the other way round. The evolution of the filament mass also seems to be correlated with the evolution of M_{16} . In some cases all components emerge at approximately the same time (e.g. in Run T1d between 105 and 110 kyr, where a dense central object is forming rapidly). In general this is however not the case. Lower density components typically grow first. In summary, the growth of the different density components is not correlated with the presence or size of a protostellar disk but is rather dependent on the turbulent gas infall onto and accretion through the filament. In the right column of Fig. 7.19, the gas infall rates onto the M_{16} and the M_{13} density component are depicted. No significant difference in \dot{M}_{infall} can be found between different runs. Only in Run T1d and T2b, where protostellar objects are rapidly formed - either through core fragmentation like in T2b or via direct gravitational collapse as in T1d - the infall rates are strongly increasing towards t_{stop} . On average, \dot{M}_{infall} onto M_{13} is between $4 \cdot 10^{-5}M_{\odot}/\text{yr}$ for T6d and $10^{-4}M_{\odot}/\text{yr}$ for e.g. T1b. The mass accretion rate after t_0 is not explicitly shown as it is roughly constant, though it has a large scatter. The mean mass accretion rate onto any forming protostellar object is $2 \cdot 10^{-5}M_{\odot}/\text{yr}$. In case of direct gravitational collapse (T1d) the average rate is a factor of two higher and equal to $4 \cdot 10^{-5}M_{\odot}/\text{yr}$. Therefore \dot{M}_{infall} is a factor of 2-5 higher than the average mass accretion rate onto the central object. A similar result was found when studying the collapse of rigidly rotating cores. Furthermore, as compared to $\dot{M}_{\text{infall}}(M_{13})$, the infall rate onto the M_{16} component (lower right panel) is on average lower, which means that the M_{16} component itself is collapsing, thus increasing the apparent infall onto the M_{13} component.

To complete the picture of turbulent core collapse, Fig. 7.4.1 illustrates the concentration parameter c , which has already been defined in the previous chapters (see section 5.2, Eq. 5.5). c relates the mass in gas at high densities to the mass accumulated at low densities (M_{13}/M_{16}). In case of rigid rotation, we found high disk concentrations in case of low core angular momentum, with a maximum of $c \approx 0.8$. High concentrations of up to 0.8 are not found in any of the turbulent simulations. In case of rigid rotation, c was continuously decreasing with increasing core angular momentum and reached a value of only 0.1 for extended and fragmenting disks. In the turbulent case the well-defined, large disk found in T6d also has low concentration of $c \approx 0.1$. However in T1d, where no disk is formed c also stays below 0.1. In T1d the collapse happens so quickly that no adiabatic disk component is established. All the gas is immediately used to contribute to the forming protostellar object. On the other hand, in the turbulent case, c is biased by the filament, which contains a significant amount of gas with $\rho > 10^{-16}\text{g cm}^{-3}$. This gas does not belong to the protostellar disk. In a nutshell, due to the unstructured way the gas is collapsing, islands of low angular momentum which are big enough to allow for the formation of a very concentrated disk are not present. As we do not find any simulation where c evolves to values as high as 0.8, one can conclude that concentrated disks do not form via compression of extended, poorly

concentrated disks. This is reasonable as the subsequent formation of a highly concentrated disk would require the viscous time scale for the redistribution of angular momentum to be shorter than the collapse time scale, which determines the time scale on which the M_{16} component is replenished. This is not the case in common disk theory.

Disks of low concentration have been found to be on average colder than concentrated disks formed in case of rigid rotation. In the following section, the radial density, temperature and azimuthal velocity profiles will be discussed for four examples. It will be shown, that the temperature profiles are rather similar to the ones which have been found for extended, low concentration disks in the previous chapters (see e.g. section 4.3, Fig. 4.12).

Radial Density, Temperature and Velocity Profiles

In order to compare the dynamics and structure of the collapsing objects in greater detail, we compare the evolution of the radial density (Fig.7.21), temperature (Fig.7.23) and azimuthal velocity profiles (Fig.7.22) shortly before and after t_0 . Again, we show three realizations (T1b, T1d, T1f) of the turbulent version of the low angular momentum run (Run 1), together with T6d, a core with high total specific angular momentum. Like before, we take the average of the density of all SPH particles found within a certain spherical radius.

Radial Density Profile:

The three cases with low core angular momentum lead to very different results, which are also different compared to the rigidly rotating case. In Run T1b a nice rotating disk is forming around a single central object. At the latest output time, the density profile in the inner disk region (about 10AU - 70AU) resembles a shallow powerlaw structure ($\rho(R) \propto R^{-1.3}$), which is much flatter than in case of rigid rotation where $\rho(R) \propto R^{-2.5}$ within all of the disk region. On the other hand, $\rho(R)$ is very steep in the outer disk region ($\rho(R) \propto R^{-4}$). The change within the density structure during the disk formation stage is a clear sign for accretion and the redistribution of angular momentum, which will be discussed later on (see section 7.5). At radii larger than ≈ 300 AU, $\rho(R)$ stays roughly constant at a value of $\rho_{\text{filament}} \approx 7 \cdot 10^{-17} \text{ g cm}^{-3}$, instead of falling off proportional to R^{-2} , the typical powerlaw expected within the outer regions of a spherically symmetric, collapsing Bonnor-Ebert sphere (see Run 1b). This flattened structure can be attributed to the extended filament that formed in Run T1b.

In Run T1d the evolving density structure is essentially different from Run T1b. Throughout the inner 100 - 200 AU $\rho(R) \propto R^{-3}$, followed by a flattened density region at $R > 200$ AU. This time, the average density within the outer region is somewhat higher than in Run T1b ($\rho_{\text{filament}} \approx 10^{-16} \text{ g cm}^{-3}$), and slightly decreasing with radius. The decrease is caused by the asymmetric position of the filament relative to the central object. In this case the central object does not form within, but rather at the edge of the dense filament. Furthermore, we do not find any signs of ordered rotation or flattening within the inner few tens of AU around the central object. Instead of a disk, a rotating, rather spherically symmetric region is surrounding the central object.

A similar density profile is developing in Run T1f, where the gas distribution surrounding the central object is almost spherically symmetric right after t_0 . In T1f, $\rho(R)$ is constantly chang-

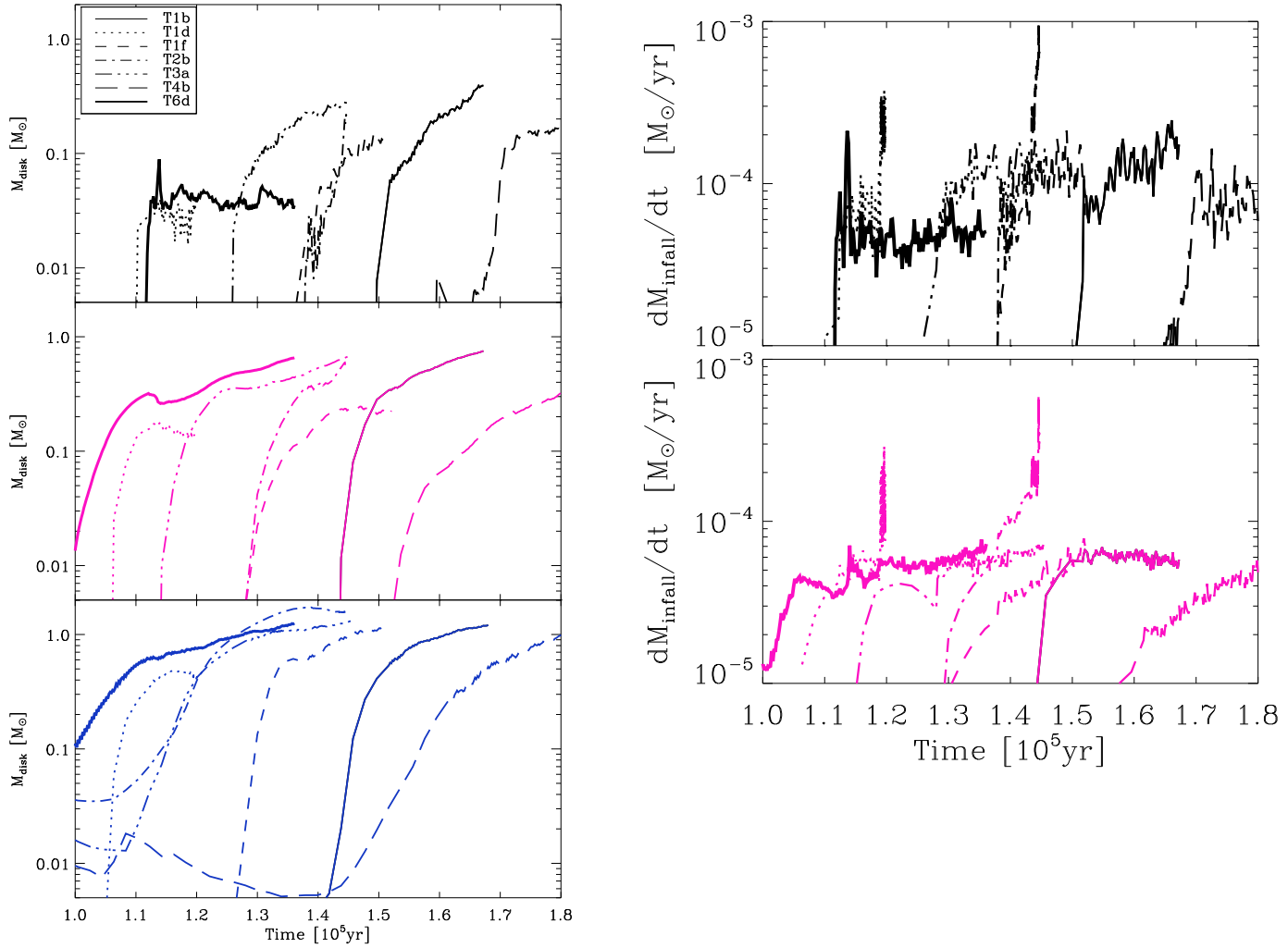


Figure 7.19: *Left column:* Mass evolution of different density components. The top panel shows the dense, adiabatic part (M_{13} in black), the middle panel illustrates M_{16} (in pink) and the bottom panel shows the mass contained within the filament with $T > 20K$, M_{filament} in blue. The filament typically grows before a dense protostellar object is formed. *Right column:* Infall rate onto the M_{13} (upper panel in black) and the M_{16} component (lower panel in pink).

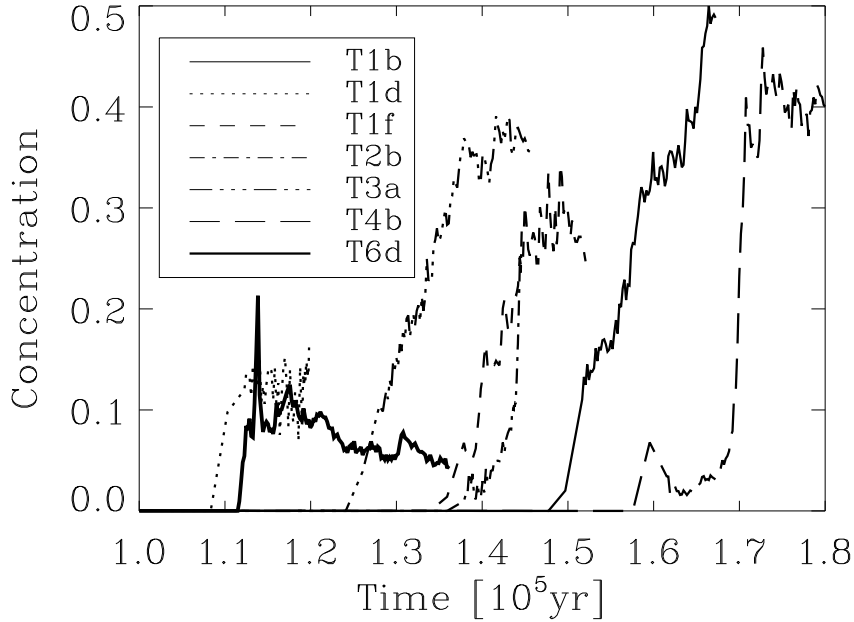


Figure 7.20: Concentration as a function of time for all turbulent runs.

ing, until a very small ($R < 20\text{-}25\text{AU}$), flattened and hence disk-like feature is forming at $t > t_0 + 15\text{kyr}$. At intermediate radii ($25\text{AU} < R < 200\text{AU}$) the small disk is surrounded by a spheroidal 'disk envelope'. At even larger radii, we again see a flattening of $\rho(R)$ at a constant value of $\rho_{\text{filament}} \approx 7 \cdot 10^{-17} \text{g cm}^{-3}$. Here, the filament is again a little less dense than in Run T1d. The central object also does not form exactly in the middle of the elongated filament, but is offset from the filament's center as well as from the center of the parental cloud core. In the turbulent cases, the disk components reside at very high densities ($\rho > 10^{-13} \text{g cm}^{-3}$). The gas at densities as low as $10^{-16} \text{g cm}^{-3}$, which could be clearly attributed to a rotating disk in case of rigid rotation, is now building up the filaments, within which central object and protostellar disk are forming. Therefore, we will have to extend our disk definition criterion for all turbulent cases.

Like in rigid rotation, the largest of all protostellar disks formed from turbulent cores is found in the simulation which features the highest amount of initial core angular momentum: Run T6, with $j_{\text{tot}} = 2.72 \cdot 10^{21} \text{cm}^2 \text{s}^{-1}$. The radial density profile of Run T6d exhibits clear signs of a relatively large ($R < 700\text{-}800\text{AU}$) disk-like structure surrounding the dense central object. The density profile of the disk region can be well fitted by two powerlaws. Within the central disk ($20\text{AU} < R < 80\text{AU}$) $\rho(R)$ follows a flat powerlaw of R^{-1} , whereas within the outer disk ($90\text{AU} < R < 700\text{-}800\text{AU}$) the density powerlaw is a little steeper ($\rho(R) \propto R^{-2.1}$). Interestingly, these results are consistent with the disk structure found in case of fast rigid rotation (Run 7), which has been discussed in chapter 4. Also the typical filamentary large scale structure is less pronounced in this case and $\rho(R)$ is continuously decreasing with increasing radius (up to a few 1000AU), approximately proportional to R^{-3} .

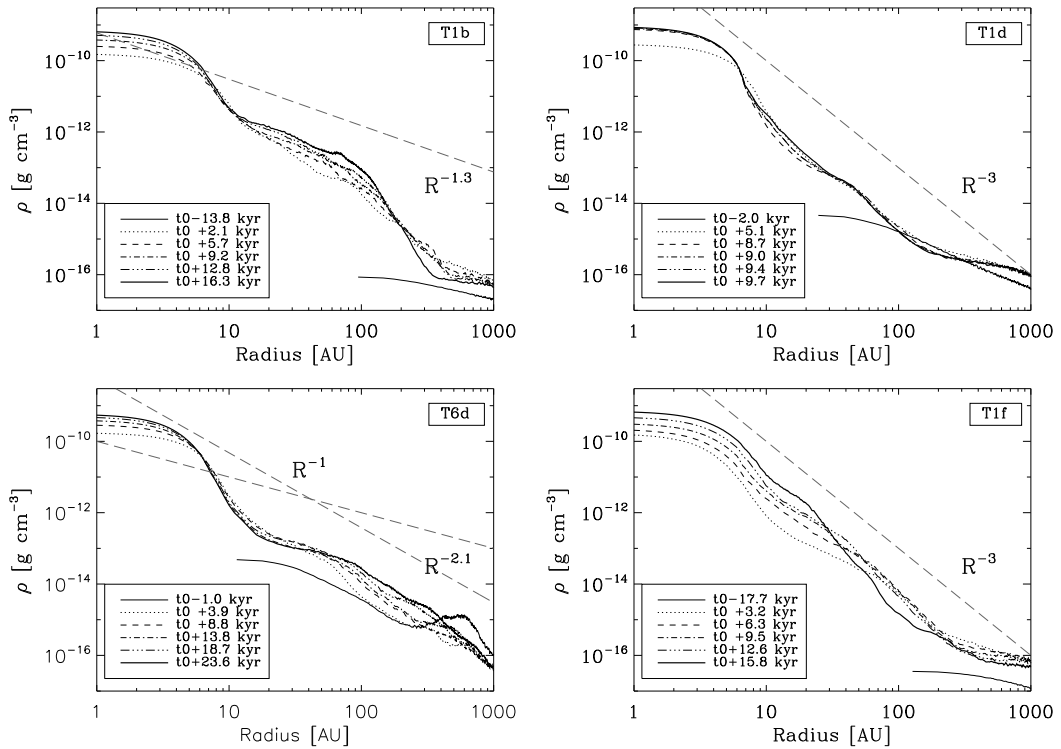


Figure 7.21: Radial density profiles at different times before and after t_0 until t_{stop} . At every output time the density was spherically averaged over 100 SPH particles. Moreover the coordinate system has been centered onto the position of the forming protostellar object. In T1b (upper left panel) and T6d (lower left panel) a protostellar disk is forming. Within the disk regions, the resulting density profile follows a powerlaw more shallow than -2.1 . In Run T1d (upper right panel) and T1f (lower right panel) the density profile is equally steep ($\rho(R) \propto R^{-3}$). No disk is forming in T1d. In T1f, $\rho(R)$ is even steeper between 20AU and 150AU. Instead, a very small disk (20AU) starts to form in the last timestep.

The evolution of the azimuthal velocity profiles as a function of radius:

Fig. 7.22 shows the azimuthal velocity component as a function of cylindrical radius ($v_\Phi(r)$) and the ratio of azimuthal velocity component to local sound speed or velocity dispersion ($v_\Phi(r)/c_s(r)$), respectively. For all simulations, we find the center (inner 5AU) to be increasingly supported by pressure rather than rotation. Thus, the structure of the central object appears to be similar in all simulations. However, when taking a closer look one finds that the absolute value of v_Φ as well as v_Φ/c_s at $r < 5\text{AU}$ is somewhat higher in T1b and T6b than in T1d or T1f. In both, Run T1b and T6b, we found the formation of a protostellar disk, whereas no disk was found in T1d, and a very small one was found in T1f, respectively. This is in agreement with disk forming calculations from the rigidly rotating sample, where the absolute value of v_Φ is higher by roughly a factor of 2 within the inner 5AU as compared to T1d. By looking at the distribution of SPH particles building up the central object we find a disk-like structure in all simulations with rigid rotation as well as in Run T1b, T1f and T6b: In short, all simulations which develop a circumstellar disk, also have a central object which has the shape of a *nuclear disk*. On the other hand, the central object in T1d, the only run of these four where no circumstellar disk was formed, is spherical. At larger radii, v_Φ/c_s shows clear signs of rotational support within the disk region within $5\text{AU} < r < 150\text{AU}$ for T1b, $5\text{AU} < r < 25\text{AU}$ for T1f and $5\text{AU} < r < 700\text{AU}$ for T6b. In T1f, the rotational support is only developed within the last few time steps. In Run T1d, $v_\Phi(r > 5\text{AU})$ is well approximated by a single powerlaw $v_\Phi \propto R^{-2}$. Therefore, at a radial distance of more than a few hundred AU from the central object, the azimuthal velocity is larger in T1d than in all other cases. The variety of azimuthal velocity profiles demonstrates the influence of the random turbulent velocity field, due to which the prestellar core is restructured immediately after the simulation has been started.

The radial temperature profiles:

The radial temperature profiles of the four discussed turbulent runs are depicted in Fig. 7.23. Within all formed disk regions $T(R) \propto R^{-0.7}$, similar to the disks formed from rigidly rotating cores. However, the temperature profiles are a little bit flatter in case of rigid rotation ($T(R) \propto R^{-0.6}$ for Run 1b and $T(R) \propto R^{-0.5}$ for Run 7). We find the hottest temperatures in Run T1d, where the collapse results in rather spherical central region (as discussed above). It should also be noted, that the temperature profile of T1d stays roughly constant after t_0 . At $t_0 + 10\text{kyr}$, the protostellar object has a mass of $0.4M_\odot$. The collapse proceeds fast, and thus the adiabatic central region is efficiently heated by shocks. Compared to T1f, where the protostellar object is about equally heavy in the last snapshot, the protostellar object grows much faster in T1d. Therefore the central regions are less heated in T1f as compared to T1d. On the other hand, the temperature also falls off rapidly in T1d such that at a radius of about 100AU, $T(R)$ is approximately equal in all runs. At 100AU the temperature is between 100K and 150K in all simulations. The lowest temperatures are seen in T6b, where we also find the largest protostellar disk. Again, this behaviour is similar to what we found in case of rigid rotation, where the temperature was significantly lower within the large disk formed in Run 7, as compared to the small, hundred AU disk formed in Run 1b. Overall the disk temperature profiles found in the turbulent collapse simulations are similar to the ones found in simulations including rigid rotation. Only one detail is missing. Except for T1b, where a well-defined small disk is found, the local temperature

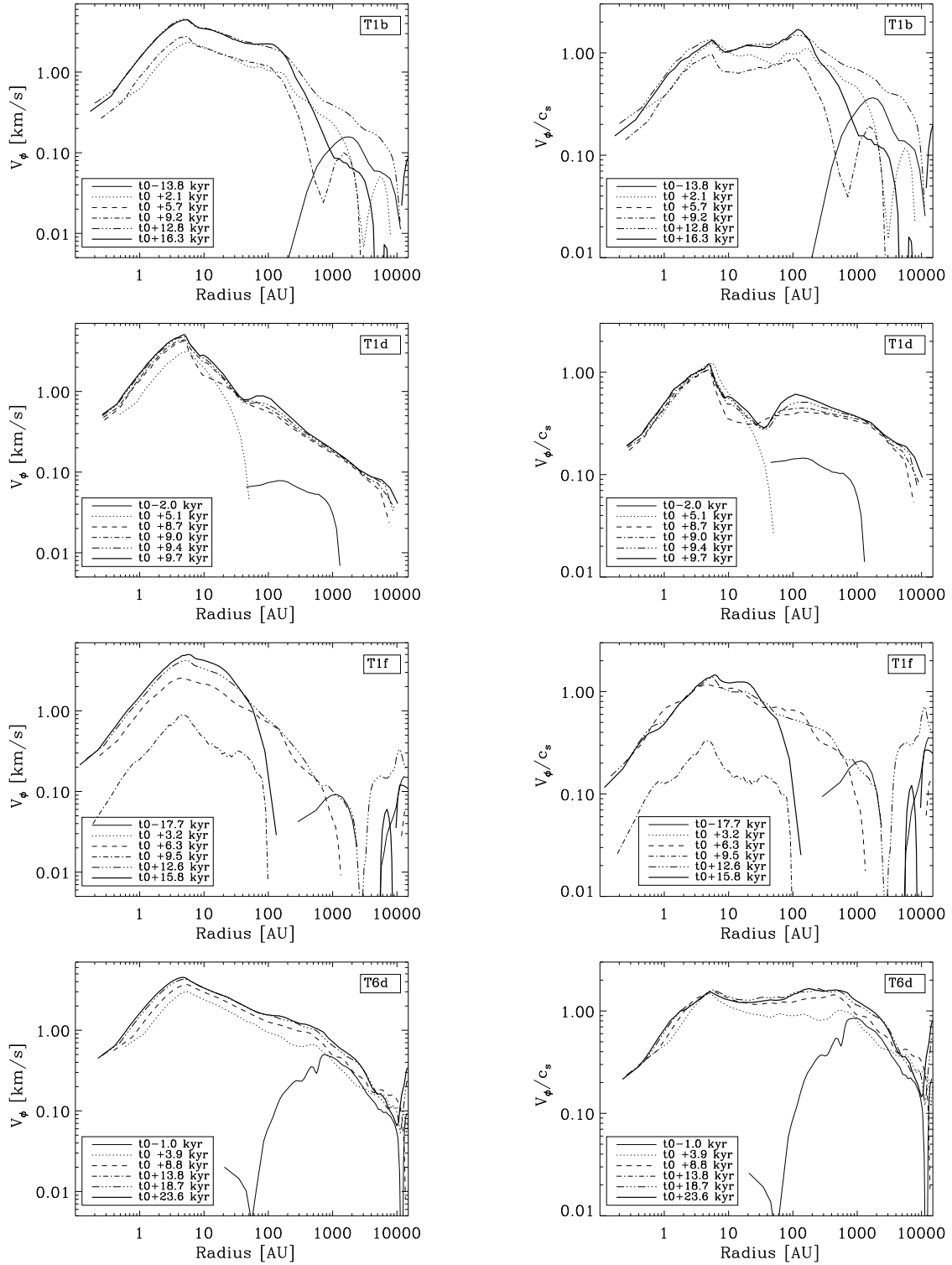


Figure 7.22: The evolution of the azimuthal velocity profiles at different times. Again, the mean value derived for 100 SPH particles is shown at every output point. In the left column v_ϕ itself is shown, whereas v_ϕ/c_s is plotted in the right column. c_s was derived for the same SPH particles as v_ϕ and is therefore an average over the local sound speed of 100 SPH particles.

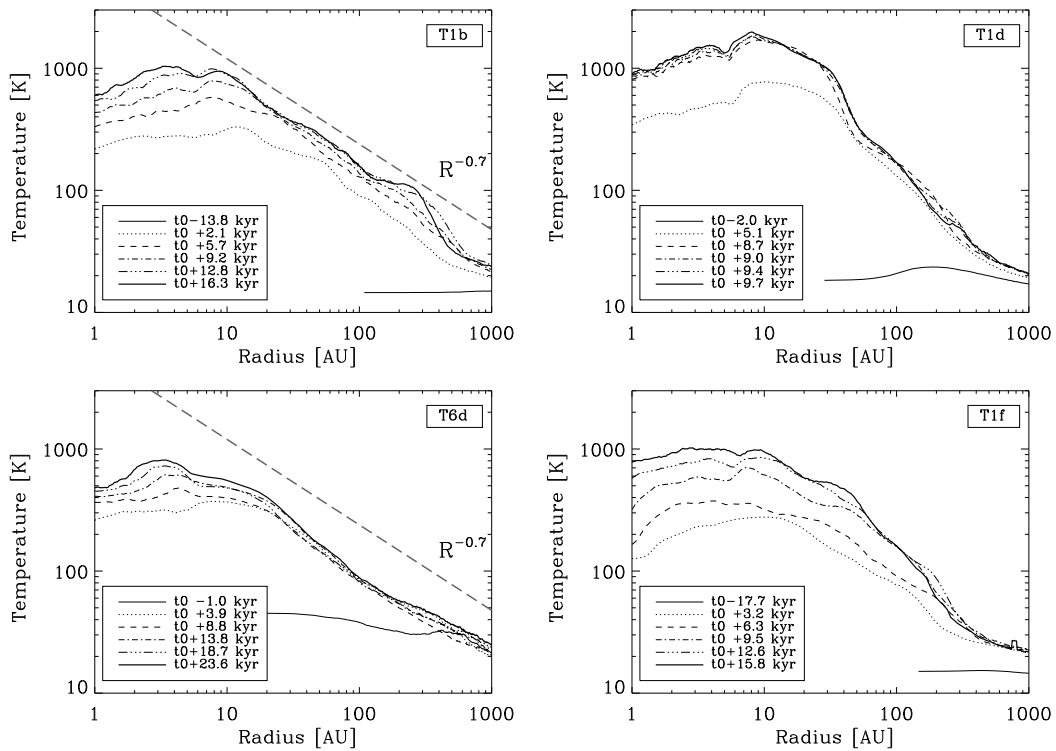


Figure 7.23: Radial temperature profile at different times in the disk formation stage. We show the same time steps as in Fig.7.21. After t_0 , the dense, central parts of the core behave adiabatically and heat up rapidly. Soon a powerlaw temperature profile is established within the disk region. In addition, there is shock heating at the outer boundary of the adiabatic core.

maximum at the outer edge of the disk, which was caused by ordered infall onto the outer disk regions in case of rigid rotation, is missing in the turbulent scenario. Again, this implies that the way a protostellar disk is growing in a turbulent environment is unpredictable. Locally, the details of heating and cooling however dominate the vertical disk structure as well as the fragmentation properties of a protostellar disk.

7.4.2 Qualitative Analysis

In this section, the protostellar disk formation and evolution of two examples (Run T1b and T6d) will be shown and discussed in greater detail. In Fig. 7.24, the evolution of Run T1b is followed beyond the comparison time $t_{\text{fin,turb}}$, which is equal to 163.5kyr for T1b. $t_{\text{fin,turb}}$ has been defined in the previous section. In the upper three panels of Fig. 7.24, the formation of the protostellar object shortly before and at t_0 is shown. In the first panel, two density enhancements are present within the filament. These quickly merge to form one central object at t_0 (third panel). As the inflowing material contains a non-negligible amount of angular momentum, the infalling gas is winding up in a protostellar disk surrounding the growing central object. Shortly after t_0 the disk appears to be warped. Gas is falling onto the disk from all sides, but mostly from the filament. At t_{stop} a rotationally supported disk component has been established. It extends out to a radius of approximately 150AU.

In case of T6d, where the largest of all protostellar disks was found, the collapse has been followed until $t_{\text{fin,turb}}$ which is equal to t_{stop} in this case ($t_{\text{stop}} = 138.1\text{kyr}$). In Fig. 7.25 the early formation and evolution of the central object is shown, whereas Fig. 7.26 illustrates the subsequent formation of an extended protostellar disk. Again, before t_0 two adjacent density enhancements are present within the filament. This time one protostellar object forms at t_0 (second panel) shortly before the second dense blob merges with the central object after 114 kyrs. As more gas is falling in, a small disk component is forming. The disk becomes large and massive. The development of weak spiral arms is enabled. Although disk structure and size is similar to the extended disks formed in Run 5-7 of the rigidly rotating sample, disk fragmentation does not take place in this case. This is probably caused by the turbulent infall, which constantly perturbs the disk within the outer parts. The outer parts of the disk could undergo local fragmentation more easily than the inner parts, where the temperature is higher (the local Jeans mass is $M_{\text{Jeans}} \propto \rho^{-1/2} T^{3/2}$). Due to turbulent infall the disk is not well concentrated along the disk mid-plane, but appears to be thick in vertical direction. According to Toomre (1964) thick disks are more stable towards fragmentation than thin disks. Therefore the outer parts of the disk seems to be gravitationally stable. However, by studying the Toomre Q parameter, one finds a small region within the central spiral arm where Q is close to 1 (see Fig. 7.27). Fragmentation might take place within this region (at R 300AU from the center) during further evolution of the disk. The simulation is still running.

Interestingly we always find more than one density enhancement within the filament before t_0 . The initial density enhancements are frequently close to each other and merge before they collapse to individual protostellar objects. However, in Run T2b or T0a, individual density enhancements collapse within the filament before they are able to merge.

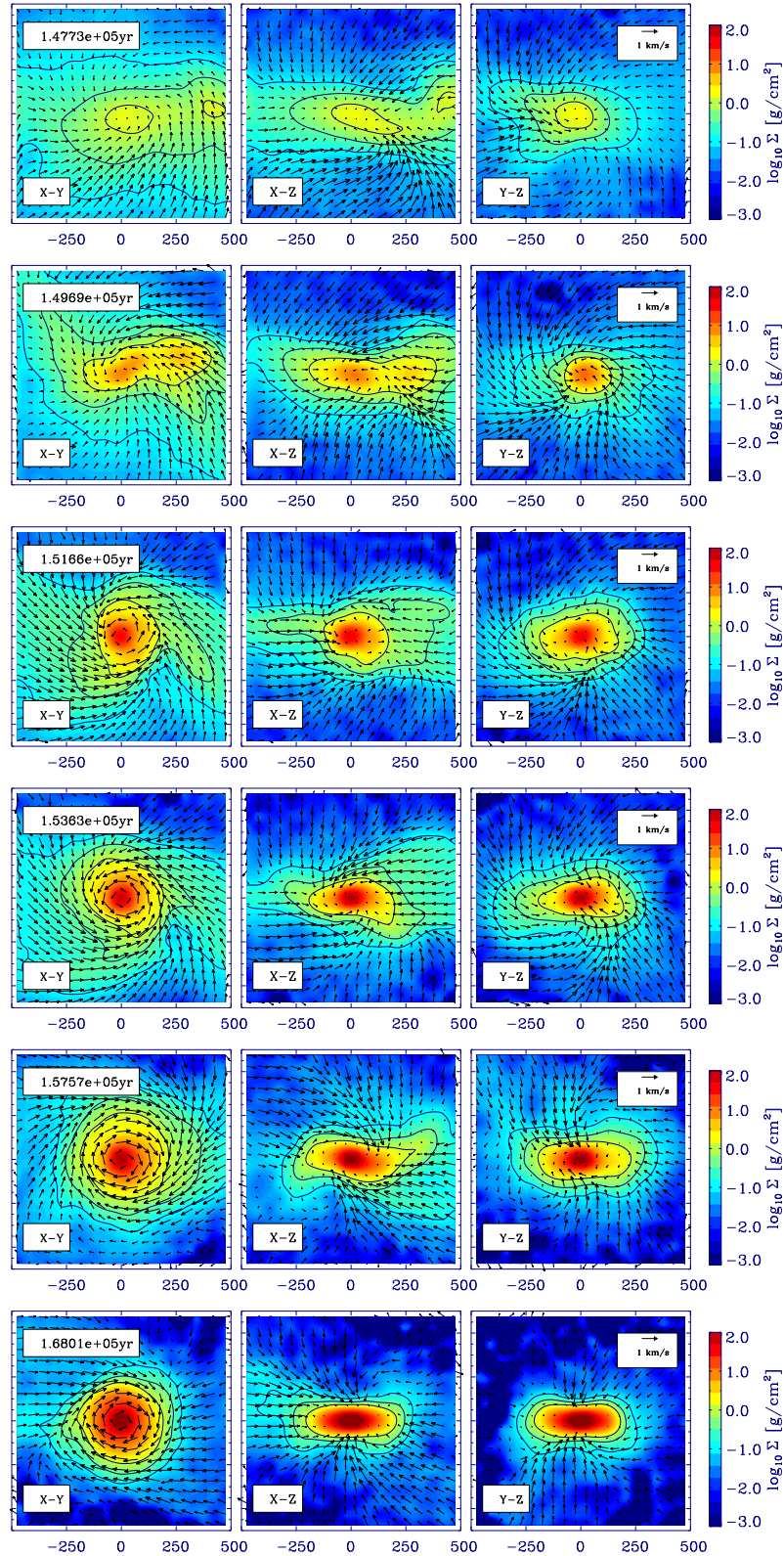


Figure 7.24: Time evolution of surface density and velocity field for Run T1b. These snapshots follow the formation of a protostellar object and circumstellar disk starting from $t_0 - 4\text{kyrs}$ up to $t_{\text{fin,turb}} + 4.6\text{kyrs}$. Shown are slices of $[-500\text{AU}; 500\text{AU}]$ and a thickness of 100AU each.

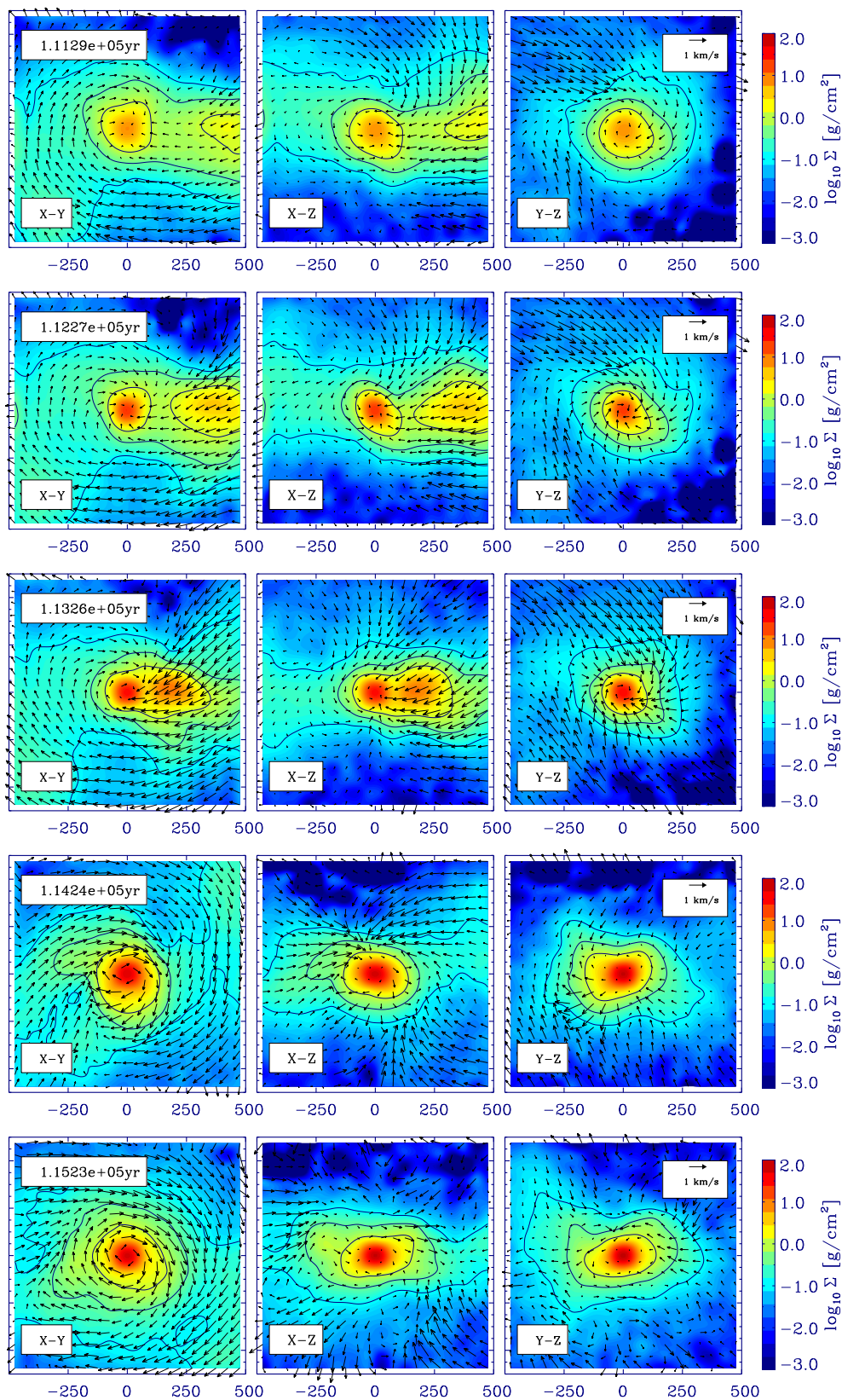


Figure 7.25: Time evolution of surface density and velocity field for Run T6d. These snapshots depict the formation of the central object shortly before and at t_0 , as well as the very early stages of subsequent disk formation. Shown are slices of $[-500\text{AU}; 500\text{AU}]$ and a thickness of 100AU each

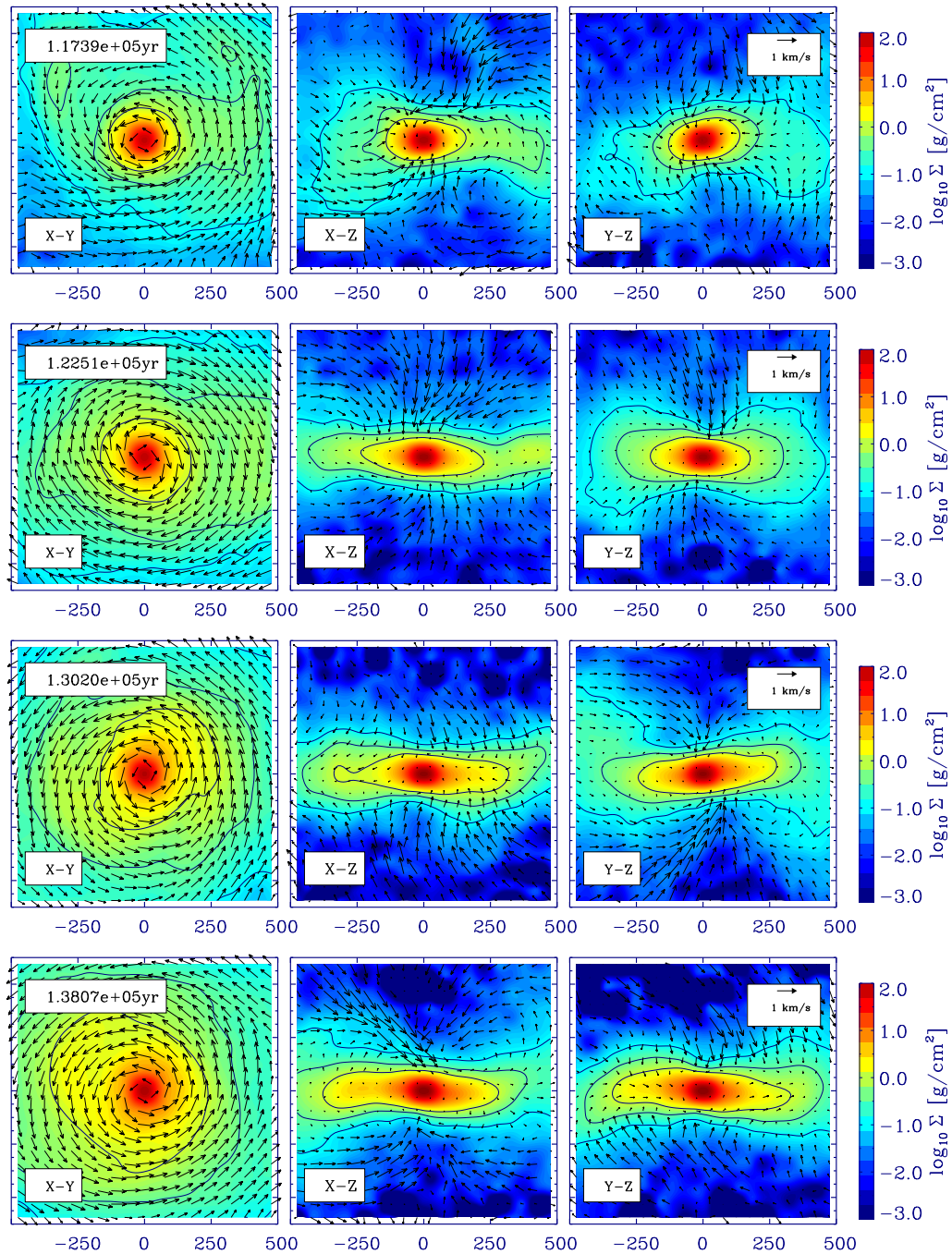
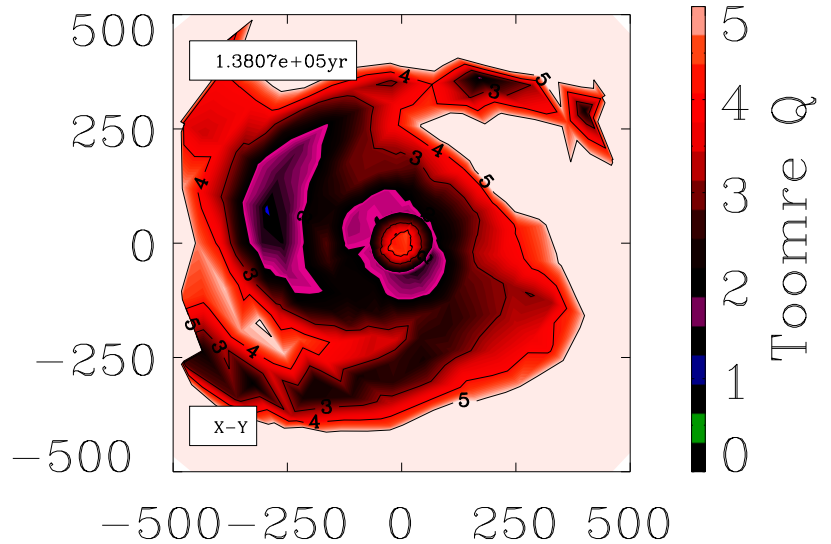


Figure 7.26: Further evolution of Run T6d. A large protostellar disk is growing via turbulent gas infall. The disk is constantly perturbed. Therefore it may form spiral arms, but it does not undergo disk fragmentation.

Figure 7.27: Toomre Q parameter for the last snapshot of Run T6d at $t_{\text{fin,turb}}$. The spiral structure of the disk is clearly visible. At a radial distance of about 300AU from the central object, a tiny region with $Q \approx 1$ can be found within the spiral arm.



In general, the process of fragmentation in turbulent simulations is remarkably different from fragmentation in case of rigid rotation: Not the forming protostellar disks but rather the initial filaments are fragmenting. Disk fragmentation is rather rare during early evolutionary stages. Only Run T6d with maximal j_{tot} resulted in an extended protostellar disk, which will probably undergo fragmentation in the near future after t_{stop} . So far we were not able to follow the simulation until disk fragmentation due to numerical limitations. However, the simulation is still running.

In collapsing turbulent cores the frequency and multiplicity of systems could therefore be dependent on the properties of the turbulent velocity field, as well as on the local gas thermodynamics. Goodwin & Kroupa (2005) suggested that the observed multiplicity frequency in young star forming regions can be explained if roughly half of the cores form two stars, and half form three stars. So far it is unclear why nature seems to be in favour of these statistics. In previous studies fragmentation in turbulent core collapse simulations has always been too efficient to fulfill this estimate. In a series of three papers Goodwin et al. (2004a,c, 2006) investigated the influence of the turbulent power spectrum on the outcome of core collapse simulations featuring a Plummer-like initial density profile. They used a barotropic EOS to capture the gas thermodynamics. We find two major differences between the results of Goodwin et al. and the simulations performed during this PhD thesis: First, Goodwin et al. (2004a,c) only find fragmentation to occur within the protostellar disk (which they call circumstellar accretion region). This is not the case in our simulations, where fragmentation of the core itself, respectively of the filament, is the dominant way of fragmentation. Second, they note that fragmentation depends on the details of the collapse, but find the turbulent cores to form between 1 and 12 stars. On average one star per initial Jeans mass is formed ($1M_{\odot}$ in their setup). The number of forming stars even increases with increasing turbulence (Goodwin et al., 2006). Therefore the number of formed stellar objects is

too high in their sample, whereas it seems to be too low in our simulations. Only 12% of all cores in our sample form fragmenting filaments and evolve into multiple systems. Triple systems are not formed at all. At t_{stop} the filaments still contain a lot of mass and may undergo fragmentation. However, the embedded (Class 0) stages of a young protostar only last for 10^5 yrs. For this reason, subsequent fragmentation of filament and/or disk has to happen quickly to account for the observed stellar multiplicities in Class 1 or later stages. In general, we find much more (disk) fragmentation in case of rigid rotation than in case of turbulent collapse. One should keep in mind that the core collapse proceeds in an outside-in manner in our simulations in contrast to the simulations performed by Goodwin et al.. This difference has to be further investigated.

Finally, the outcome of turbulent and rigidly rotating core collapse is compared in Fig. 7.28. From top to bottom, the total core angular momentum is increasing. Adjacent panels belong to runs with equal j_{tot} . In general we find no correlation of disk presence or size with j_{tot} in case of turbulent core collapse. In case of rigid rotation, disks were formed in all simulations and the disk size is increasing with increasing angular momentum. Furthermore we find the larger disks shown in the lower two panels (right column) to undergo disk fragmentation, whereas smaller disks are more concentrated, warm and gravitationally stable. In the turbulent scenario the forming filament, rather than the protostellar disk, is fragmenting independent of the strength of the initial core angular momentum. It might well be a coincidence that the largest disk formed in all turbulent simulations corresponds to the setup with the highest initial j_{tot} . From our simulations, the formation of such large disks seems rather unlikely, because we find only one case where the disk radius is greater than 200AU. However, once an extended disk is formed, it would be expected to become gravitationally unstable and fragment. We find disk fragmentation to be delayed by turbulent gas infall, which continuously disturbs the disk. The turbulent infall results in a vertical 'turbulent pressure', which stabilises the disk against local gravitational instabilities.

7.5 The (re-)distribution of angular momentum: Influence of the Artificial Viscosity implementation

Observations show that angular momentum must be lost at all stages of the star formation process. The total specific angular momentum estimated for molecular clouds is of the order of $10^{23} \text{cm}^2 \text{s}^{-1}$, for prestellar core it is reduced to $10^{21} \text{cm}^2 \text{s}^{-1}$, and for protostars j_{tot} is as low as $10^{17} \text{cm}^2 \text{s}^{-1}$. A typical solar-type main-sequence star has $j_{\text{tot}} \approx 10^{15} \text{cm}^2 \text{s}^{-1}$. In addition, most of the angular momentum contained in our solar system is carried by Jupiter, even though Jupiter only contributes a small fraction to the total mass of the solar system. Assuming that angular momentum has been distributed rather uniformly amongst the gas cloud out of which our solar system has formed, this finding suggests very efficient redistribution of angular momentum during formation. A differentially rotating accretion disk enables the efficient redistribution of angular momentum in shear flows and by various instabilities, like the gravitational instability (Durisen et al., 2000), the magneto-rotational instability (Balbus, 2003), the baroclinic instability (Klahr & Bodenheimer, 2003), and others.

This section is focused on examining the way angular momentum is redistributed and on the

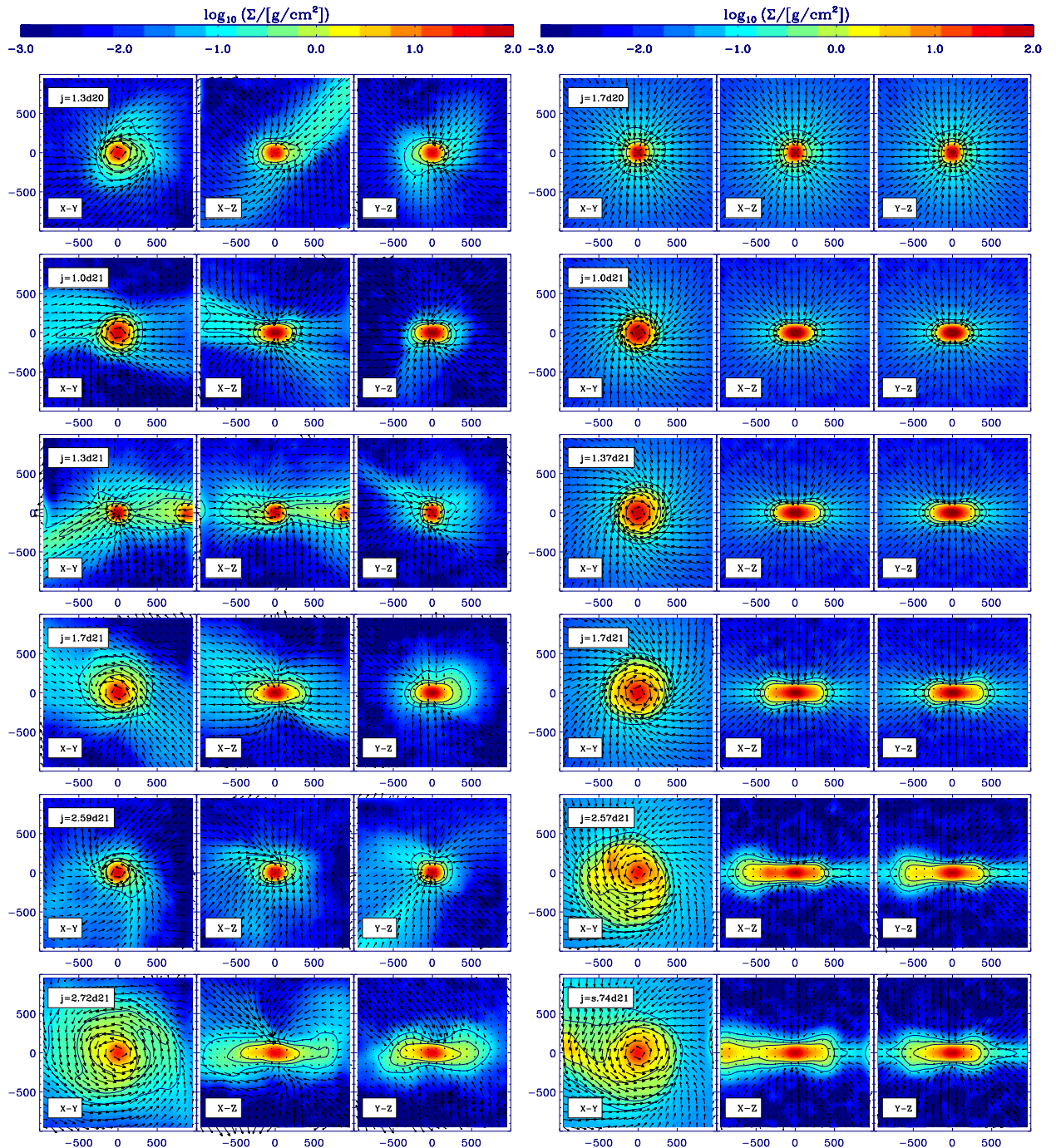


Figure 7.28: Disk formation from the collapse of turbulent (left) vs. rigidly rotating (right) BESS for different initial core angular momenta. For every simulation we show the surface density and the velocities within the inner core region at the same scale ($-1000, +1000$)AU. From inside out, the overlaid isocontours correspond to $1, 0.3$ and 0.1 g cm^{-2} .

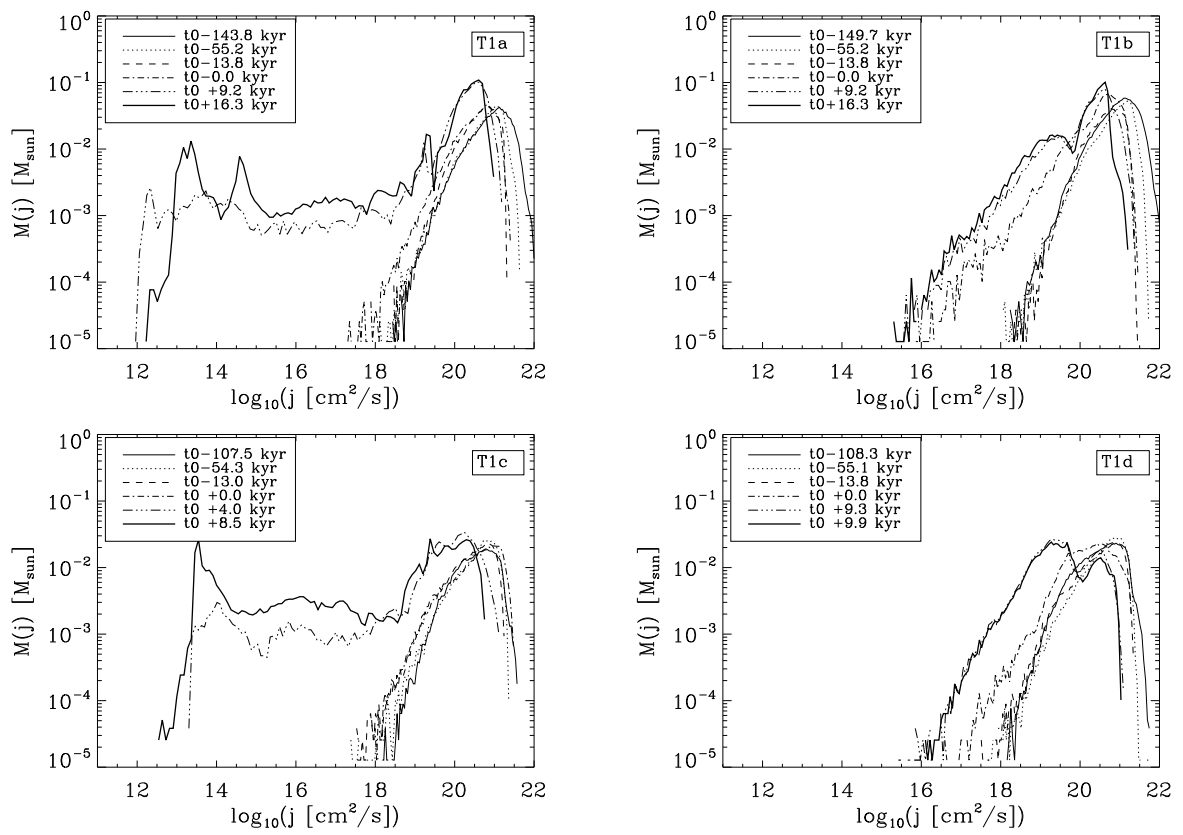


Figure 7.29: Mass vs specific angular momentum at different evolutionary stages for Run T1a (upper left panel), T1b (upper right panel), T1c (lower left panel), and T1d (lower right panel). In (T1a and) T1b a disk was formed, whereas T1d only collapses to one dense prestellar object. Only particles which finally end up with $\rho > 10^{-16} \text{g cm}^{-3}$ at t_{stop} are considered. The first time step shows the original distribution of angular momentum within this particle subset.

amount of transport that occurs during collapse as well as during early protostellar disk evolution shortly after t_0 . In Fig. 7.29 the time evolution of the gas mass distribution as a function of specific angular momentum $M(j)$ is illustrated for two examples. All gas contained in SPH 'core' particles which will accumulate at densities $\rho > 10^{-16} \text{g cm}^{-3}$ at t_{stop} have been included for this purpose. Only these particles contribute to the formation of protostellar object and disk. Before calculating $M(j)$ for these particles, the coordinate system has been centered onto the forming protostellar object and all particles have been transformed to the center of inertia frame of the relevant subset. In the upper row we show $M(j)$ for Run T1a and T1b, a case in which a protostellar disk is formed. In the lower row T1c and T1d are shown. In T1c and T1d the core is directly collapsing to form a single protostellar object. An accretion disk is not formed. The difference between left and right column of Fig. 7.29 is the implementation of the SPH Artificial Viscosity (AV) which has been used to evolve the systems. Run T1a and T1b feature equal core and turbulent velocity setups, but T1a was calculated using the standard prescription of SPH AV (Gingold & Monaghan, 1983) whereas T1b employs the modifications of (Balsara, 1995) (see chapter 3 for more details on the SPH AV). In the following, the AV implementation including the changes of (Balsara & Norman, 1990; Balsara, 1995) will simply be called 'Balsara-AV'. The special characteristics of the Balsara-AV is the fact that it reduces the amount of spurious numerical angular momentum transport in shear flows. Shocks are treated equivalently with either standard AV or Balsara-AV. In both cases, standard values for the AV parameters for bulk ($\alpha = 1$) and shear ($\beta = 2$) terms are employed.

For T1a and T1b equal output times relative to the collapse time t_0 are shown. t_0 is different for the two simulations. T1b ($t_0 = 151.7 \text{kyr}$) collapses about 6kyr later than T1a ($t_0 = 145.8 \text{kyr}$). In principle Fig. 7.29 illustrates that the amount of angular momentum redistribution before t_0 is negligible. In T1a, the whole distribution of $M(j)$ is slightly shifted to smaller values of j at t_0 . In T1b, $M(j)$ becomes more narrow before t_0 . In this case most angular momentum is redistributed between the two snapshots taken at $t_0 - 13.8 \text{kyr}$ and $t_0 + 9.2 \text{kyr}$. At this time protostellar object and disk are quickly formed. In T1a, angular momentum is redistributed most efficiently after t_0 . In this case the transport of j within the forming protostellar object and disk are most efficient. The low angular momentum component formed in T1a is completely missing in T1b. Therefore the central object in T1b has the form of a 'nuclear disk'. The same has been found in case of rigid rotation and has been discussed in section 4.2. In T1d, where no protostellar disk has been found, the evolution of $M(j)$ is comparable to T1b. However, also T1c is comparable to T1a even though no disk is formed in T1c. When analysing the dynamics close to and within the protostellar object in T1c more closely, one finds the whole central object to be differentially rotating. Therefore, even though no disk is formed, angular momentum is redistributed in shear flows.

From Fig. 7.29 it is obvious that different AV prescriptions strongly influence the evolution of $M(j)$. In order to clarify whether the redistribution of angular momentum is different in turbulent and rigidly rotating setups, or whether the numerical prescription dominates, we show the cumulative mass distribution $M(< j)$ at t_{stop} for all runs with initial $j_{\text{tot}} = 10^{21} \text{cm}^2 \text{s}^{-1}$ in Fig. 7.30. Again only 'core' particles which form the $\rho > 10^{-16} \text{g cm}^{-3}$ at t_{stop} are taken into account for each simulation. For every simulation, all particle positions and velocities have been

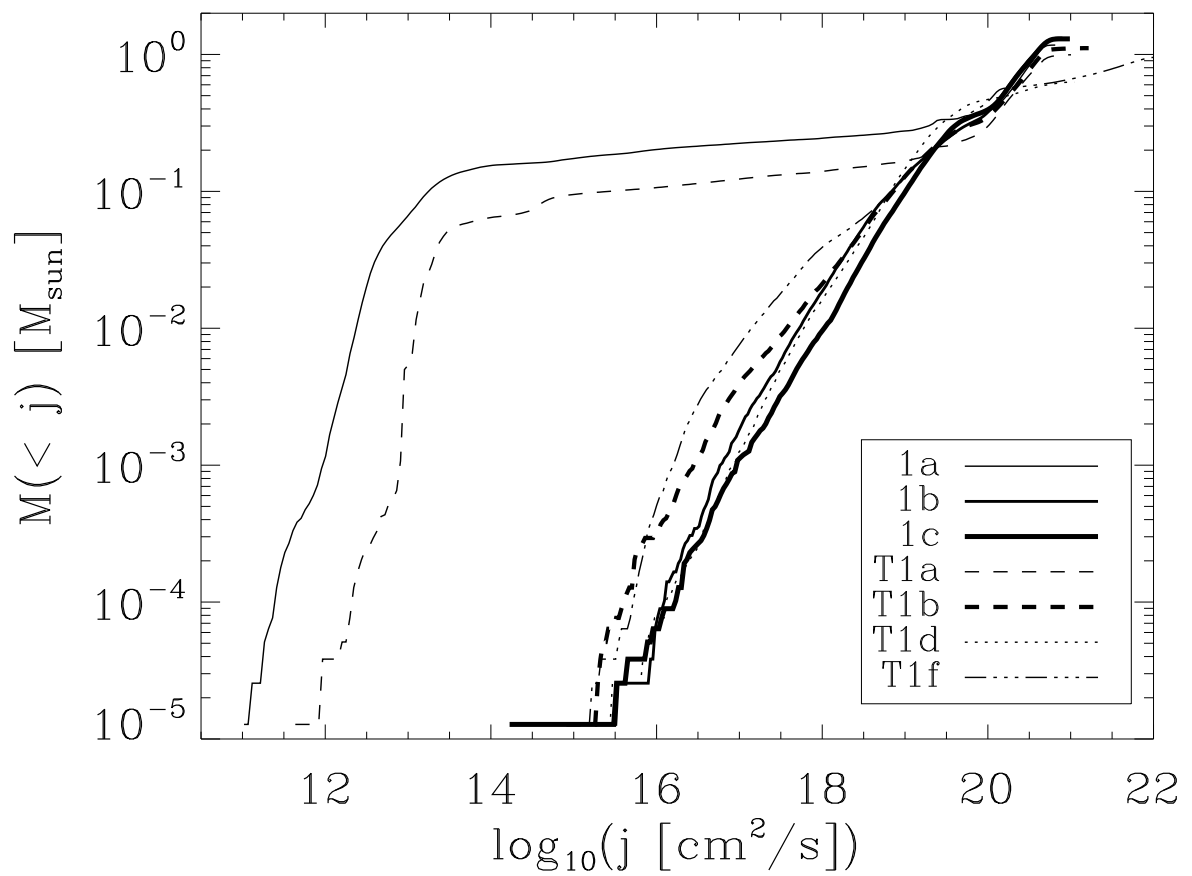


Figure 7.30: Cumulative mass distribution as a function of specific angular momentum with respect to the forming protostellar object. All analysed calculations have the same initial core angular momentum $j_{\text{tot}} = 10^{21} \text{cm}^2 \text{s}^{-1}$.

transformed to the center of inertia frame for the considered particle subset. The two profiles (T1a and 1a) where the Balsara-AV was employed clearly exhibit significantly different $M(< j)$ -distributions than all other runs. Thus, the AV implementation seems to dominate the way angular momentum is redistributed once a prestellar object is formed. Whether turbulence or rigid rotation forms the basis of a setup seems to be unimportant in this respect. In summary, employing the standard AV, too much angular momentum is transported in shear flows. As the shock treatment is equivalent in the standard and the Balsara implementation the differences have to be caused by shear. This demonstrates that shear flows must be much more important for the transport of angular momentum than shocks. The conclusions which can be drawn from this result are twofold: First, for the same AV implementation, $M(j)$ is similar in turbulent and non-turbulent collapse calculations. Moreover, the simulations show that direct gravitational collapse can only be important for the formation of very low mass objects or in case of very low initial core angular momentum. Therefore angular momentum has to be redistributed in order to allow for the growth of the central object - no matter if the core angular momentum originates from turbulence or rigid rotation. As accretion disks represent the most efficient way to redistribute angular momentum, they are essential to allow for the further growth of a protostellar object in any scenario. Second, the SPH viscosity prescription has to be used with caution. Most of the simulations performed to date (in star as well as in galaxy formation) consider the effects of particle resolution but do not study the influence of numerical characteristics like SPH AV. However, solutions to a specific problem are usually degenerate and increasing the resolution of a simulation does not necessarily improve the result.

7.6 Conclusions

In this chapter the collapse of turbulent prestellar cores has been investigated. Sub- or transonic turbulence has been found to provide a natural and elegant source of core angular momentum. In general, the collapse of turbulent cores is fundamentally different from the collapse of a prestellar core in ordered, rigid rotation. In the beginning, the turbulent velocity field superimposed onto the BESs causes random outflowing and inflowing motions with respect to the core center. Therefore the initial density distribution is disturbed. Filamentary structure emerges and is enhanced due to the overall collapse. Always one main dense filament is formed. It typically is prolate and its length is comparable to the initial radius of the core (17000AU). Within or at the edge of the filament the local Jeans mass is exceeded at some point and further collapse to one or more protostellar objects is triggered. The protostellar objects always form around a radial offset of 5000AU from the original center of the cloud. This is where the BES density profile changes from being flat within the central region to $\rho(R) \propto R^{-2}$ at larger radii ($R > 5000 - 7000$ AU in this setup). The origin of this result has been investigated. By analysing the amount of kinetic energy induced within the central core regions one finds that for most setups $E_{\text{kin}}/E_{\text{pot}}$ is large within the core center. This causes irregular flows within the central regions, which locally disturb the hydrostatic solution in an irregular way. However, one important characteristic feature of a BES is that it always collapses outside-in. Therefore gas from the outer core regions is swept up and falling onto the turbulent central region. Locally collapse to a protostellar object is triggered

where outstreaming and infalling gas flows collide. The initial density profile plays a crucial role in the outcome of molecular cloud core collapse, as it determines the way a core is collapsing (e.g. outside-in or inside-out).

In total, protostellar disks are formed in 82% of all turbulent cases. This frequency fits very well to the observed frequency of circumstellar disks surrounding young low-mass stars in near-by star forming regions. In addition, the disks are on average smaller than in case of rigid rotation. Like all other disk parameters, the disk size is in general not correlated with the initial angular momentum of the parental core. In many cases the radius of the adiabatic disk component R_{13} is comparable to the half mass radius of the disk R_{half} . Here we find R_{half} to be between 40AU-60AU and R_{16} to be around 200AU-300AU. In some cases R_{16} appears to be very extended. This is the case for both runs which formed two fragments within the filament, because the gas which determines R_{16} is surrounding both protostellar objects. In both fragmenting cases no protostellar disks were found to surround the fragments up to t_{stop} . This can be explained by the transfer of angular momentum into orbital angular momentum of the binary. Furthermore, only one setup resulted in a single protostellar object without a circumstellar disk. In this case the angular momentum within the collapsing region is low enough to allow for direct gravitational collapse. Even though disk size and mass seemed to be uncorrelated with j_{tot} for all turbulent simulations, the most extended disk can be found in the setup featuring the highest angular momentum (T6). The large, rotationally supported disk has an outer radius of $\approx 700\text{AU}$.

In contrast to the disks formed from rigidly rotating cores with $j_{\text{tot}} > 2 \cdot 10^{21} \text{cm}^2 \text{s}^{-1}$, the disks formed from turbulent cores did not become gravitationally unstable and were never fragmenting during runtime. The disks are not well concentrated to the midplane because turbulent gas infall causes perturbations to the disk structure, especially in vertical direction. Therefore local fragmentation seems to be suppressed. In the two cases (T0a and T2b) where more than one protostellar object was formed, the filament rather than the disk was fragmenting. As j_{tot} is relatively low for these two cases, there is no correlation between the occurrence of filament fragmentation and initial core angular momentum. Fragmentation is therefore completely different in turbulent simulations and should lead to different statistics, e.g. with respect to binary frequency and separation, which will be separately addressed in a future paper. In addition, filament fragmentation is highly non-linear and not correlated with the total angular momentum of the parental core. In general, the current simulations produce too few protostellar objects as compared to observed multiplicity rates of young stellar systems. However, the subsequent fragmentation of at least one protostellar disk cannot be excluded. The Toomre stability analysis of e.g. the extended disk formed in T6d showed that Q is very close to 1 within the most massive of the present spiral arms. Thus, this disk should become unstable to disk fragmentation in the near future. Due to numerical limitations none of the disks could actually be evolved far enough to study disk fragmentation in turbulent core collapse. We also found the filaments to be collapsing at opposing ends in some simulations, which might cause the formation of wide binary systems.

It should also be noted that the forming protostellar disks are always oriented in such a way that the disk plane is roughly parallel to the long axis of the filament. Thus, the disks are oriented along the filament. Protostellar jets and outflows, which are eventually forming within later evolutionary stages would then be oriented perpendicular to the filament. This is in agreement with observations of protostellar outflows (see Anathpindika & Whitworth, 2008).

Concerning mass infall and accretion rates, the values extracted from turbulent collapse simulations are comparable to the ones found in case of rigid rotation. In general the mean mass accretion rate onto the central object is a factor of 2-5 lower than the mass infall rate onto the disk (between few $\times 10^{-5}$ and $10^{-4}M_{\odot}/\text{yr}$). Hence the dense disk component is constantly growing and we do not find an equilibrium state, in which the disk could transport mass as efficiently as it grows ($\dot{M}_{\text{infall}} = \dot{M}_{\text{accretion}}$). The gas is stratified in different density components. We find a smooth transition between the gas mass contained within the adiabatic, dense component, the low density component M_{16} , which is formed by protostellar disk and parts of the filament and the filament, which contains all the gas within the core region at $T > 20\text{K}$. By analysing the time evolution of these three mass components, one finds that the growth of the densest component is dictated by the growth of the filament. Gas from the outer core regions is collapsing onto the filament, which is contracting. Mostly gas is accreted through the filament onto disk and central object. Once a disk is formed, its density profile appears to be flatter than in case of rigid rotation. This is caused by the dense filament which is surrounding the protostellar disk and alters the radial density profile at intermediate radii. The disk temperature profiles are always comparable to the temperature profiles found for the extended disk formed in case of fast rigid rotation. Even though turbulent disks are typically small, they don't ever become as concentrated and warm as the small protostellar disks formed from slowly rotating cores.

When studying the time evolution of the mass distribution vs specific angular momentum $M(j)$, one finds most of the angular momentum to be redistributed around t_0 . However, major differences in $M(j)$ or in the cumulative mass distribution $M(< j)$ are caused by different implementations of the SPH Artificial Viscosity, rather than by the different mechanisms of angular momentum transport in turbulent setups. The standard AV prescription (also called constant AV) leads to strong numerical angular momentum transport, and thus enables the formation of a slowly rotating gas component. This component with low specific angular momentum belongs to the forming protostellar object. Therefore in simulations with constant AV, the distribution of SPH particles within the central object is spherical rather than disk-like. This is however not physical. A central or 'nuclear disk' has been found in all simulations with Balsara AV. In this case angular momentum is slowly redistributed within the circumstellar accretion disk. In case of Balsara AV the numerical viscosity is reduced for shear flows. This shows that the correct numerical prescription of shear flows rather than shocks is crucial for the correct numerical prescription of a circumstellar accretion disk. In summary it has been found that turbulence does not alter the redistribution of angular momentum as compared to rigid rotation and therefore cannot explain the change in $M(j)$, which is observed from prestellar cores to protostars.

Chapter 8

Summary & Outlook

Star formation is a highly non-linear process. It involves complex gas dynamics, determined by the interplay of turbulence, gravity, pressure, radiation and magnetic fields on more than seven orders of magnitude in space as well as over more than twenty orders of magnitude in density. Even the process of single and multiple low-mass star formation from individual dark molecular cloud cores is still an unresolved problem in modern astrophysics. Since observations show, that the total angular momentum contained within dense prestellar cores is non-negligible, the collapse of a prestellar core will naturally result in the formation of a circumstellar disk. In the early and embedded stages of protostellar evolution the circumstellar disks are called protostellar disks. On a time scale of few $\times 10^5$ years they evolve into low-mass protoplanetary disks which are frequently observed. In general, protostellar disks are accretion disks, and thus are most important for the redistribution of angular momentum. Despite substantial numerical and observational progress in the field of star formation, the fundamental properties of the forming protostellar disks have not yet been satisfactorily linked to the initial conditions prevailing within prestellar cores. In this thesis, three of the most important open questions in low-mass starformation have been addressed:

- 1) Which physical process determines the protostellar mass and how is it accreted?
- 2) What determines the (fragmentation) properties of forming protostellar disks and how do they depend on the given initial conditions in the parental cores?
- 3) Is the protostellar disk formation and evolution process significantly altered in a moderately turbulent environment?

In this thesis the collapse of prestellar cores and the formation and early evolution of protostellar disks has been investigated in fully three-dimensional SPH simulations performed with the Smoothed Particle Hydrodynamics code VINE (Wetzstein et al., 2008; Nelson et al., 2008). As this thesis was aiming for insight into the basics of the dynamical evolution of the systems, the calculations do neither include magnetic fields nor full radiation transport or feedback from the forming central star. The prestellar cores are modeled as slightly supercritical Bonnor-Ebert spheres, which provide density profiles that are in well agreement with recent observations. A Bonnor-Ebert sphere is an isothermal sphere of gas in hydrostatic equilibrium confined by external pressure. The internal velocity dispersion of prestellar cores is observed to be small and com-

parable to the isothermal soundspeed of gas with a temperature of $T = 10\text{K}$. Internal core motions are hence sub- or transonic, but not supersonic like the highly turbulent motions observed within molecular clouds on parsec scales. The projected rotational properties of individual cores can be explained by either ordered (rigid) rotation or mildly turbulent motions. For this reason both, the collapse of rigidly rotating as well as turbulent molecular cloud cores has been studied within the framework of this thesis. In case of rigid rotation, various rotational frequencies Ω have been chosen, each resulting in a different total specific angular momentum of the prestellar core. The choice of the total angular momentum of the simulated cores is also based on recent observations. After defining a sample of cores in rigid rotation, a few turbulent setups (each with a total core angular momentum that is equivalent to a setup with rigid rotation) have been selected out of a sample of 400 generated turbulent initial conditions. All turbulent setups are based on random Gaussian velocity fields generated for Burger's power spectrum of supersonic turbulence ($P(k) \propto k^n$ in Fourier space with $n = -4$). Burger's ($n = -4$) and Kolmogorov's ($n = -11/3$) power spectral indices were found to provide turbulent velocity fields which are in well agreement with observations and recent numerical models of supersonic molecular cloud turbulence over three orders of magnitude in spatial scale. Therefore one can assume that the power spectrum is also established at core scales and below. In principle, the physical scale of the longest populated mode k_0 can be chosen freely. Here, both radius ($k_0 = 2$) and diameter ($k_0 = 1$) of the initial sphere have been tested in different setups. Interestingly, the mean total core angular momentum (j_{tot}) resulting from setups with $k_0 = 2$ is an order of magnitude lower than the mean observed j_{tot} , as well as an order of magnitude lower than j_{tot} for setups with $k_0 = 1$. This result indicates that the typical scale of prestellar cores is linked to the turbulent dissipation scale or the typical scale corresponding to the transition from super- to subsonic turbulence, respectively. Here, most of the relevant simulations are based on turbulent velocity fields with $k_0 = 1$. The gas thermodynamics has been described by assuming an ideal gas equation of state with an adiabatic index $\gamma = 1.4$, which is appropriate for diatomic gas like molecular hydrogen. Apart from H_2 , the most abundant molecules found in molecular clouds are CO , CO_2 , H_2O , HCl , HCN , O_2 . In fact, more than 118, partly complicated molecules have been detected in molecular clouds. They typically radiate at sub-mm and mm wavelengths in the radio regime and are used as tracers for the mostly unvisibile cold molecular hydrogen. Assuming standard molecular abundances Neufeld et al. (1995) calculated and tabulated the gas cooling rates of prestellar cores resulting from optically thin molecular line emission of the most important coolants. In addition to the adiabatic equation of state, these cooling rates were implemented in the SPH code to approximately capture the gas thermodynamics. The integration of this cooling prescription into the numerical scheme was part of this thesis.

Three chapters (chapter 4, 5, and 6) are purely dedicated to the discussion of the collapse of rigidly rotating molecular cloud cores. In chapter 4, the collapse of two prestellar cores has been studied in detail. Both cores are identical apart from the amount of initial core angular momentum they contain. In the first case the constant rotational frequency is $\Omega = 6 \cdot 10^{-14}\text{s}^{-1}$, resulting in a low total core angular momentum ($j_{\text{tot}} = 1 \cdot 10^{21}\text{cm}^2\text{s}^{-1}$). In the second case, $\Omega = 2 \cdot 10^{-13}\text{s}^{-1}$, and $j_{\text{tot}} = 2.72 \cdot 10^{21}\text{cm}^2\text{s}^{-1}$ is high. In case of slow core rotation a moderately sized ($R \approx 100 - 200\text{AU}$), relatively warm, and highly concentrated protostellar disk was

formed. Most of the disk mass is accumulated at densities higher than $\rho_{\text{crit},0} = 10^{-13} \text{ g cm}^{-3}$. Since gas, which is denser than $\rho_{\text{crit},0}$ behaves adiabatically and cannot cool efficiently the disk heats up and the midplane temperature exceeds 800K within the inner 15-20AU in radius. Due to the high temperature as well as fast azimuthal velocities within the disk, fragmentation is suppressed. However, angular momentum is transported through weak spiral arms, allowing for a mass accretion rate onto the central object of the order of $\dot{M}_* \approx \text{a few} \cdot 10^{-5} M_\odot/\text{yr}$. The disk is in approximate vertical hydrostatic equilibrium. The vertical density profile can be well fitted by a sum of two hyperbolic secants. Typically **isothermal**, self-gravitating disks in hydrostatic equilibrium are expected to develop a vertical density profile which follows a *sech*²-function. Although the simulated protostellar disks are not isothermal, the temperature difference between disk midplane and disk surface is small compared to the change in density in this range, which can be greater than four orders of magnitude. The dense, adiabatic disk component formed close to the disk midplane is typically hotter than the surface layers. Therefore one *sech*² profile represents the disk midplane, and a second one is adjusted to fit the disk surface layers. The vertical scale height necessary to fit the disk surface layers was used to define a disk pressure scale height.

In case of rapid core rotation a large ($R \approx 500 - 1000 \text{ AU}$), a less concentrated and thus colder disk has been formed. The average disk temperature is below 100K within the disk region. Although the total disk mass is comparable to the total disk mass accumulated in case of slow rotation, the resulting disk structure is completely different. The disks show strong spiral arms, within which only a small fraction of the core gas locally exceeds $\rho_{\text{crit},0}$. Most of the gas contributing to the total disk mass is located within a disk-like envelope of low density gas ($\rho > 10^{-16} \text{ g cm}^{-3}$) surrounding the denser spiral arms. Therefore the overall disk concentration is low in this case. Furthermore, as most of the disk is made up of low density gas ($10^{-16} > \rho > 10^{-14} \text{ g cm}^{-3}$), it can still cool and disk fragmentation is promoted. Fragmentation occurs within the spiral arms once the local Jeans mass happens to be exceeded. The fragments grow by mass accretion through circumfragmentary disks, which are important for the redistribution of angular momentum. Compared to the case of low angular momentum, the average mass accretion rate is a factor of 2-5 lower in this case, thus leading to a slightly slower growth of the central protostellar object. It should be noted that a protostellar disk has already accumulated before a central object is formed. Therefore a pure protostellar disk dominated phase is present in case of high initial core rotation.

Due to the structured way a core is collapsing the forming protostellar disks have a 'flaring' structure: The ratio of pressure scale height to radius is roughly constant and equal to 1/4. This behaviour is typically expected for protoplanetary disks which are heated by stellar irradiation. In the latter scenario, irradiation causes the disk surface layer to expand and flare. In our case the flaring structure is a secondary effect. The inner disk region (close to the rotation axis of the system) is depleted of gas as low angular momentum material close to the rotation axis collapses first. At larger radii gas is rapidly falling onto the disk and the disk appears thicker. This results in a flaring structure.

Both disks are rotationally supported and radial velocities within the disks are small. Moreover, they are massive, thus self-gravitating, and in differential rotation. Angular momentum

can be transported by gravitational torques. In differentially rotating disks, shear flows are expected to play an important role in redistributing the angular momentum of the gas. In the SPH formalism a numerical trick - the so-called Artificial Viscosity (AV) - is necessary to treat shocks and describe the transport of angular momentum in shear flows. As shear flows are important in every differentially rotating system, the results have been tested against two different AV implementations. On scales of a few hundred AU, the disk properties appear to be mostly unaffected by the employed AV prescription. The SPH AV has been found to significantly influence the redistribution of angular momentum close to and within the central object. With the standard implementation angular momentum is transported efficiently and the central object becomes circular. However, with the improved implementation of Balsara & Norman (1990); Balsara (1995), which was designed to reduce spurious angular momentum transport in shear flows, the central object retains the shape of a 'nuclear disk'. Thus, assuming the implementation of Balsara to be more advanced, the protostellar objects formed in our simulations cannot lose angular momentum efficiently enough to avoid the spin-up of the forming protostar. In setups based on turbulence rather than ordered rotation this result remains the same. However, observations suggest that most of the angular momentum contained within a prestellar core must be lost or redistributed, since young T Tauri stars typically have a specific angular momentum of $j_{\text{tot}} \approx 10^{-17} \text{ cm}^2 \text{ s}^{-1}$, which is four orders of magnitude lower than the average total angular momentum contained in a prestellar core. Within our solar system most of the angular momentum is contained in a very small amount of mass: Jupiter carries most of the angular momentum of the whole system. The reasons why this transport and redistribution is not found in these simulations has to be further investigated. A possible solution might be represented by the inclusion of magnetic fields. The magneto-rotational instability has been found to provide an efficient mechanism to transport angular momentum in disks, especially close to the central star where the disk temperature is high.

In chapter 5 the structure of the forming protostellar disks has been investigated as a function of angular momentum. There is a clear correlation between disk structure and core angular momentum in case of rigid rotation. On the one hand, at the time a central object is forming, the disk half mass radius as well as the outer radius of the low density disk component ($\rho_{\star} > \rho > 10^{-16} \text{ g cm}^{-3}$) are systematically increasing with increasing j_{tot} . On the other hand, the disk concentration, which relates the amount of mass accumulated within dense gas to the total disk mass, is decreasing with increasing j_{tot} . Disks formed from low angular momentum cores have a high concentration (up to 80%), whereas the extended disks formed from high angular momentum cores have a low concentration (as low as 10%). Slowly rotating cores with $\Omega < 1.2 \cdot 10^{-13} \text{ s}^{-1}$ are found to form gravitationally stable disks. Only large disks with low concentration found in simulations with $\Omega > 1.2 \cdot 10^{-13} \text{ s}^{-1}$ form spiral arms and undergo fragmentation once the local Jeans mass is exceeded within a spiral arm. The local fragmentation properties can be well understood by applying the Toomre criterion. The Toomre criterion means that fragmentation can only occur in regions where the Toomre parameter Q drops below 1, whereas the formation of spiral arms is promoted if $1 < Q < 3$. The stability of the disk against local fragmentation is found to be more accurately described by the Toomre criterion than e.g. by a comparison of local cooling and dynamical timescales. The cooling time scale criterium has

been used by other authors to investigate the local stability of isolated self-gravitating disks, and is probably not accurate here because continuous gas infall from the parental envelope disturbs the local balance of heating and cooling. Stable protostellar disks might still be able to undergo fragmentation during later evolutionary stages when most of the core has collapsed and gas infall onto the disk is ceasing. However, if late disk fragmentation takes place, it must happen within the early embedded stages of protostellar evolution (Class 0) in order to result in *stellar* companions of the primary protostar, and thus change the stellar multiplicity of the forming system. Otherwise disk fragmentation might only be relevant for the formation of brown dwarf and gas giant planets rather than the formation of companion stars, since there is only little mass left within the protoplanetary disks (typically $< 0.1M_{\odot}$).

In summary, the simulations of rigidly rotating core collapse show that protostellar disk fragmentation is only enabled if the parental core was rotating with $\Omega > 1.2 \cdot 10^{-13} \text{s}^{-1}$ or $\beta > 0.1$. In this case the resulting disks have a mean disk density $\bar{\rho}$ which is smaller than $\rho_{\text{crit},1} = 3 \cdot 10^{-16} \text{g cm}^{-3}$ (see chapter 6). For $\bar{\rho} > \rho_{\text{crit},1}$ fragmentation is prohibited (see chapter 7). We ascribe this behaviour to the cooling properties of the gas. In our prescription, gas cooling mimics complete isothermal behaviour for densities below $\rho_{\text{crit},1}$. Above $\rho_{\text{crit},1}$ cooling becomes increasingly inefficient until the gas behaves in an adiabatic manner above $\rho_{\text{crit},0} \approx 10^{-13} \text{g cm}^{-3}$. Many other authors use a barotropic equation of state, which employs a rapid transition from isothermal to adiabatic gas at a critical density which is typically equal to $\rho_{\text{crit},0}$. Therefore both, $\rho_{\text{crit},1}$ and $\rho_{\text{crit},0}$ have been applied to predict the fragmentation properties of observed prestellar cores in chapter 6. Two samples of dense molecular cloud cores were considered (Goodman et al., 1993; Caselli et al., 2002). For every core, the core mass, radius and rotational energy fraction β is known. From these three parameters the mean density of the forming protostellar disk, $\bar{\rho}$, can be deduced. One additional assumption has to be made in order to calculate $\bar{\rho}$, since the mass of the disk has to be known. We therefore assumed the disk mass to be a fraction of the core mass, i.e. $0.01M_{\text{core}} < M_{\text{disk}} < 0.3M_{\text{core}}$. As the typical star formation efficiency for prestellar cores is of the order of $1/3$, the upper limit of the disk mass is well approximated by $0.3M_{\text{core}}$.

Observations show that β is roughly independent of the initial core radius. For constant β it follows that $\bar{\rho} \propto M_{\text{disk}} R_{\text{core}}^{-3}$. The observed mass-radius relation for prestellar cores suggests a powerlaw dependence of $M_{\text{core}} \propto R_{\text{core}}^p$, with a powerlaw index p of $1 \leq p \leq 3$. In many studies $p \approx 2$ has been found. In this case $\bar{\rho}$ is inversely proportional to the core radius. Therefore a low-mass core, which is typically small, is less likely forming a protostellar disk which is able to fragment, than a larger, high-mass core with the same β . Low-mass cores are hence more stable towards disk fragmentation than high-mass cores. If the principle of a global star formation efficiency (typically 30%) is applicable, the mass of the stars which form within a certain core is on average correlated to the total initial core mass. This means that lower-mass cores also form lower-mass stars and vice versa. Therefore low-mass stars formed from low-mass cores tend to be singles rather than multiples. As a result, the observational trend that the frequency of binary or multiple stellar systems increases with the mass of the system's constituents, can be reproduced with this simple analytical prescription. Only in case of $p = 3$, which corresponds to a core with constant density, it follows that $\bar{\rho} = \text{const}$ for the same β , and the fragmentation

properties of every core are preset by the amount of angular momentum it contains.

When these findings are applied to observations, the fraction of predicted multiple stellar systems for $\bar{\rho} = \rho_{\text{crit},1}$ is too low as compared to observations. On average only 13% of all cores are predicted to undergo subsequent disk fragmentation. However, since the critical density is probably related to the specific description of gas cooling, a second critical density ($\rho_{\text{crit},0}$) has been investigated. The application of $\rho_{\text{crit},0}$ can possibly be motivated by further dust cooling in regions where all molecular lines are optically thick. In this case 58% of all cores in the sample are expected to undergo disk fragmentation - all high-mass cores (apart from 1) but also many cores of intermediate mass (few M_{\odot}). This fraction agrees well with observations. Dust cooling has not been included in these simulations, since it would require the inclusion of radiation transport, dust chemistry and dust grain evolution. Currently numerical limitations prohibit consideration of dust physics in core collapse simulations. However, also in our sample of simulations a higher critical density like $\rho_{\text{crit},0}$ would imply the fragmentation of all but one formed protostellar disks. Concerning disk fragmentation our conclusions from this study are threefold:

- 1) Fragmentation within later evolutionary stages (the 'late phases of hot disks') cannot be excluded. In protostellar disks which are further evolved, heating by accretion and infall subsides since the gas infall from the parental envelope is shut off and the most of the disk mass has been already been accreted (observed protoplanetary disks typically have small masses of $\approx 0.1M_{\odot}$). However, the late fragmentation of low mass disks will be more important for brown dwarf and gas giant planet formation, rather than for the formation of multiple stellar systems, simply because most of the gas reservoir is gone. The formation of multiple stellar systems thus has to take place during early evolutionary stages of young protostars (Class 0 phase).
- 2) We found that gas cooling within the density regime of 10^{-16}g cm^{-3} to 10^{-13}g cm^{-3} is of immense importance to the fragmentation properties of protostellar disks. Therefore the comparison of different numerical treatments of the gas thermodynamics within core collapse simulations plays a key role in improving our understanding of star formation and fragmentation. This problem has to be addressed in further studies.
- 3) If $\rho_{\text{crit},1}$ is assumed to be the more realistic critical density, disk fragmentation cannot be the dominant mode of binary or multiple formation. This result is found to be unaffected by low levels of turbulence, as $< 20\%$ or all turbulent cores were found to be fragmenting.

The collapse of turbulent prestellar cores has been investigated in chapter 7. In many respects the collapse of turbulent cores is fundamentally different from the collapse of a prestellar cores in ordered, rigid rotation. Right after the simulations have been started the turbulent velocity field superimposed onto the Bonnor-Ebert sphere causes random outflowing and inflowing motions with respect to the core center. Therefore the initial density distribution is disturbed. Filamentary structure emerges and is enhanced due to the overall collapse. Only one main dense filament is formed in all setups. It typically is prolate and its length is comparable to the initial radius of the core (17000AU). As the collapse proceeds the local Jeans mass happens to be exceeded within or at the edge of the filament and the formation of one or more protostellar object(s) is triggered. The protostellar objects always form at a radial distance of a few thousand AU from the original center of the cloud. The origin of this result has been investigated. By analysing

the amount of kinetic energy induced within the central core regions one finds that for most setups $E_{\text{kin}}/E_{\text{pot}}$ is large within the inner few thousand AU. This causes irregular flows within the central regions, which locally disturb the hydrostatic solution in an irregular way. However, one important characteristic feature of a BES is that it always collapses outside-in. Therefore gas from the outer core regions is swept up and falling onto the turbulent center. Locally, collapse to a protostellar object is triggered where outstreaming and infalling gas flows collide. Therefore, the initial density profile plays a crucial role in the outcome of molecular cloud core collapse, as it determines the way a core is collapsing (e.g. outside-in or inside-out).

In total, protostellar disks are formed in 82% of all turbulent cases. This frequency agrees very well with the observed frequency of circumstellar disks surrounding young low-mass stars in near-by star forming regions. In addition, the disks are on average smaller than in case of rigid rotation. Like all other disk parameters, the disk size is in general not correlated with the initial angular momentum of the parental core. In many cases the radius of the adiabatic disk component R_{13} is comparable to the half mass radius of the disk R_{half} . Here we find R_{half} to be between 40AU-60AU. The radius R_{16} of the low density disk component is typically around 200AU-300AU but appears to be very extended for both runs where the filament broke up into two fragments, as the gas which determines R_{16} is surrounding both protostellar objects. In both cases neither a circumbinary disk nor individual protostellar disks were found to surround the fragments until t_{stop} . Only one setup resulted in a single protostellar object without a circumstellar disk. Even though disk size and mass seemed to be uncorrelated with j_{tot} for all turbulent simulations, the most extended disk can be found in the setup featuring the highest angular momentum. The large, rotationally supported disk has an outer radius of ≈ 700 AU. It should also be noted that the forming protostellar disks are always oriented in such a way that the disk plane is roughly parallel to the long axis of the filament. Thus, the disks are oriented along the filament. Protostellar jets and outflows, which are eventually forming within later evolutionary stages would then be oriented perpendicular to the filament. This is in agreement with observations of protostellar outflows (see Anathpindika & Whitworth, 2008).

In contrast to the disks formed from rigidly rotating cores with $j_{\text{tot}} > 2 \cdot 10^{21} \text{cm}^2 \text{s}^{-1}$, none of the disks formed from turbulent cores was fragmenting during runtime. In the two cases where more than one protostellar object was formed, the filament rather than the disk was fragmenting. As j_{tot} is relatively low for these two cases, there is no correlation between the occurrence of filament fragmentation and initial core angular momentum. Fragmentation is therefore completely different in turbulent simulations and should lead to different statistics, e.g. with respect to binary frequency and separation. In addition, fragmentation is not correlated with the total angular momentum of the parental core. In general, the current simulations produce too few protostellar objects as compared to observed multiplicity rates of young stellar systems. However, the subsequent fragmentation of some protostellar disks cannot be excluded, since the disks formed within turbulent cores are relatively cold and have intermediate concentrations ($\approx 0.3 - 0.4$). The Toomre stability analysis of e.g. the extended disk formed in T6d showed that Q is very close to 1 within the most massive of the present spiral arms. Thus, this disk should become unstable to local gravitational stability in the near future. We also found the filaments to be collapsing at opposing ends in some simulations, which might cause the formation of wide binary systems. It

should finally be noted that the fraction of turbulent, fragmenting cores is comparable to the total number of cores which are predicted to undergo fragmentation by applying the analytical ansatz. In both cases, this fraction is around 15% only. Even though the dynamics and disk properties of turbulent and rigidly rotating collapse are significantly different, fragmentation seems to be determined by local gas cooling properties. This question has to be further investigated, e.g. by varying the critical density for fragmentation in the simulations. On the other hand, the initial core density profile could be responsible for the low fraction of fragmenting cores in the turbulent case. Goodwin et al. (2004a) have tested the fragmentation of cores with Plummer-like initial density profile which collapse inside-out. They found the cores to fragment into three to twelve stars and fragmentation is thus too efficient as compared to observations. The initial density profile of a core might therefore strongly influence its fragmentation.

Both, the collapse of cores in rigid rotation as well as the collapse of turbulent prestellar cores is discussed in two papers, which will be submitted by the end of this year.

The simulations still contain a lot of additional information. For instance it would be interesting to place the numerical results in an observational context, in order to constrain the observability of the forming young stellar objects. Especially the warm inner regions comprising the forming central object and the inner protostellar disk might provide a theoretical explanation for observed so-called Very Low Luminosity Objects (VELLOs) (Andre et al., 1993, 2000). VELLOs are rare and therefore they are thought to evolve on a time scale which is very short compared to the time scale on which a system evolves from Class 0 to Class I stage, which is of the order of a few $\times 10^5$ yrs. Spectral energy distributions (SEDs) of the simulated cores will be calculated with a three-dimensional Monte-Carlo radiation transport code. The resulting spectra will be compared to observed spectra of deeply embedded, very young stellar objects. Apart from SEDs, molecular line profiles can be constructed in order to help disentangling the complicated dynamics of observed molecular cloud cores.

Furthermore, the correctness of the cooling prescription employed in these simulations can be further investigated via crystalline dust, which is a tracer for high temperatures. Observations show, that crystals are found at radii of up to 20AU from the central star in some protoplanetary disks (PPDs). However, PPDs are much too cold at these radii as to allow for the formation of crystals. The formation of crystalline silicate via thermal annealing is enabled within regions where the temperature exceeds 800K. Within the protostellar disk such high temperatures are only reached in concentrated disks and at small radii. Therefore different fractions of crystalline dust will be obtained in dependence on the disks' temperature structure. As long as the temperature does not exceed 1500K, the formed crystals are maintained, can survive and become observable in protoplanetary disks. Following the fraction of crystalline dust formed in our simulations and comparing the results to observations of protoplanetary disks would allow for constraining the cooling prescription. In case the simulations would predict crystallinity fractions which are too high, cooling is not efficient enough. The formation of crystalline silicate has already been investigated in a simple 1D model for protostellar disk formation (Dullemond et al., 2006). These simulations provide the possibility to dynamically follow the formation and destruction of crystalline dust in 3D.

In the near future, it will be necessary to study the effects of full radiation transport. The de-

velopment of an extension to the SPH code VINE, including the treatment of full radiation transport with a three-dimensional Monte-Carlo scheme is currently under construction. Once it is working many new physical effects can be explored. One example is the photoevaporation of core and disk surface around the forming protostar by ionising radiation from the young source. Ionising radiation is already known to shape a molecular cloud on larger scales and induce turbulence into dense and cold gas of neutral hydrogen (Gritschneder et al., 2008). Of course, also the effects of magnetic fields have to be included to complete the picture of low-mass star formation. Magnetic fields are probably increasingly important the further the forming protostellar object evolves.

In addition, the generation of better turbulent initial conditions will play a major role in my future work. There seems to be no way to setup turbulent Bonnor-Ebert spheres in a self-consistent, equilibrium state. It would hence be much better to follow the collapse of a core, which was formed in a large-scale simulation of molecular cloud formation, like e.g. in a colliding flow. During my PhD, I was already involved in studying the colliding flow scenario (Heitsch, Naab & Walch, submitted).

Bibliography

- Agertz O., Moore B., Stadel J., Potter D., Miniati F., Read J., Mayer L., Gawryszczak A., Kravtsov A., Nordlund Å., Pearce F., Quilis V., Rudd D., Springel V., Stone J., Tasker E., Teyssier R., Wadsley J., Walder R., 2007, MNRAS, 380, 963
- Alcalá J. M., Spezzi L., Chapman N., Evans II N. J., Huard T. L., Jørgensen J. K., Merín B., Stapelfeldt K. R., Covino E., Frasca A., Gandolfi D., Oliveira I., 2008, ApJ, 676, 427
- Alves J., Lada C. J., Lada E. A., Kenyon S. J., Phelps R., 1998, ApJ, 506, 292
- Alves J., Lombardi M., Lada C. J., 2007, A&A, 462, L17
- Alves J. F., Lada C. J., Lada E. A., 2001, Nature, 409, 159
- Anathpindika S., Whitworth A. P., 2008, A&A, 487, 605
- Andre M., Ferlet R., Vidal-Madjar A., Hebrard G., Lecavelier A., Gry C., Lemoine M., Pineau des Forets G., Roueff E., Rachford B. L., Snow T. P., Tumlinson J., FUSE Science Team 2000, in Bulletin of the American Astronomical Society Vol. 32 of Bulletin of the American Astronomical Society, FUSE observation of HD molecule toward HD 73882. p. 882
- André P., Belloche A., Motte F., Peretto N., 2007, ArXiv e-prints, 706
- André P., Bouwman J., Belloche A., Hennebelle P., 2004, Ap&SS, 292, 325
- Andre P., Ward-Thompson D., Barsony M., 1993, ApJ, 406, 122
- Attwood R. E., Goodwin S. P., Whitworth A. P., 2007, A&A, 464, 447
- Audit E., Hennebelle P., 2005, A&A, 433, 1
- Avila-Reese V., Vázquez-Semadeni E., 2001, ApJ, 553, 645
- Balbus S. A., 2003, ARA&A, 41, 555
- Balbus S. A., Papaloizou J. C. B., 1999, ApJ, 521, 650
- Ballesteros-Paredes J., Hartmann L., Vázquez-Semadeni E., 1999, ApJ, 527, 285
- Ballesteros-Paredes J., Klessen R. S., Vázquez-Semadeni E., 2003, ApJ, 592, 188

- Ballesteros-Paredes J., Vázquez-Semadeni E., Scalo J., 1999, *ApJ*, 515, 286
- Balsara D. S., 1995, *Journal of Computational Physics*, 121, 357
- Balsara D. S., Norman M. L., 1990, in *Bulletin of the American Astronomical Society Vol. 22 of Bulletin of the American Astronomical Society, 3 D Hydrodynamical Study of Radio Sources.* p. 810
- Banerjee R., Pudritz R. E., Holmes L., 2004, *MNRAS*, 355, 248
- Barranco J. A., Goodman A. A., 1998, *ApJ*, 504, 207
- Bate M. R., 1998, *ApJ Letters*, 508, L95
- Bate M. R., Bonnell I. A., Bromm V., 2003, *MNRAS*, 339, 577
- Bate M. R., Bonnell I. A., Price N. M., 1995, *MNRAS*, 277, 362
- Bate M. R., Burkert A., 1997, *MNRAS*, 288, 1060
- Belloche A., André P., Motte F., 2001, in Montmerle T., André P., eds, *From Darkness to Light: Origin and Evolution of Young Stellar Clusters Vol. 243 of Astronomical Society of the Pacific Conference Series, Kinematics of Millimeter Prestellar Condensations in the ρ Ophiuchi Protocluster.* p. 313
- Benz W., 1990, in Buchler J. R., ed., *Numerical Modelling of Nonlinear Stellar Pulsations Problems and Prospects Smooth Particle Hydrodynamics - a Review.* p. 269
- Bertout C., Basri G., Bouvier J., 1988, *ApJ*, 330, 350
- Black D. C., Bodenheimer P., 1975, *ApJ*, 199, 619
- Bodenheimer P., Burkert A., Klein R. I., Boss A. P., 2000, *Protostars and Planets IV*, p. 675
- Bodenheimer P., Tscharnuter W., 1979, *A&A*, 74, 288
- Bonnell I. A., Bate M. R., Vine S. G., 2003, *MNRAS*, 343, 413
- Bonnell I. A., Larson R. B., Zinnecker H., 2007, in Reipurth B., Jewitt D., Keil K., eds, *Protostars and Planets V The Origin of the Initial Mass Function.* pp 149–164
- Bonnor W. B., 1956, *MNRAS*, 116, 351
- Boss A. P., 1980a, *ApJ*, 236, 619
- Boss A. P., 1980b, *ApJ*, 237, 563
- Boss A. P., 1993, *ApJ*, 410, 157
- Boss A. P., 1998, *ApJ*, 503, 923

- Boss A. P., 2002, *ApJ*, 576, 462
- Boss A. P., Fisher R. T., Klein R. I., McKee C. F., 2000, *ApJ*, 528, 325
- Bouwman J., Meeus G., de Koter A., Hony S., Dominik C., Waters L. B. F. M., 2001, *A&A*, 375, 950
- Burkert A., Bodenheimer P., 1993, *MNRAS*, 264, 798
- Burkert A., Bodenheimer P., 1996, *MNRAS*, 280, 1190
- Burkert A., Bodenheimer P., 2000, *ApJ*, 543, 822
- Burkert A., Hartmann L., 2004, *ApJ*, 616, 288
- Burrows C. J., Stapelfeldt K. R., Watson A. M., Krist J. E., Ballester G. E., Clarke J. T., Crisp D., Gallagher III J. S., Griffiths R. E., Hester J. J., Hoessel J. G., Holtzman J. A., Mould J. R., Scowen P. A., Trauger J. T., Westphal J. A., 1996, *ApJ*, 473, 437
- Caselli P., Benson P. J., Myers P. C., Tafalla M., 2002, *ApJ*, 572, 238
- Chabrier G., 2003, *PASP*, 115, 763
- Chiang E. I., Goldreich P., 1997, *ApJ*, 490, 368
- Commerçon B., Hennebelle P., Audit E., Chabrier G., Teyssier R., 2008, *A&A*, 482, 371
- Corbelli E., Palla F., Zinnecker H., eds, 2005, *The Initial Mass Function 50 years later Vol. 327 of Astrophysics and Space Science Library*
- Deagum L., Menon R. L., 1999, *IEEE Computational Science and Engineering*, 5, 46
- Dehnen W., 2001, *MNRAS*, 324, 273
- Delgado-Donate E. J., Clarke C. J., Bate M. R., 2004, *MNRAS*, 347, 759
- Dominik C., Dullemond C. P., Waters L. B. F. M., Walch S., 2003, *A&A*, 398, 607
- Doppmann G. W., Greene T. P., Covey K. R., Lada C. J., 2005, *AJ*, 130, 1145
- Dubinski J., Narayan R., Phillips T. G., 1995, *ApJ*, 448, 226
- Duchêne G., Bontemps S., Bouvier J., André P., Djupvik A. A., Ghez A. M., 2007, *A&A*, 476, 229
- Dullemond C. P., Apai D., Walch S., 2006, *ApJ Letters*, 640, L67
- Dullemond C. P., Dominik C., 2008, *A&A*, 487, 205
- Dullemond C. P., Dominik C., Natta A., 2001, *ApJ*, 560, 957

- Durisen R. H., Pickett B. K., Bate M. R., Imamura J. N., Brandl A., Sterzik M. F., 2000, in IAU Symposium Vol. 200 of IAU Symposium, Dynamic Instability of Barlike Modes. p. 187P
- Ebert R., 1955, *Zeitschrift für Astrophysik*, 37, 217
- Elmegreen B. G., 1993, *ApJ Letters*, 419, L29+
- Elmegreen B. G., 2000, *ApJ*, 530, 277
- Emden R., 1907, p. Table 14
- Ewell M. W. J., 1988, PhD thesis, AA(Princeton Univ., NJ.)
- Foster P. N., Chevalier R. A., 1993, *ApJ*, 416, 303
- Gammie C. F., 2001, *ApJ*, 553, 174
- Gingold R. A., Monaghan J. J., 1977, *MNRAS*, 181, 375
- Gingold R. A., Monaghan J. J., 1983, *MNRAS*, 204, 715
- Goldreich P., Lynden-Bell D., 1965, *MNRAS*, 130, 125
- Goldsmith P. F., Arquilla R., 1985, in Black D. C., Matthews M. S., eds, *Protostars and Planets II Rotation in dark clouds*. pp 137–149
- Goodman A. A., Barranco J. A., Wilner D. J., Heyer M. H., 1998, *ApJ*, 504, 223
- Goodman A. A., Benson P. J., Fuller G. A., Myers P. C., 1993, *ApJ*, 406, 528
- Goodwin S. P., Kroupa P., 2005, *A&A*, 439, 565
- Goodwin S. P., Kroupa P., Goodman A. A., Burkert A., 2006, in Reipurth B., Jewitt D., Keil K., eds, *Protostars and Planets V The fragmentation of cores and the initial binary population*
- Goodwin S. P., Whitworth A. P., Ward-Thompson D., 2004a, *A&A*, 414, 633
- Goodwin S. P., Whitworth A. P., Ward-Thompson D., 2004b, *A&A*, 414, 633
- Goodwin S. P., Whitworth A. P., Ward-Thompson D., 2004c, *A&A*, 423, 169
- Goodwin S. P., Whitworth A. P., Ward-Thompson D., 2006, *A&A*, 452, 487
- Gritschneider M., Naab T., Burkert A., Walch S., Heitsch F., Wetzstein M., 2008, ArXiv e-prints
- Gullbring E., Hartmann L., Briceno C., Calvet N., 1998, *ApJ*, 492, 323
- Hartigan P., Edwards S., Ghandour L., 1995, *ApJ*, 452, 736
- Hartmann L., 2003, *ApJ*, 585, 398

- Hartmann L., Ballesteros-Paredes J., Bergin E. A., 2001, *ApJ*, 562, 852
- Heitsch F., Burkert A., Hartmann L. W., Slyz A. D., Devriendt J. E. G., 2005, *ApJ Letters*, 633, L113
- Hennebelle P., Whitworth A. P., Gladwin P. P., André P., 2003, *MNRAS*, 340, 870
- Hernquist L., Katz N., 1989, *ApJS*, 70, 419
- Heyer M. H., Brunt C. M., 2004, *ApJ Letters*, 615, L45
- Hockney R. W., Eastwood J. W., 1981, *Computer Simulation Using Particles. Computer Simulation Using Particles*, New York: McGraw-Hill, 1981
- Hogerheijde M. R., Sandell G., 2000, *ApJ*, 534, 880
- Hubber D. A., Whitworth A. P., 2005, *A&A*, 437, 113
- Inutsuka S., Masunaga H., 2001, in Montmerle T., André P., eds, *From Darkness to Light: Origin and Evolution of Young Stellar Clusters Vol. 243 of Astronomical Society of the Pacific Conference Series, Radiation Hydrodynamical Models for Protostellar Collapse*. p. 199
- Jeans J. H., 1928, *Astronomy and cosmogony*. Cambridge [Eng.] The University press, 1928.
- Jessop N. E., Ward-Thompson D., 2000, *MNRAS*, 311, 63
- Jijina J., Myers P. C., Adams F. C., 1999, *ApJS*, 125, 161
- Johnstone D., Wilson C. D., Moriarty-Schieven G., Joncas G., Smith G., Gregersen E., Fich M., 2000, *ApJ*, 545, 327
- Jørgensen J. K., Johnstone D., Kirk H., Myers P. C., 2007, *ApJ*, 656, 293
- Joung M. K. R., Mac Low M.-M., 2006, *ApJ*, 653, 1266
- Joy A. H., 1949, *ApJ*, 110, 424
- Kandori R., Nakajima Y., Tamura M., Tatematsu K., Aikawa Y., Naoi T., Irsf/Sirius Team 2005, in *Protostars and Planets V Near Infrared Imaging Survey of Bok Globules: Density Structure*. p. 8071
- Kenyon S. J., Hartmann L., 1987, *ApJ*, 323, 714
- Kenyon S. J., Hartmann L., 1995, *ApJS*, 101, 117
- Kirk J. M., Ward-Thompson D., André P., 2005, *MNRAS*, 360, 1506
- Klahr H. H., Bodenheimer P., 2003, *ApJ*, 582, 869

- Klein R. I., Fisher R., McKee C. F., 2001, in Zinnecker H., Mathieu R., eds, *The Formation of Binary Stars* Vol. 200 of IAU Symposium, Fragmentation and Star Formation in Turbulent Cores. p. 361
- Klein R. I., Fisher R. T., McKee C. F., Krumholz M. R., 2004, in Johnstone D., Adams F. C., Lin D. N. C., Neufeld D. A., Ostriker E. C., eds, *Star Formation in the Interstellar Medium: In Honor of David Hollenbach* Vol. 323 of Astronomical Society of the Pacific Conference Series, Recent Advances in the Collapse and Fragmentation of Turbulent Molecular Cloud Cores. p. 227
- Klessen R. S., 2001, *ApJ*, 556, 837
- Kolmogorov A., 1941, *Akademiia Nauk SSSR Doklady*, 30, 301
- Kroupa P., 1995, *MNRAS*, 277, 1507
- Kroupa P., 2001, *MNRAS*, 322, 231
- Kroupa P., Burkert A., 2001, *ApJ*, 555, 945
- Krumholz M. R., McKee C. F., Klein R. I., 2006, *ApJ*, 638, 369
- Kuiper G. P., 1951, *Proceedings of the National Academy of Science*, 37, 383
- Lacey C. G., Fall S. M., 1985, *ApJ*, 290, 154
- Lada C. J., 1987, in Peimbert M., Jugaku J., eds, *Star Forming Regions* Vol. 115 of IAU Symposium, *Star formation - From OB associations to protostars*. pp 1–17
- Lada C. J., 2006, *ApJ Letters*, 640, L63
- Lada C. J., Alves J. F., Lombardi M., 2007, in Reipurth B., Jewitt D., Keil K., eds, *Protostars and Planets V Near-Infrared Extinction and Molecular Cloud Structure*. pp 3–15
- Lada C. J., Bergin E. A., Alves J. F., Huard T. L., 2003, *ApJ*, 586, 286
- Lada C. J., Lada E. A., Clemens D. P., Bally J., 1994, *ApJ*, 429, 694
- Lada C. J., Muench A. A., Lada E. A., Alves J. F., 2004, *AJ*, 128, 1254
- Lada C. J., Wilking B. A., 1984, *ApJ*, 287, 610
- Landau L. D., Lifschitz E. M., 1966, *Lehrbuch der theoretischen Physik, Band VI, Hydrodynamik. Lehrbuch der theoretischen Physik, Band VI, Hydrodynamik*, Berlin: Akademie-Verlag, 1966
- Larson R. B., 1969, *MNRAS*, 145, 271
- Larson R. B., 1981, *MNRAS*, 194, 809

- Lattanzio J. C., Monaghan C. C., Pongracic H., Schwarz M. P., 1986, *SIAM J. Scient. Comp.*, 7, 591
- Li Y., Mac Low M.-M., Klessen R. S., 2005, *ApJ Letters*, 620, L19
- Lilley A. E., 1955, *ApJ*, 121, 559
- Liverts E., Griv E., Eichler D., Gedalin M., 2000, *Ap&SS*, 274, 315
- Lombardi J. C., Sills A., Rasio F. A., Shapiro S. L., 1999, *Journal of Computational Physics*, 152, 687
- Lombardi M., Alves J., 2001, *A&A*, 377, 1023
- Lombardi M., Alves J., Lada C. J., 2006, *A&A*, 454, 781
- Looney L. W., Mundy L. G., Welch W. J., 2003, *ApJ*, 592, 255
- Lucy L. B., 1977, *AJ*, 82, 1013
- Lynden-Bell D., 1964, *ApJ*, 139, 1195
- Mac Low M.-M., Klessen R. S., 2004, *Reviews of Modern Physics*, 76, 125
- Mac Low M.-M., Ossenkopf V., 2000, *A&A*, 353, 339
- Mac Low M.-M., Smith M. D., Klessen R. S., Burkert A., 1998, *Ap&SS*, 261, 195
- Matsumoto T., Hanawa T., 2003, *ApJ*, 595, 913
- Mayer L., Quinn T., Wadsley J., Stadel J., 2004, *ApJ*, 609, 1045
- McCaughrean M. J., O'Dell C. R., 1996, *AJ*, 111, 1977
- McLaughlin D. E., Pudritz R. E., 1996, *ApJ*, 469, 194
- Meyer M. R., Adams F. C., Hillenbrand L. A., Carpenter J., Larson R. B., 2000, *Protostars and Planets IV*, p. 121
- Miyama S. M., Hayashi C., Narita S., 1984, *ApJ*, 279, 621
- Monaghan J. J., 1989, *J. Comp. Phys.*, 48, 89ff
- Monaghan J. J., 1992, *ARA&A*, 30, 543
- Monaghan J. J., Gingold R. A., 1983, *J. Comp. Phys.*, 52, 374
- Monaghan J. J., Lattanzio J. C., 1985, *A&A*, 149, 135
- Morris J. P., Monaghan J. J., 1997, *Journal of Computational Physics*, 136, 41

- Motte F., André P., 2001, *A&A*, 365, 440
- Motte F., Andre P., Neri R., 1998, *A&A*, 336, 150
- Muench A. A., Lada E. A., Lada C. J., Alves J., 2002, *ApJ*, 573, 366
- Myers P. C., 1983, *ApJ*, 270, 105
- Myers P. C., 2005, *ApJ*, 623, 280
- Myers P. C., Fuller G. A., 1993, in Cassinelli J. P., Churchwell E. B., eds, *Massive Stars: Their Lives in the Interstellar Medium Vol. 35 of Astronomical Society of the Pacific Conference Series, Star Formation with Nonthermal Motions*. p. 70
- Myers P. C., Gammie C. F., 1999, *ApJ Letters*, 522, L141
- Naab T., Jesseit R., Burkert A., 2006, *MNRAS*, 372, 839
- Narayanan G., Heyer M. H., Brunt C., Goldsmith P. F., Snell R., Li D., 2008, *ApJS*, 177, 341
- Nelson A. F., 2006, *MNRAS*, 373, 1039
- Nelson A. F., Wetzstein M., Naab T., . 2008, *ArXiv e-prints*, 802
- Neufeld D. A., Green S., 1994, *ApJ*, 432, 158
- Neufeld D. A., Lepp S., Melnick G. J., 1995, *ApJS*, 100, 132
- Onishi T., Mizuno A., Kawamura A., Ogawa H., Fukui Y., 1998, *ApJ*, 502, 296
- Onishi T., Mizuno A., Kawamura A., Tachihara K., Fukui Y., 2002, *ApJ*, 575, 950
- Padgett D. L., Brandner W., Stapelfeldt K. R., Strom S. E., Terebey S., Koerner D., 1999, *AJ*, 117, 1490
- Padoan P., Goodman A. A., Juvela M., 2003, *ApJ*, 588, 881
- Padoan P., Jimenez R., Juvela M., Nordlund Å., 2004, *ApJ Letters*, 604, L49
- Padoan P., Juvela M., Kritsuk A., Norman M. L., 2006, *ApJ Letters*, 653, L125
- Padoan P., Nordlund Å., 1999, *ApJ*, 526, 279
- Pavlovski G., Smith M. D., Mac Low M.-M., Rosen A., 2002, *MNRAS*, 337, 477
- Penston M. V., 1969, *MNRAS*, 144, 425
- Pickett B. K., Cassen P., Durisen R. H., Link R., 1998, *ApJ*, 504, 468
- Pickett B. K., Cassen P., Durisen R. H., Link R., 2000, *ApJ*, 529, 1034

- Porter D. H., 1985, PhD thesis, AA(California Univ., Berkeley.)
- Predehl P., Schmitt J. H. M. M., 1995, *A&A*, 293, 889
- Press W. H., 1986, in Hut P., McMillan S. L. W., eds, *The Use of Supercomputers in Stellar Dynamics Vol. 267 of Lecture Notes in Physics*, Berlin Springer Verlag, Techniques and Tricks for N-Body Computation. p. 184
- Pudritz R. E., Norman C. A., 1986, *ApJ*, 301, 571
- Rice W. K. M., Armitage P. J., Bate M. R., Bonnell I. A., 2003, *MNRAS*, 339, 1025
- Roberts Jr. W. W., Huntley J. M., van Albada G. D., 1979, *ApJ*, 233, 67
- Rosswog S., Davies M. B., Thielemann F.-K., Piran T., 2000, *A&A*, 360, 171
- Salpeter E. E., 1955, *ApJ*, 121, 161
- Shu F. H., 1977, *ApJ*, 214, 488
- Sicilia-Aguilar A., Hartmann L., Calvet N., Megeath S. T., Muzerolle J., Allen L., D'Alessio P., Merín B., Stauffer J., Young E., Lada C., 2006, *ApJ*, 638, 897
- Spitzer L. J., 1942, *ApJ*, 95, 329
- Springel V., Yoshida N., White S. D. M., 2001, *New Astronomy*, 6, 79
- Steinmetz M., Mueller E., 1993, *A&A*, 268, 391
- Stolte A., Brandner W., Brandl B., Zinnecker H., 2006, *AJ*, 132, 253
- Stone J. M., Ostriker E. C., Gammie C. F., 1998, *ApJ Letters*, 508, L99
- Swift J. J., 2006, PhD thesis, University of California, Berkeley
- Teixeira P. S., Lada C. J., Alves J. F., 2005, *ApJ*, 629, 276
- Terebey S., Shu F. H., Cassen P., 1984, *ApJ*, 286, 529
- Testi L., Sargent A. I., 1998, *ApJ Letters*, 508, L91
- Tohline J. E., 1982, *Fundamentals of Cosmic Physics*, 8, 1
- Toomre A., 1964, *ApJ*, 139, 1217
- Truelove J. K., Klein R. I., McKee C. F., Holliman II J. H., Howell L. H., Greenough J. A., 1997, *ApJ Letters*, 489, L179+
- Vázquez-Semadeni E., Ryu D., Passot T., González R. F., Gazol A., 2006, *ApJ*, 643, 245

Vazquez-Semadent E., Passot T., Pouquet A., 1995, *ApJ*, 441, 702

Vicente S. M., Alves J., 2005, *A&A*, 441, 195

Walker M. F., 1956, *ApJS*, 2, 365

Ward-Thompson D., Motte F., Andre P., 1999, *MNRAS*, 305, 143

Wetzstein M., Nelson A. F., Naab T., Burkert A., 2008, *ArXiv e-prints*, 802

White R. J., Hillenbrand L. A., 2004, *ApJ*, 616, 998

Whitworth A. P., Goodwin S. P., 2005, *Astronomische Nachrichten*, 326, 899

Young C. H., Bourke T. L., Young K. E., Evans II N. J., Jørgensen J. K., Shirley Y. L., van Dishoeck E. F., Hogerheijde M., 2006, *AJ*, 132, 1998

Zuckerman B., Palmer P., 1974, *ARA&A*, 12, 279

Acknowledgments / Danksagung

First of all, I would like to thank my supervisor Andreas Burkert for his generous financial support which enabled me to attend nice conferences and meet the right people to establish my further career in Astrophysics. Thank you for always being the spark who ignited to deeply dig for - and into - more physics.

This work also owes much inspiration to Thorsten Naab, who's contributions and detailed comments have been of great value to me. Thank you for supporting my work as well as my intellectual, mental and emotional sanity during the last two years of my PhD.

Furthermore I would like to thank

Matthias Gritschneider, who has been one of my best friends and colleagues since my undergraduate years in Regensburg. I cherish our fruitful discussions and hope that you will resist the Dark Side for some more years so that we can still work together.

'The Boyz', who have played a decisive role in saving me from leaving Astrophysics. Michael Hilz, Ludwig Oser and Simon Karl, without your continuous 5* food supply, your reconstructive words and the relaxing afternoon get-togethers at the terrace this thesis would not have been written.

Kees Dullemond for encouraging me to start working in Astrophysics, for giving me the opportunity to do so, and for his time and patience in supporting my first steps.

Hanna Kotarba and Michaela Hirschmann - the best office mates ever - for establishing an inspiring environment with a new interior design, in addition to just being girls.

Peter Johansson for not deleting my files before I finish my PhD and for teaching me the most important finnish words.

Roland Jesseit for making me aware of exacerbated deadline constraints.

Pawel Ciecielag for his patience and his help during the first two years of my PhD. I learned more about numerical methods than I would have ever guessed. Also thanks for dragging me out of the ice bar in time...

The rest of the CAST group for lively meetings with many delicious cakes and a warm atmosphere.

Julia Bonini for being back in my life and making it so much more cheerful. I will miss you so much when I move. Like I will of course miss my Mum, who is always backing me all the way, but who also set me back on the right track throughout my whole life. Thank you for your love and support. I equally much thank my Dad, even though I cannot possibly miss him more than I do already. It has always been a great experience to watch the stars with you and I hope you are fine if I make a career in science even though there is no money in that. I guess concerning the

money issue I will have to follow the advice of my clever Grandma Alice and marry a rich man. She is the best Grandma anyway, and I very much enjoy our lively discussions at lunch time. Of course I also thank my sister Reni for getting my mathematical carrier started many years ago. Thank you for your inspiration, cheerfulness and valuable ideals which have been accompanying me throughout my life. I also thank Laura and Benni for making me the most proud of all aunts alive, as well as my own aunt Inge for her good nature and her interest in my work. Thanks also to Max for making me grow up enough to fledge and finally leave this country.

And last but not least, a big thank you to all the people in the institute for providing such a friendly work atmosphere, and for a number of nice barbequees and Christmas parties.

CURRICULUM VITAE RESUME

Stefanie Walch

ADDRESS

Stefanie Walch
Universitäts-Sternwarte München
Lehrstuhl: Computational Astrophysics
Scheinerstr. 1
D-81679 München
Germany

PhD Student
Email: swalch@usm.uni-muenchen.de

Phone: +49-89-2180-6030
Fax: +49-89-2180-6003

PERSONAL DATA

Date of birth: July, 30th, 1979
Place of birth: Landshut, Bavaria, Germany
Nationality: German

EDUCATION

- 09/2004 - 10/2008: PhD Thesis;
Research at Universitäts-Sternwarte München, München
Advisor: Prof. Dr. Andreas Burkert
- 2004: Diplom in Physics, Ludwig-Maximilians University, München;
Diploma Thesis research at the
Max-Planck Institut for Astrophysics, Garching
- 2000: Vordiplom in Physics, Universität Regensburg, Regensburg
- 1998: Girls High School Kloster Seligenthal, Landshut

LANGUAGES

German (native), English (fluent), French (basic)

AWARDS

PhD Fellowship of the International Max-Planck Research School

RESEARCH INTERESTS AND QUALIFICATIONS

Formation and evolution of stars, formation and evolution of disks (protostellar and protoplanetary), stellar multiplicity, planet formation, stellar feedback, ionization, winds and outflows, radiation transport, angular momentum transport in general (also viscous evolution of spiral galaxies, tidal torques, growth of the galactic dynamo), grid or adaptive mesh refinement and SPH simulations, special purpose hardware for astrophysical applications.

INVITED COLLOQUIA AND SEMINARS

- *Star Formation Seminar*: "The Formation and Evolution of Protostellar Disks - Results from 3D SPH Simulations", European Southern Observatory, Garching, Germany 2008 (invited)
- *Star Formation Seminar*: "The Formation of Protostellar Disks around low-mass Stars", Leiden University, Leiden, The Netherlands 2007 (invited)
- *Institute Colloquium*: "The Formation and Evolution of Protostellar Disks", Cardiff University, Cardiff, UK 2007 (invited)
- *International Max-Planck Research School Seminar*: "Formation and Evolution of Protostellar Disks - Numerical Techniques", Max-Planck Institute for Extraterrestrial Physics, Garching, Germany 2007 (invited)
- *Astrophysical Colloquium*: "Viscous Evolution in Protoplanetary Disks", Nicolaus Copernicus Astronomical Center, Warsaw, Poland 2005 (invited)
- *Evaluation of the International Max-Planck Research School*: "The Formation of Protostellar Disks around low-mass Stars", Max-Planck Institute for Extraterrestrial Physics, Garching, Germany 2005 (invited)
- *International Max-Planck Research School Seminar*: "Viscous Evolution in Protoplanetary Disks", Max-Planck Institute for Extraterrestrial Physics, Garching, Germany 2005 (invited)
- *Institute Colloquium*: "The Long-Term Evolution of Protoplanetary Disks", Max-Planck Institute for Astrophysics, Garching, Germany, 2004 (invited)

TALKS AT CONFERENCES AND WORKSHOPS

- *AstroSim Conference: Frontiers in Computational Astrophysics: The Origin of Stars, Planets and Galaxies* "The Formation and Early Evolution of Protostellar Disks around low-mass Stars - Turbulent vs. Non-turbulent Core Collapse", Ascona, Switzerland 2008 (invited)

- *Next Generation of Computational Models of Baryonic Physics in Galaxy Formation: From Protostellar Cores to Disk Galaxies* "The Formation and Early Evolution of Protostellar Disks around low-mass Stars", Zürich, Switzerland 2007 (invited)
- *Introductory Workshop: Excellence Cluster Universe Research Area G* "The Formation of low-mass Stars", University Observatory, Munich, Germany 2007 (invited)
- *Disks 2006: Workshop on Physical Processes in Circumstellar Disks around Young Stars* "The Formation and Early Evolution of Protostellar Disks around low-mass Stars", Vidago, Portugal 2006 (invited)
- *2nd Munich-Zurich Workshop on Computational Astrophysics* "Viscous Evolution in Spiral Galaxies", Zürich, Switzerland, 2005 (invited)
- *Ringberg Workshop on Planet Formation: Theory meets Observation* "Formation and Viscous Evolution of Protoplanetary Disks", Ringberg Castle, Tegernsee, Germany 2004 (invited)

CONFERENCES ATTENDED (Poster Presentations)

- *The Molecular Universe* Arcachon, France, 2008 (Poster Presentation)
- *12 Questions on Star and Massive Star Cluster Formation* ESO, Garching, Germany, 2006 (Poster Presentation)
- *IAU General Assembly* Prague, Czech Republic, 2006 (Poster Presentation)
- *Meeting of the EU Network 'Planets'* Fréjus, France, 2004 (Poster Presentation)
- *Workshop: Modeling the Structure, Chemistry and Appearance of Protoplanetary Disks* Ringberg Castle, Tegernsee, 2004 (Poster Presentation)

TEACHING EXPERIENCE

- Since February 2008: Diploma student supervision
- Since September 2006: Student Seminar supervision
- April 2005 - August 2005: Supervision of exercises in 'Theoretical Physics I: Theoretical Mechanics' at the University of Munich.
- October 2003 - March 2004: Supervision of student practical excersises at the Technical University of Munich

- October 2000 - March 2001: Supervision of excersises in mathematics: 'Mathematics for Physicists' at the University of Regensburg

PUBLICATIONS

Refereed Articles

- Sollerman, J.; Jaunsen, A. O.; Fynbo, J. P. U.; Hjorth, J.; Jakobsson, P.; Stritzinger, M.; Féron, C.; Laursen, P.; Ovaldsen, J.-E.; Selj, J.; Thöne, C. C.; Xu, D.; Davis, T.; Gorosabel, J.; Watson, D.; Duro, R.; Ilyin, I.; Jensen, B. L.; Lysfjord, N.; Marquart, T.; Nielsen, T. B.; Näränen, J.; Schwarz, H. E.; Walch, S.; Wold, M.; Östlin, G., “*Supernova 2006aj and the associated X-Ray Flash 060218*”, A&A 454, 503ff, (2006)
- Stritzinger, M.; Leibundgut, B.; Walch, S.; Contardo, G., “*Constraints on the progenitor systems of type Ia supernovae*”, A&A 450, 241ff, (2006)
- Dullemond, C. P.; Apai, D.; Walch, S., “*Crystalline Silicates as a Probe of Disk Formation History*”, ApJ 640, 67ff (2006)
- Dominik, C.; Dullemond, C. P.; Waters, L. B. F. M.; Walch, S., “*Understanding the spectra of isolated Herbig stars in the frame of a passive disk model*”, A&A 398, 607ff, (2003)

Conference Proceedings

- Edgar, R. G.; Gawryszczak, A.; Walch, S., “*Self-Gravity Troubles with Adaptive Mesh Refinement*”, Protostars and Planets V, Proceedings of the Conference held October 24-28, 2005, LPI Contribution No. 1286., p.8005

To be submitted in 2008

- Walch, S.; Burkert, A.; Naab, T.; Gritschneder, M.; “*Protostellar disks in low-mass star formation: - I.Thin and thick disks: The role of gas thermodynamics*”, to be submitted
- Walch, S.; Burkert, A.; Naab, T.; Gritschneder, M.; “*Protostellar disks in low-mass star formation: - II.The collapse of turbulent cores*”, to be submitted
- Gritschneder, M.; Naab, T.; Walch, S.; Heitsch, F.; Burkert, A.; “*IVINE: A new implementation of treating ionizing radiation with SPH*”, accepted for publication
- Gritschneder, M.; Naab, T.; Walch, S.; Heitsch, F.; Burkert, A.; “*Shaping molecular clouds by ionizing radiation: Formation of the Horsehead Nebula*”, to be submitted

- Kitsionas, S.; Klessen, R.; Schmidt, W.; Dursi, J.; Price, D.; Federrath, C.; Walch, S.; Gritschneider, M.; Piontek, M.; Kim, J.; Ciecielag, P.; Jappsen, A.-K.; Niemeyer, J.; Mac Low, M.-M.; “*Algorithmic comparisons of decaying, isothermal, compressible turbulence*”
- Heitsch, F.; Naab, T.; Walch, S.; “*The clump mass function from fragmentation of shocked flows: Results from Eulerian and Lagrangian simulations*”
- Junk, V.; Naab, T.; Heitsch, F.; Walch, S.; Burkert, A.; “*Analytic and numerical growth rates of the Kelvin-Helmholtz Instability*”, to be submitted

OTHER ACTIVITIES AND INTERESTS

- Co-author of popular science books: 2 published
 - “Physics for the waistcoat pocket”, Harald Lesch & das Quot-Team, Piper-Verlag, 10/2003, 125 pages, in german; translated to korean, italian and dutch
 - “Quantum mechanics in everyday life”, Harald Lesch & das Quot-Team, Piper-Verlag, 10/2007, 125 pages, in german
- Since November 2005 I take care of the homepage of the Numerical Astrophysics Group at the University Observatory
- Organization of Meetings:
 - RTN ‘PLANETS’ Meeting in Heidelberg, October 2006 (<http://www.usm.uni-muenchen.de/Planets/LastMeeting/>)
 - Computational Astrophysics Group Meeting 2007 at Kloster Seeon, Chiemsee
 - Group Retreat 2008: Computational Astrophysics Group and AGNΦ@MPE at Alpenclub Schliersee, Schliersee.
- In 2000/2001: Elected student representative at the University of Regensburg
- Further interests, hobbies: Horse-riding (active), Skiing, Art